The development of hepatocellular carcinoma models in precision-cut tissue slices for therapeutic screening and precision medicine

Amy Lauren Collins

Doctor of Philosophy

Newcastle University

Biosciences Institute

November 2023

Abstract

Liver cancer is the third most common cause of cancer-related death worldwide, and hepatocellular carcinoma (HCC) accounts for approximately 90% of cases. Recent therapeutic advances extend overall survival by a few months, but only for a minority of patients. Realistic HCC models are necessary in order to provide valuable insight into disease pathogenesis and drug discovery. Here I describe the development of two HCC models in precision-cut liver slices (PCLS): a murine precision-cut tumour slice (PCTS) model and a spheroid-engrafted human PCLS model. An orthotopic mouse model of HCC was generated using the Hep-53.4 cell line, and PCTS were subsequently generated from the tumours. Histological characterisation determined that Hep-53.4 PCTS retain the histological characteristics of *in vivo* tumours, and mimic the *in vivo* therapeutic responses to sorafenib and lenvatinib. Intervention with anti-PD1 immunotherapy significantly increased CD3 T cell numbers and apoptosis – a response that was lost upon lipid-loading of the PCTS. After initial optimisation using murine PCLS and Hep-53.4 cells, a human HCC model was developed by engrafting spheroids generated from HuH7 cells that express a secreted luciferase onto human PCLS. Complete invasion of the spheroids into the PCLS was confirmed via multiphoton imaging, and measurement of luciferase secreted following treatment with tyrosine kinase inhibitors indicated a significant and dose-dependent reduction in cancer growth, whilst the PCLS remained viable. A patient-derived HCC cell line library was generated to tailor the spheroid-PCLS model for precision medicine. Hyperion imaging mass cytometry revealed that both the HuH7 and patient-derived spheroid-PCLS systems stimulated a response from immune components in the surrounding PCLS, alongside potential matrix formation within the HCC spheroid. Thus, the *ex vivo* models developed potentially present as useful tools for discovery biology and precision medicine, where therapies can be tested on patient-derived HCC cells in the context of the tumour microenvironment.

Acknowledgements

I am extremely grateful to my supervisors Professor Fiona Oakley, Professor Derek Mann, Professor Helen Reeves and Professor Kenny Dalgarno for their invaluable advice and continued support throughout this project. In addition to the mentorship I received from them, I appreciate the fantastic opportunities I have been given to present my work at various conferences and meetings.

I would like to extend my thanks to all members of the Newcastle Fibrosis Research Group who have made my time working on this project so enjoyable, with a special thanks to Dr Jack Leslie who has provided valuable guidance, as well as Maja Laszczewska, Erik Ramon-Gil, Rhys Muir and Rainie Cameron who have made important contributions to this project. Additionally, I would like to thank Dr Glyn Nelson from the Newcastle University Bioimaging Unit who has provided continued support.

This work would not be possible without the surgeons and pathologists from the Newcastle upon Tyne Hospitals NHS Foundation Trust, as well as the consenting tissue donors who I am very grateful to.

The work completed during this project was funded by the WE Harker Foundation and FibroFind Ltd.

Finally, I would like to express my gratitude towards my family and friends, particularly my parents and my partner Alex who have been a constant support throughout my PhD.

Table of contents

1 Abbreviations

αSMA	Alpha-smooth muscle actin
AFP	Alpha-fetoprotein
AFP-L3	Lens culinaris agglutinin-reactive AFP
ALD	Alcohol-related liver disease
ALK5	TGF-β type I receptor kinase
ANOVA	Analysis of variance
ARID1A	AT-rich interaction domain 1A
ASH	Alcoholic steatohepatitis
ASPA	Animals (Scientific Procedures) Act 1986
BCLC	Barcelona-Clinic Liver Cancer
BrdU	Bromodeoxyuridine
BSA	Bovine serum albumin
BSC	Best supportive care
CAF	Cancer associated fibroblast
CAR	Chimeric antigen receptor
CCl_4	Carbon tetrachloride
CDAHFD	Choline-deficient, L-amino acid-defined, high fat diet
cDNA	Complementary DNA
CK18	Cytokeratin 18
CLD	Chronic liver disease
CLIP	Cancer of the Liver Italian Program
CRC	Colorectal cancer
CT	Computed tomography
CTL	Cytotoxic T lymphocyte
CTLA-4	Cytotoxic T-lymphocyte-associated protein 4
CUPI	Chinese University Prognostic Index
CyTOF	Cytometry by time-of-flight
DC	Dendritic cell
DCP	Des-gamma-carboxyprothrombin

DEN	Di-ethylnitrosamine
ECM	Extracellular matrix
EDTA	Ethylenediaminetetraacetic acid
EGF	Epidermal growth factor
ELISA	Enzyme linked immunosorbent assay
EMT	Epithelial-mesenchymal transition
EPCAM	Epithelial cell adhesion molecule
FFPE	Formalin-fixed paraffin-embedded
FGF	Fibroblast growth factor
GAN	Gubra Amylin NASH
GEM	Genetically engineered mouse
GLI1	GLI family zinc finger 1
GPC3	Glypican-3
H&E	Haematoxylin & Eosin
HBV	Hepatitis B virus
HCA	Hepatic adenoma
HCC	Hepatocellular carcinoma
HCV	Hepatitis C virus
HepPar1	Hepatocyte specific antigen/hepatocyte paraffin 1
HGDN	High-grade dysplastic nodule
HGF	Hepatocyte growth factor
HRP	Horseradish peroxidase
HSC	Hepatic stellate cell
HSD17B13	Hydroxysteroid 17-beta dehydrogenase 13
HUVEC	Human umbilical vein endothelial cell
ICI	Immune checkpoint inhibitor
IDO	Indoleamine 2,3-dioxygenase
IF	Immunofluorescence
IFN-γ	Interferon-γ
IHC	Immunohistochemistry
IL	Interleukin

IMC	Imaging mass cytometry
IVIS	In vivo imaging systems
JIS	Japanese integrated staging
LAG-3	Lymphocyte-activation gene 3
LDH	Lactate dehydrogenase
LDL	Low-density lipoprotein
LGDN	Low-grade dysplastic nodule
LI-RADS	Liver imaging reporting and data system
LPS	Lipopolysaccharide
LRP	Lipoprotein receptor-related protein
LSEC	Liver sinusoidal endothelial cell
MASH	Metabolic associated steatohepatitis
MASLD	Metabolic dysfunction-associated steatotic liver disease
MCTS	Multicellular tumour spheroids
MDSC	Myeloid derived suppressor cell
MHC	Major histocompatibility complex
M-MDSC	Monocytic myeloid derived suppressor cell
MMP	Matrix metalloproteinase
MRI	Magnetic resonance imaging
NAFLD	Non-alcoholic fatty liver disease
NASH	Non-alcoholic steatohepatitis
NET	Neutrophil extracellular trap
NF-κB	Nuclear factor-κB
NK	Natural killer
NKG2A	Natural killer group 2, member A
NKG2D	Natural killer group 2, member D
NLR	Neutrophil-to-lymphocyte ratio
NOX2	NADPH oxidase
ORR	Overall response rate
OS	Overall survival
PARP1	Poly (ADP-ribose) polymerase 1

PBMC	Peripheral blood mononuclear cell
PCLS	Precision-cut liver slice
PCTS	Precision-cut tumour slice
PD-1	Programmed cell death protein 1
PDGF	Platelet-derived growth factor
PDGFR	Platelet-derived growth factor receptor
PD-L1	Programmed death ligand 1
PFA	Paraformaldehyde
PFS	Progression-free survival
PLC	Primary liver cancer
PMN-MDSC	Polymorphonuclear myeloid derived suppressor cell
PNPLA3	Patatin-like phospholipase domain containing 3
PTEN	Phosphatase and tensin homolog
qPCR	Quantitative polymerase chain reaction
RD	Reagent diluent
ReJI	Reactive jet impingement
RFP	Red fluorescent protein
RNA	Ribonucleic acid
ROI	Region of interest
ROS	Reactive oxygen species
RTK	Receptor tyrosine kinase
SCID	Severe combined immunodeficiency
SEM	Standard error of the mean
SHARP	Sorafenib HCC Assessment Randomized Protocol
SNP	Single nucleotide polymorphism
SNV	Single nucleotide variant
STAM	Stelic animal model
TACE	Transarterial chemoembolization
TAM	Tumour associated macrophage
TAN	Tumour associated neutrophil
TBS-T	Tris-Buffered Saline + 0.1% Tween

TERT	Telomerase reverse transcriptase
TGF-β	Transforming growth factor beta
THOC5	THO complex subunit 5 homolog
TIM-3	T cell immunoglobulin and mucin-containing molecule 3
TKI	Tyrosine kinase inhibitor
TLR	Toll-like receptor
TM6SF2	Transmembrane 6 superfamily member 2
TME	Tumour microenvironment
TNF	Tumour necrosis factor
TNM	Tumour node metastasis
Tregs	Regulatory T cells
TUNEL	Terminal deoxynucleotidyl transferase-mediated dUTP nick end labelling
VEGF	Vascular endothelial growth factor
VEGFR	Vascular endothelial growth factor receptor
WT	Wild type

2 List of figures

3 List of tables

4 Introduction

4.1 HCC epidemiology & risk factors

4.1.1 Epidemiology

Liver cancer is the third most common cause of cancer-related deaths worldwide, with an incidence of approximately 906,000 new cases each year (1-3). While the mortality rates have fallen for many types of cancer over the past two decades, liver cancer mortality has increased by 75% between 1990 and 2015, with the mortality rate expected to reach 1 million deaths annually worldwide by 2030 (4). Additionally, the relative five-year survival rate is approximately 20%, and the comparable incidence and mortality rates (906,000 and 830,000 respectively) highlight the poor prognosis associated with liver cancer (5). Incidence and mortality rates vary according to geographical region and socioeconomic status, and are commonly a consequence of exposure to various risk factors – primary liver cancer (PLC) mortality is highest in Asian and sub-Saharan populations, where incidence rates exceed 15 per 100,000 inhabitants, while the incidence in Western countries is on an upwards trajectory (6). Of the PLCs, hepatocellular carcinoma (HCC) is the most common type, accounting for over 85% of cases (1). The majority of HCC cases are diagnosed in those between 60 and 70 years of age, and the disease predominantly affects men (7).

4.1.2 Risk factors

The worldwide incidence of HCC is variable due to numerous risk factors and their prevalence in different populations. HCC predominantly develops on the background of chronic liver disease (CLD) and cirrhosis, which is the end-stage of fibrogenesis and excessive wound healing; the major aetiological agents responsible include infection with hepatitis B virus (HBV) and hepatitis C virus (HCV), metabolic dysfunction-associated steatotic liver disease (MASLD) or metabolic associated steatohepatitis (MASH), and alcohol-related liver disease (ALD) or alcoholic steatohepatitis (ASH) (3, 8). It is important to note that MASLD and MASH are the new nomenclature for non-alcoholic fatty liver disease (NAFLD) and non-alcoholic steatohepatitis (NASH) respectively, after a consensus to change the definition due to the exclusionary phrase “non-alcoholic” inaccurately capturing the aetiology of the disease, and term “fatty” being considered stigmatising to some (9, 10). In Asia and sub-Saharan Africa where the highest number of HCC cases occur, the major risk factors are aflatoxin B1 exposure

and chronic hepatitis B infection, where risk of disease development correlates with viral load and the duration of infection (11, 12). However, the incidence of viral hepatitis-induced HCC has declined in the past two decades as a result of effective antiviral treatments and the implementation of a vaccination programme against HBV (13-15). In contrast to the decrease in virally driven HCC, the incidence of MASLD and MASH-related HCC is increasing (16). In Europe and North America where diets are typically high in fat and sugar, MASLD and metabolic disorders such as diabetes are increasingly associated with HCC, and are of particular interest due to the high numbers of HCC cases they induce without the typical underlying fibrosis (17). Polymorphisms in patatin-like phospholipase domain containing 3 (PNPLA3) and transmembrane 6 superfamily member 2 (TM6SF2) are associated with an increased risk of HCC development in individuals with MASLD, MASH and alcoholic liver disease (18, 19), whilst a variant of hydroxysteroid 17-beta dehydrogenase 13 (HSD17B13) is linked with a reduced risk of CLD (20). Though exposure to a given risk factor can predispose an individual to develop HCC, development of the disease is typically multifactorial and will often be a culmination of multiple factors relating to genetics, lifestyle (smoking and alcohol intake), metabolism (diet, obesity and diabetes), underlying liver disease and demographic factors such as age, sex and ethnicity (21-28).

4.1.3 Preventative measures against HCC

As CLD has been identified as a major factor predisposing people to HCC, measures taken to reduce the risk of underlying liver disease therefore act as a preventative measure for HCC. For example, the introduction of a HBV vaccination programme in 1984 for new-born children in Taiwan resulted in a 35.9% reduction in the incidence of HCC, and the administration of antiviral therapy for middle-aged individuals reduced HCC incidence by approximately 15% (15, 29). There is currently no effective vaccine against HCV, but successful direct-acting antiviral treatments have elicited a sustained virological response in over 95% of patients, a response which has been linked to a reduction in both liver-related mortality and HCC (30, 31). Conversely, public health measures that address the increasingly significant risk factors MASLD, MASH and ASH are scarce, with little known about the conditions outside of those in the hepatology and gastroenterology community (3, 32). Chemoprevention can be implemented in individuals with established liver disease with the intention of preventing HCC development, and measures include low-dose aspirin, statins and metformin (33-35). In

addition, surveillance in individuals at high risk of HCC development can lead to early detection and drastically improve the disease prognosis. In these populations, an abdominal ultrasound alongside the determination of serum alpha-fetoprotein (AFP) levels at six-monthly intervals has the ability to detect HCC in the early stages of development (36). However, the accuracy and effectiveness of these measures are controversial, with ultrasound demonstrating limited sensitivity and AFP measurements yielding false-positives and suboptimal cost-effectiveness (37-39).

4.2 Pathogenesis

4.2.1 Hepatocarcinogenesis in the context of cirrhosis

HCC develops predominantly of the background of liver cirrhosis, accounting for 70-80% of cases, and arises via a complex multistep process (40). On average, HCC development occurs approximately 10 years after cirrhosis develops, as cirrhotic pre-cancerous nodules undergo malignant transformation as hepatocytes adopt a proliferative phenotype and gain an invasive and metastatic potential in a vascularised environment (41). Solid hepatic nodules identified via screening methods such as abdominal ultrasound, computed tomography (CT) or magnetic resonance imaging (MRI) should be investigated to assess whether they possess malignant qualities, and the liver imaging reporting and data system (LI-RADS) was developed to aid in the diagnosis of HCC without requiring an invasive tissue biopsy. The system considers tumour size, growth rate and capsule properties to distinguish between HCC, other hepatic malignancies, and benign nodules (42).

4.2.2 Hepatocarcinogenesis in the context of MASLD

Hepatocarcinogenesis commonly occurs in the context of MASLD, progressing through a sequence of liver disease phenotypes. Steatosis describes an accumulation of lipids, often resultant of high-fructose diets or metabolic disorders. This steatotic environment progresses to MASH in a minority of cases, with sustained hepatic inflammation, fibrosis and aberrant hepatocyte necrosis and regeneration (43, 44). These events can culminate in cirrhosis, which describes the severe scarring of the liver alongside poor liver function, creating an abnormal niche which favours multiple genetic and epigenetic alterations leading to HCC initiation (Figure 1) (45, 46). It is possible for HCC to develop in patients with MASLD or MASH in the absence of cirrhosis – an observation which is present in 25-50% of MASLD-HCC cases and presents significant obstacles. Although these patients may benefit from curative therapies

such as resection, limited surveillance in patients without cirrhosis often prevents HCC detection at early stages and results in a poor prognosis (47).

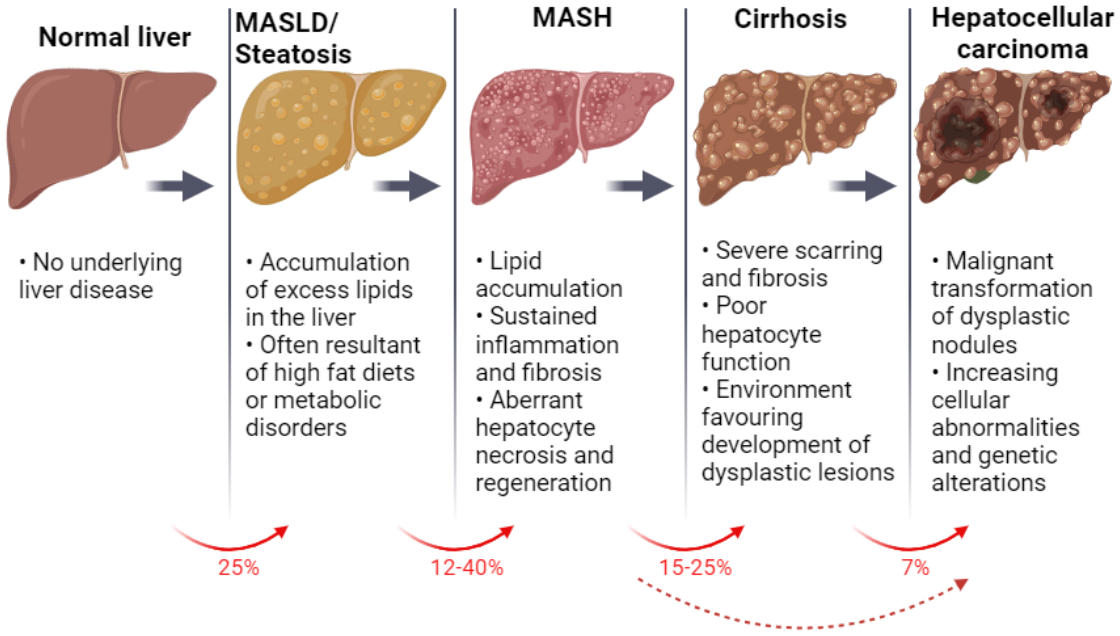

Figure 1. Hepatocarcinogenesis in the context of metabolic dysfunction-associated steatotic liver disease (MASLD). A schematic demonstrating the pathogenesis of HCC developing on a background of MASLD. Approximately 25% of the population develop steatosis, and 12-40% of individuals with steatosis progress to MASH as the environment becomes inflammatory and fibrotic. 15-25% of MASH cases evolve into cirrhosis with severe scarring and poor liver function, before malignant transformation occurs in 7% of cirrhotic livers, resulting in HCC (10-13). HCC also develops in a number of patients with MASH in the absence of cirrhosis. Created with BioRender.com

4.2.3 Hepatocarcinogenesis in the context of ALD

In individuals with alcohol-related HCC, fibrosis and cirrhosis develop following the metabolism of alcohol to acetaldehyde by alcohol dehydrogenase and cytochrome P450 2E1 (48). The production of reactive oxygen species (ROS) during this process activates hepatic stellate cells (HSCs) and leads to fibrosis, and acetaldehyde production results in inflammation and DNA hypomethylation through the formation of DNA adducts, culminating in hepatocarcinogenesis as genetic stability is lost (23, 49). Other contributing factors to alcohol-related hepatocarcinogenesis include the alcohol-mediated alteration in gut permeability and subsequent translocation of gut bacteria and lipopolysaccharides (LPS) to the liver. This results in the activation of Kupffer cells, which secrete pro-inflammatory cytokines and chemokines; the secretion of these pro-inflammatory factors promotes fibrosis and activation of the oncogenic interleukin (IL) 6/STAT3 and tumour necrosis factor (TNF)-nuclear factor-κB (NF-κB) signalling pathways (23, 50).

4.2.4 Dysplastic lesions

Dysplastic foci (<1mm diameter) and dysplastic nodules (<2cm diameter) develop as groups of hepatocytes with premalignant cytological abnormalities. Epigenetic factors have been identified as important regulators in the advancement of dysplastic lesions to HCC, following genome-wide DNA-methylation studies (51, 52). A retrospective study of patients with cirrhosis and at least one identified hypervascular, pre-neoplastic nodule deduced that the severity of underlying liver disease predicts the risk of hepatocarcinogenesis; the risk of individuals undergoing malignant transformation was 10.1 and 32.6-fold greater for those with Child-Pugh B and C respectively, in comparison to Child-Pugh A patients (53). A sequence of lesions is observed as HCC develops; low-grade dysplastic nodules (LGDNs) with little cytological atypia progress to high-grade dysplastic nodules (HGDNs) with increased abnormalities and cell density, before evolving into early and advanced HCC (54). The risk of malignant transformation in LGDNs and HGDNs is 9% and 32% respectively, increasing as cellular abnormalities become more abundant (Figure 2) (55).

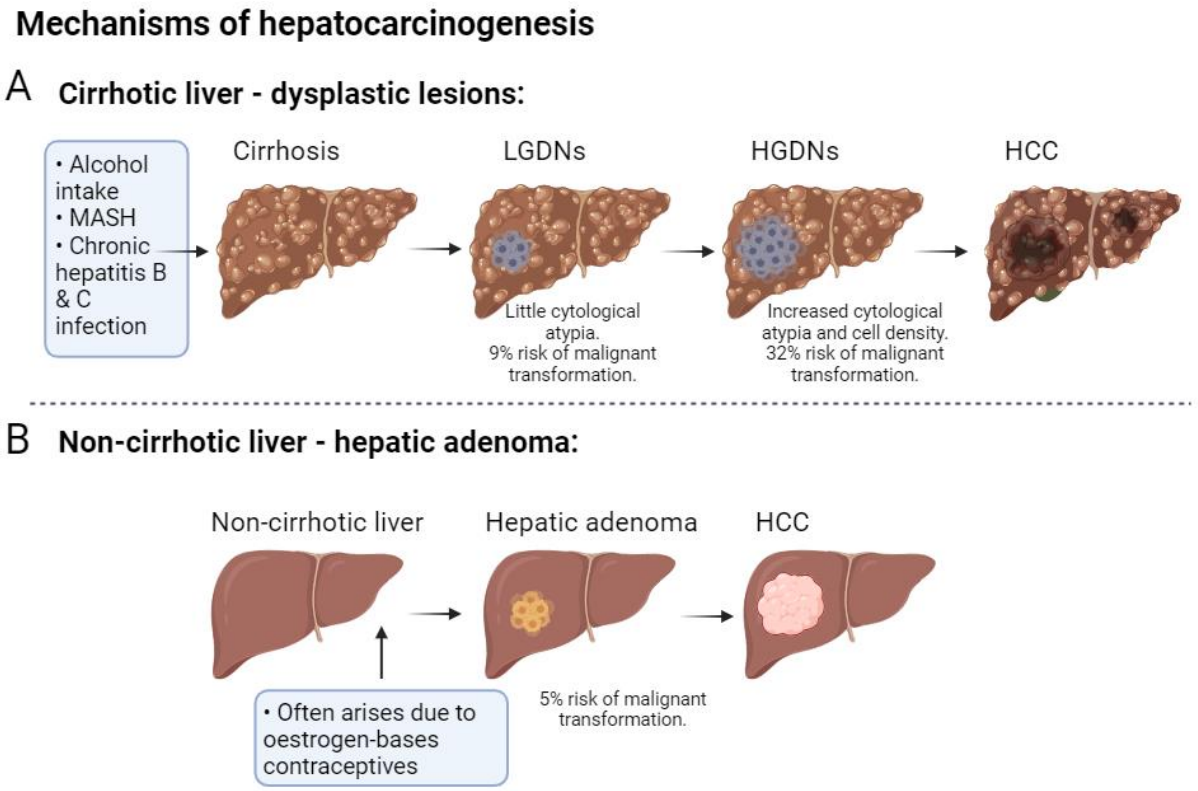

Figure 2. Mechanisms of hepatocarcinogenesis. Different mechanisms of hepatocarcinogenesis: (A) HCC arising in a cirrhotic liver where dysplastic nodules arise as areas with premalignant abnormalities, progressing from LGDNs to HGDNs with increased cytological abnormalities, before progressing to early HCC (14, 15). (B) HCC arising with no underlying liver disease, as HCAs arise and undergo malignant transformation (16, 17). Created with BioRender.com

4.2.5 Hepatic adenomas

While the vast majority of HCC cases develop in patients with CLD, HCC can develop in patients without underlying liver disease and cirrhosis. This occurs when hepatic adenomas (HCA), a rare benign proliferation of hepatocytes, undergo malignant transformation, often arising in women taking oral contraceptives (56, 57). Other risk factors include the use of anabolic steroids, metabolic disorders and obesity (57, 58). Histologically, there is a loss of the typical lobular architecture, with dilated sinusoids and cells arranged into cords (59). The risk of malignant transformation of HCAs is relatively low, at less than 5% (58).

4.3 Molecular heterogeneity

4.3.1 Overview of heterogeneity in HCC

The development of HCC is a complex process, resultant of interplay between genetic and environmental factors. As well as the physical manifestation of the disease in which the tumour interacts with various stromal and immune components, a number of genetic alterations must be considered in relation to the initiation and progression of HCC. There are several single nucleotide polymorphisms (SNPs) associated with HCC at different stages of the disease, impacting factors involved in carcinogenesis such as inflammation, oxidative stress, DNA repair and the cell cycle (60-64). A number of studies have highlighted the existence of trunk mutations, which occur at an earlier stage of development and are present in all tumour cells, and branch mutations, which only occur in a portion of tumour subclones and therefore appear later in tumour development (55). The polymorphisms that are associated with HCC contribute to an increased risk of developing the disease via a number of mechanisms, including through a predisposition to risk factors, the manner in which liver disease progresses to cirrhosis, and the malignant transformation of dysplastic lesions (60).

4.3.2 Categories of heterogeneity

The significant molecular heterogeneity of HCC contributes to the ability of the tumour to grow and evade the immune system (43). This heterogeneity can be observed in different degrees (Figure 3). Firstly, comparing tumours between different patients highlights interpatient heterogeneity, and can aid in the categorising of patients and use of personalised therapy (65). The other forms of heterogeneity observed are intertumoural heterogeneity, which occurs between different tumour nodules in the same patient, and intratumoural heterogeneity, which is between different areas of the same tumour nodule (46). Identifying

genetic alterations in HCC and tracing the evolution of the tumour is crucial in order to target the appropriate pathways and improve the clinical management of HCC.

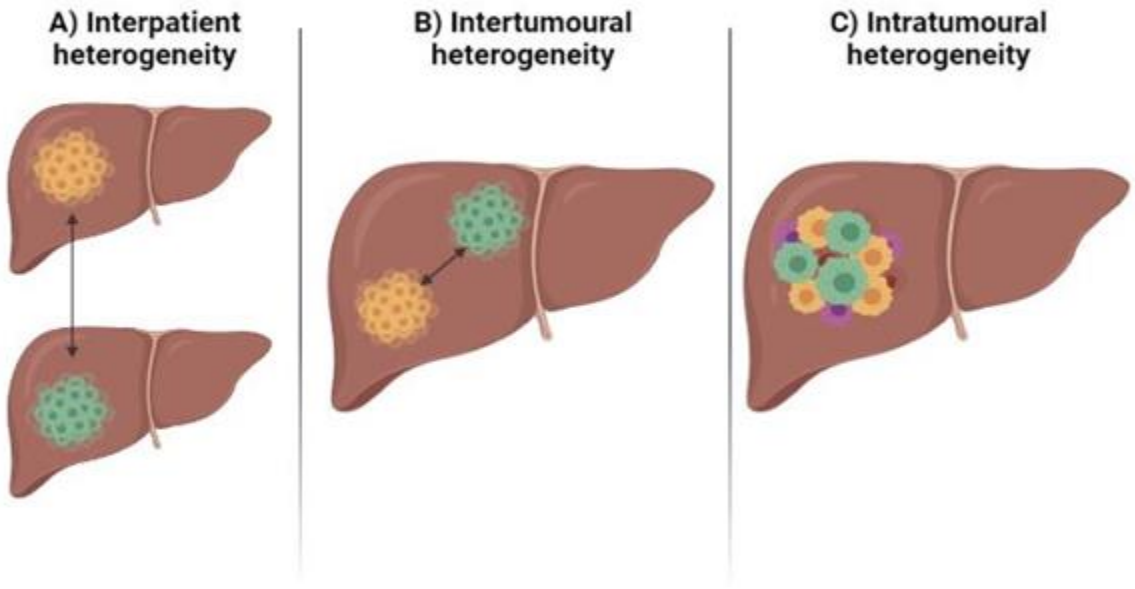

Figure 3. Types of tumour heterogeneity. Different levels of tumour heterogeneity: (A) Interpatient heterogeneity, (B) intertumoural heterogeneity, and (C) intratumoural heterogeneity (13, 25). Created with BioRender.com

4.3.3 Commonly mutated genes in HCC

There are an average of 60-70 somatic mutations detected in protein-coding regions of the genome in each HCC (66). While many of these mutations occur in “passenger” genes and are not directly linked to carcinogenesis, some play a key role in tumour initiation and development (1). Whole-exome sequencing studies and SNP array analyses have highlighted numerous pivotal gene mutations and copy number aberrations considered to be “drivers” of HCC, resulting in the activation of pathways linked to hepatocarcinogenesis, promoting proliferation, survival, invasion and immune evasion. These mutations relate to telomere maintenance (telomerase reverse transcriptase (TERT) mutations), inactivation of the tumour suppressor p53 (encoded by TP53), activation of WNT-β-catenin signalling (mutation in CTNNB1), oxidative stress, chromatin modification (mutation in ARID1A), and PI3K signalling cascades (67-69). The presence of mutations in TERT, TP53 and CTNNB1 in 51% of small, early-stage HCC tumours highlights the significance of these variations in tumour initiation. A continued accumulation of genetic alterations enable tumour progression resulting in advanced disease, with driver alterations such as DNA amplifications (Vascular endothelial growth factor (VEGF) A, MYC), DNA deletions (CDKN2A, AXIN1, IRF2) and DNA methylation

(IGF2) contributing to broad intratumoural heterogeneity (66). Unfortunately, the majority of these alterations are not currently targetable; just 20-25% of HCCs bear mutations that can be targeted clinically with existing drugs (67, 70). Furthermore, a mere 6 of the 34 most commonly reported genes in HCC are targetable by FDA-approved drugs (66).

4.3.4 TERT promoter mutations

The most common genetic alteration observed in HCC that develops on a background of cirrhosis occurs in the TERT promoter, responsible for encoding the catalytic subunit of telomerase for telomere DNA synthesis (71, 72). A decrease in telomerase activity is often observed in cirrhotic tissue, alongside shortened telomeres and replicative senescence (54). However, a reactivation of telomerase activity and TERT expression is reported to be required to erase the senescence barrier and enable malignant transformation, resulting in telomere lengthening and contributing to tumour initiation (54, 73). An upregulation of telomerase activity is reported in 90% of cancers, and TERT promoter mutations are reported in up to 60% of HCC cases (66, 74). TERT reactivation is usually a result of somatic mutations in the TERT promoter, but can also be resultant of TERT amplification, translocation or via viral insertion in the promoter (75). Somatic alterations in the TERT promoter are the earliest genetic event in hepatocarcinogenesis, present in 6% of LGDN and 20% of HGDN (76). The frequency of TERT promoter mutations remains stable during a comparison of early and advanced HCCs, while additional genetic alterations occur, indicating that TERT mutations act as a gatekeeper for malignant transformation, and play a role in tumour initiation rather than tumour evolution (55, 77).

4.3.5 CTNNB1 mutations

Mutations in CTNNB1 occur in approximately 30% of HCC cases, meaning it is the second most commonly altered gene in HCC after TERT (66). CTNNB1 encodes β-catenin, which is typically targeted for degradation in the cytoplasm when there is an absence of Wnt signalling, as a destruction complex is formed from the APC protein, AXIN, GSK-3β and CK-1α. The destruction complex then releases phosphorylated β-catenin which is bound by the E3 ubiquitin ligase β-TrCP, for ubiquitination and degradation (78). Conversely, Wnt signalling is activated when Wnt binds to its receptor lipoprotein receptor-related protein (LRP). The intracellular section of LRP becomes phosphorylated, disrupting the β-catenin destruction complex as AXIN and GSK-3β are recruited to the plasma membrane (79). Stabilised β-catenin then translocates to

the nucleus where it regulates target genes via the TCF/LEF transcription factors (80). As Wnt-β-catenin signalling is predominantly limited to zone 3 of the hepatic lobules, HCC that arises as a result of mutations in this pathway typically arise in this zone of the liver (66, 81). Specific alterations in CTNNB1 have been associated with malignant transformation and tumour progression, as a consequent of the unregulated transcription of genes relating to cell proliferation, migration, survival and differentiation (82). Such genes include c-Myc and matrix metalloproteinases (MMPs) (83). HCCs that arise from CTNNB1 mutations are described to have a suppressed immune landscape, with limited infiltration of CD8+ and CD4+ T cells, therefore leading to a resistance to anti-programmed cell death protein 1 (PD-1) immunotherapy which activates cytotoxic T cells (78, 84, 85).

4.3.6 Chromosomal aberrations

Chromosomal aberrations have also been identified as gatekeepers for malignant transformation in dysplastic nodules, with the frequency of copy number variations increasing during hepatocarcinogenesis. Alterations in chromosomes 1 and 8 are reported to be trunk gatekeepers in dysplastic nodules which are maintained when the lesions progress to early HCCs (46, 86). In order to identify common copy number variations, SNP array data from LGDNs and HGDNs obtained from patients with cirrhosis was utilised. Both gains (6.9%) and losses (6.9%) in chromosome 8 were observed to be the most frequent events, alongside gains in chromosome 1q (3.4%) and losses in chromosome 22q (3.4%). Chromosomes 1q and 8q - affected by aberrations in 13.8% of dysplastic tissues - include the oncogenes MDM4/Poly (ADP-ribose) polymerase-1 (PARP1) and MYC respectively (46). There is a significant increase in the frequency of aberrant chromosomes in early HCCs compared to dysplastic nodules, with broad gains in chromosome 8q (29.4%) and 1q (47.1%), and broad losses in 8p (35.3%). Additional chromosomal aberrations that are absent in dysplastic nodules have been identified in early HCCs, including focal amplifications in 6p21.1 (VEGFA) and 8q24.21 (MYC). The absence of these aberrations in premalignant lesions identifies them as trunk drivers of tumour progression (46).

4.3.7 Crossover between genetic aberrations and risk factors

The pathogenesis of HCC is often a result of both the mutations in cancer driver genes and the risk factors associated with the disease; the observation that HCC commonly develops on a background of CLD is often due to polymorphisms that increase the predisposition of the

patient to risk factors such as obesity, alcohol intake and viral hepatitis (40, 60). For example, polymorphisms in the genes PNPLA3 and TM6SF2 are associated with MASH and HCC development, particularly in patients with alcohol related cirrhosis (18, 19, 87). As well as cirrhosis-related HCC, TERT promoter mutations strongly correlate with HCV-related HCCs where no HBV is present, indicating a link between this genetic alteration and a predisposition to infection with HCV, as well as suggesting that HBV-associated HCCs maintain telomeres via different mechanisms (88). Similarly, an activating polymorphism in the epidermal growth factor (EGF) gene strongly correlates with the development of HCC from HCV-related cirrhosis (89, 90).

4.3.8 HCA genetic mutations

HCAs can be characterised into the following five molecular subgroups based on the genetic mutations they include: HNF1A-mutated (30-40%), CTNNB1-mutated (10-15%), inflammatory subtype pertaining to mutations in genes including IL6ST, JAK1, STAT3 and FRK and activation of the JAK-STAT pathway (40-50%), sonic hedgehog adenomas involving an overexpression of GLI family zinc finger 1 (GLI1) (5%), and unclassified HCAs which lack the described mutations and inflammatory phenotype (<7%) (56, 91). Unlike HCC cases that develop on a background of cirrhosis where TERT promoter mutations are the gatekeepers for malignant transformation, CTNNB1 mutations activating β-catenin are the earliest genetic event leading to malignancy in HCAs (92). Chromosomal aberrations and DNA hypomethylation also contribute to the malignant transformation of HCAs (93).

4.3.9 Targeting genetic alterations

Utilising knowledge of the molecular signature of a tumour for precision medicine is not currently a successful strategy in the treatment of HCC, as the most frequent genetic alterations in TERT, TP53 and CTNNB1 are not targetable by FDA-approved drugs (66, 67, 94, 95). Approved systemic therapies do not target biomarkers that could be employed to predict treatment response, with the exception of elevated AFP levels (≥400 ng/ml) being an indicator of improved overall survival (OS) in response to ramucirumab after sorafenib (96). Clinical sequencing of tumours from a cohort of more than 10,000 patients deduced that whilst it was possible to target genetic aberrations in 60-75% of patients with breast cancer, thyroid cancer, melanoma, glioma or gastrointestinal stromal tumours, actionable aberrations were only identified in 5% of HCC cases (97). Intratumoural heterogeneity has also proven to be a

significant barrier in the quest to identify useful HCC biomarkers, and impacts decision-making for cancer care when the molecular information available derives from a single biopsy (98-100).

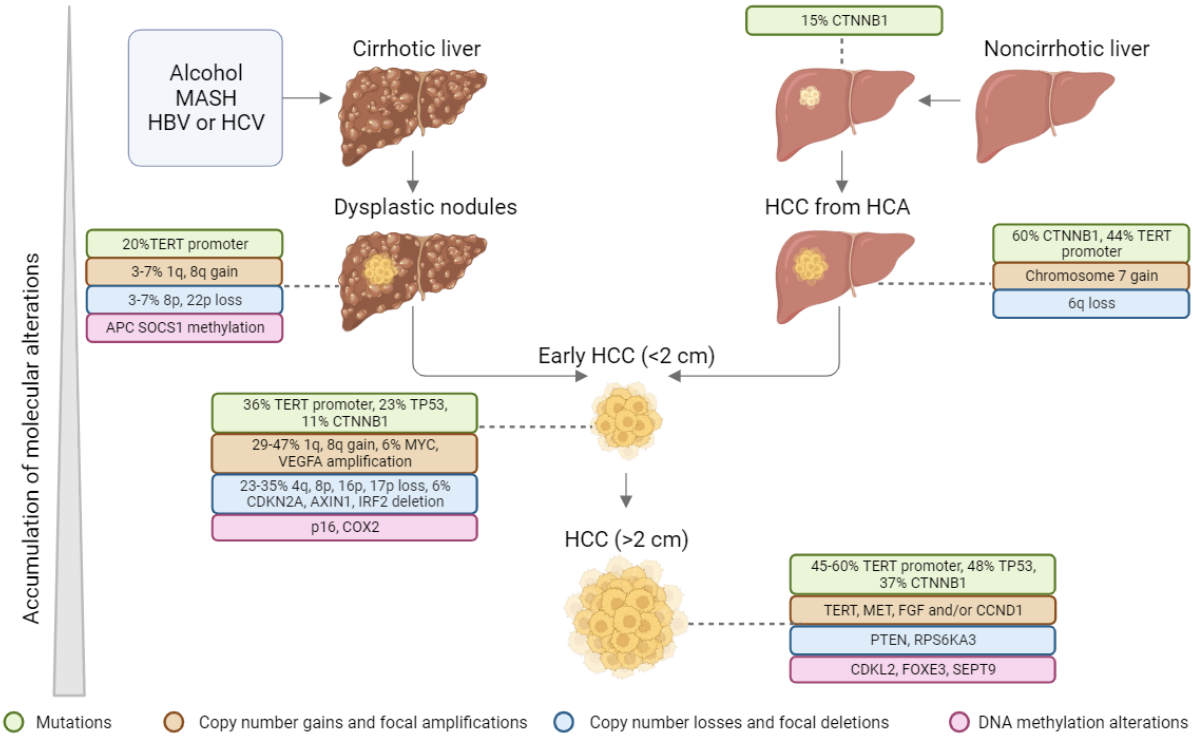

Figure 4. Molecular events contributing to HCC development. HCC typically develops as a series of molecular alterations accumulate: mutations, copy number gains and focal amplifications, copy number losses and focal deletions, and DNA methylation alterations. HCC often arises on the background of liver inflammation and cirrhosis, as dysplastic nodules contain molecular alterations that function as gatekeepers for malignant transformation. In the absence of cirrhosis, HCAs gain molecular alterations that culminate in HCC development. Subsequent alterations that are present in early HCC, but not in dysplastic nodules or HCAs, are considered to function as drivers of progression rather than gatekeepers. Figure adapted from Craig *et al.*, 2019 (55).

4.4 Classification

4.4.1 Overview of HCC classification

The classification of HCCs into distinct groups can aid the stratification of patients, ensuring that they receive the appropriate treatment. There are a number of assessments and techniques used to separate patients into subclasses; HCCs were previously assessed using tumour node metastasis (TNM) staging, which involves assessing the tumour burden (T), presence of cancer cells at lymph nodes (N), and distant metastases (M) (101). However, this method is limited and has been altered frequently due to its poor accuracy – the technique fails to consider alternative factors in the tumour microenvironment and does not factor in liver function (102). The Okuda classification is another stratification method that has been

extensively used, and accounts for tumour burden and three parameters relating to liver function – ascites, serum albumin and serum bilirubin levels (103). Despite considering liver function as well as the tumour parameters, the method is limited in that it accurately classifies just the patients with end-stage disease, rather than those with early HCC, and does not account for the effects of vessel, lymph node and adjacent organ invasion (104, 105). In order to overcome the limitations presented by TNM and Okuda classification, 5 other classification systems were established: Japanese Integrated Staging (JIS) score, French, Cancer of the Liver Italian Program (CLIP), Chinese University Prognostic Index (CUPI) score, and Barcelona-Clinic Liver Cancer (BCLC) staging (106-110).

4.4.2 Japanese Integrated Staging (JIS) score

The JIS score combines both TNM staging and Child-Pugh classification, which is a staging system for individuals with CLD and is used as a predictor of whether the individual is suitable for elective surgery (111-113). Use of the JIS score was found to be a superior staging system compared to TNM staging and the CLIP score in a cohort of 722 Japanese patients with HCC (114). This observation was validated in a further study of 4,525 patients (115). A TNM score is assigned using criteria from the Liver Cancer study Group of Japan (114). Individuals classified as stage I (score 0) present with three conditions: no vascular invasion, and a single tumour smaller than 2 cm in size. Those with stage II (score 1) disease present with two of the aforementioned conditions, stage III (score 2) presents with one, and stage IV (score 3) presents with none (116). A score between 0 and 3 is also assigned to the Child-Pugh score (A = score 0, B = score 1, C = score 2), and the combination of these scores is defined as the JIS score. The biomarker-combined JIS scoring system was later proposed by Kitai et al., and evaluates the presence of three HCC biomarkers in combination with the conventional JIS score: AFP, *lens culinaris* agglutinin-reactive AFP (AFP-L3), and des-gamma-carboxyprothrombin (DCP). Consideration of these biomarkers was found to be a better prediction of prognosis than the standard JIS system (117).

4.4.3 Cancer of the Liver Italian Program (CLIP) score

The CLIP scoring system was developed in 1998 from a retrospective study of 435 Italian patients with HCC. Multiple tumour-related features are taken into consideration when calculating the CLIP score: macroscopic tumour morphology, serum AFP levels, and portal vein thrombosis, whilst also taking the Child-Pugh score into account. This stratifies the patients

into groups with a score of between 0 and 6 assigned; the higher the score, the worse the prognosis (116, 118). Limitations of the system include an inability to differentiate between patients with CLIP scores between 4 and 6, and the discovery that Asian populations are not accurately stratified by the system (116, 119).

4.4.4 French classification

The French classification system was established following a prospective study of 761 HCC patients who were enrolled over a 30-month period. Five variables contribute to the classification of individuals into groups according to their estimated risk of death. These groups are A (low risk), B (intermediate risk) and C (high risk). The five prognostic factors considered are Karnofksy performance status, serum bilirubin level, serum AFP, serum alkaline phosphatase level and sonographic portal obstruction (116, 119, 120). The survival of individuals in groups A, B and C were 51%, 17% and 3% respectively, highlighting that the study mostly included patients with advanced disease (120). Moreover, the system has been shown to have limited capability in predicting prognosis in patients with early-stage HCC (121).

4.4.5 Chinese University Prognostic Index (CUPI) score

The CUPI score was developed following a prospective study of 595 Chinese patients, predominantly with HBV-related cirrhosis. Six prognostic factors are considered: TNM stage, total bilirubin level, asymptomatic disease at presentation, AFP level, alkaline phosphatase level and ascites. This results in the classification of patients into three groups: low risk (CUPI score ≤1), intermediate risk (CUPI score = 2-7) or high risk (CUPI score ≥8) (109, 122). Due to HBV-related cirrhosis being the predominant underlying liver aetiology of individuals in the initial study, the CUPI score has a better prognostic power for patients infected with HBV (123).

4.4.6 Barcelona-Clinic Liver Cancer (BCLC) staging

In comparison to the JIS score, CLIP score, French classification and CUPI score which are useful for predicting the outcome of advanced HCC, the BCLC staging system has proven to be particularly useful for identifying and assigning the appropriate treatment to patients with early tumours (124, 125). The BCLC system accounts for parameters such as tumour burden, number of nodules, vascular invasion, extrahepatic spread, and liver function determined by the Child-Pugh score (104). Using the BCLC system, patients identified to be asymptomatic with very early HCC (score of BCLC 0/A) become candidates for local curative treatments such

as surgical resection, ablation and liver transplantation; those with intermediate-stage disease, with adequate liver function but multinodular disease (BCLC B) are treated with locoregional therapies such as transarterial chemoembolization (TACE); patients with extrahepatic spread or portal thrombosis are classified as having advanced disease (BCLC C) and are therefore treated with systemic therapies (Figure 5) (70, 126, 127). External validation of the BCLC staging system has identified it as having superior prognostic abilities than other systems, and is a useful tool for identifying patients who would benefit from curative treatments (128). A potential limitation of the methodology is that measurement of the hepatic venous pressure necessary for the subclassification of early-stage disease may not be routinely performed in the clinic. Additionally, it has been suggested that the CLIP scoring system is superior for predicting survival in non-surgical patients with advanced disease (116, 129).

4.4.7 Molecular classification

Molecular classes of HCC have been established using factors such as the immune status of the tumour, as well as the main molecular drivers and pathways involved. This separates HCCs into two major classes: the proliferation class and the non-proliferation class (40). The proliferation class accounts for approximately 50% of all HCCs, and is characterised by mutations in TP53 impacting cell cycle control, more aggressive tumours, vascular invasion and poor histological differentiation (130). HCCs in this group are associated with poor prognosis and can be divided into two further subclasses. The proliferation-progenitor cell subclass (S2) is characterised by increased expression of AFP, overexpression of epithelial cell adhesion molecule (EPCAM), and activation of cell proliferation pathways such as PI3K-AKT-mTOR signalling and the RAS-MAPK pathway (54). The second subclass is the proliferation-WNT/transforming growth factor beta (TGF-β) group (S1), and is characterised by non-canonical activation of Wnt and an associated immune-exhausted phenotype (70, 130). Conversely, the non-proliferation class describes less aggressive HCCs, with well-differentiated tumours, lower AFP levels and less vascular invasion. These HCCs are commonly associated with MASH, ALD and HCV infection, and are associated with a better clinical outcome. Within the non-proliferation class there are distinct subgroups: the interferon subclass with increased IL6-JAK-STAT signalling, and the WNT-β-catenin subgroup with mutations in CTNNB1 and subsequent “cold” tumours with low immune infiltration (70, 131).

4.4.8 Immune classification

Knowledge of the relationship between tumour and immune cells enables further stratification of the tumour, with the characterisation of “hot” or “cold” tumours according to the immune infiltrate (132). Previously, the quantification of CD3+ and CD8+ lymphocytes in the tumour core and invasive margin provided the rationale for the Immunoscore; low densities or an absence of these cell types in a “cold” tumour resulted an Immunoscore of I0, whilst high densities of both CD3+ and CD8+ T cells in a “hot” tumour resulted in an Immunoscore of I4 (133-135). More recent methods of immunogenomic characterisation stratify HCC tumours into inflamed, intermediate or excluded subclasses of HCC. Approximately 37% of tumours are immunologically “hot” and therefore belong to the inflamed class, which has recently been delineated to better understand immunotherapy responses (134). This includes tumours belonging to the previously reported immune subclass (22%), whereby tumours present with minimal chromosomal alterations and increased expression levels of the immune checkpoint molecules PD-1 and programmed death ligand 1 (PD-L1), and a newly-defined immune-like subclass (15%) which possesses a more diverse T cell repertoire, high interferon signalling and expression of immune-effector cytokines (131, 133, 134). The non-inflamed class describes tumours in both the intermediate class (43%) with TP53 mutations, a mild immune infiltrate and chromosomal abnormalities relating to antigen presentation, and the excluded class (20%) with enriched CTNNB1 mutations and PTK2 overexpression. Tumours outside of the excluded class with CTNNB1 mutations are typically accompanied by high interferon signalling or weak activation of the Wnt-β-catenin pathway (134). Considering the immune classification of a tumour is a superior prognostic factor than through use of the TNM staging system alone, which does not consider the immune infiltrate. Immune excluded “cold” tumours have a higher frequency of recurrence following tumour resection as T cell-mediated anti-tumour responses are prevented (101). Knowledge of the immune profile of a tumour enables these components to be targeted with immune checkpoint inhibitors, therefore enhancing the immune response against the tumour (136, 137).

4.5 Tumour microenvironment (TME)

4.5.1 TME overview

The HCC tumour microenvironment (TME) is a complicated network comprised of the tumour itself, as well as stromal cells, infiltrating immune cells, proteins secreted by the cells, and the extracellular matrix (ECM) in which it all exists. Despite the purpose of many of the cell types recruited to the TME being to combat the cancer, the outcome of crosstalk between the tumour cells and the stroma often contributes to carcinogenesis, and the stroma can be inappropriately activated to contribute to the manifestation of the disease (138). An understanding of the components that constitute the tumour microenvironment and their accompanying crosstalk is essential when assessing the most suitable immunotherapeutic options. The mechanisms by which the TME can contribute to the pathogenesis of HCC are numerous. Tumour growth and progression can be favoured as the components surrounding the tumour contribute to processes including immune evasion, sustained proliferation, induction of angiogenesis, invasion and metastasis, and resistance of apoptosis (138).

4.5.2 Liver sinusoidal endothelial cells (LSECs)

Liver sinusoidal endothelial cells (LSECs) are specialised cells that constitute the vascular endothelium of the sinusoids (139). The presence of fenestrae in LSECs in combination with Kupffer cells, the liver-resident macrophages, presents an efficient scavenger system whereby virus particles, low-density lipoprotein (LDL) cholesterol and advanced glycation end products can be recycled from the blood (140-143). LSECs are capable of antigen-presentation via pattern recognition receptors, and play a role in regulating the inflammatory response in the liver. For example, the recognition of the toll-like receptor (TLR) 4 ligand LPS by LSECs is linked to reduced leukocyte adhesion following reduced nuclear translocation of NF-κB, preventing the liver from being in a constantly inflamed state as a result of exposure to bacterial products from the gut (144, 145). Additionally, immune cell recruitment is modulated by LSECs through integrins such as αLβ2, α4β1 and α4β7 (144, 146). Intercellular crosstalk involving LSECs contributes to HCC development; CD8+ T cell activation is inhibited by the overexpression of PD-L1 on LSECs, leading to immune evasion of HCC (147). Moreover, LSECs from human HCCs display a higher capacity for angiogenesis, fibrinolysis and coagulation (148). The recruitment of myeloid derived suppressor cells (MDSCs), an immature population of myeloid cells, results in an immunosuppressive TME, promoting tumorigenesis and metastasis (149-151).

4.5.3 Neutrophils

Neutrophils are the most common leukocyte in circulation and are key players in the innate immune response (152). They are capable of eliminating pathogens through a number of mechanisms, including through the release of neutrophil extracellular traps (NETs), the production of ROS by NADPH oxidase (NOX2), phagocytosis and degranulation (153-158). Initial attempts at classifying neutrophils defined them as having either and N1 or N2 phenotype. Most tumour associated neutrophils (TANs) present with an immunosuppressive "N2" phenotype, polarised by the high levels of TGF-β in the TME, and show an increased expression of pro-angiogenic factors such as VEGF, MMP9 and CXCR4 (159-161). Meanwhile, "N1" neutrophils express higher levels of inflammatory cytokines and exhibit more cytotoxicity (162). However, an emerging understanding of the complex heterogeneity displayed by neutrophils in cancer means it is difficult to accurately distinguish between these two populations. An example of the overlap in functional characteristics between N1 and N2 neutrophils is that ROS is utilised by both populations: for tumour killing by N1 neutrophils and for T cell suppression by N2 neutrophils (163, 164). Neutrophils comprise a large proportion of the immune infiltrate in both CLD and HCC, and there is a growing body of evidence that identifies neutrophils as key drivers of tumour progression and metastasis (165-167).

A study of two independent cohorts of HCC patients ascertained that neutrophils were the only cell type to be associated with patient outcome, with high neutrophil counts significantly correlating with more advanced disease and worse OS (168). It has been demonstrated that neutrophils are a requirement for HCC development in a diethylnitrosamine (DEN) mouse model, in which antibody-mediated depletion of neutrophils attenuated the HCC, normalising the liver/body weight ratio and blunting tumour growth (169). Additionally, it has been shown that neutrophils induce telomere dysfunction and senescence in adjacent cells via the release of ROS, potentially underpinning the liver disease that often precedes HCC (170). Stelic animal model (STAM) mice present a system whereby HCC develops on the background of MASH. In this model of HCC neutrophils were found to be vital for HCC development, where it is speculated that free fatty acids stimulate NET production, leading to high levels of inflammation and tumorigenesis. Inhibition of NET formation attenuated these effects (171).

These findings are potentially highly relevant to human HCC given that it commonly arises on the background of CLD (166).

4.5.4 T cells

The presence of infiltrating cytotoxic T lymphocytes (CTLs) is associated with a significant improvement in overall and progression-free survival (PFS) in HCC. A meta-analysis of 7905 HCC patients determined that there was a positive correlation between improved survival and the density of tumour-infiltrating CD8+, CD3+, FOXP3+ and Granzyme B+ CTLs (172). CD8+ T cells have been identified as the predominant cytotoxic lymphocyte capable of killing cancer cells, and act via several mechanisms following the recognition of tumour-specific antigens presented by major histocompatibility complex (MHC) class I. These include the FasL ligand-mediated induction of apoptosis, granular exocytosis, and the production of interferon-γ (IFN-γ) and TNF-α (173). However, the exhaustion of CTLs results in impaired pro-inflammatory responses, a reduction in cytokine production and an accumulation of regulatory T cells (Tregs); An immunosuppressive niche rich in cytokines such as IL-10 and TGF-β prevents the activation of CTLs and T helper type 1 (Th1) CD4+ T cells (146). CTL exhaustion is typically a consequence of overexpression of inhibitory molecules such as PD-1, cytotoxic T-lymphocyte-associated protein 4 (CTLA-4), lymphocyte-activation gene 3 (LAG-3) and T cell immunoglobulin and mucin-containing molecule 3 (TIM-3) (174-177).

Immune exhaustion in HCC is commonly driven by the PD-1/PD-L1 pathway, whereby T cell receptor signalling is suppressed via the PI3K/AKT pathway (178, 179). A high expression of PD-1 and PD-L1 is therefore associated with poor prognosis (180, 181). Nevertheless, exhausted infiltrating T cells with a high expression of PD-1 can have their cytotoxic effects restored via PD-1 inhibition (182).

The immune checkpoint molecule CTLA-4 is also a major contributor to immune escape in HCC, as it competes with CD28 to bind to B7-1 (CD80) or B7-2 (CD86). The binding of CD28 to CD80/CD86 would typically promote T cell proliferation, survival, and differentiation through the production of IL-2. However, the higher binding affinity of CTLA-4 to CD80/CD86 prevents the stimulatory signal usually provided by CD28, resulting in limited T cell proliferation and survival (183).

Alternative drivers of T cell exhaustion include LAG-3 and TIM-3. LAG-3 regulates CD8+ T cell accumulation, and the hypofunctional CD8+ T cell function can be reversed via LAG-3 blockade (184). Whilst the anti-LAG-3 monoclonal antibody relatlimab is FDA-approved for the treatment of melanoma, its relevance in HCC has also been highlighted (185-187). TIM-3 is expressed on CD8+ and CD4+ T cells, as well as on multiple other immune cell populations, and has been associated with a poor prognosis in HCC and a greater risk of HCC development in individuals with HBV (177, 188, 189).

4.5.5 Regulatory T cells (Tregs)

Whilst CTLs exhibit anti-tumour effects prior to immune exhaustion, CD4+CD25+FOXP3+ Tregs are an immunosuppressive T cell population that have also been shown to infiltrate tumours and are associated with poor prognosis in HCC (190, 191). Their recruitment to the tumour is promoted by CCL28, CCL22 and CCL5, cytokines that have been shown to be produced by infiltrating macrophages, dendritic cells (DCs), CD8+ T cells and cancer associated fibroblasts (CAFs) (192, 193). Tregs contribute to the immunosuppressive TME by producing anti-inflammatory IL-10 and TGF-β, and express CTLA-4 resultant in reduced survival of CTLs (194, 195). Furthermore, the downregulation of CD80 and CD86 on DCs further contributes to impaired antigen presentation and T cell exhaustion (196). In addition to CTLA-4, Tregs also express the immune checkpoint PD-L1 and inhibit IFN-γ secretion (197).

4.5.6 Myeloid cells

Tumour-associated macrophages (TAMs) and MDSCs are the two main myeloid cell types in the HCC TME, whereby MDSCs represent a more immature population present in both the circulation and intratumorally, and TAMs represent a tissue-resident population of macrophages (146). Two subtypes of MDSCs have been identified: monocytic MDSCs (M-MDSC) and polymorphonuclear MDSCs (PMN-MDSC), the latter of which are phenotypically and morphologically similar to immunosuppressive neutrophils (198). Myeloid cells are recruited to tumours through the binding of CXCR4 to CXCL12 released from HSCs and endothelial cells (199). Infiltrating MDSCs have been shown to contribute to tumour progression by supressing T cell proliferation through the depletion of arginine, and promoting the expansion of Tregs by producing immunosuppressive IL-10 and TGF-β (200). Moreover, MDSCs have been shown to express higher levels of the immune checkpoint molecule PD-L1

in HCC patients, and increase the risk of HCC recurrence following liver transplantation via CXCL10/TLR4/MMP14 signalling (201, 202).

Whilst macrophages have the potential to elicit antitumour responses (M1), with CD68+CD169+ macrophages correlating with improved OS in HCC, their heterogeneity can result in polarisation to produce anti-inflammatory, pro-tumour (M2) TAMs (203, 204). A high density of CD68+ tumour infiltrating macrophages predicts poor prognosis, and single cell RNA sequencing has identified the presence of CD68+MARCO+ (anti-inflammatory) and CD68+MARCO- (pro-inflammatory) macrophages (204, 205). A high number of TAMs in the tumour microenvironment is associated with poor prognosis, angiogenesis, metastasis and tumour cell proliferation (206). MDSCs engage in immunosuppressive crosstalk with TAMs, whereby IL-10 released by the former and IL-6 released by the latter amplify the immunosuppressive activity of the other cell type (207). Additionally, TAMs further contribute to the immunosuppressive niche in HCC by recruiting Tregs and expressing PD-L1, TGF-β, indoleamine 2,3-dioxygenase (IDO) and arginase 1, reducing T cell and natural killer (NK) cell activity (208-210). It is important to note that multiple studies have detected overlaps in genes in M1 and M2 macrophage populations, highlighting that the binary classification of macrophages into M1 and M2 subgroups does not truly reflect the complexity of macrophage interactions in the TME (211, 212).

4.5.7 Natural killer (NK) cells

NK cells play a key role in innate immune surveillance and comprise a large proportion of intrahepatic lymphocytes (30-50%) (146, 213). They exhibit rapid target-cell killing without the requirement for antigen presentation, via the release of cytokines (predominantly IFN-γ and TNF-α) and chemokines, and through Fas/FasL-mediated apoptosis (191, 214, 215). The presence of the cell surface receptors CD56 and CD16 identifies NK cells, with conventional circulating NK cells being $CD56^{dim}CD16^{bright}$ and liver-resident NK cells typically classified as $CD56^{bright}CD16^{dim}$ (216). Upon secretion of cytokines such as IL-2, IL-12, IL-15 and IL-18 from hepatocytes and Kupffer cells, circulating NK cells are recruited to the inflamed liver and activated alongside liver-resident NK cells (217).

In HCC, it has been demonstrated that intratumoural NK cells with high expression of CD96 are functionally exhausted, with the production of IFN-γ and TNF-α impeded and poorer clinical outcomes for the patients (218). An accumulation of CD49a+ $CD56^{bright}$ NK cells in HCC

correlates with poor prognosis; $CD56^{bright}$ NK cells are considered to be a more immature subset of NK cells with lower cytotoxic capabilities (213, 219). The impairment to NK cell function observed in HCC can be attributed to various components on the TME, including CAFs (through secretion of immunosuppressive prostaglandin E_2 and IDO), MDSCs (by impairing IFN-γ secretion) and TAMs (induces NK cell exhaustion and apoptosis via binding to the 2B4 receptor) (220-223). Similar to T cells, the expression of PD-1 on tumour infiltrating NK cells and subsequent binding to PD-L1 results in suppression of the PI3/AKT pathway, impairing their cytotoxicity (224). Changes in expression of activating and inhibitory receptors on NK cells contributes to their change in functionality. An upregulation of the inhibitory natural killer group 2, member A (NKG2A) on NK cells in advanced HCC is associated with a worse outcome (225). Meanwhile, the binding of the activating receptor natural killer group 2, member D (NKG2D) to ligands including MHC class I chain-related protein A/B and ULBP1, which are expressed by malignant cells, leads to the downregulation of NKG2D and suppression of NK cell activity (226, 227). Reduced activation of NKG2D correlates with early recurrence in HCC, in contrast to the finding that NKG2D promotes tumorigenesis in a mouse model of HCC (228, 229).

4.5.8 Cancer associated fibroblasts (CAFs)

CAFs are a heterogeneous group of tumour-infiltrating fibroblasts derived from multiple cell types in the TME, including HSCs, HCC cells that undergo epithelial-mesenchymal transition (EMT), mesenchymal stromal cells and LSECs (230). The HSCs that CAFs often evolve from are another constituent of the TME with a critical pro-tumorigenic role. They are one of the main producers of ECM in the liver, and contribute to tumour progression through a number of mechanisms, including via the release of hepatocyte growth factor (HGF) to promote invasion, and by inducing the expansion of regulatory T cells, contributing to the immunosuppressive TME (231-234). CAFs similarly secrete ECM proteins, growth factors such as EGF and platelet-derived growth factor (PDGF), MMPs and an array of cytokines and chemokines (235). Secretion of the cytokine CXCL11 by CAFs has been shown to enhance HCC progression and metastasis by promoting the self-renewal of tumour-initiating cells (236, 237). Furthermore, preclinical studies have demonstrated that the release of CCL5 by CAFs promotes HCC metastasis via HIF1α/ZEB1 signalling (238). HCC cell stemness is enhanced via multiple CAF-mediated mechanisms: HGF secreted by CAFs binds to c-Met and promotes cell cycle

progression and abnormal proliferation, and through the activation of Notch signalling by IL-6 released by CAFs (239, 240). The expression of proangiogenic factors by CAFs, such as VEGF, PDGF and angiopoietin-1 contributes to tumorigenesis and metastasis (191, 241, 242). The numerous mechanisms by which CAFs contribute to hepatocarcinogenesis highlight it as an emerging target in HCC (243).

4.6 Therapies

4.6.1 Treatment strategies for HCC

Over the two past decades, the management of HCC has improved significantly. The most suitable treatment must be assigned to each patient based on the classification of the HCC, taking into account the number and size of the nodules, the molecular status of the tumour and the immune profile of the TME (101, 110). Treatment options can typically be separated into those that are curative and those that are palliative. As previously described, curative treatments assigned to patients with early stage disease (BCLC 0/A) include liver transplantation, resection and percutaneous ablation, and result in a high response rate capable of improving survival by over 60 months (38, 40, 244). Despite this, up to 70% of patients treated with these curative approaches present with disease recurrence within 5 years (1). The majority of patients are diagnosed with HCC in the later stages of disease, and are therefore treated with palliative treatments. Although these treatments are not designed to cure HCC, they can improve survival and achieve good response rates. TACE (BCLC B) is used to treat unresectable HCC in patients with intermediate disease, and involves administering embolism agents to the hepatic artery to isolate the tumour from the vasculature, in combination with chemotherapy drugs such as doxorubicin and cisplatin to induce severe necrosis (244-246). This therapy has the potential to delay tumour progression and invasion (247). Systemic therapies are used to treat those with advanced HCC (BCLC C), and approximately 50% of patients will receive this form of treatment at some point (Figure 5) (1). Individuals with end-stage HCC (BCLC D) will not benefit from therapeutic intervention and should therefore receive symptomatic management and palliative care (244).

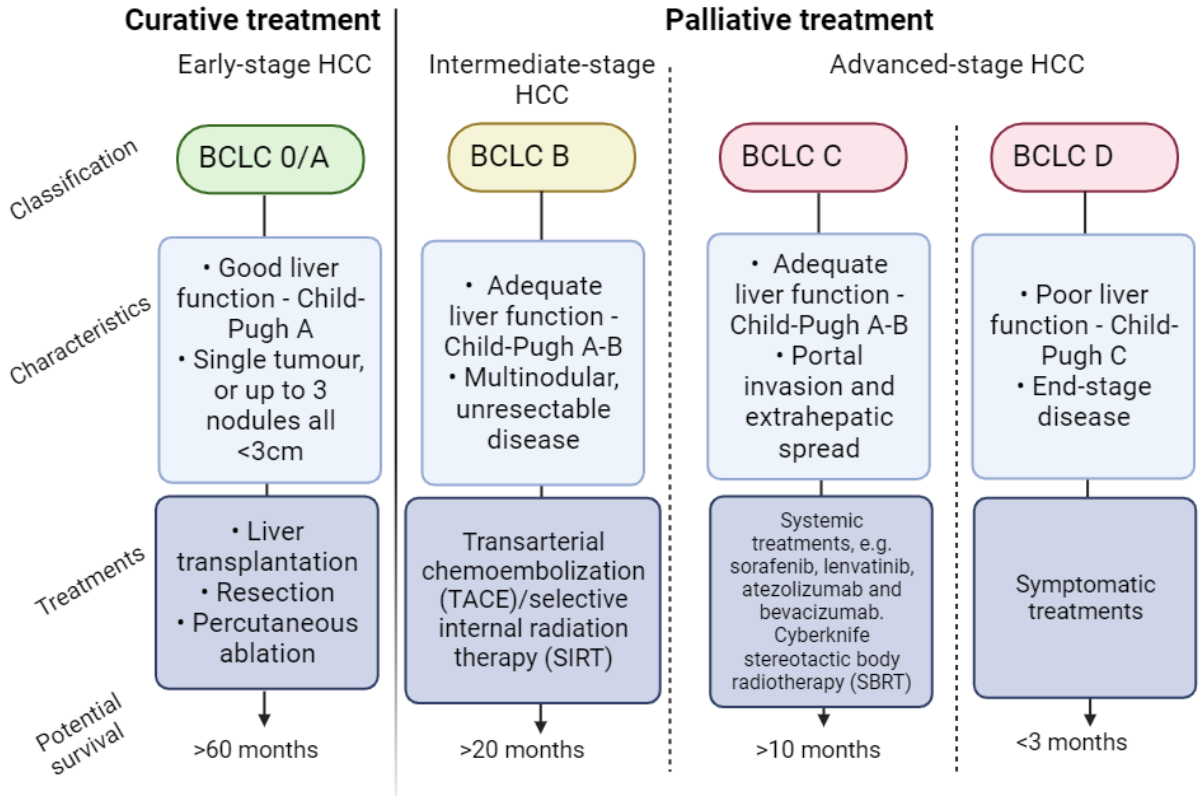

Figure 5. Barcelona Clinic Liver Cancer (BCLC) classification system. Curative and palliative treatment options applied to patients depending on their BCLC classification (49, 50). Created with BioRender.com

4.6.2 First-line tyrosine kinase inhibitors (TKIs)

Approximately 60-70% of HCC patients are treated with systemic therapies, due to either diagnoses at advanced stages of disease or due to disease progression after surgical or loco-regional therapies (66). In 2007, the Sorafenib HCC Assessment Randomised Protocol (SHARP) trial demonstrated the effectiveness of sorafenib at extending the survival of advanced-stage HCC patients from 7.9 months to 10.7 months, and it became the standard of care and only approved systemic therapy until 2016 (248, 249). Sorafenib is a multi-target receptor tyrosine kinase inhibitor (TKI) with up to 40 targets, including vascular endothelial growth factor receptor (VEGFR), platelet-derived growth factor receptor (PDGFR), c-Kit and Raf signalling. Its efficacy may be due to the vast number of targets, meaning sorafenib targets both the cancer cells and other cells in the TME, exhibiting anti-proliferative and anti-angiogenic effects (250). A meta-analysis of two placebo-controlled phase III clinical trials (SHARP and Asia Pacific) deduced that sorafenib improved OS in all patient subgroups, but OS was significantly greater in patients with HCV, without extrahepatic spread, and with a low neutrophil-to-lymphocyte ratio (NLR) (8, 248). Multiple phase III trials have demonstrated the failure of many potential first-line therapies to meet the standard of sorafenib, accompanied by significant liver toxicity

and problematic trial designs (40, 251). Lenvatinib was approved as an alternative first-line therapy for advanced HCC a decade after sorafenib, after its efficacy was demonstrated in a multinational, randomised phase III trial (REFLECT) (252, 253). The study proved lenvatinib to be non-inferior to sorafenib in terms of OS (median of 13.6 months with lenvatinib; 12.3 months with sorafenib), and elicited a greater effect in patients with AFP levels higher than 200 ng/ml compared to sorafenib (40, 252). In contrast to sorafenib, lenvatinib is a type V TKI, with a higher potency against VEGF receptors and fibroblast growth factor (FGF) receptors (70, 252).

4.6.3 Second-line TKIs

Second-line therapies are administered to patients following disease progression after treatment with sorafenib. Three separate phase III trials have led to the approval of three agents: regorafenib, cabozantinib and ramucirumab (96, 254, 255). Regorafenib is a multikinase inhibitor with targets including VEGFR1-3 and was the first second-line therapy approved for HCC following progression or intolerance to sorafenib. Although there are structural similarities between regorafenib and sorafenib, the former is more potent against VEGF receptors and exhibits a broader activity (256). There is a resultant survival advantage of 10.6 months verses 7.8 months in the placebo treatment group (254). Cabozantinib is a TKI targeting VEGFR2, MET and AXL. It approves OS compared to those treated with a placebo, extending survival from 8 months to 10.2 months (255). The HGF receptor MET plays a role in the pathogenesis of HCC and notably, sorafenib resistance (257). Ramucirumab is the first approved HCC therapy for a biomarker-selected population of patients, improving OS in a subgroup of patients with baseline serum AFP levels of over 400 ng/ml (7.3 months in placebo group; 8.5 months with ramucirumab) (96). Rather than acting as a TKI, ramucirumab is a monoclonal antibody targeting VEGFR2 (258).

4.6.4 Immune checkpoint inhibitors (ICIs)

Information on the immune profile of a tumour can provide targets for novel therapeutic approaches, and has been utilised in the development of immune checkpoint inhibitor (ICI) drugs such as anti-CTLA-4, anti-PD-1 and anti-PD-L1 (135-137, 259). Targeting these checkpoint molecules blocks negative feedback pathways that enable immunosuppression. The IMbrave150 trial demonstrated that combining atezolizumab (anti-PD-L1) and bevacizumab (anti-VEGFA) was superior to sorafenib, improving OS from 13.4 months in the

sorafenib arm to 19.2 months with the combination treatment, as well as significantly improving PFS (260, 261). This therefore led to the combination treatment being approved as a first-line therapy for HCC and the new gold standard of care (261). Other aspects in which the combination treatment proved more favourable than sorafenib were in drug tolerability and median time of deterioration to quality of life (70).

In recent years, the effectiveness of a number of ICIs combined with the requirement for HCC treatment options in the second-line setting has led to the accelerated approval of a number of agents by the FDA. The PD-1 inhibitors nivolumab and pembrolizumab are approved as single agents for use as second-line therapies. The CheckMate-040 study demonstrated nivolumab to be well tolerated by patients, as well as having an overall response rate (ORR) of 14% and median OS of 15.6 months in a cohort of 262 patients (262). Similarly, the KEYNOTE-224 trial demonstrated pembrolizumab to induce an ORR of 17% and median OS of 12.9 months in 104 patients enrolled in the study (263). Interestingly, both nivolumab and pembrolizumab were observed to improve OS in the first-line setting. However, the results did not reach statistical significance (264, 265). Moreover, the CTLA-4 inhibitor ipilimumab was approved for use in combination with nivolumab for patients who showed disease progression after treatment with sorafenib, resulting in a median OS of 23 months (266). This combination treatment in currently under investigation in the US, in comparison with first-line therapies sorafenib and lenvatinib (267).

Recent findings have highlighted the importance of stratifying patients according to underlying liver aetiology prior to immunotherapy. Anti-PD-1 and anti-PD-L1 have been shown to have limited efficacy in MASH-HCC, following a meta-analysis of 1,600 patients and studies in preclinical mouse models of HCC. This impaired immune surveillance is due to an expansion of exhausted CD8+PD1+ T cells which contributes to a worse prognosis. Indeed, anti-PD-1 immunotherapy increased the incidence, tumour size and number of nodules in mice with MASH-HCC, whilst patients with MASH-related HCC displayed reduced OS compared to patients with different aetiologies (268). A subsequent study using an orthotopic mouse model of HCC identified that anti-PD-1 in combination with a CXCR2 antagonist enables MASH-HCC immunotherapy. A reduction in tumour burden and improved OS was observed, alongside increased CD8+ T cell numbers, increased activation of intratumoural XCR1+ DCs, and an unexpected increase in TANs, as neutrophils switched from a pro-tumour to anti-

tumour phenotype (269). These findings further emphasise the complexity of the tumour microenvironment in HCC.

4.6.5 Combining TKIs and ICIs

Investigation into whether the efficacy ICIs can be enhanced by use in combination with multi-target TKIs is currently underway. The combination of the TKI lenvatinib, which exhibits anti-angiogenic activity, and the ICI pembrolizumab are currently in phase III trials following encouraging results in a phase 1b trial; an objective response was achieved in ∼40% of patients, as well as a median PFS of 8.6 months and OS of 22 months (270). To further rationalise the use of lenvatinib and pembrolizumab in patients, a study utilising multiple mouse models of HCC determined that the combination therapy induced an immune-active TME, reduced the Treg infiltrate and inhibited TGF-β signalling (271). Similarly, the phase III COSMIC-312 trial combining cabozantinib with atezolizumab ascertained that the combination therapy significantly improved PFS compared to sorafenib, though there was no difference in OS between the treatment groups (272).

4.6.6 Targeting immune "cold" tumours

Insight into the TME composition allows a different therapeutic approach to be taken for the treatment of "cold" tumours, where there is an absence of infiltrating T cell and defects in antigen presentation, and typical lines of immunotherapy would be ineffective. The strategy applied in this instance is to alter the "cold" tumour microenvironment and transform it into a "hot" tumour, achieved through the trafficking of T cells into the tumour via TGF-β-blocking antibodies, anti-angiogenic therapies and immunocytokines such as CEA-IL2v. The use of chimeric antigen receptor (CAR) T cells to target tumour antigens is another method of targeting immune deficient tumours (273). However, whilst the effectiveness of CAR-T cell therapy has been demonstrated in B cell malignancies, limited efficacy has been observed in solid tumours, and further investigation into improving the tumour specificity of CAR-T cells may be required (274). Furthermore, toxicity (resultant of both "on-target off-tumour" activity and excessive cytokine production due to CAR-T cells surpassing their threshold level of activation) is a limitation of CAR-T cell therapy (275, 276). Potential targets for CAR-T cells in HCC are glypican-3 (GPC3) and AFP due to their high expression in HCC tissue (approximately 70% and 50% respectively) concurrent with low expression of both markers in surrounding non-tumour tissue (277-279).

While the management of HCC has undeniably advanced over the last decade, there is still an unmet need for novel therapies to further improve survival, particularly in advanced HCC.

4.7 HCC models

4.7.1 Requirement for novel HCC models

Preclinical models of HCC have led to vital insights into the pathogenesis of disease and have proved to be essential drug discovery tools used in the validation of novel therapies. Despite these models, the success rate of drugs that progress from Phase I of clinical trials to approval is notably low, at less than 10% (280). An explanation for this failure is inadequate preclinical research, in which the disease models developed are not physiologically relevant to human disease (281). As such, it is imperative that new experimental approaches are developed that succeed in bridging the gap between preclinical models of HCC and the treatment of patients.

4.7.2 2D cell culture

A commonly utilised system of modelling disease is the use of 2D mono-cultures and co-cultures of both human and rodent cells (primary cells and immortalised cell lines), which are often used to investigate cell proliferation and therapeutic responses. Currently, there are over 30 commercially available immortalised HCC cell lines which potentially offer a tool for identifying links between molecular signatures and drug responsiveness (282, 283). HepG2 is the most commonly utilised HCC line, often selected due to its lack of viral infection, although controversy over its use exists as there is evidence to suggest that it originated from a hepatoblastoma rather than HCC (284). Although these methods are cost-effective, reproducible, and provide a homogenous population of cells for consistent data, they come with many limitations. 2D cultures lack the structural architecture of native tissue, failing to reflect *in vivo* situations with the correct cell-cell interactions, as well as interactions between cells and the ECM (285, 286). Furthermore, the plastic on which the cells are cultured subjects them to mechanical stress, and subsequent de-differentiation, metabolic changes, and loss of typical characteristics (287, 288). Likewise, long-term culture of 2D cell lines can give rise to genetic drift, potentially altering gene expression, morphology and drug sensitivity (289). However, co-culture systems enable the cell-cell interactions between multiple cell types to be accounted for and provide utility as drug screening tools (285).

4.7.3 Animal models

Animal models are often utilised to model disease, and mouse models in particular regularly act as the basis for preclinical research in HCC (290). Different mouse models can be used depending on the scope of the research and the underlying liver injury that is required alongside the development HCC.

Genetically engineered mouse (GEM) models are preferable when investigating genetic alterations and their associated pathways, and exploit the activation of oncogenes and inactivation of tumour suppressors to induce tumour formation (291, 292). The development of GEM models with a liver-specific knockout of p53 have demonstrated that loss of p53 alone is sufficient to induce hepatocarcinogenesis, whilst mutating p53 alongside phosphatase and tensin homolog (PTEN) accelerates tumour growth in HBV transgenic mice (293, 294). In contrast, transgenic mice overexpressing the oncogene MYC and the transcription factor E2F1 develop tumours more rapidly than mice overexpressing MYC alone, alluding to synergy between E2F1 and MYC during carcinogenesis (295).

The use of carcinogenic agents encourages tumour formation via two mechanisms: inducing DNA damage or promotion of the clonal expansion of preneoplastic cells (291, 296). For instance, the alkylating agent DEN promotes hepatocarcinogenesis in mice via the production of ROS and though its ability to alkylate DNA. This DNA damage results in hyperplastic nodules and HCA development before culminating in HCC (296-298). It is important to note that the single intraperitoneal injection of DEN required to induce HCC does not result in the underlying fibrosis and cirrhosis that often precede HCC. Therefore, establishing a two-stage model may be necessary; combining the DEN-induced HCC model with regular injections of carbon tetrachloride (CCl_4) provides a model of HCC that arises on a background of advanced liver fibrosis (299). Diet-induced models of MASH and HCC involve the use of the Gubra Amylin NASH (GAN) diet and the choline-deficient, L-amino acid-defined, high fat diet (CDAHFD) (300, 301). These methods offer tools for investigating the molecular mechanisms responsible for hepatocarcinogenesis and HCC development.

Xenograft models describe the implantation of HCC cell lines into recipient mice, either directly to the liver tissue (orthotopically), to a foreign nearby tissue (heterotopically) or underneath the skin (ectopically). This type of model is ideal for rapid generation of reproducible tumours for the screening of novel treatment strategies, but do not capture the

process of hepatocarcinogenesis (302, 303). Murine HCC cell lines previously used to generate xenograft models include Hepa1-6 and HCa-1 (304, 305). Implanting human HCC cells or solid tumour fragments into mice can tailor xenograft models to better represent human HCC and has been achieved with PLC/PRF/5, HuH7, SNU-475 and SNU-761 cells (306, 307). To overcome the limitation of using immunodeficient mice to avoid cell and tissue rejection, humanised mice containing components of the human immune system enables contributions from the TME to be considered (303, 308, 309). For instance, severe combined immunodeficiency (SCID) mice engrafted with human peripheral blood mononuclear cells (PBMCs) or foetal tissues serves as a preclinical bridge for the study the human immune system in the context of a whole physiological organism (310).

4.7.4 3D cell culture

3D models of HCC overcome some of the shortcomings presented by 2D and animal models. They are more reflective of the *in situ* liver, accounting for cell to cell signalling and cellular organisation to a higher extent than 2D models, and can utilise human cells and tissue to be more applicable to human disease (311). Tumour-derived organoid cultures accurately capture the architecture, function and genetic landscape of native tissue *in vitro*, providing insights into tumour pathogenesis and useful drug discovery tools (312). Eight tumour-organoid cultures derived from patients with PLC demonstrate the maintenance of characteristics from the original tumour following long-term *in vitro* expansion. The maintenance of transcriptomic and expression profiles specific to individual patients enables the identification of prognostic biomarkers, and have highlighted ERK as a potential target in PLC (313).

Spheroids offer 3D culture systems replicating the spatial conformation of solid tumours, mimicking the heterogeneous access to oxygen and nutrients. Grown as free-floating cultures, spheroids are not subjected to the mechanical stress applied to cells by plastic and enable standardised drug screening due to their reproducibility (314, 315). Spheroids comprised of multiple cell types better recapitulate the TME, accounting for prominent cells in a native tumour, such as tumour associated fibroblasts (316). Multicellular spheroids formed from HCC cell lines alongside stromal cells such as hepatic stellate cells (LX2), fibroblasts (WI38) and human umbilical vein endothelial cells (HUVECs) demonstrate an increased spheroid compactness and increased chemoresistance, outlining stromal cells as promising targets to

enhance HCC therapy (317, 318). Spheroid models of HCC have demonstrated a higher drug resistance compared to 2D cell culture models, further highlighting the limitations of 2D cell culture in drug discovery (319, 320).

4.7.5 Organ-on-a-chip

Organ-on-a-chip describes the use of microfluidic chips to culture natural or engineered tissues, giving rise to a system whereby solutions can be guided and manipulated within fine microchannels to mimic *in vivo* microenvironments (321, 322). Combining multiple cell types also contribute to the simulation of native microenvironments, recapitulating cell-cell interactions, chemical gradients, mechanical properties and vascular perfusion (323). Organ-on-a-chip systems modelling many organ types have been developed (324-326). HepG2 cells have been utilised in an organ-on-a-chip system to simulate liver injury induced by ingested nanoparticles (327). The prospect of a platform that allows the dynamics of the microenvironment to be studied, as well as drug efficacy and toxicity presents organ-on-a-chip technology as an exciting platform for modelling HCC (328).

4.7.6 3D bioprinting

Reproducible 3D culture models can be generated via bioprinting. Customised, multicomponent bio-inks can be utilised to construct biomimetic tissue models, reflecting complex native tissue with multiple cell types and various other biomaterials (329). The ECM is specifically organised to support the function of a tissue or organ, and bio-inks can be engineered to recapitulate these dynamics, exhibiting changes in response to stimuli such as pH and temperature (330). The development of a tri-component hydrogel consisting of collagen, alginate and fibrin replicates physiological conditions displaying a stiffness comparable to native soft tissues, and enables cells to be printed at a high density and viability via the bioprinting system recently developed by the Dalgarno laboratory, reactive jet impingement (ReJI) (331, 332). The ReJI bioprinting system creates a gel by fusing two jet streams: the collagen-alginate-fibrin polymer solution and a cross-linking solution capable of containing cells and growth factors (332). *In vitro* liver constructs have been successfully printed using bioprinting technology, combining ECM-based solutions containing collagen, elastin, glycosaminoglycans and a range of growth factors with crosslinkers to generate a hydrogel capable of printing liver spheroids (333). HCC constructs have been successfully bioprinted, utilising both patient derived cells and immortalised HCC cell lines, and display an

expression of tumour-related genes comparable to real tumours (334, 335). Vascularised structures can be introduced to tissue via bioprinting, accounting for an important hallmark of many cancers. A template resembling the vasculature is first deposited, before being replaced by an endothelialised hydrogel matrix (336, 337). A number of studies have demonstrated the potential of 3D printed liver tissues to mimic drug responses observed in humans, proposing the model as a tool for screening novel therapies. Nguyen *et al.* modelled drug induced liver injury in response to the antibiotics Trovafloxacin and Levofloxacin in a bioprinted liver model comprised of patient-derived hepatocytes and non-parenchymal cells, allowing a distinction in toxicity between highly related compounds (338). The responsiveness of bioprinted liver models to drugs, alongside the potential to print HCC constructs presents bioprinting as a valuable tool for anticancer drug discovery.

4.7.7 Precision-cut liver slices

While 2D and 3D cellular models provide an insight into disease driving mechanisms and subsequent drug discovery, they do not recapitulate the physiological composition and heterogeneity of *in situ* tissue. Precision-cut liver slices (PCLS) generated from human and rodent tissue offer a reproducible *ex vivo* culture model that retains the 3D structure and cellular composition of native liver tissue, in which various disease pathologies can be investigated and treated (339-341). A drawback of this methodology is that normal static conditions result in a functional life span of approximately 48 hours, due to hypoxia. This limitation can be overcome by the development of a bioreactor system within the Newcastle Fibrosis Research Group, which generates a bi-directional flow of media to oxygenate PCLS maintaining their viability for up to 7 days. The extended potential culture period offered by this bioreactor system enables both tissue manipulation and therapeutic intervention within the viable lifespan of the PCLS (340). Referring specifically to cancer, Koch *et al.* demonstrated the adherence and invasiveness of multiple cancer cell lines into liver tissue. This model highlights the potential role for THO complex subunit 5 homolog (THOC5), as PCLS generated from THOC5 knockout mice display a greater than 80% reduction in adhesion of cancer cells (342). Precision-cut tumour slices (PCTS) generated from solid tumours retain the characteristics of the *in situ* tumour and are responsive to different anticancer therapies, proving tissue slices to be a platform for the exploration of novel therapeutics, and alleviating the contrast between human disease and most preclinical models (343-345).

5 Aims and objectives

The aim of my PhD project was to develop *ex vivo* 3D models of HCC using PCLS as a foundation. HCC is typically diagnosed at advanced stages due to the asymptomatic nature of the disease at earlier stages. Approved systemic therapies currently employed to treat those with advanced HCC only offer the prospect of survival for a few months, in a small proportion of patients. There is therefore an urgent requirement for models that accurately recapitulate the pathophysiology of HCC, while accounting for the important crosstalk from the surrounding TME that so often influences HCC development. Physiologic models of HCC provide a useful platform for both drug discovery and investigation into the various mechanisms of HCC development. The methods of modelling HCC exploited are as follows:

1. The generation and characterisation of an *in vivo* orthotopic mouse model of HCC and subsequent generation of PCTS from the tumours, to produce an *ex vivo* culture system containing important components of the TME capable of undergoing manipulation and therapeutic intervention.
2. Combining HCC spheroids generated from murine and human HCC cell lines with PCLS generated from mouse and human liver tissue, respectively. Demonstrate that the resulting system accounts for both the HCC itself and the surrounding non-tumour liver tissue, mimicking the TME. Therapies incorporated into the culture system can be assessed for both efficacy against the HCC and toxicity to the background liver tissue.
3. Generation of a patient-derived HCC cell line library following isolation and expansion of primary HCC cells from patient biopsies. Utilisation of these patient-derived cells in the spheroid-engrafted PCLS model, tailoring the model for a use in precision medicine.

6 Materials and Methods

6.1 Human tissue

Human liver tissue for PCLS generation was obtained from the normal margin following resection of colorectal metastasis or HCC. Liver tissue was collected under full ethical approval by the North East – Newcastle and North Tyneside 1 Research Ethics Committee through the CEPA biobank (REC17/NE/0070) or by the Newcastle and North Tyneside 2 Research Ethics Committee (REC19/NE/0251) and used subject to patients' written consent. PCLS were generated in fewer than two hours post resection to minimize ischemic time and preserve hepatocyte viability. Tissue from all donors was frozen and formalin-fixed before being processed and embedded in paraffin blocks. Human HCC biopsies were obtained under full ethical approval by the Newcastle and North Tyneside 2 Research Ethics Committee (REC19/NE/0251) and subject to patients' written consent.

6.2 Animal work

6.2.1 *In vivo* ethical statement

All animal experiments were approved by the Newcastle Ethical Review Committee and performed under a UK Home Office licence, in accordance with the ARRIVE guidelines. All mice were housed in the Comparative Biology Centre at Newcastle University with free access to food and water.

6.2.2 General animal work

C57BL/6 wild type (WT) mice were obtained from an in-house breeding colony in the Comparative Biology Centre and were used as a source of WT liver tissue. C57BL/6 WT mice were purchased from Envigo to generate an orthotopic model of HCC.

6.2.3 Murine orthotopic model of HCC

Orthotopic models of HCC were generated in C57BL/6 mice using the immortalised murine cell lines Hep-53.4, Hepa1-6 and H22. Surgeries were performed under isoflurane general anaesthesia and all animals were given pain relief. Following a laparotomy, $1x0^6$ luciferase-expressing Hep-53.4, Hepa1-6 or H22 cells were implanted into the left lobe of C57BL/6 mice via intrahepatic injection. In vivo imaging systems (IVIS) imaging was performed on day 1, day 7, day 14 and day 21 post injection to assess tumour growth via bioluminescence, before mice

were humanely killed, and samples harvested on day 21. After the Hep-53.4 cell line was selected for orthotopic model generation, mice with Hep-53.4 tumours were harvested at day 14, day 21 and day 28 for characterisation of the tumour and liver tissue. Therapeutic intervention with 45 mg/kg sorafenib (Tocris), 10 mg/kg lenvatinib (Selleckchem) or a PEG/DMSO control was started at 14 days post implantation and was administered via daily oral gavage until mice were harvested at day 28, at which point tumour burden and liver to body weight ratio was measured.

6.3 Precision-cut Liver/Tumour Slices

6.3.1 Precision-cut tissue slice generation

Liver and tumour tissue was cored from human or mouse tissue using an 8 mm Stiefel biopsy punch (Medisave) to generate PCLS and PCTS. Cores were submerged in 3% low gelling temperature agarose (Sigma-Aldrich) in metal moulds and placed at 4°C for 10 minutes to set. The tissue cores embedded in agarose were superglued to the vibratome mounting stage and cut using a Leica VT1200S vibrating blade microtome (Leica Biosystems) at a thickness of 250 µm, speed of 0.3 mm/sec and amplitude of 2 mm. The PCLS/PCTS generated were cultured in 8-µm-pore Transwell inserts in BioR plates with a total of 3 ml of cell culture media per paired-well, and cultured in a patented bioreactor platform (340). Tissue was cultured in Williams' Medium E (Sigma-Aldrich) supplemented with 1% penicillin-streptomycin, 1% L-glutamine, 1% pyruvate, 1 x insulin transferrin-selenium X, 2% fetal bovine serum and 100 nM dexamethasone, at 37°C supplemented with 5% CO_2.

6.3.2 Tissue culture treatments

PCTS and PCLS were rested in culture for 24 hours prior to treatment with receptor tyrosine kinase inhibitors or a mixture of free fatty acids ± anti-PD1 immunotherapy. Murine PCTS and spheroid HCC-PCLS were treated with the small molecule inhibitors sorafenib (5 µM – 20 µM) (Tocris), regorafenib (20 µM – 5 µM) (Selleckchem), or lenvatinib (0.1 µM – 2.5 µM) (Selleckchem) for a further 3 days after the rest period. Murine PCTS were also treated with a 2mM free fatty acid mixture comprising of linoleic acid, oleic acid and palmitic acid in a 1:1:1 ratio in 2.6% fatty acid-free bovine serum albumin (BSA) (Sigma) from day 1, and then 20 µg/ml Ultra-LEAF™ Purified anti-mouse CD279 (PD-1) (Biolegend) or IgG control from day 2. The PCTS were harvested at day 4. GPC3scFv-TM-CD28-CD3z CAR-T cells (Amsbio) were stained with CellVue™ Jade Cell Labelling Kit (Thermo Fisher) and added to HuH7 spheroid-

PCLS culture for 48 hours (85,000 CAR-T cells per PCLS). Media and treatments were refreshed daily on all PCLS/PCTS.

6.4 Cell line culture and stable transfections

Stable transfections were performed on the HuH7 and Hep-53.4 cell lines with tdTomato-N1 (Figure 6A) or a custom pNL(sNLuc/CMV/NeoR) (Figure 6B) expression vector using the Lipofectamine 3000 Transfection Reagent kit (Thermo Fisher). 100,000 cells were seeded in each well of a 6-well plate. The following day, a transfection complex comprised of 250 µl Opti-MEM™ (Thermo Fisher), 5 µl P3000 Reagent, 7.5 µl Lipofectamine 3000 Reagent and 2.5 µg plasmid DNA was mixed and left for 10 minutes to enable DNA-lipid formation. The cell culture media on the cells was refreshed and the transfection complex was added to the cells in a drop-wise manner. The following day, the media was removed from all cells and replaced with selection media containing 1 mg/ml G418 disulfate salt (Sigma-Aldrich). The cells remained in selection media until all cells in a control well had visibly died. Transfected cell lines were cultured in selection media approximately once every two months to prevent an expansion of WT cells. Hep-53.4, HuH1 and Hepa1-6 cells were cultured in DMEM with high glucose (Sigma), and HuH7, SNU-182, SNU-387, SNU-398, SNU-475 and H22 cells were cultured in RPMI-1640 (Sigma), at 37°C with 5% CO_2. All culture media was supplemented with 10% FBS, 1% penicillin-streptomycin, 1% L-glutamine and 1% pyruvate.

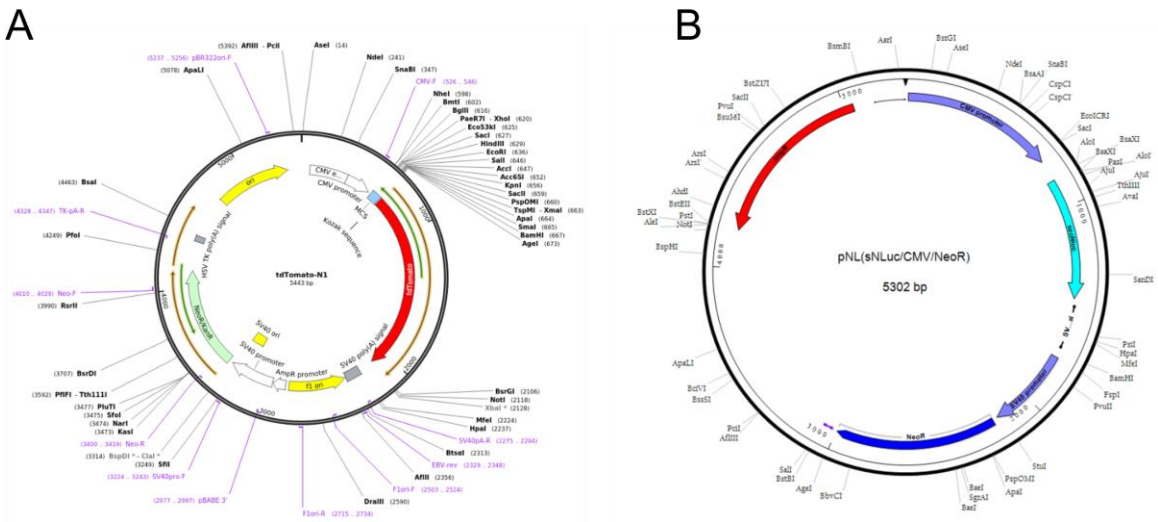

Figure 6. Expression vectors employed for stable transfections of HCC cell lines. (A) tdTomato-N1 plasmid to induce red fluorescence purchased from Addgene. (B) Custom "SecLuc" vector designed by Promega to induce expression of secreted NanoLuc luciferase.

Table 1. Information pertaining to the immortalised cell lines employed: origins and mutated genes.

Cell line	Species	Origin	Mutations
Hep-53.4	Mouse	DEN HCC tumour, C57BL/6J mouse	
Hepa1-6	Mouse	Spontaneous BW7756 HCC tumour, C57/L mouse	
H22	Mouse	HCC tumour, C3HA mouse	
HuH7	Human	HCC, 57Y, male, Japanese	TP53 TERT POLD3 VEGFR2
SNU-398	Human	HCC, 42Y, male, Korean	CTNNB1 TP53
SNU-182	Human	HCC, 24Y, male, Korean	TP53
SNU-387	Human	HCC, 41Y, female, Korean	TP53 TERT NRAS
SNU-475	Human	HCC, 43Y, male, Korean	TP53 TERT
HuH1	Human	HCC, 53Y, male, Japanese	TP53 AXIN1

6.5 Primary cell culture and lentiviral transduction

Patient-derived HCC cell lines were isolated from HCC biopsies obtained from the Freeman Hospital. The biopsies were initially dissociated with a scalpel in a sterile cell culture dish. Further dissociation was performed by incubating the tissue with the enzyme mixture from the human Tumour Dissociated Kit (Miltenyi) at 37°C and 170 rpm for 60 minutes. Following this, the falcon tube was topped up with ice cold DMEM supplemented with 1% L-glutamine, pyruvate and penicillin-streptomycin and centrifuged at 1000 rpm for 5 minutes. The media was discarded and the cell pellet was resuspended in ice cold PBS and centrifuged at 8000 rpm for 5 minutes. The PBS was discarded and the cell pellet was washed in ice cold PBS for a second time. The cells were centrifuged at 6000 rpm for 5 minutes. The cell pellet was resuspended and expanded in RPMI-1640 supplemented with 1% L-glutamine, pyruvate and penicillin-streptomycin, 10% FBS, 1 x insulin transferrin-selenium X, 40 ng/ml EGF, 10 µM ROCK inhibitor Y-27632 (Sigma) and 5 µM TGF-β pathway inhibitor A 83-01 (Tocris). The resultant cells were transduced with a lentivirus pLV[Exp]-mCherry:T2A:PuroCMV>MetLuc (VectorBuilder) at a titre of $1x10^6$ to express the red fluorescent protein (RFP) mCherry and a secreted luciferase. After 24-48 hours, the media containing the lentivirus was removed and

the cells were cultured in selection media containing 2 µg/ml puromycin dihydrochloride for a further 7 days to select for successfully transduced cells.

6.6 Spheroid generation

Round-bottom 96-well plates were coated with 1% agarose (Sigma). Cells were trypsinised and counted using an EVE Automated Cell Counter. Spheroids were formed by seeding between 2,500 and 40,000 cells per well in a total volume of 100 µl DMEM with high glucose (Sigma) (Hep-53.4) or RPMI-1640 (Sigma) (HuH7) supplemented with 10% FBS, 1% penicillin-streptomycin, 1% L-glutamine and 1% pyruvate, at 37°C with 5% CO_2. Patient-derived spheroids were cultured in RPMI-1640 supplemented with 1% L-glutamine, pyruvate and penicillin-streptomycin, 10% FBS, 1 x insulin transferrin-selenium X, 40 ng/ml EGF, 10 µM ROCK inhibitor Y-27632 (Sigma) and 5 µM TGF-β pathway inhibitor A 83-01 (Tocris). Spheroids were imaged using a Zeiss AXIO Observer D1 microscope and spheroid measurements were recorded using Zen (blue edition) software.

6.7 Spheroid implantation

Human or murine PCLS were removed from the BioR plates and placed into a sterile 10 cm cell culture dish. The media inside the insert was transferred back to the relevant paired-well in the BioR plate via pipette. Spheroids were aspirated with a pipette in a total volume of 5 µl and slowly expelled directly onto the liver slice. The resultant spheroid-PCLS were left for approximately 5 minutes to enable spheroid engraftment before the 8-µm-pore Transwell inserts were placed back into the appropriate paired-wells so the volume of culture media inside and outside of the insert could slowly equilibrate without disturbing the implanted spheroid. The BioR plates were returned to the incubator and cultured at 37°C supplemented with 5% CO_2.

6.8 Scratch wound assay

A 96-well ImageLock plate (Sartorius) was coated with 50 µg/ml rat tail collagen I (Gibco) in 20mM acetic acid to replicate the typical cell culture conditions for patient-derived HCC cell lines. 30,000 primary patient derived cells from lines ML018B, ML031 or ML043 were seeded per well for confluency the following day. Two hours prior to wound generation the cells were treated with 4 µg/ml mitomycin c to prevent cellular proliferation. A scratch was generated in each well using the Sartorius Woundmaker and the culture media containing mitomycin c was

removed. The cells were washed three times with PBS to remove debris from the scratch. 100 µl fresh cell culture media was added to each well and the plate was incubated in the Sartorius Incucyte Live Cell Imaging instrument for 72 hours. One phase-contrast image was taken of each well every hour at 10x magnification. Image analysis and graph generation was performed using Incucyte 2022B Rev1 software.

6.9 Multiphoton imaging

Spheroid-engrafted PCLS were fixed in 4% paraformaldehyde (PFA) solution for 30 minutes, then stained with 10 µg/ml Hoechst 33342 for a further 30 minutes. The tissue samples were then washed in PBS and transferred onto a microscope slide inside a gene frame with the side of the tissue engrafted to the HCC spheroid facing upwards. The PCLS were then mounted in the gene frames with VECTASHIELD© Antifade Mounting Medium (Vector Laboratories) and cover slipped. Multiphoton imaging was performed by Dr Glyn Nelson using a Zeiss LSM880 NLO Multiphoton microscope in the Bioimaging Unit at Newcastle University.

6.10 Enzyme-linked immunosorbent assay (ELISA)

Sandwich ELISA quantification for mouse albumin (Abcam) and human albumin (R&D Systems) was performed on culture media samples harvested daily from murine and human PCLS. 96-well half-area plates (Corning) were incubated overnight with capture antibodies, and then washed with 1x PBS/0.05% Tween. Non-specific binding was blocked with reagent diluent (RD) comprised of 1% BSA in PBS for 1 hour and the plate was washed. Standards were prepared by performing a serial dilution resulting in 8 standard samples; the highest concentration being 8000 pg/ml for mouse albumin and 160 ng/ml for human albumin, and the lowest concentration being 0 (RD only). Samples were diluted in RD to an appropriate concentration for the sensitivity of the assay, and standards and samples were incubated in duplicate in the ELISA plate for 2 hours before the plate was washed. The plate was then incubated with detection antibodies for 2 hours, then washed and incubated with streptavidin conjugated to horseradish peroxidase (HRP) in the dark for 20 minutes. The plates were washed, incubated with a substrate solution which initiated a colour change, and stopped with a sulfuric acid solution when the standard curve had developed into a clear gradient of colour. The optical density was measured at 450nm and 570 nm. Sandwich ELISA quantification for RFP (Cell Biolabs, Inc.) and mCherry (Abcam) were performed as per the manufacturers' instructions on

pre-coated plates. All sample concentrations were calculated using the relevant standard curve generated for each protein and plate.

6.11 Lactate dehydrogenase (LDH) assay

Lactate dehydrogenase (LDH) was quantified in culture media samples harvested daily from murine and human PCLS, using the CyQUANT™ LDH Cytotoxicity Assay kit (Thermo Fisher). Reaction Mixture was created by dissolving Substrate Mix in 11.4 ml of molecular grade water and mixing with Assay Buffer. A positive control was created by adding a PCLS to a mixture of 200 µl 20% Triton X-100 and 1.3 ml Williams' Medium E. This mixture was vortexed at room temperature to ensure tissue death and LDH release. Blank Williams' Medium E was used as a negative control. 25 µl of all samples and controls were added to a 96-well half-area plate (Corning) in duplicate and combined in a 1:1 ratio with the Reaction Mixture. The plate was incubated in the dark for 30 minutes, at which point the reaction was stopped with Stop Solution and the optical density was measured at 490 nm and 680 nm. The negative control absorbance values were subtracted from the sample absorbance values and normalised against the positive control to determine the LDH levels in each sample.

6.12 Triglyceride assay

The triglyceride levels in PCTS and PCLS were determined using the Triglyceride Quantification Assay Kit (Colorimetric/Fluorometric) (Abcam). A set of five standards was prepared ranging from 10 nmol/well to 2 nmol/well by diluting TG Standard in Assay Buffer, with Assay Buffer alone used as a negative control. PCTS and PCLS were homogenised at 90°C in 250 µl 5% NP-40/ddH_2O solution and diluted in Assay Buffer to an appropriate concentration for the sensitivity of the assay. The Triglyceride Reaction Mix was prepared by creating a 4% solution of the Triglyceride Probe and Triglyceride Enzyme Mix in Assay Buffer. 50 µl of all standards and samples were added to a 96-well half-area plate (Corning) in duplicate and were mixed with 2 µl Lipase to convert the triglycerides to fatty acids and glycerol. The samples were then incubated in a 1:1 ratio with the Triglyceride Reaction Mixture for 1 hour before the optical density was measured at 570 nm. Sample concentrations were calculated using the standard curve generated.

6.13 Resazurin assay

A resazurin assay was performed to determine the metabolic activity of PCTS or PCLS between day 1 and day 4 of the tissue culture period. A 4.5 mM resazurin stock solution was diluted in Williams' Medium E to a working concentration of 450 µM. Each tissue slice was incubated in a 96-well plate with 100 µl of the working resazurin solution for 1 hour at 37°C with 5% CO_2. 100 µl of the working resazurin solution was used as a negative control. After 1 hour, the solution was transferred to an opaque 96-well plate (Greiner) and the fluorescence was measured.

6.14 Luciferase assay

A luciferase assay was performed to assess the levels of NanoLuc luciferase secreted into the culture media by SecLuc transfected HCC cells, using the Nano-Glo® Luciferase Assay System (Promega). Nano-Glo® Luciferase Assay Reagent was prepared by combining one volume of Nano-Glo® Luciferase Assay Substrate with 50 volumes of Nano-Glo® Luciferase Assay Buffer. 40 µl of undiluted tissue or cell culture media samples were added to an opaque 96-well plate (Greiner) and 40 µl of the relevant culture media was used as a negative control. The samples were combined in a 1:1 ratio with the Nano-Glo® Luciferase Assay Reagent and left for at least 3 minutes for the reaction to take place. The luminescence values were then measured.

6.15 Bromodeoxyuridine (BrdU) assay

A bromodeoxyuridine (BrdU) assay was performed to determine the proliferation rates of patient-derived HCC cell lines treated with anticancer therapies. To replicate the usual cell culture conditions, a 96-well cell culture plate was coated in 50 µg/ml rat tail collagen I (Gibco) in 20mM acetic acid. The plate was washed three times with sterile PBS and 10,000 cells were seeded per well in a total volume of 100 µl. The following day, the cell culture media was removed and replaced with fresh media containing either a vehicle control (0.05% DMSO), sorafenib (5 µM or 10 µM) or dose lenvatinib (0.1 µM or 0.63 µM) and the cells were incubated for 4 hours at 37°C supplemented with 5% CO_2. 10 µl BrdU labelling solution was then added to each well to create a final concentration of 10 µM BrdU and the cells were incubated with the treatments and BrdU solution for a further 24 hours. The BrdU labelling solution was then removed from the cells and 200 µl of FixDenat was added to each well and incubated at room temperature for 30 minutes. The FixDenat was removed from the cells and replaced with 100

µl of Anti-BrdU-POD working solution per well, followed by a 90-minute incubation at room temperature. The Anti-BrdU-POD working solution was removed and the cells were washed three times with 300 µl of PBS per well. 100 µl of Substrate Solution was added to each well and the optical density was measured at 5-minute intervals for a total of 30 minutes using a TECAN Infinite® M Nano plate reader at 370 nm and 492 nm. Multiple absorbance readings were recorded to obtain readings at a suitable timepoint whereby the colour development was sufficient for photometric detection.

6.16 Ribonucleic acid (RNA) isolation

Snap-frozen PCLS and PCTS were homogenised in 500 µl of QIAzol lysis reagent (QIAGEN), before being combined with 140 µl of chloroform and centrifuged at 12,000 x g for 4 minutes at 4°C. The clear layer of solution was transferred to a new tube and combined in a 1:1 ratio with 50% ethanol. The mixture was then transferred to a RNeasy Mini Spin column from the QIAGEN RNeasy Mini Kit (QIAGEN), and centrifuged briefly at 8,000 x g. The flow-through was discarded. The RNeasy Mini Spin column was then washed once with 700 µl of Buffer RW1 and twice with 500 µl of Buffer RPE, each time discarding the flow-through. The spin column was transferred to a new tube and the RNA was eluted in 30 µl of RNase-free water by centrifugation for 1 minute at 8,000 x g. The resulting RNA was stored at -80°C.

6.17 RNA quantification

The purity and quantity of isolated RNA was measured using an IMPLEN nanophotometer which measured the absorbance of the samples at 260 nm and 280 nm. After a blank measurement was obtained from 1 µl RNase-free water, 1 µl of the RNA sample was loaded onto the optical pedestal and measured.

6.18 Complementary DNA (cDNA) synthesis

Complementary DNA (cDNA) was synthesised from RNA using reagents from Promega and a 2720 Geneamp thermal cycler (Life Technologies). Between 0.25-1 µg was diluted in RNase-free water to a total volume of 8 µl. Each RNA sample was then treated with 1 µl DNase and 1 µl Dnase Buffer at 37°C for 30 minutes to digest any contaminating DNA. DNase activity was stopped with 1 µl Stop Solution, before 0.5 µl Random Hexamer was added and the sample was incubated at 70°C for 5 minutes. The samples were then immediately placed on ice for 5 minutes. RT mixture was made by combining 2 µl RNase-free water, 1 µl M-MLV Reverse

Transcriptase, 4 µl M-MLV RT 5X Buffer, 0.5 µl RNasin and 1µl 10mM PCR Nucleotide Mix per sample. The RT mixture was added to the RNA sample on ice and the mixture was incubated at 42°C for 60 minutes. The resultant cDNA was diluted to 10 ng/µl and stored at -30°C.

6.19 Quantitative PCR (qPCR)

Quantitative polymerase chain reaction (qPCR) was carried out using 6.5 µl SYBR Green JumpStart Taq ReadyMix (Sigma-Aldrich), 1 µl of 10 ng/µl cDNA and 1 µl of the forward and reverse 2.5 µM primers, diluted to a total volume of 13 µl with nuclease-free water. The primers used are listed in Table 2. Each reaction underwent 40 cycles of denaturing at 95°C for 15 seconds, followed by annealing at 55°C for 20 seconds and elongation at 72°C for 30 seconds. A final cycle of 15 seconds at 95°C, 60 seconds at 60°C and 30 seconds at 95°C produced a dissociation curve. All results were normalised to the control housekeeping gene GAPDH.

Table 2. Forward and reverse sequences of mouse primers (5'-3') used for quantitative PCR.

	Forward sequence	**Reverse sequence**
CXCL1	CTGGGATTCACCTCAAGAACATC	CAGGGTCAAGGCAAGCCTC
CXCL2	CCAACCACCAGGCTACAGG	GCGTCACACTCAAGCTCTG
CXCL5	GTTCCATCTCGCCATTCA	TCCACCGTAGGGCACTGT
CXCL9	AAAATTTCATCACGCCCTTG	CTCTCCAGCTTGGTGAGGTC
CXCL10	GGATGGCTGTCCTAGCTCTG	ATAACCCCTTGGGAAGATGG
CCL2	CCAATGAGTAGGCTGGAGAG	TTCAAAGGTGCTGAAGACCT
CCL3	GATCTGCGCTGACTCCAAAG	GTCCCTCGATGTGGCTACTT
CCL4	TCCCACTTCCTGCTGTTTCT	CTCTCCTGAAGTGGCTCCTC
CCL5	TGCTGCTTTGCCTACCTCTCC	TGGCACACTTGGCGGTTCC
GADPH	GCACAGTCAAGGAAGAGAAT	GCCTTCTCCATGGTGGTGAA

6.20 Immunohistochemistry (IHC)

To perform immunohistochemistry (IHC), formalin-fixed paraffin-embedded (FFPE) 5 µm thick tissue sections were first deparaffinised by passing the sections through clearene, followed by 100% and 70% ethanol solution for 5 minutes each. Endogenous peroxidase activity was blocked with 0.6% hydrogen peroxide/methanol solution for 15 minutes. Heat-mediated

antigen retrieval was performed using either antigen unmasking solution (Vector Laboratories) at pH 6.0, or 1 mM ethylenediaminetetraacetic acid (EDTA) solution at pH 8.0 or Tris-EDTA solution at pH 9.0. The antigen retrieval method applied for each primary antibody is detailed in Table 3. The sections were allowed to cool and washed with PBS. The Avidin/Biotin Blocking Kit (Vector Laboratories) was used to block endogenous avidin and biotin for 20 minutes each with a PBS was in between, followed by blocking of non-specific binding with 20% swine serum for 45 minutes. The sections were incubated with the relevant primary antibodies overnight at 4°C, at the dilutions detailed in Table 3. Primary antibodies were washed off and sections were incubated with the relevant secondary antibodies listed in Table 3 for 45 minutes. Slides were washed with PBS and incubated with Vectastain Elite ABC HRP Reagent (Vector Laboratories) for 30 minutes. The slides were washed with PBS and positive staining was developed using DAB peroxidase substrate kit (Vector Laboratories), followed by a counterstain with Mayer's haematoxylin for 2 minutes. The nuclei were "blued" with Scott's tap water for 1 minute and the sections were then dehydrated through 50%, 70% and 100% ethanol sequentially, before being transferred to clearene for 10 minutes. The sections were then mounted in Pertex Mounting Medium (Cell Path). Terminal deoxynucleotidyl transferase-mediated dUTP nick end (TUNEL) labelling was performed using the TUNEL Assay Kit – HRP-DAB (Abcam) as per the manufacturer's instructions.

Table 3. Primary and secondary antibodies and relevant antigen retrievals used to perform immunohistochemistry.

Antigen	Catalogue number & supplier	Species applied to	Clonality/host species	Antigen retrieval	Primary antibody	Secondary antibody	Antigen function/cell type
αSMA	F3777, Sigma-Aldrich	M, H	Mouse monoclonal (1A4)	Citrate pH 6.0	1/1000	Goat anti-fluorescein (BA-0601-.5) (1/300)	Myofibroblasts
CD3	MCA1477, Bio-Rad	M	Rat monoclonal (CD3-12)	EDTA pH 8.0	1/200	Goat anti-rat (BA-9401-.5) (1/200)	CD3 T cells
CD4	Ab181724, Abcam	H	Rabbit monoclonal (EPR6855)	Tris-EDTA pH 9.0	1/400	Goat anti-rabbit (BA-1000-1.5) (1/600)	CD4 T cells
CD8	372902, BioLegend	H	Mouse monoclonal (C8/144B)	Tris-EDTA pH 9.0	1/100	Rabbit anti-mouse (E0354) (1/200)	CD8 T cells
CD68	OABB00472, Aviva	H	Rabbit polyclonal	Citrate pH 6.0	1/200	Goat anti-rabbit (BA-	CD68 macrophages

	Systems Biology					1000-1.5) (1/600)	
CD94	Ab238166, Abcam	H	Rabbit monoclonal (EPR21003)	Tris-EDTA pH 9.0	1/4000	Goat anti-rabbit (BA-1000-1.5) (1/600)	CD94 NK cells
Cytokeratin 18	Ab181597, Abcam	M, H	Rabbit monoclonal (EPR17347)	EDTA pH 8.0	1/800	Goat anti-rabbit (BA-1000-1.5) (1/600)	Cytoskeletal protein expressed by hepatocytes
Cytokeratin 19	Ab84632	M	Rabbit polyclonal	Citrate pH 6.0	1/250	Goat anti-rabbit (BA-1000-1.5) (1/600)	Cytoskeletal protein expressed by biliary cells
Cleaved caspase-3	9661, Cell Signaling	M	Rabbit monoclonal (Asp175)	Citrate pH 6.0	1/400	Goat anti-rabbit (BA-1000-1.5) (1/600)	Cell apoptosis
F4/80	70076, Cell Signaling	M	Rabbit monoclonal (D2S9R)	Tris-EDTA pH 9.0	1/800	Goat anti-rabbit (BA-1000-1.5) (1/600)	F4/80 macrophages
Ki67	14-5698-82,	M	Rat monoclonal (SolA15)	Tris-EDTA pH 9.0	1/10,000	Goat anti-rat (BA-9401-.5) (1/200)	Cellular proliferation
Ly6G	Ab210204, Abcam	M	Rat monoclonal (1A8)	Trypsin & citrate pH 6.0	1/200	Goat anti-rat (BA-9401-.5) (1/200)	Ly6G neutrophils
PCNA	Ab18197, Abcam	M, H	Rabbit polyclonal	Citrate pH 6.0	1/5000	Goat anti-rabbit (BA-1000-1.5) (1/600)	Cellular proliferation

6.21 Hyperion Imaging Mass Cytometry (IMC)

Hyperion Imaging Mass Cytometry (IMC) was performed on human spheroid-engrafted PCLS samples. 5 µm thick FFPE tissue sections were first deparaffinised by passing the sections through clearene, followed by 100%, 90%, 70% and 50% ethanol solution for 5 minutes each. Sections were then washed in deionised water for 5 minutes, before heat-mediated antigen retrieval was performed using Tris-EDTA solution at pH 9.0. The sections were allowed to cool and were washed in PBS for 5 minutes. A ring was drawn around each tissue section with a hydrophobic pen and non-specific binding was blocked with 3% BSA/PBS for 45 minutes. 200 µl of a metal-conjugated primary antibody cocktail was then added to each section in 0.5% BSA/PBS and incubated overnight at 4°C. The primary antibody cocktail was comprised of the antibodies listed in Table 4 which were labelled with metal isotopes using the Maxpar® X8 Multimetal Labeling Kit—40 Rxn (Standard Biotools). The sections were washed in Tris-Buffered Saline + 0.1% Tween (TBS-T) for 8 minutes followed by two consecutive 8 minute

washes in PBS. The sections were then incubated for 30 minutes with 125 µM (193Ir) Intercalator at a dilution of 1:400. The sections were washed in ultra-pure water for 5 minutes and subsequently air-dried at room temperature. A region of interest (ROI) was selected around the HCC spheroid and the tissue was ablated by the Hyperion Fluidigm Imaging System. The data was analysed using the Bodenmiller pipeline.

Table 4. Primary and secondary antibodies and relevant antigen retrievals and used to perform Hyperion IMC.

Antigen	Catalogue number & supplier	Metal conjugate	Clonality/host species	Antigen retrieval	Primary antibody	Secondary antibody	Antigen function/cell type
αSMA	F3777, Sigma-Aldrich	174 Yb	Mouse monoclonal (1A4)	Citrate pH 6.0	1/1000	Goat anti-fluorescein (BA-0601-.5) (1/300)	Myofibroblasts
CD3	85061, Cell Signaling	161 Dy	Rabbit monoclonal (D7A6E™)	Tris-EDTA pH 9.0	1/500	Goat anti-rabbit (BA-1000-1.5) (1/600)	CD3 T cells
CD4	Ab181724, Abcam	153 Eu	Rabbit monoclonal (EPR6855)	Tris-EDTA pH 9.0	1/400	Goat anti-rabbit (BA-1000-1.5) (1/600)	CD4 T cells
CD8	372902, BioLegend	151 Eu	Mouse monoclonal (C8/144B)	Tris-EDTA pH 9.0	1/100	Rabbit anti-mouse (E0354) (1/200)	CD8 T cells
CD16	Ab215977, Abcam	170 Er	Rabbit monoclonal (EPR16784)	Tris-EDTA pH 9.0	1/100	Goat anti-rabbit (BA-1000-1.5) (1/600)	T cells, NK cells, neutrophils, monocytes
CD31	85873SF, Cell Signaling	158 Gd	Mouse monoclonal (89C2)	Tris-EDTA pH 9.0	1/500	Rabbit anti-mouse (E0354) (1/200)	Endothelial cells
CD56	88856SF, Cell Signaling	168 Er	Rabbit monoclonal (E7X9M)	Tris-EDTA pH 9.0	1/100	Goat anti-rabbit (BA-1000-1.5) (1/600)	CD56 NK cells
CD68	Ab213098, Abcam	176 Yb	Mouse monoclonal (C68/684)	Tris-EDTA pH 9.0	1/100	Rabbit anti-mouse (E0354) (1/200)	CD68 macrophages
CD163	MCA1853, Bio-Rad	145 Nd	Mouse monoclonal (EDHu-1)	Tris-EDTA pH 9.0	1/100	Rabbit anti-mouse (E0354) (1/200)	Monocytes/ macrophages
Col1a1	81375SF, Cell Signaling	150 Nd	Rabbit monoclonal (E8F4L)	Tris-EDTA pH 9.0	1/100	Goat anti-rabbit (BA-1000-1.5) (1/600)	Collagen, type I, alpha 1
Granzyme B	79903SF, Cell Signaling	171 Yb	Rabbit monoclonal (D6E9W)	Tris-EDTA pH 9.0	1/100	Goat anti-rabbit (BA-1000-1.5) (1/600)	NK cells, cytotoxic T cells

Ki67	9027	146 Nd	Rabbit monoclonal (D2H10)	Tris-EDTA pH 9.0	1/200	Goat anti-rabbit (BA-1000-1.5) (1/600)	Cellular proliferation
p21	556432, BD Biosciences	157 Gd	Mouse monoclonal (SXM30)	Tris-EDTA pH 9.0	1/100	Rabbit anti-mouse (E0354) (1/200)	Cell cycle arrest
Pan Cytokeratin	CF190321, Thermo Fisher	147 Sm	Mouse monoclonal (AE1+AE3)	Tris-EDTA pH 9.0	1/100	Rabbit anti-mouse (E0354) (1/200)	Various keratins: 4, 5, 6, 7, 8, 10, 13, 14, 18, 19
PD-1	Ab201811, Abcam	159 Tb	Mouse monoclonal (NAT105)	Tris-EDTA pH 9.0	1/20	Rabbit anti-mouse (E0354) (1/200)	Immune checkpoint on T cells/B cells
Vimentin	46173, Cell Signaling	142 Nd	Rabbit monoclonal (D21H3)	Tris-EDTA pH 9.0	1/500	Goat anti-rabbit (BA-1000-1.5) (1/600)	Type III intermediate filament protein

6.22 Immunofluorescence (IF)

Immunofluorescence (IF) staining was performed to determine the expression of mesenchymal cell markers and typical HCC and liver-specific biomarkers in HuH7 cells and patient-derived HCC cell lines. Cells were seeded in chamber slides (Falcon) the day before performing IF staining. The following day the cell culture media was removed and the cells were washed with PBS. The cells were fixed with 4% PFA for 15 minutes and washed with PBS. The cells were permeabilised with 0.1% Triton X-100 in PBS for 10 minutes and then washed with PBS. Non-specific binding was blocked with 1% BSA in PBS for 30 minutes, and primary antibodies diluted in 1%BSA/PBS were subsequently added to the cells and incubated for 1 hour at room temperature or overnight at 4°C. The cells were washed with PBS and incubated with the relevant secondary antibodies for 1 hour at room temperature. The primary and secondary antibodies and required dilutions are listed in Table 5. The cells were washed with PBS, before the nuclei were labelled with 10 µg/ml Hoechst 33342 for 15 minutes. The cells were mounted with ProLong™ Gold Antifade Mountant (Thermo Fisher).

Table 5. Primary and secondary antibodies used to perform immunofluorescence.

Antigen	Catalogue number & supplier	Species applied to	Clonality/host species	Primary antibody	Secondary antibody
Alpha 1 Fetoprotein	Ab133617, Abcam	H	Rabbit monoclonal (EPAFP61)	1:100	Donkey anti-rabbit (A32754) (1:1000)
Cytokeratin 18	Ab181597, Abcam	H	Rabbit monoclonal (EPR17347)	1:100	Donkey anti-rabbit (A32754) (1:1000)

Glypican-3	Ab207080, Abcam	H	Rabbit monoclonal (EPR20569)	1:100	Donkey anti-rabbit (A32754) (1:1000)
Hepatocyte specific antigen	Ab190706, Abcam	H	Mouse monoclonal (OCH1E5)	1:100	Goat anti-mouse (A-11005) (1:1000)
αSMA-FITC	F3777, Sigma-Aldrich	M, H	Mouse monoclonal (1A4)	1:100	N/A
Vimentin-FITC	Ab128507. Abcam	H	Mouse monoclonal (RV202)	1:100	N/A

6.23 Histology

6.23.1 Haematoxylin & Eosin (H&E) stain

5 µm thick FFPE issue sections were first deparaffinised by passing the sections through clearene, followed by 100% and 70% ethanol solution. Sections were then rinsed with running tap water and counterstained in Mayer's Haematoxylin for 2 minutes. The sections were then washed with running tap water to remove excess stain from the slides and the nuclei were "blued" in Scott's tap water for 1 minute. The sections were rinsed with running tap water for 1 minute before being stained in Eosin for 1 minute. The sections were quickly washed in tap water to remove excess Eosin without causing the stain to leach out the tissue, and then placed into 100% ethanol for 5 minutes before being transferred to clearene for 10 minutes. The sections were then mounted in Pertex Mounting Medium (Cell Path).

6.23.2 Oil Red O stain

Oil Red O staining was performed to detect lipids in murine PCLS and PCTS. A 0.5% stock solution was made by dissolving Oil Red O (C.I. 26125) (Sigma) in 100% isopropanol. This was diluted in a 3:2 ratio with deionised water to create a 60% Oil Red O working solution, which was left to stand for 10 minutes before being filtered to remove undissolved powder. The stock and working Oil Red O solutions were covered with foil. 10 µm sections of cryo-frozen tissue were generated via cryosectioning and fixed in formalin for 30 minutes. The sections were then washed with running deionised water for 2 minutes, then rinsed with 60% isopropanol for 2 minutes. Following this, the sections were stained in freshly prepared Oil Red O working solution for 15 minutes. The sections were then rinsed with 60% isopropanol for 1.5 minutes, before being counterstained with Mayer's Haematoxylin for 2 minutes. The sections were rinsed in deionised water and mounted with Glycergel (Dako).

6.24 Image Analysis

Brightfield image analysis was performed on sections stained via IHC, H&E or Oil Red O using a Nikon Eclipse Ni-U microscope and NIS-Elements BR analysis software. Densitometry was

performed on IHC stained sections by applying predefined threshold settings to images acquired at 20x magnification. This yielded data pertaining to individual object counts in the image or the percentage area of positively stained tissue. A minimum of 12 non-overlapping fields were analysed from *in vivo* mouse tissue sections, and a minimum of 6 non-overlapping fields were analysed from PCLS and PCTS due to the smaller available area of tissue.

6.25 Statistical analysis

Results are presented as means ± standard error of the mean (SEM). GraphPad prism 9 was used to perform an unpaired Student's t-test or a two-way analysis of variance (ANOVA) with a Tukey's post hoc test. * $P<0.05$, ** $P<0.01$ or *** $P<0.001$ was considered statistically significant. Outlier tests were performed on all data sets by calculating "mean ± 2 x standard deviation", where data outside of this range was considered as an outlier.

7 An *in vivo* and *ex vivo* orthotopic model of murine HCC

7.1 Introduction

Treatment options for advanced HCC are sparse, and currently improve OS and PFS by a matter of months. Moreover, this slight improvement in prognosis only applies to a minority of patients (66, 133). Mice have commonly been utilised to model HCC via numerous strategies, often forming the basis of preclinical research and drug screening. Although it is impossible for animal models to completely capture human disease, they offer a method of studying disease in terms of a whole physiological system and consider factors such as the tumour microenvironment and circulating immune cells. Methods implemented to induce HCC in mice include GEM models (useful for understanding the implications of various mutations on HCC initiation, progression and therapy response), the use of carcinogenic agents (useful for studying hepatocarcinogenesis), and xenograft models (gives rise to rapidly growing tumours for drug screening) (283, 346).

Orthotopic models describe xenograft models whereby the tumour cells are implanted or injected directly into the organ from which the cancer originated. Orthotopic models of HCC, involving direct implantation of HCC cells into the liver, prove useful in investigating therapy responses due to their ease of use, reproducibility, disease kinetics, and the manner in which they consider the TME (346). Luciferase-expressing human HuH7 cells have previously been orthotopically transplanted into immunodeficient mice, providing a method of repeatedly monitoring tumour growth via *in vivo* bioluminescence (347). However, this model does not account for the important immune interactions that mediate tumorigenesis and treatment response. Enabling the TME to be considered, the murine Hep-53.4 cell line has been employed to generate successful orthotopic tumours in C57BL/6 mice which have been exploited to improve the efficacy of immunotherapy (269, 271). Key disadvantages of orthotopic models are that they are not useful for studying tumour progression or genetic alterations relating to hepatocarcinogenesis, and that animals must be sacrificed in order to gain in depth knowledge of tumour growth and histological features (283).

Whilst animal models can provide a breadth of information in relation to disease and treatment responses, there are of course ethical considerations and strict rules that must be adhered to regarding the use of animals in scientific procedures. The Animals (Scientific

Procedures) Act 1986 (ASPA) regulates the use of animals for scientific research in the UK through a set of laws pertaining to the licences required to undertake procedures with animals (348). The Three Rs are principles promoting more ethical use of animals in research and describe replacement (using methods other than animals), reduction (use of fewer animals whilst still obtaining significant levels of information), and refinement (refining procedures with animals to cause as little suffering as possible) (349).

PCTS generated from whole tumour tissue allows individual patient responses to multiple therapies to be investigated. They permit *ex vivo* examination of *in vivo* tumours, with retention of complex tumour biology and TME components (350). HCC PCTS have been employed to study the effects on proliferation and apoptosis of antineoplastic agents, as well as in the screening of immunotherapeutic agents (351, 352). In relation to the 3Rs and the ethical use of animals in research, generating PCTS from murine orthotopic tumours would enable multiple treatment strategies to be employed using the tissue from one mouse, therefore reducing the number of animals used.

Here I describe the characterisation of an *in vivo* mouse model of HCC, which has previously provided a tool for enhancing immunotherapy responses (269, 271). In addition, I describe the characterisation of PCTS generated from these murine tumours and illustrate their utility in the assessment of anticancer therapies.

7.2 Results

7.2.1 Hep-53.4 cells establish orthotopic tumours in 100% of C57BL/6 mice

A rapid orthotopic mouse model of HCC was developed to provide both an *in vivo* HCC model and a large supply of fresh tumour tissue suitable for generating PCTS for *ex vivo* culture. All *in vivo* animal work was performed by Dr Jack Leslie and Rainie Cameron from the Newcastle Fibrosis Research Group. Three commercially available murine cell lines of hepatocellular origin were selected to assess their utility in generating *in vivo* tumours: H22 hepatoma line, Hepa1-6 hepatoma line and Hep-53.4 HCC line. The cell lines were luciferase-tagged and implanted into C57BL/6 mice via intrahepatic injection of $1x10^6$ cells to the left lateral lobe following a laparotomy under surgical anaesthesia. Bioluminescence IVIS imaging was performed at day 1, day 7, day 14 and day 21 to assess tumour engraftment and growth (Figure 7A). The mice were humanely killed and the livers were harvested after 21 days for histological and biochemical analysis. Intrahepatic injection of H22 cells did not result in tumour growth in any of the mice injected, whilst Hepa1-6 and Hep-53.4 cells yielded macroscopic tumours in 20% and 100% of the mice injected respectively (Figure 7B).

Measurement of the tumour burden at day 21 determined that tumours generated with Hep-53.4 cells were significantly larger than those generated with Hepa1-6 cells (Figure 7C). Weekly IVIS imaging to monitor tumour growth demonstrated that although Hepa1-6 tumour growth was initially observed in 60% of the mice injected, a decrease in bioluminescence was observed in all mice after day 7 or day 14 (Figure 7D), indicating that the tumours decreased in size after an initial period of growth leaving 20% of the mice with a macroscopic tumour at day 21. Conversely, IVIS imaging determined that there was an exponential increase in bioluminescence between day 1 and day 21 in 100% of mice orthotopically injected with Hep-53.4 cells (Figure 7E), indicating that the Hep-53.4 cell line can be employed to establish reproducible orthotopic tumours in C57BL/6 mice with a 100% success rate.

Following intrahepatic transplant of $1x10^6$ Hep-53.4 cells, large macroscopic tumours were established primarily in one half of the left lateral lobe, without spread to the other lobes of the liver (Figure 7F).

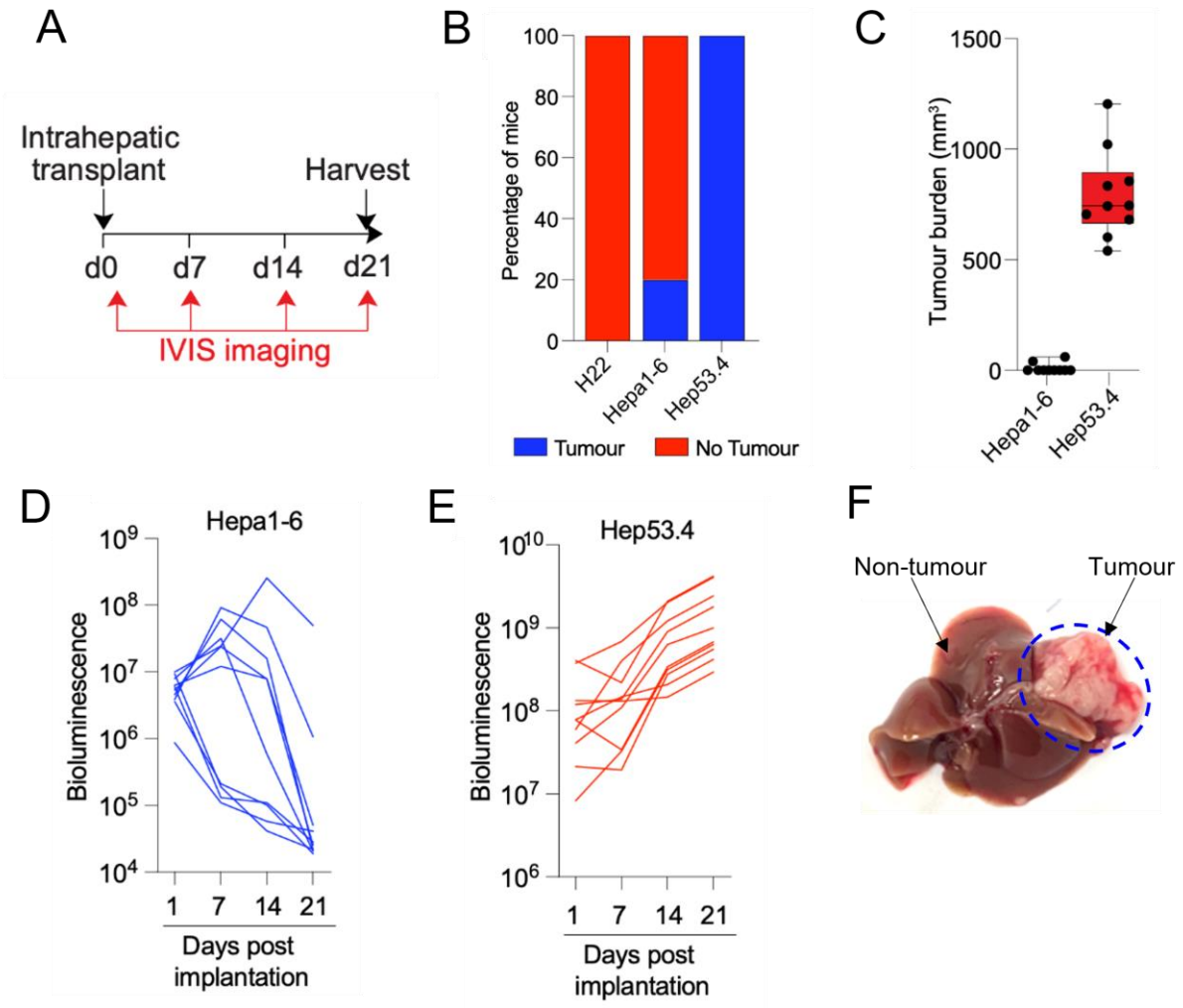

Figure 7. Establishment of the orthotopic tumour model. (A) Schematic detailing the timeline of intrahepatic transplant of Hep-53.4, Hepa1-6 or H22 cells in WT C57BL/6 mice to generate murine orthotopic tumours, and subsequent IVIS imaging at day 1, 7, 14 and 21 to assess HCC engraftment and growth. (B) Stacked bar chart displays the percentage of mice that developed tumours 21 days after intrahepatic injection with Hep-53.4, Hepa1-6 or H22 cells. N = 10 mice. (C) Graph showing tumour burden and representative images of *ex vivo* livers with Hepa1-6 or Hep-53.4 orthotopic tumours. Data are mean ± SEM for N = 10 mice per cell line. (D-E) Graph showing bioluminescence levels from IVIS imaging of mice at 1, 7, 14 and 21 days following intrahepatic injection of (D) Hepa1-6 or (E) Hep-53.4 cells. (F) Image displaying a mouse liver harvested 21 days after intrahepatic transplant of $1x10^6$ Hep-53.4 cells with a large macroscopic tumour in the left lateral lobe. All work presented in this figure was performed by Dr Jack Leslie.

7.2.2 Characterisation of Hep-53.4 orthotopic tumours

Following the establishment of reproducible orthotopic tumours with Hep-53.4 cells, characterisation of the tumours was performed to ascertain the features of the *in vivo* tumours. Under surgical anaesthesia, C57BL/6 mice underwent an intrahepatic transplant of $1x10^6$ Hep-53.4 cells and were subsequently harvested at day 14, day 21 and day 28 (Figure 8A). Small macroscopic tumours were visible at day 14, while tumour burden increased in tumours harvested at day 28. There was an exponential increase in tumour growth between day 21 and day 28 (Figure 8B), at which point the humane endpoint was identified and the mice were culled due to tumour burden.

Assessing the expression of multiple genes relating to inflammation determined that there was an upregulation of 9 proinflammatory genes (*Cxcl1, Cxcl2, Cxcl5, Cxcl9, Cxcl10, Ccl2, Ccl3, Ccl4* and *Ccl5*) in tumour tissue harvested at day 14 compared to normal non-tumour liver tissue. Furthermore, there was a further upregulation of these proinflammatory genes in tumour tissue harvested 28 days after intrahepatic injection of Hep-53.4 cells, compared to in tumour tissue at day 14 (Figure 8C). The increased expression of these genes suggested that Hep-53.4 orthotopic tumours are likely to be immunogenic.

To ascertain whether the immune infiltrate in the Hep-53.4 orthotopic tumours reflected the upregulated inflammatory genetic landscape, histological and immunohistochemical analysis was performed to further characterise the model. H&E staining determined that the tumours have a dense stroma compared to non-tumour tissue (Figure 8D), and immunohistochemical staining for cytokeratin 18 and cytokeratin 19 demonstrated that Hep-53.4 tumours are not positive for the biliary marker cytokeratin 19, and are indeed of hepatocellular origin (Figure 8E). Further immunohistochemical analysis revealed that compared to non-tumour liver tissue, Hep-53.4 tumours has significantly higher numbers of PCNA+ proliferative cells ($p<0.0001$) (Figure 8F), fibrotic alpha-smooth muscle actin (αSMA+) cells ($p=0.011$) (Figure 8G), CD3+ T cells ($p=0.0002$) (Figure 8H), F4/80+ macrophages ($p=0.0365$) (Figure 8I) and Ly6G+ neutrophils ($p=0.0026$) (Figure 8J) This analysis confirmed that Hep-53.4 tumours have a rich immune infiltrate which would potentially be responsive to immunotherapy.

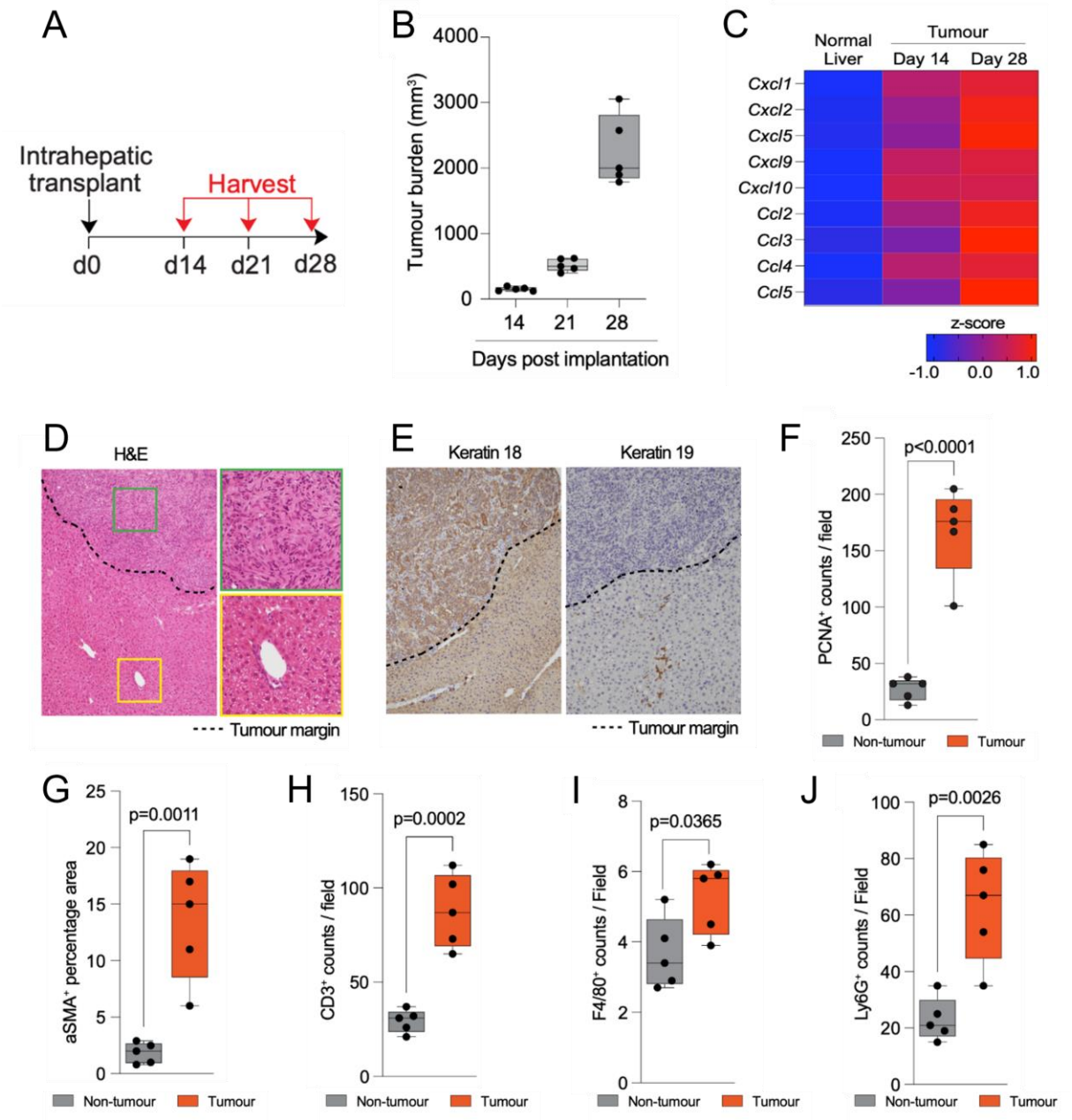

Figure 8. Characterisation of Hep-53.4 orthotopic tumours. (A) Schematic detailing the timeline of intrahepatic transplant of Hep-53.4 cells to generate orthotopic tumours, and subsequent harvest at 14, 21, and 28 days post injection. (B) Graph showing tumour burden of Hep-53.4 tumours at 14, 21 and 28 days post intrahepatic injection. Data are mean ± SEM for n = 5 mice per timepoint. (C) Heatmap showing expression of Cxcl1, Cxcl2, Cxcl5, Cxcl9, Cxcl10, Ccl2, Ccl3, Ccl4 and Ccl5 in normal liver tissue and Hep-53.4 tumour tissue 14 and 28 days post intrahepatic injection. (D-E) Representative image of (D) H&E-stained and (E) keratin-18- and keratin-19-stained tumour and non-tumour tissue. Black dotted line denotes tumour margin. (F-J) Histological quantification of (F) PCNA-stained, (G) αSMA-stained, (H) CD3-stained, (I) F4/80-stained and (J) Ly6G-stained tumour and non-tumour tissue harvested 28 days post intrahepatic injection. Data are mean ± SEM for N = 5 mice. Sections A-C of this figure were performed by Dr Jack Leslie.

7.2.3 Hep-53.4 orthotopic tumours respond to first-line TKIs

After the establishment and characterisation of syngeneic orthotopic tumours, the mice underwent therapeutic intervention with first-line therapies for the treatment of advanced HCC, to determine whether the orthotopic mouse model was responsive to currently employed, approved therapies. Following the intrahepatic transplant of $1x10^6$ Hep-53.4 cells in C57BL/6 mice, orthotopic tumours were allowed to develop for 14 days before therapeutic intervention via daily oral gavage with either a vehicle treatment or the first-line TKIs sorafenib (45 mg/kg) or lenvatinib (10 mg/kg) for a further 14 days until the mice were culled and livers were harvested at day 28 (Figure 9A).

Compared to the vehicle treatment group, tumour burden was significantly lower in mice treated for 14 days with both sorafenib ($p=0.0017$) and lenvatinib ($p=0.0014$) (Figure 9B). Moreover, there was a significant reduction in the liver to body weight ratio of mice in the sorafenib ($p=0.0295$) and lenvatinib ($p=0.025$) treatment arms when compared to the vehicle control group (Figure 9C).

Following a reduction in size of the macroscopic tumours, immunohistochemical staining was performed to investigate the impact of sorafenib and lenvatinib on Hep-53.4 tumours at the cellular level. There was a trend towards higher numbers of apoptotic active-caspase 3+ cells with both TKIs (Figure 9D), whilst there were significantly lower numbers of proliferative Ki-67+ cells following treatment with lenvatinib ($p=0.0039$) and a trend towards fewer Ki-67+ cells following treatment with sorafenib (Figure 9E).

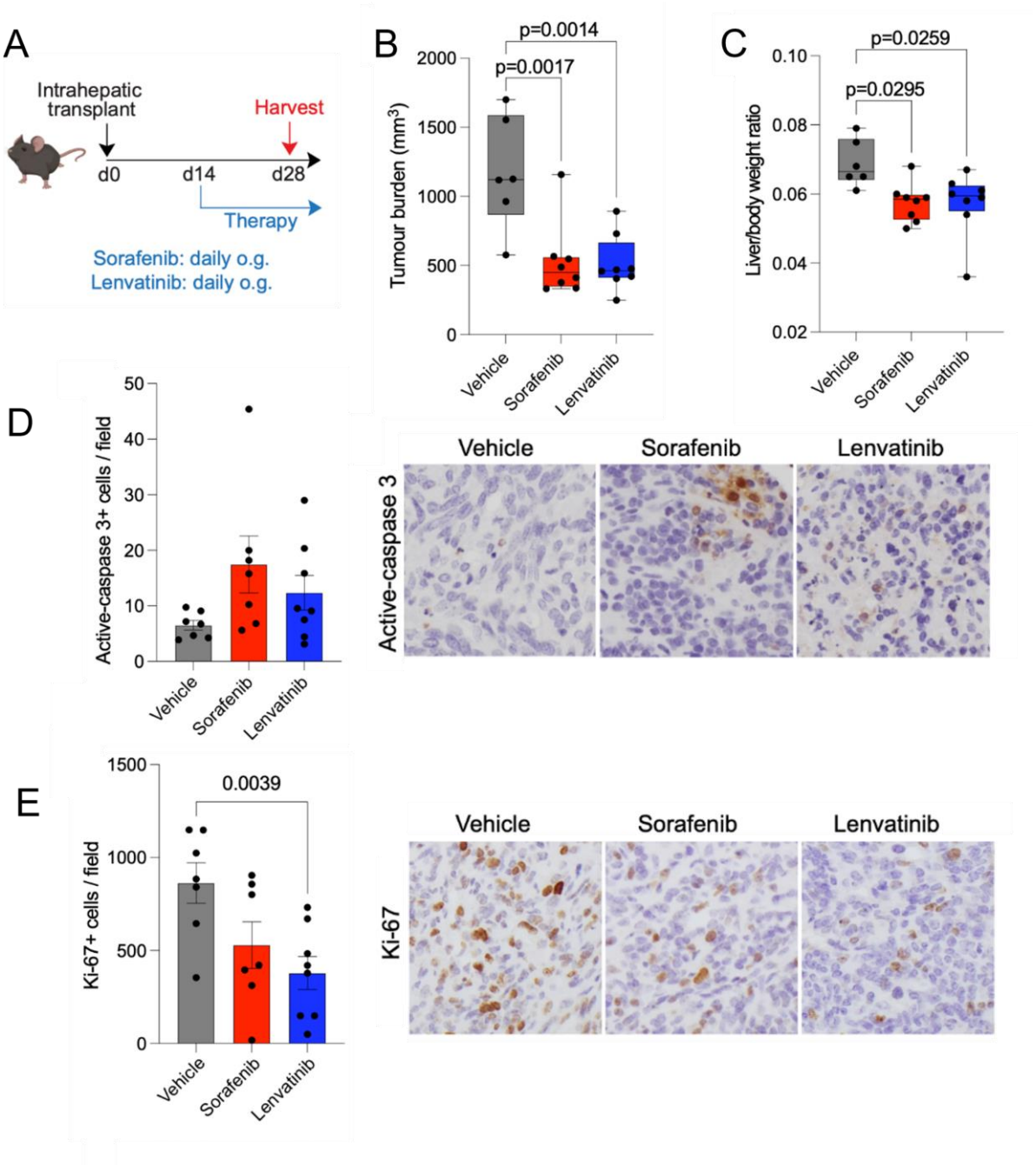

Figure 9. Hep-53.4 orthotopic tumours respond to first-line TKIs. (A) Schematic detailing the timeline of intrahepatic injection of Hep-53.4 cells at day 0 to generate orthotopic tumours, followed by therapeutic intervention at day 14 with sorafenib (45 mg/kg) or lenvatinib (10 mg/kg) via daily oral gavage. Tumours were harvested at day 28. (B) Graph showing tumour burden at day 28 of orthotopic tumours in the vehicle, sorafenib (p=0.0017) and lenvatinib (p=0.0014) treatment arms. (C) Graph showing liver to body weight ratio at day 28 of orthotopic tumours in the vehicle, sorafenib (p=0.0295) and lenvatinib (p=0.0259) treatment arms. (D-E) Histological quantification of (D) active-caspase 3-stained and (E) Ki-67-stained orthotopic tumour tissue following treatment for 14 days with either a vehicle control, sorafenib or lenvatinib. Data are mean ± SEM for up to N = 8 mice per treatment group. Images were taken at 20x magnification. Sections A-C of this figure were performed by Dr Jack Leslie.

7.2.4 Rocked bioreactor platform improves the metabolic function of PCTS

PCTS provide an effective method of modelling HCC *ex vivo*, where therapeutic responses can be studied in the context of the tumour immune microenvironment. Acquiring large samples of fresh HCC tumour tissue for the generation of PCTS presents a challenge, so the Hep-53.4 orthotopic tumours characterised previously were utilised to generate murine PCTS for *ex vivo* manipulation and drug screening. It has previously been demonstrated that the in-house bioreactor system developed by the Newcastle Fibrosis Research Group successfully extends the functional lifespan of PCLS generated from human and rat tissue. To assess whether this "rocked" bioreactor system is required for culturing PCLS and PCTS generated from murine tissue, livers were harvested 28 days after intrahepatic transplant of $1x10^6$ Hep-53.4 cells and PCTS and PCLS were generated from the tumour and non-tumour regions of tissue respectively (Figure 10A).

H&E staining was employed to provide a visual representation of the PCLS and PCTS after 4 days in either typical static culture or the in-house rocked bioreactor system. This revealed that in both the rocked and static culture, PCTS cultured for 4 days maintained a dense stroma with live nuclei. PCLS generated from non-tumour tissue displayed a distinct lack of live nuclei and appeared nonviable in static culture, whilst a higher number of viable nuclei were observed in PCLS following 4 days in rocked culture (Figure 10B). Daily resazurin assays were performed on PCLS and PCTS during the 4-day culture period to assess their metabolic function. This revealed that the rocked bioreactor system significantly improved the metabolic activity of PCLS compared to static culture ($p=0.007$ at day 4), and also resulted in a trend towards higher metabolic activity in PCTS ($p=0.0629$ at day 4) (Figure 10C). The process of generating PCLS typically results in the release of high levels of LDH from the tissue, particularly within the first 24 hours. PCTS in rocked culture released significantly lower levels of LDH within the first 24 hours compared to static PCTS ($p<0.0001$), rocked PCLS ($p=0.0044$) and static PCLS ($p=0.0005$) (Figure 10D). Whilst PCTS are certainly viable in typical static culture, this data suggests that rocked culture results in lower levels of cytotoxicity, whilst rocked culture is indeed a requirement for non-tumour PCLS.

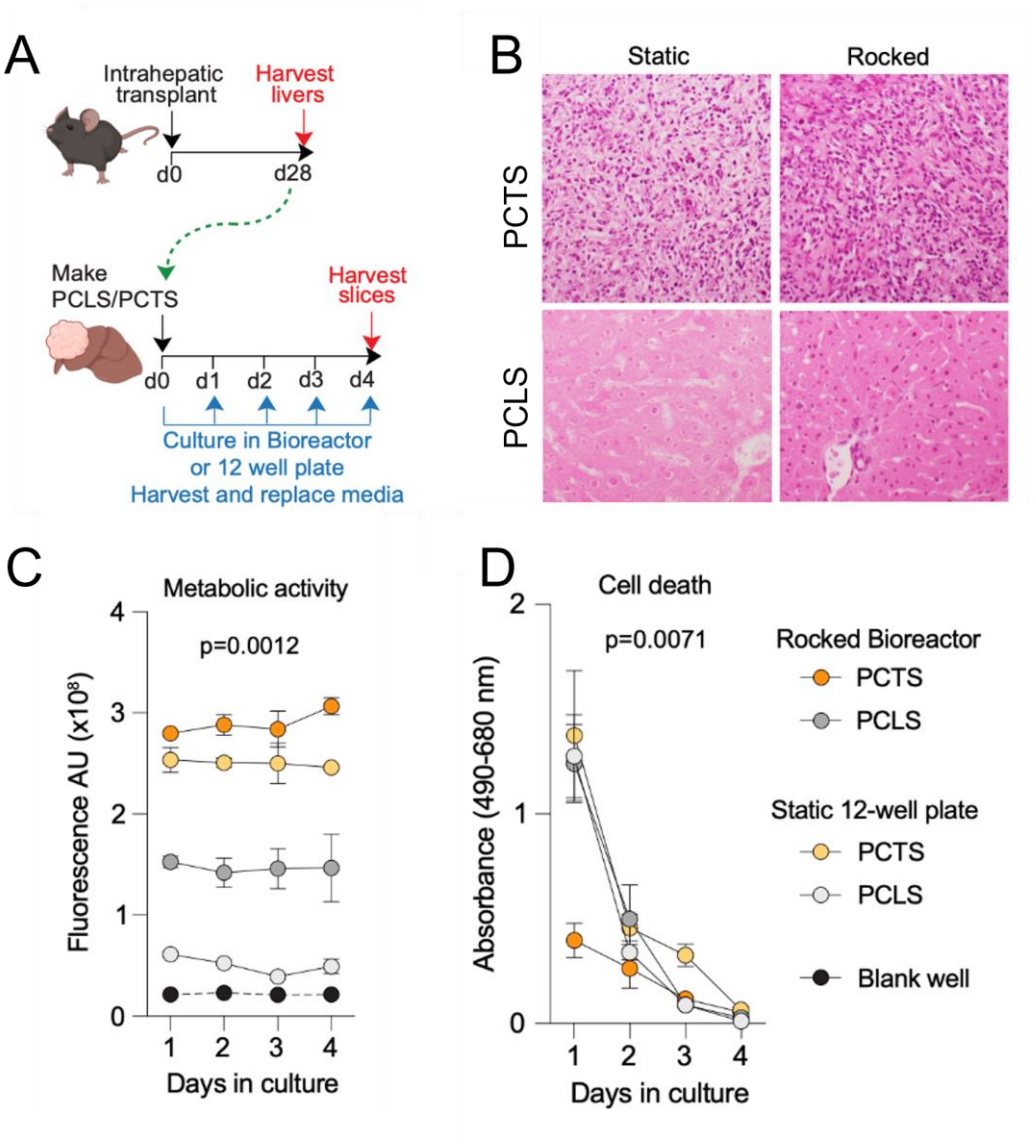

Figure 10. Rocked bioreactor platform is superior for culturing murine PCLS and PCTS. (A) Schematic detailing the timeline of intrahepatic transplant of Hep-53.4 cells to generate orthotopic tumours before generation of PCTS or PCLS and subsequent culture period in static or rocked culture. (B) Representative images of H&E-stained PCTS and PCLS after 4 days in either static or rocked culture. (C) Graph showing fluorescence quantification from a resazurin assay performed on PCTS and PCLS across 4 days in either static or rocked culture. Data are mean ± SEM for n = 3 PCLS/PCTS per timepoint and treatment group. (D) Soluble LDH quantification for PCTS and PCLS across 4 days in either static or rocked culture. Data are mean ± SEM for n = 3 PCLS/PCTS paired wells per timepoint and treatment group. Images were taken at 20x magnification.

7.2.5 PCTS retain the histological characteristics of *in vivo* tumours

After determining that the rocked culture system would be beneficial for culturing PCTS generated from Hep-53.4, histological characterisation of the PCTS and non-tumour PCLS was performed. Tumour-bearing livers were harvested from C57BL/6 mice 28 days after intrahepatic transplant of $1x10^6$ Hep-53.4 cells and PCTS and PCLS were subsequently generated from the tumour and non-tumour regions respectively. The PCTS and PCLS were cultured in the rocked bioreactor platform for 4 days, with tissue harvested daily for histological characterisation (Figure 11A). H&E staining confirmed that PCTS maintain densely packed tissue architecture between day 0 (PCTS generation) and day 4, while PCLS also retain their day 0 tissue structure at day 4 (Figure 11B).

Immunohistochemical staining was performed to ascertain whether specific markers and cell types remained present in the tissue during *ex vivo* culture. Pertaining to immune components present in the tissue, there were significantly higher numbers of F4/80+ macrophages in the PCTS than in PCLS, and although the number of F4/80+ cells decreased in the tissue from day 0 to day 4, there were still viable macrophages present in the tissue at the final time point (Figure 11C). Similarly, there were significantly greater numbers of CD3+ T cells present in PCTS than in PCLS; there were fewer CD3+ cells present in tissue harvested at day 3 and day 4 than in the initial three days of *ex vivo* culture, but viable CD3+ T cells were still abundant in tissue harvested at the latest time point (Figure 11D). In contrast, despite the presence of Ly6G+ neutrophils in PCTS at day 0, with very few of the cell type present in PCLS, the abundance of Ly6G+ cells drastically decreased in PCTS harvested at day 1, and there were no Ly6G+ cells present in tissue harvested from day 2 onwards (Figure 11E). This was not unsurprising due to the short lifespan of neutrophils which have entered the circulation and tissues. Quantification of proliferating PCNA+ cells determined that PCTS have significantly higher numbers of proliferating cells than non-tumour PCLS, and whilst there is a reduction in PCNA+ cells from day 0 to day 1, the number of proliferating cells in the tumour tissue is consistent between day 1 and day 4 of the *ex vivo* culture period (Figure 11F). The level of αSMA+ staining was also significantly higher in PCTS than in PCLS, and the fibrotic tumour stroma was maintained throughout the 4-day culture period (Figure 11G).

These findings demonstrate that PCTS cultured *ex vivo* reflect the *in vivo* Hep-53.4 tumours and retain many histological features displayed in the whole physiological system. In scenarios

where certain cell types are not retained or maintained in PCTS, there is the potential to supplement these components into the culture system if the activity of the cell type is integral to the study.

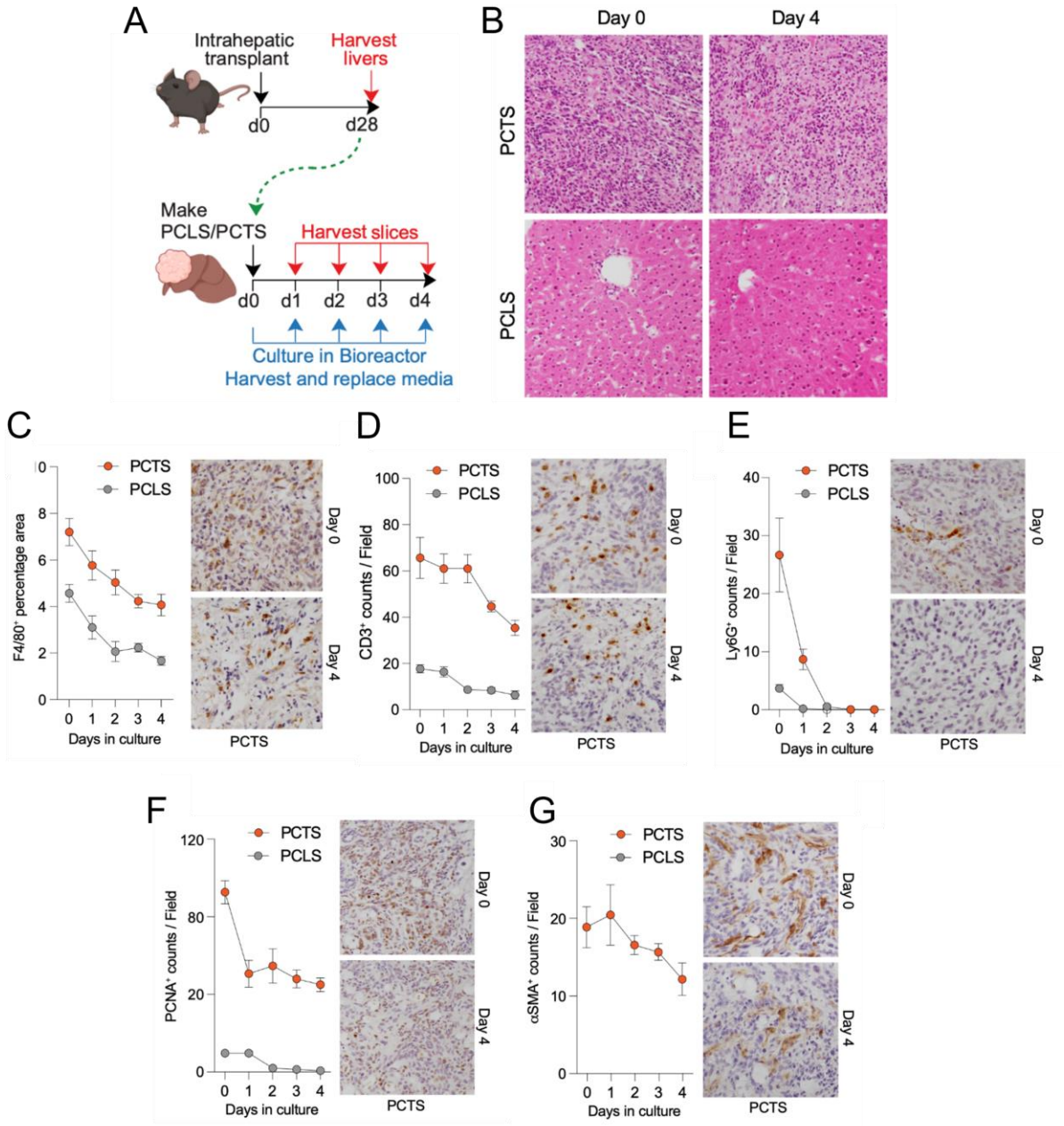

Figure 11. PCTS retain the characteristics of original Hep-53.4 tumours. (A) Schematic detailing the timeline of intrahepatic transplant of Hep-53.4 cells to generate orthotopic tumours before generation of PCTS or PCLS and subsequent 4-day culture period in rocked bioreactor system. (B) Representative images of H&E-stained PCTS and PCLS across 4 days of culture in a rocked bioreactor system. (C-G) Histological quantification of (C) F4/80-stained, (D) CD3-stained, (E) Ly6G-stained, (F) PCNA-stained and (G) αSMA-stained PCTS and PCLS across 4 days in rocked culture. Representative images of PCTS at day 0 and day 4 of culture period. Data are mean ± SEM for N = 6 PCTS/PCLS. Images were taken at 20x magnification.

7.2.6 PCTS recapitulate *in vivo* responses to first-line therapies

The aim was to utilise PCTS generated from Hep-53.4 tumours in the *ex vivo* assessment of potential novel anticancer therapies, providing a platform whereby different therapeutic strategies can be tested on tissue from the same tumour and individual, also reducing the number of animals used in drug screening studies. Therefore, PCTS were cultured with various anticancer drugs to demonstrate that they respond to therapies currently employed to treat advanced HCC in the same manner as *in vivo* tumours.

To assess whether PCTS respond to first-line multi-target TKIs, they were cultured with sorafenib (20 µM), lenvatinib (0.5 µM) or a vehicle control from day 1 to day 4 prior to being harvested for histological analysis (Figure 12A). Quantification of active-caspase 3 revealed that there was a significant increase in apoptotic cells following therapeutic intervention with sorafenib compared to the vehicle control ($p=0.0122$) (Figure 12B), reflecting the trend observed following the treatment of tumour-bearing mice with sorafenib. Likewise, there were significantly fewer proliferative Ki-67+ cells following treatment with lenvatinib ($p=0.0387$) (Figure 12C), mimicking the in vivo response to lenvatinib.

It has been demonstrated previously that anti-PD1 immunotherapy is efficacious in the orthotopic mouse model characterised here. Since ICIs are increasingly employed to treat advanced HCC, PCTS generated from Hep-53.4 orthotopic tumours were cultured with anti-PD1 to determine their utility in the screening of immunotherapies. PCTS and PCLS were generated from livers bearing Hep-53.4 orthotopic tumours and cultured in the rocked bioreactor system for 4 days, with therapeutic intervention with IgG control or anti-PD1 (20 µg/ml) from day 2 to day 4, at which point the PCTS were harvested for histological analysis (Figure 12E). Quantification of TUNEL determined that while anti-PD1 did not induce apoptosis in PCLS, it resulted in significantly more apoptotic TUNEL+ staining in PCTS ($p<0.0001$) (Figure 12F). Similarly, there was no difference in CD3+ positive cells in PCLS cultured with either an IgG control or anti-PD1, whilst anti-PD1 immunotherapy resulted in significantly higher numbers of CD3+ T cells in PCTS ($p=0.0008$) (Figure 12G). The correlation between the increased CD3+ cells and TUNEL staining suggests that anti-PD1 stimulates an expansion of T cells which induce apoptosis in the tumour tissue.

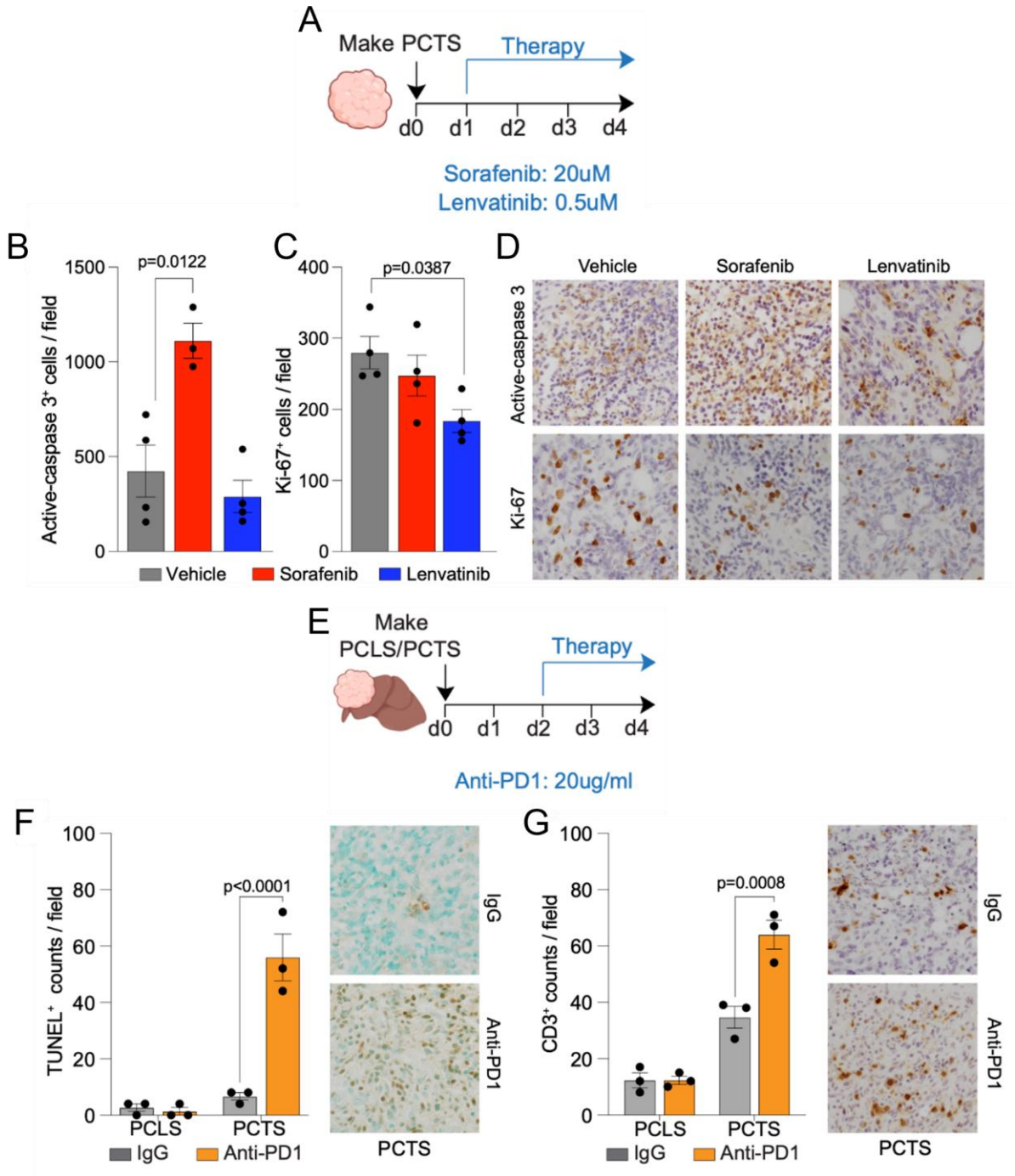

Figure 12. PCTS recapitulate *in vivo* responses to therapy. (A) Schematic detailing the timeline of PCTS generation from *in vivo* tumours and subsequent treatment with or without 20 µM sorafenib or 0.5 µM lenvatinib across a 4-day culture period. (B-C) Histological quantification of (B) active-caspase 3-stained and (C) Ki-67-stained PCTS following 3 days of treatment with or without sorafenib or lenvatinib. Data are mean ± SEM for up to N = 4 paired PCTS per treatment group. (D) Representative images of active-caspase 3- and Ki-67-stained PCTS following 3 days of treatment with or without sorafenib or lenvatinib. (E) Schematic detailing the timeline of PCTS and PCLS generation and subsequent treatment with IgG isotype control or 20 µg/ml anti-PD1 immunotherapy across a 4-day culture period. (F-G) Histological quantification of (F) TUNEL-stained and (G) CD3-stained PCTS and PCLS following treatment with or without anti-PD1 immunotherapy. Representative images of isotype control and anti-PD1 treated PCTS after 4 days in culture. Data are mean ± SEM for N = 3 paired PCTS/PCLS.

7.2.7 Efficacy of immunotherapy is limited in lipid-loaded PCTS

The efficacy of anti-PD1 in Hep-53.4 PCTS suggests that there is the potential to exploit the *ex vivo* culture model to study responses to immunotherapy drugs. It is known that ICIs are not effective in all patients and are typically more effective in individuals with immune rich "hot" tumours with increased levels of immune checkpoint molecules. Furthermore, the response to immunotherapy is limited in patients with MASH-related HCC. To determine whether these findings could also be modelled in Hep-53.4 PCTS, the PCTS were first cultured with either a control mixture containing BSA or a 2mM lipid-loading cocktail comprised of oleic, linoleic and palmitic acid from day 1 to day 4 of the culture period, at which point the tissue was harvested (Figure 13A). Triglyceride levels in the PCLS and PCTS were quantified and Oil Red O staining was performed to determine whether the tissue was capable of metabolising lipids from the culture media. This determined that both PCTS and PCLS cultured in the presence of the lipid-loading mixture contained higher triglyceride levels than tissue cultured with the BSA control, with lipids also visible at higher quantities in lipid-cultured tissue from Oil Red O staining (Figure 13B). Quantification of PCNA+ cells via immunohistochemistry identified that the presence of lipids further exacerbates the proliferative capacity of Hep-53.4 PCTS, with higher numbers of PCNA+ cells present in lipid-loaded PCTS compared to the BSA control group (Figure 13C).

After ascertaining that PCTS were capable of metabolising lipids to become "fat-loaded", PCTS were again cultured in the presence of a 2mM lipid-loading cocktail from day 1 to day 4, with therapeutic intervention with an IgG isotype control or anti-PD1 (20 µg/ml) from day 2 to day 4, at which point the tissue was harvested for immunohistochemical analysis (Figure 13D). Quantification of TUNEL+ staining determined that anti-PD1 resulted in a significant increase in apoptotic cells compared to the isotype control in PCTS cultured in BSA control media ($p=0.08$) (Figure 13E). However, when PCTS were cultured the presence of lipids, therapeutic intervention with anti-PD1 caused no difference in TUNEL+ staining compared to the isotype control, though there were more TUNEL+ apoptotic cells in all lipid-loaded PCTS than in IgG/BSA control treated PCTS implying that lipid-loading contributes to apoptosis (Figure 13E). These findings are reflected in the CD3+ T cell numbers; anti-PD1 resulted in significantly higher CD3+ cell numbers compared to the isotype control in BSA control treated PCTS

(p=0.013), whilst there was no difference in CD3+ between anti-PD1 and isotype control treated PCTS cultured in the presence of lipids (p=0.95) (Figure 13F).

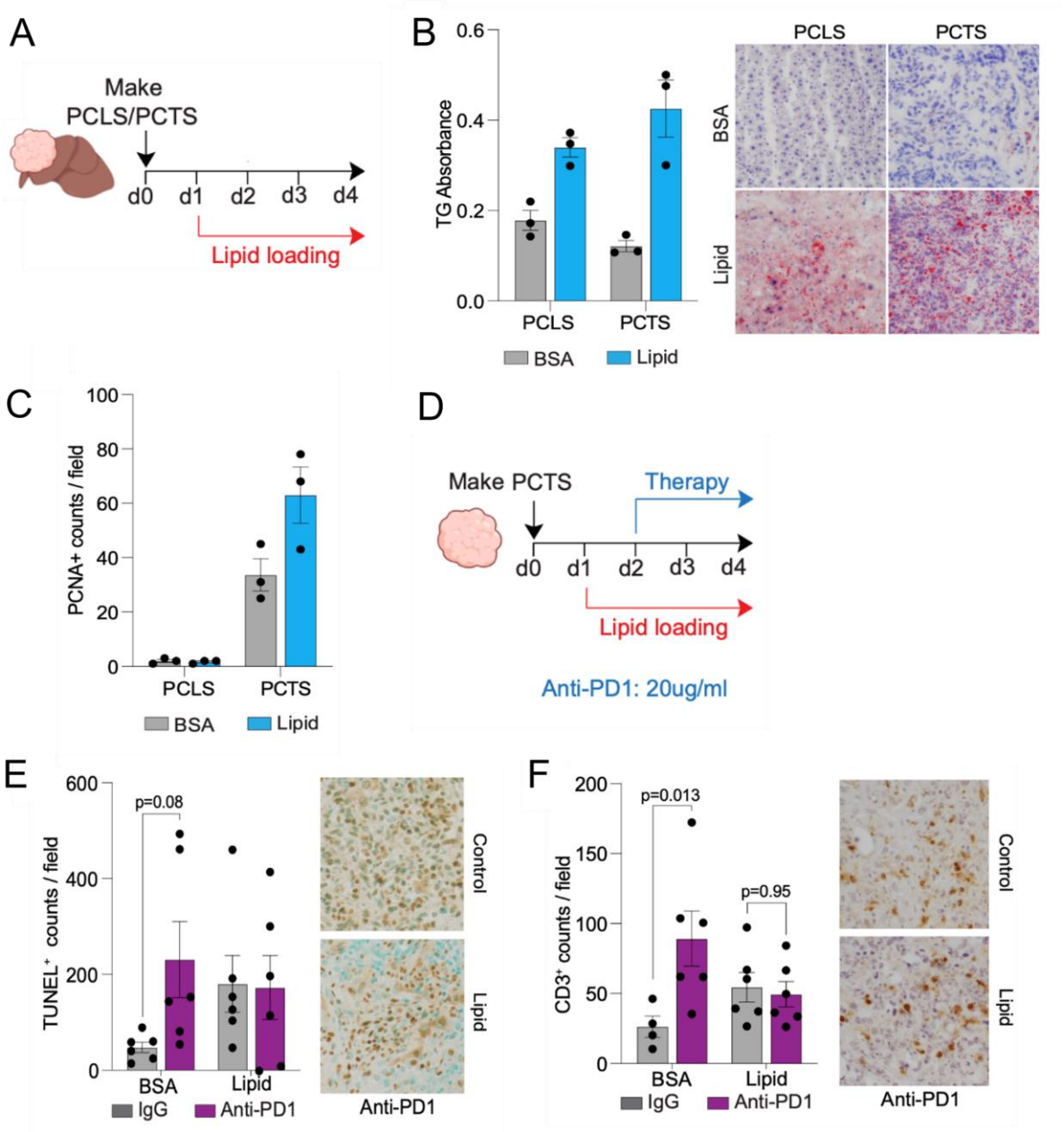

Figure 13. Lipids reduce the efficacy of anti-PD1 in Hep-53.4 PCTS. (A) Schematic detailing the timeline of PCLS/PCTS generation and subsequent culture period with a 2mM lipid-loading mixture. (B) Graph showing triglyceride assay absorbance values for PCLS and PCTS cultured for 3 days with or without a 2mM lipid loading mixture. Data are mean ± SEM for N = 3 PCLS/PCTS. Representative images of Oil Red O-stained PCLS and PCTS following 3 days of culture with or without a 2mM lipid loading mixture. (C) Histological quantification of PCNA-stained PCLS and PCTS following 3 days of culture with or without a 2mM lipid loading mixture. Data are mean ± SEM for N = 3 PCTS/PCLS. (D) Schematic detailing the timeline of PCTS generation and subsequent culture period with or without lipid-loading and 20 µg/ml anti-PD1. (E-F) Histological quantification of (E) TUNEL-stained and (F) CD3-stained PCTS following treatment with or without lipid loading and anti-PD1. Date are mean ± SEM for N = 6 paired PCTS. Representative images of control and lipid loaded PCTS treated with anti-PD1.

7.3 Results summary

The murine HCC line Hep-53.4 was employed to generate an orthotopic mouse model of HCC via intrahepatic transplant of $1x10^6$ cells in C57BL/6 mice, and resulted in rapidly-growing, aggressive *in vivo* tumours. An exponential increase in tumour growth was observed between day 21 and day 28, indicating that this was the humane end-point at which the mice should be humanely killed and the livers should be harvested for analysis. Numerous proinflammatory genes were upregulated in Hep-53.4 tumours in comparison to non-tumour liver tissue, suggesting that the tumours were potentially immune rich. Furthermore, histological characterisation revealed that the dense tumours contained infiltrating CD3+ T cells, F4/80+ macrophages and Ly6G+ neutrophils.

Therapeutic intervention in tumour-bearing mice with the first-line TKIs sorafenib and lenvatinib indicated that there was a significant reduction in both tumour burden and liver to body weight ratio in response to both drugs. Immunohistochemical analysis to investigate the impact of the TKIs at a cellular level determined that lenvatinib significantly decreased the number of proliferative Ki-67+ cells and there was a trend towards increased apoptotic active-caspase 3+ cells in response to sorafenib.

PCTS were generated from the Hep-53.4 tumours for *ex vivo* culture whereby fewer animals could be utilised to investigate multiple treatment strategies. The in-house "rocked" bioreactor system was employed as it improved the metabolic function and viability of the PCTS. Histological characterisation determined that PCTS retained many features of the *in vivo* tumours, with tissue cultured for 4 days still displaying proliferative potential and the presence of viable T cells and macrophages. Neutrophils were not maintained in PCTS cultured for an excess of two days due to their lack of longevity. In addition, PCTS mimicked the *in vivo* response to first-line TKIs, with significantly increased active-caspase 3 staining in response to sorafenib and significantly less Ki-67 staining in response to lenvatinib. Immunotherapeutic approaches are increasingly used to target advanced HCC, specifically in individuals with immune rich tumours. PCTS treated with anti-PD1 immunotherapy displayed a significant increase in both CD3 T cell numbers and apoptotic cells; interestingly, this response was lost when PCTS were cultured in the presence of a lipid-loading cocktail, a finding which is line with previously published data concerning preclinical models of NASH-related HCC and a meta-analysis of 1,600 HCC patients.

7.4 Discussion

Precision cut slices generated from whole tumour tissue present a platform with utility for modelling HCC *ex vivo*, retaining many of the structural, functional and cellular properties of *in vivo* tissue (339, 353). The static culture of PCTS has previously been described as models of both human and murine HCC offering an insight into therapeutic efficacy (353, 354). The development of a Hep-53.4 orthotopic mouse model of HCC, followed by PCTS generation and subsequent tissue culture in an in-house rocked bioreactor system offers a method of modelling HCC and therapeutic responses *ex vivo.* The possibility to apply multiple treatment options to PCTS derived from the same tumour offers a higher throughput system compared to *in vivo* mouse models, therefore being more cost efficient and ethical in relation to the Three Rs of scientific research – specifically the reduction in the number of animals used in experiments.

Murine HCC and hepatoma cell lines previously used to generate orthotopic liver tumours include Hepa1-6 and HCa-1 (304, 305). Whilst the use of the aforementioned cell lines has culminated in successful tumour growth, a common limitation of these models is the variable engraftment and growth rate of the cells following intrahepatic transplant (355, 356). Cell lines that were readily available in the laboratory were employed when initially optimising the orthotopic HCC model: Hep-53.4, Hepa1-6 and H22. Prior to intrahepatic transplantation in mice, Hep-53.4 cells displayed a highly proliferative phenotype in 2D cell culture and a high expression of epithelial cell marker genes. Therefore, it was hypothesised that the use of Hep-53.4 cells would result in aggressive *in vivo* tumours before the revelation that use of the cell lines resulted in a 100% engraftment and growth rate in C57BL/6 mice. The future use of alternative cell lines to generate contrasting orthotopic models of HCC would provide a platform whereby potential novel anticancer therapies could be screened both *in vivo* and *ex vivo* in tumour tissue possessing varied characteristics and mutational signatures. The Hep-53.4 orthotopic model described here displayed a high immune infiltrate comprised of macrophages, T cells and neutrophils and may therefore contribute to the investigation of immunotherapeutic strategies. A theoretical orthotopic model displaying a lack of infiltrating immune cells may offer an alternative use to screen therapies specifically targeting immune "cold" tumours, whether that relates to improving immune cell infiltration or through the use of small molecule inhibitors that do not target immune components.

The PCTS generated from Hep-53.4 orthotopic tumours were determined to be highly metabolically active via daily resazurin assays performed on the tissue throughout the 4-day culture period. Additionally, in a separate experiment conducted by another member of the laboratory Hep-53.4 PCTS displayed consistently high levels of metabolic activity for a total of 10 days. William's E medium supplemented with 2% FBS, penicillin-streptomycin, L-glutamine, pyruvate, insulin transferrin-selenium and dexamethasone was identified as the essential culture medium for maintaining the viability of hepatocytes in PCLS when the technology was initially developed as a model of liver fibrosis (340). PCTS were also cultured in this medium to standardise the culture conditions when comparing PCTS to PCLS for histological analysis and viability assessments. It is important to consider that the PCTS are comprised predominantly of Hep-53.4 cells which are typically cultured in high glucose DMEM supplemented with 10% FBS. It may be the case that Hep-53.4 cells do not require highly specific culture medium, and the viability of the immune populations in the PCTS should be probed via flow cytometry in addition to the resazurin assay which primarily yields metabolic information on the Hep-53.4 cells due to their prominent presence in the PCTS. Both the HCC cells and various other components of the tumour immune microenvironment should be considered when selecting a tissue culture medium.

IHC analysis has been utilised to identify the presence of particular markers and immune populations in the tissue. This has revealed that PCTS cultured for 4 days retain a proliferative capacity, alongside macrophages and T cells that have infiltrated the tumour tissue. An alternative method of assessing the presence and viability of components in the tumour microenvironment would be via flow cytometry, which would not only give a more accurate depiction of the cell viability through live/dead staining but would provide a more reliable quantification of the cell types present throughout the whole 250 µm thick PCTS, in contrast to IHC which provides a window into 5 µm sections of tissue. The FFX Tissue Grinder (Fast Forward Discoveries) is an instrument available in the laboratory providing a method of enzyme-free tissue dissociation and has demonstrated the ability to digest PCTS and whole tumour tissue from Hep-53.4 orthotopic tumours in preparation for flow cytometry analysis. Another method of more robustly characterising Hep-53.4 PCTS would be by employing Hyperion IMC, which combines laser ablation with cytometry by time-of-flight (CyTOF) using

metal-conjugated antibodies to visualise over 40 markers in the same tissue section, providing insight into the spatial configuration of components within the tissue.

Comparing standard static tissue culture to the in-house bioreactor system in which the tissue slices are rocked yielded initial information about the viability of PCTS and PCLS. Whilst rocked tissue culture is vital for maintaining the viability of non-tumour PCLS (340), further investigation is required to determine whether it is essential for PCTS culture. Initial investigation revealed that in the first 24 hours after PCTS generation tissue cultured in the rocked bioreactor system released significantly lower levels of the cytotoxic marker LDH compared to PCTS in static culture. Despite the indication that rocked culture may reduce the initial levels of cell death, resazurin assays demonstrated that the PCTS remained metabolically active in static culture throughout the 4-day culture period, with no decrease in in the levels of the reduced by-product resorufin at the later timepoints. This metabolic activity is likely to be predominantly due to Hep-53.4 cells which are the most prevalent cells present in the PCTS. PCTS in static culture did display a slightly lower level of metabolic activity than those in rocked culture, however this different was negligible and unsignificant. The LDH assay data led to the initial statement that rocked PCTS culture is advantageous to static culture. However, the impact of static culture on the individual cellular components, such as important immune factors, had not be studied. The potential revelation that various components in the tumour microenvironment are not impeded by static tissue culture would allow Hep-53.4 PCTS to be cultured without the equipment required for the rocked system.

Therapeutic and immunotherapeutic drugs applied to Hep-53.4 PCTS revealed the potential utility of the model as an *ex vivo* therapeutic screening platform; changes to the number of proliferative and apoptotic cells were observed in response to lenvatinib and sorafenib respectively, and the response to anti-PD1 immunotherapy in the presence and absence of free fatty acids mimicked previously published findings from both mouse models and human data (268). CD3 T cells increase in BSA control treated PCTS in response to anti-PD1 immunotherapy; performing a dual stain for Ki67 and CD3 in these samples will provide evidence that immunotherapy is stimulating a clonal expansion of the T cells retained in the PCTS. Continued investigation into the loss of anti-PD1 efficacy in lipid-loaded PCTS may reveal the exhausted subset of $CD8^{+}PD1^{+}$ T cells that has been identified in MASH mice and human patients with MASLD or MASH. An interesting investigation would involve deciphering

whether rescuing the steatotic phenotype in the PCTS by intervening with drugs such as pioglitazone or metformin simultaneously rescues immunotherapeutic efficacy. Further work would involve assessing whether additional therapeutic strategies for the treatment of advanced HCC display an anticancer effect in the PCTS. For example, additional anticancer therapies such as the small molecule inhibitor cabozantinib and the monoclonal antibody ramucirumab, or the gold-standard combination of atezolizumab (anti-PDL1) and bevacizumab (anti-VEGFA). Despite PCTS being detached from the circulation and VEGFA commonly impacting the vasculature and stimulating angiogenesis, targeting VEGFA directly on renal cell carcinoma cells has previously been shown to increase apoptosis and limit cancer cell proliferation, migration and invasion (357, 358).

Exploiting the PCTS platform by modulating components of the tumour microenvironment *ex vivo* has the potential to provide a novel understanding of how the immune microenvironment exhibits pro-tumorigenic effects. Moreover, targeting various components present in the tumour has capacity to give rise to the generation of novel anticancer agents. It was recently discovered that targeting the recruitment of neutrophils in NASH-HCC with the chemokine receptor CXCR2 antagonist AZD5069 improves the efficacy of anti-PD1 immunotherapy by reprogramming neutrophils from a pro-tumour to an anti-cancer phenotype, while intratumoural $XCR1^+$ DCs became activated (269). Furthermore, AZD5069 has been shown to reverse resistance to androgen receptor signalling inhibition in a subset of castration-resistant prostate cancer patients (359). These examples of synergistic treatment combinations suggest that targeting the immune system in a cooperative manner, whether that is in combination with other immune modulators or small molecule inhibitors, may reveal novel treatment strategies, particular in the PCTS system where macrophages and T cells are retained and neutrophils can be supplemented into the culture system. ER-Hoxb8 cells are immortalised estrogen-controlled neutrophil progenitors which possess the capacity to differentiate to an immature neutrophil phenotype, and may provide a method of investigating neutrophil interactions in PCTS (360, 361).

Generating PCTS from human HCC tumours would offer a more physiologically relevant model with a higher likelihood of novel findings translating to human disease. Moreover, patient-specific PCTS generation from human tumours would elevate the model to offer utility in precision medicine, and has been achieved by research groups with access to sufficient

tumour tissue (362). Given the restricted access to whole tumour tissue in the laboratory this approach was not possible. Alternatively, the development of orthotopic tumours in humanised mice with human HCC lines and subsequent PCTS generation would partially overcome this complication. This has previously been achieved in SCID mice which lack T and B cells, with the cell lines PLC/PRF/5, HuH7, SNU-475 and SNU-761 (306-308, 355). Moreover, xenograft models have been successfully developed using primary HCC cell lines offering the potential to generate patient-derived PCTS for precision medicine – a possibility given the access within the Newcastle Fibrosis Research Group to human HCC biopsies (355).

More recent PCTS development by other members of the laboratory include miniaturisation of the 12-well system by generating PCTS 3 mm in diameter which are subsequently cultured in 96-well plates. This improves the throughput of the platform by yielding higher numbers of PCTS per tumour, enabling the PCTS to be probed with a greater number of treatment combinations to provide an in-depth screening platform. A single Hep-53.4 tumour typically yields approximately 24 PCTS for use in the standard 12-well system. In comparison, it is possible to generate more than 96 slices for use in the 3 mm 96-well system thereby enabling a greater number of therapeutic approaches to be screened. Additionally, the use of an expression vector inducing the expression of a secreted NanoLuc luciferase by Hep-53.4 cells enabled the proliferation and viability of HCC cells in Hep-53.4 PCTS to be tracked longitudinally via luciferase levels detected in the culture medium. The measurement of the secreted luciferase offers an alternative technique to previously used and time-consuming IHC analysis to monitor therapeutic response in PCTS.

8 Bioengineering HCC tumour microenvironments with spheroids and precision-cut liver slices

8.1 Introduction

Knowledge of the TME in HCC is imperative to accurately stratify patients and apply the most suitable treatment strategy for the individual, in addition to improving the understanding of how complex interactions between cell types contributes to the pathogenesis of HCC. The TME is a complicated network of interacting factors and does not consider just the tumour cells alone. Indeed, communication between HCC cells and various immune cells, stromal cells, the ECM and other factors secreted by these cell types all contribute to HCC pathogenesis and the immunosuppressive niche in which HCC thrives (191). For example, despite the capacity of neutrophils to target pathogens they have been identified as key mediators of immunosuppression and tumour progression in HCC, leading to a number of clinical trials investigating the efficacy of neutrophil-directed therapies (165). Likewise, TAMs in the TME are associated with poor prognosis, angiogenesis and metastasis (363, 364). In relation to stromal components of the TME, tumour cells exploit ECM remodelling via ECM deposition, degradation, and force-mediated modification to promote tumorigenesis and metastasis (365). Considering these relationships enables novel therapeutic approaches to be researched, in addition to the assignment of suitable currently approved immunotherapies.

3D spheroids present the opportunity to culture HCC cells alongside other important components of the TME in a superior modality to typical 2D cell culture. The mechanical stress resultant of culturing cells on plastic is avoided, and a greater physiological relevance is provided as cell-cell and cell-matrix interactions are formed. In addition to mimicking the spatial conformation of an *in situ* tumour, spheroids also reflect the heterogeneous access to oxygen and nutrients that an *in vivo* tumour would receive (366, 367). HCC spheroids have demonstrated an increased resistance to apoptosis-inducing drugs compared to 2D cell cultures, reflective of the chemoresistance observed in solid tumours, and produce elevated cytokine factors linked to immune cell recruitment, ECM regulation and angiogenesis (320, 368). Pertaining to the chronic liver disease which frequently underpins HCC, murine liver-derived spheroids have been utilised to model fatty liver disease and assess the effectiveness of anti-MASLD drugs (369).

Whilst spheroids provide an improved system for modelling cell-cell interactions and are more physiologically accurate than 2D cell culture, the system does not offer a method of modelling HCC in the context of structurally intact liver tissue, in which resides various immune cells capable of responding to cancer cells to elicit pro-tumour or anti-tumour effects. Here I describe the development of a spheroid-engrafted PCLS model of HCC and the subsequent utility of the model for determining therapeutic efficacy. The system developed presents as a unique tool whereby HCC is modelled in 3D within PCLS that retain the structural architecture, function and cellular components of native liver tissue.

8.2 Results

8.2.1 Spheroid formation utilising the murine HCC cell line Hep-53.4

Prior to the combination of HCC spheroids with PCLS technology to create an *ex vivo* spheroid-PCLS model, it was necessary to identify suitable HCC cell lines capable of forming robust spheroids. Preliminary experiments were conducted with murine cells and tissue due to the limited supply of human liver tissue. The murine HCC line Hep-53.4, which was derived from a DEN-induced HCC, was previously shown to result in large, aggressive tumours in C57BL/6 mice in an orthotopic model of HCC. Resultant of this finding, and due to the cell line being readily available in the laboratory, the spheroid-forming capacity of Hep-53.4 cells was investigated. Round-bottom 96-well plates were coated with 1% low gelling temperature agarose, resulting in low adherence. Then, Hep-53.4 cells were seeded into each well at densities of 40,000, 20,000, 10,000, 5,000 and 2,500 cells per well. Following spheroid formation within the first 24 hours, the spheroids were imaged daily between day 1 and day 4 (Figure 14A). The diameter was measured using Zeiss Zen Blue software and spheroid volumes were calculated (Figure 14B).

Across the 4-day culture period, spheroids generated from 40,000, 20,000, 10,000 and 5,000 cells decreased in volume by 55.7%, 41.1%, 42.8% and 22.9% respectively (Figure 14C). The only condition by which spheroid volume increased between day 1 and day 4 was when 2,500 cells were used at day 0 and spheroid volume increased by 90.36%, suggesting that spheroids generated from 2,500 cells or less are required if cell growth is to be measured by volume from day 1 (Figure 14C). Brightfield imaging showed that the surface of the spheroid appeared irregular at day 1 and more uniform at day 4, whilst the spheroid density seemed to be higher at day 4 (Figure 14A). These findings suggest that the decrease in spheroid volume observed in many cases was potentially due to spheroids becoming more compact, rather than due to the cells dying. Of note, spheroids of all size display a small increase in size between day 3 and day 4, indicating that volume measurements can be utilised as a measure of growth after 3 days of spheroid formation (Figure 14B-C). To investigate the integrity and rate of formation of Hep-53.4 spheroids, spheroids were generated from 20,000 cells each and transferred from the original well via pipette to a new well in the 96-well plate at day 1, day 2 and day 3 following spheroid generation (Figure 14D). There was a significant decrease in the volume of spheroids transferred to a new well at day 1 ($P=0.0010$), indicating that Hep-53.4 spheroids

have not completely formed cell-cell interactions and become damaged upon transfer at this early timepoint. Consistent with previous data, the volume of Hep-53.4 spheroids is smaller at day 2 and 3 compared to day 1, although spheroids transferred to new wells at this timepoint retained their “before transfer” volume, suggesting that Hep-53.4 spheroids had become more compact and possessed the necessary cell-cell interactions to be transferred from day 2 onwards (Figure 14E).

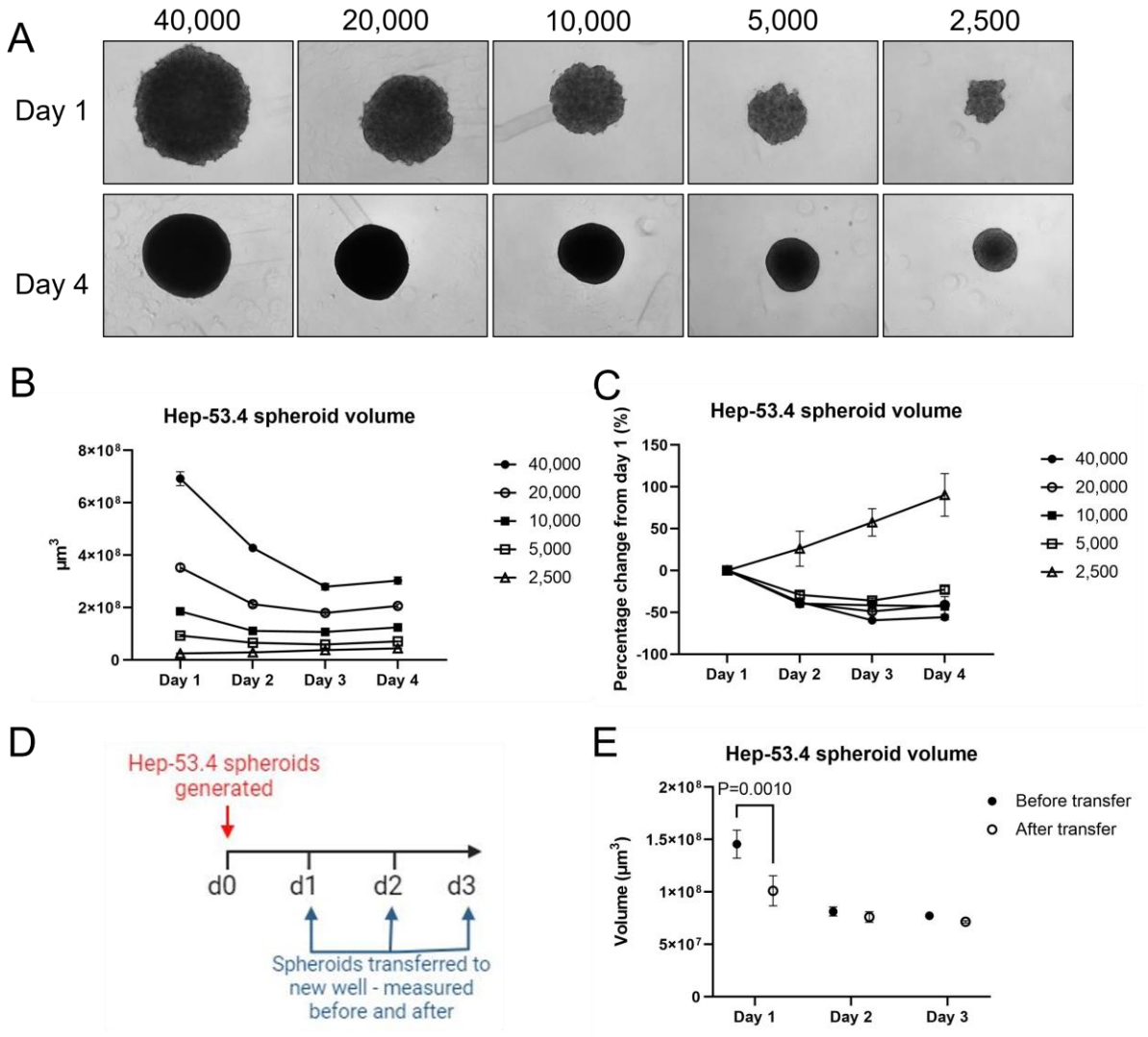

Figure 14. Spheroid formation utilising Hep-53.4 cell line. (A) Representative brightfield images of spheroids generated from 40,000 – 2,500 Hep-53.4 cells at day 1 and day 4, at 4X magnification. (B) Graph showing the volume of spheroids generated from 40,000 – 2,500 Hep-53.4 cells between day 1 and day 4, using calculations from diameter measurements recorded on Zeiss Zen Blue software. (C) Graph showing changes in spheroid volume between day 1 and day 4 presented as percentage change from day 1 volume measurement. Data are mean ± SEM for N = 6 spheroids. (D) Schematic detailing the timeline of Hep-53.4 spheroid generation and subsequent transfer to new well at day 1, day 2 and day 3 to assess spheroid integrity. (E) Graph showing Hep-53.4 spheroid volume before and after transfer to a new well at day 1, day 2 and day 3. Data are mean ± SEM for N = 16 spheroids.

8.2.2 Hep-53.4 spheroids engraft on, invade and proliferate in murine PCLS

After ascertaining that robust, compact spheroids could be formed from Hep-53.4 cells, they were cultured in combination with murine PCLS to generate a spheroid-engrafted PCLS model. In order to induce tdTomato red fluorescence for visualisation of the cells once implanted on PCLS, Hep-53.4 cells were stably transfected with the vector tdTomato-N1. Hep-53.4 spheroids were generated from 20,000 cells, which was the lowest number of cells whereby the resulting spheroids could be confidently visualised by eye for transfer onto PCLS. The spheroids were allowed to form for 3 days, at which point murine PCLS were generated followed by implantation of the spheroids onto the tissue, before being cultured in the rocked bioreactor system for 4 days (Figure 15A).

Fluorescent imaging of PCLS with implanted Hep-53.4 spheroids between day 1 and day 4 revealed that the spheroids had engrafted to the tissue and remained adhered to the same region of tissue throughout the culture period (Figure 15B). Furthermore, z-stack images generated via multiphoton imaging with assistance from Dr Glyn Nelson in the Newcastle University Bioimaging Unit confirmed that in addition to engrafting to the tissue, Hep-53.4 spheroids (red, tdTomato) migrated through the PCLS (blue, Hoechst), invading the whole 250 µm thick PCLS (Figure 15C). ELISA quantification of the red fluorescent protein (RFP) expressed by Hep-53.4 cells determined that there were significantly higher RFP levels in the PCLS at day 4 compared to day 1 ($P=0.0055$), indicating that Hep-53.4 cells proliferate in the PCLS (Figure 15D). Following therapeutic intervention with sorafenib (5 µM - 20 µM) between day 1 and day 4, there were significantly lower RFP levels in PCLS treated with 20 µM sorafenib compared to the vehicle control at day 4 ($P=0.0009$) demonstrating that specific drug doses elicit an anticancer response in the HCC-mPCLS model generated (Figure 15E).

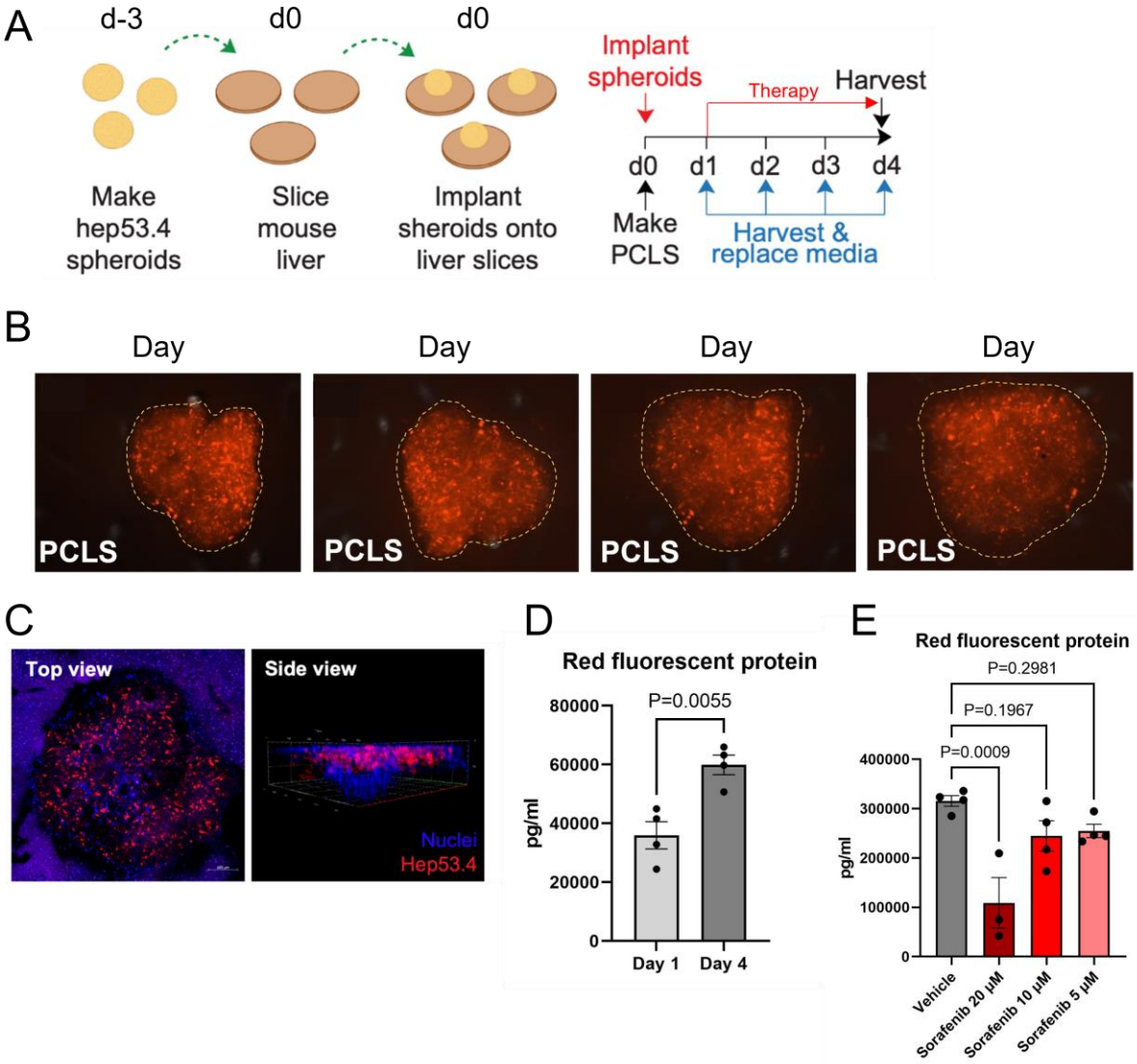

Figure 15. The formation of a Hep-53.4 engrafted HCC-mPCLS model. (A) Schematic detailing the timeline of spheroid generation and implantation on murine PCLS, and subsequent culture period. (B) Representative fluorescent images of Hep-53.4 cells (red tdTomato) engrafted on murine PCLS between day 1 and day 4 at 4X magnification. Yellow dotted line denotes border between spheroid and PCLS. (C) Representative multiphoton images of Hep-53.4 spheroids (red, tdTomato) invading PCLS (blue, Hoechst), showing top view and side view of a z-stack image. (D) ELISA quantification of RFP levels in PCLS at day 1 and day 4 (P=0.0055). (E) ELISA quantification of RFP levels at day 4 in PCLS treated with a vehicle control or 20 µM (P=0.0009), 10 µM (P=0.1967) or 5 µM (P=0.2981) sorafenib. Data are mean ± SEM for up to N = 4 PCLS.

8.2.3 Use of a secreted luciferase to track cancer growth and drug responses

Whilst assessing the levels of RFP in the PCLS presents an end-stage measurement of the Hep-53.4 growth in the tissue, the method does not yield information relating to cancer growth prior to the final day of a culture period when the PCLS are harvested. To overcome this and provide a method of longitudinally tracking cancer growth within the same sample, Hep-53.4 cells were stably transfected with a custom-made vector from Promega (pNL(sNLuc/CMV/NeoR), inducing the expression of a secreted NanoLuc luciferase. This luciferase could then be detected and measured at daily intervals in the culture media, which was completely replaced every 24 hours.

Initial validation of the secreted luciferase system involved confirmation that the luciferase assay utilised was sensitive enough to differentiate between spheroids of different sizes. Hep-53.4 SecLuc spheroids were generated from 40,000, 20,000, 10,000, 5,000 and 2,500 cells and cultured for 4 days, after which the levels of secreted luciferase were assessed. This demonstrated that at day 1, there were significant differences in the luciferase levels detected between PCLS engrafted with 40,000- and 20,000-cell spheroids ($P<0.0001$), and between PCLS engrafted with 20,000- and 10,000-cell spheroids ($P=0.0008$). At day 4 there were significant differences between 40,000 and 20,000 ($P=0.0011$), 20,000 and 10,000 ($P=0.0234$) and 10,000 and 5,000 ($P=0.0042$). The luciferase levels remained consistent throughout the culture period despite the lack of therapeutic intervention (Figure 16A).

To investigate whether responses to anticancer therapies were detectable in the secreted luciferase system, spheroids were generated from 20,000 Hep-53.4 SecLuc cells. After spheroid formation in the first 24 hours, the spheroids were cultured with a vehicle control, sorafenib (5 µM or 10 µM) or lenvatinib (0.1 µM or 1 µM) between day 1 and day 4. A dose dependent reduction in secreted luciferase was observed in response to both sorafenib and lenvatinib (Figure 16B).

After determining that the luciferase assay employed was suitably sensitive, spheroids generated from 20,000 cells were engrafted onto murine PCLS and subsequently treated with a vehicle control, sorafenib (5 µM – 20 µM), lenvatinib (1.25 µM – 5 µM) or regorafenib (5 µM – 20 µM) between day 1 and day 4 (Figure 16C). A significant and dose-dependent reduction in luciferase was observed in response to 20 µM ($P<0.0001$), 10 µM ($P=0.0001$) and 5 µM ($P=0.0035$) sorafenib compared to the vehicle control, which displayed increased luciferase

levels at day 4 compared to day 1 (Figure 16D). Following therapeutic intervention with lenvatinib there were significantly lower levels of luciferase secreted by spheroid-PCLS treated with the highest dose of 5 µM (P=0.0011) compared to the vehicle (Figure 16E). Similarly, there were significantly lower luciferase levels in response to the highest dose of regorafenib (20 µM) compared to the vehicle control (P=0.0395) (Figure 16F).

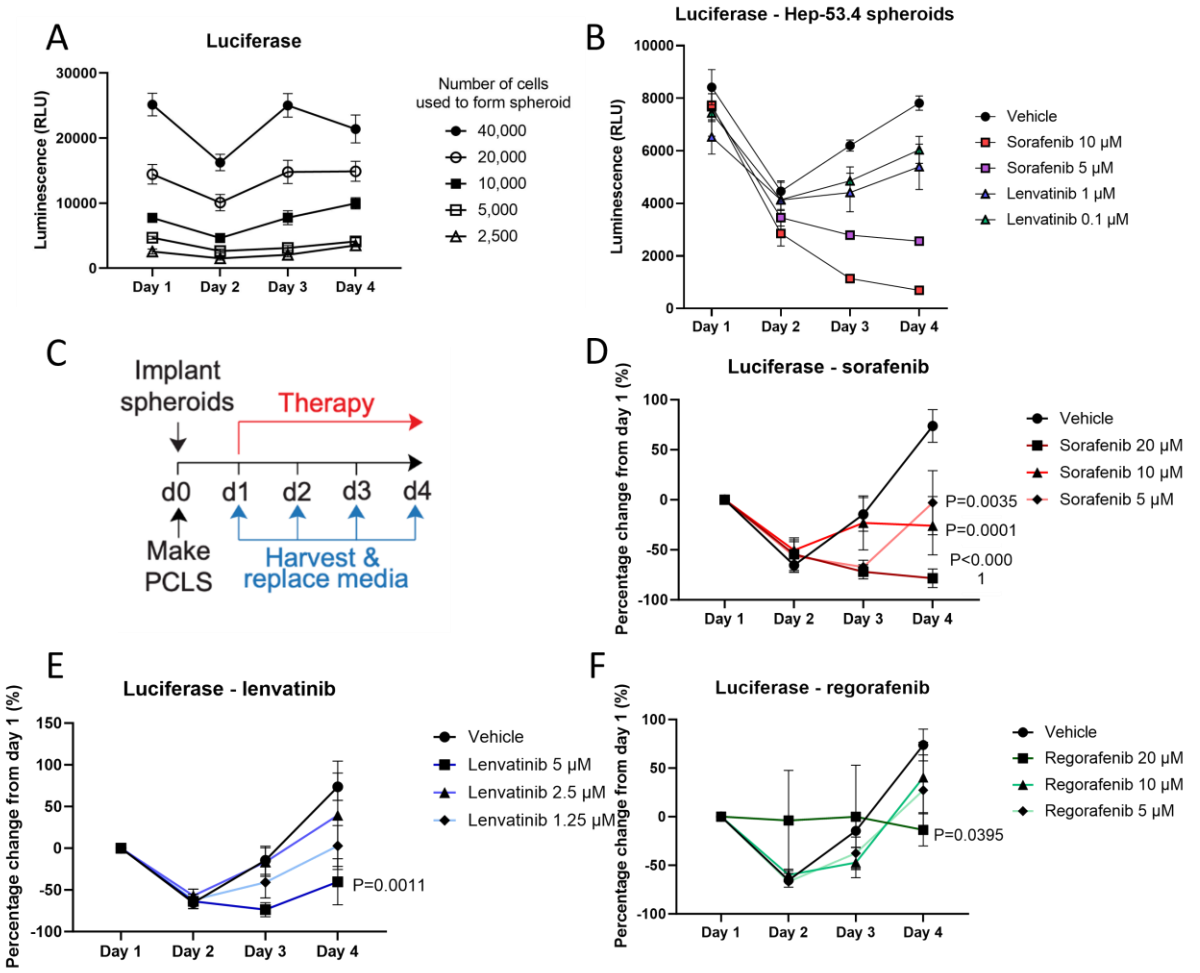

Figure 16. Secreted luciferase for tracking cancer growth and drug responses. (A) Graph showing luciferase assay luminescence values from Hep-53.4 SecLuc spheroids generated from 40,000 – 2,500 cells. (B) Graph showing luciferase assay luminescence values from Hep-53.4 SecLuc spheroids treated with sorafenib (5 µM or 10 µM) or lenvatinib (0.1 µM or 1 µM). (C) Schematic detailing the timeline of implanting Hep-53.4 SecLuc spheroids onto murine PCLS and subsequent culture period with or without TKIs. (D-F) Graphs showing luciferase assay data presented as percentage change from day 1 from Hep-53.4 SecLuc-engrafted PCLS treated with a vehicle control or (D) sorafenib (5 µM – 20 µM) (E) lenvatinib (1.25 µM – 5 µM) or (F) regorafenib (5 µM – 20 µM). Data are mean ± SEM for N = 4 paired Hep-53.4-PCLS.

8.2.4 Murine PCLS viability is maintained following anticancer killing with TKIs

Measuring the levels of luciferase secreted from spheroids engrafted to PCLS provides a method of closely tracking both the growth of HCC cells in the model and responses to anticancer agents implemented in the system. However, this data does not provide information pertaining to the viability and response of the background liver tissue. The combination of HCC spheroids and non-tumour liver tissue in this model presents an opportunity to gain information on the anticancer effects of a therapy alongside identification of any toxic impacts to the surrounding liver tissue, which would inevitably translate to toxicity in humans. The viability of Hep-53.4 spheroid-engrafted PCLS was assessed in response to sorafenib (5 µM – 20 µM), lenvatinib (1.25 µM – 5 µM) and regorafenib (5 µM – 20 µM) by measuring two soluble factors: albumin which is synthesised and secreted by viable hepatocytes, and LDH which is an enzyme released upon damage to the cell membrane, providing a measure of cellular cytotoxicity. It is important to note that following the process of generating PCLS, high levels of LDH are released within the first day due to the mechanical damage induced by cutting through liver tissue with a vibratome. The level of LDH secreted typically decreases and stabilises as the culture period progresses.

The viability of Hep-53.4 spheroid-engrafted PCLS cultured with three doses of sorafenib was maintained throughout the 4-day culture period. Despite a decrease in the levels of secreted soluble albumin after day 1, the levels of albumin secreted remained consistent until day 4 when the Hep-53.4-PCLS were harvested (Figure 17A). Similarly, the amount of LDH secreted by vehicle-treated and sorafenib-treated Hep-53.4-PCLS decreased from day 1 to day 4, with no treatment group producing elevated levels of LDH (Figure 17B). The same trend was observed in Hep-53.4-PCLS cultured with three doses of lenvatinib (Figure 17C-D) and regorafenib (Figure 17E-F), whereby the soluble albumin levels remained consistent between day 2 and day 4, and LDH levels attenuated with the absence of a specific treatment group producing elevated levels of cytotoxicity. Whilst a multitude of secreted factors could be inspected in response to the tissue culture conditions, albumin and LDH have been investigated here to confirm tissue viability.

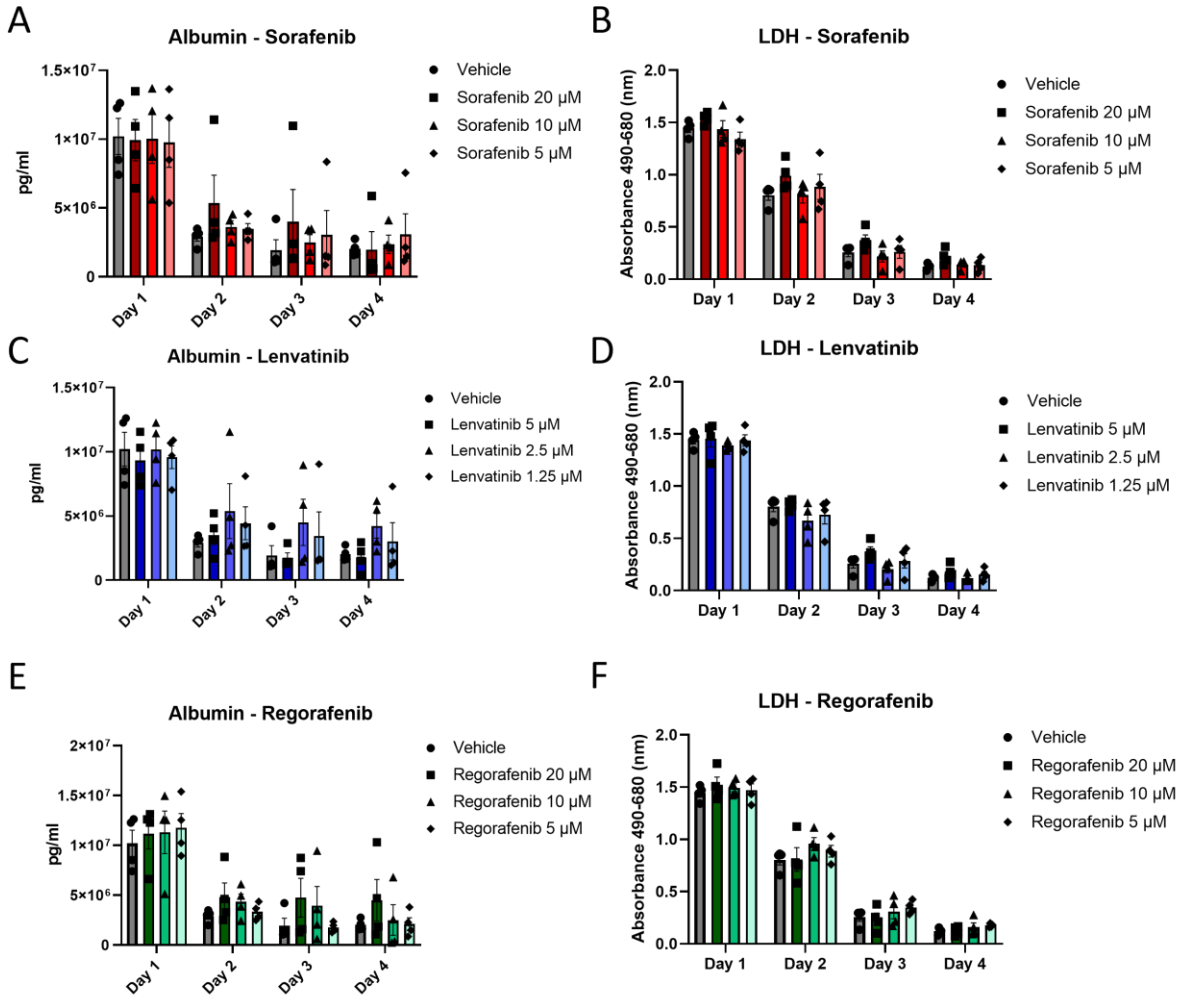

Figure 17. Murine PCLS viability is maintained in response to TKIs. (A-B) Graphs showing levels of soluble (A) albumin and (B) LDH secreted by Hep-53.4-PCLS in response to a vehicle control or sorafenib (5 µM – 20 µM). (C-D) Graphs showing levels of soluble (C) albumin and (D) LDH secreted by Hep-53.4-PCLS in response to a vehicle control or lenvatinib (1.25 µM – 5 µM). (E-F) Graphs showing levels of soluble (E) albumin and (F) LDH secreted by Hep-53.4-PCLS in response to a vehicle control or regorafenib (5 µM – 20 µM). Data are mean ± SEM for N = 4 paired Hep-53.4-PCLS.

8.2.5 Spheroid generation from commercially available human HCC cell lines

Initial optimisation of the spheroid-engrafted PCLS model utilised murine tissue and cells, due to the limited access to human liver tissue from HCC or colorectal cancer (CRC) metastases resections. However, this was not physiologically relevant to human HCC and omits the benefit of mouse models which consider the whole physiological system. Therefore, advancements were made to the spheroid-PCLS model by developing it in human PCLS in combination with human HCC cell lines. Six commercially available HCC lines were selected and assessed for their spheroid-forming ability: HuH7, SNU-398, SNU-182, SNU-387, SNU-475 and HuH1. Cells were seeded in agarose-coated round-bottom 96-well plates at densities of 5,000, 10,000 and 20,000 cells per well and daily brightfield images were taken from day 1 to day 4 (Figure 18A). The spheroid diameter was measured using the Zeiss Zen Blue software and spheroid volumes were calculated.

Only spheroids generated from HuH7 and SNU-398 cells displayed an increase in spheroid volume between day 1 and day 4. Regarding HuH7 spheroids, volume increases of 248.9%, 263.5% and 148.0% between day 1 and day 4 were observed for spheroids generated from 5,000, 10,000 and 20,000 cells respectively (Figure 18B). Brightfield imaging showed HuH7 spheroids to have a dense, compact appearance (Figure 18A). SNU-398 spheroid volume increased by 443.0% (5,000), 347.1% (10,000) and 216.7% (20,000) between day 1 and day 4 (Figure 18C), while brightfield imaging showed that SNU-398 spheroids lacked the compact appearance of HuH7 cells, with an irregular spheroid surface (Figure 18A). Changes in spheroid volume for the cell lines SNU-182, SNU-387 and SNU-475 followed the same trend regardless of whether the spheroids were generated from 5,000, 10,000 or 20,000 cells. In contrast to HuH7 and SNU-398, spheroids generated from SNU-182, SNU-387 and SNU-475 cells all decreased in volume between day 1 and day 4. SNU-182 spheroids displayed a decrease in volume of 44.2% (5,000), 55.3% (10,000) and 58.5% (20,000) (Figure 18D); brightfield imaging of SNU-182 spheroids at day 1 and day 4 indicated that the spheroids lacked the compactness necessary for transfer onto a PCLS (Figure 18A). SNU-387 spheroids decreased in volume by 44.8% (5,000), 50.9% (10,000) and 54.8% (20,000) (Figure 18E), with visible debris around the spheroid at day 4 suggesting that cell death may be responsible for the decrease in size. SNU-475 spheroids displayed a decrease in volume of 60.6% (5,000), 57.6% (10,000) and 58.8% (20,000) (Figure 18F). Whilst SNU-475 spheroids appear more dense at day 4 suggesting that

the spheroids could be more compact than at day 1, there is also visible debris surrounding the spheroid indicative of cell death (Figure 18A). Spheroids generated from HuH1 cells decreased in volume between day 1 and day 4, but gained a denser appearance suggesting that the spheroids became more compact during this period. Interestingly, spheroids generated from 5,000 HuH1 cells displayed an increase in volume after day 3, indicating that HuH1 spheroids generated from fewer cells become compact at a quicker rate before visually increasing in volume as a response to cell proliferation (Figure 18G). Given the linear growth and compact spheroid appearance exhibited by HuH7 spheroids, the HuH7 cell line was selected to develop the human spheroid-engrafted HCC model.

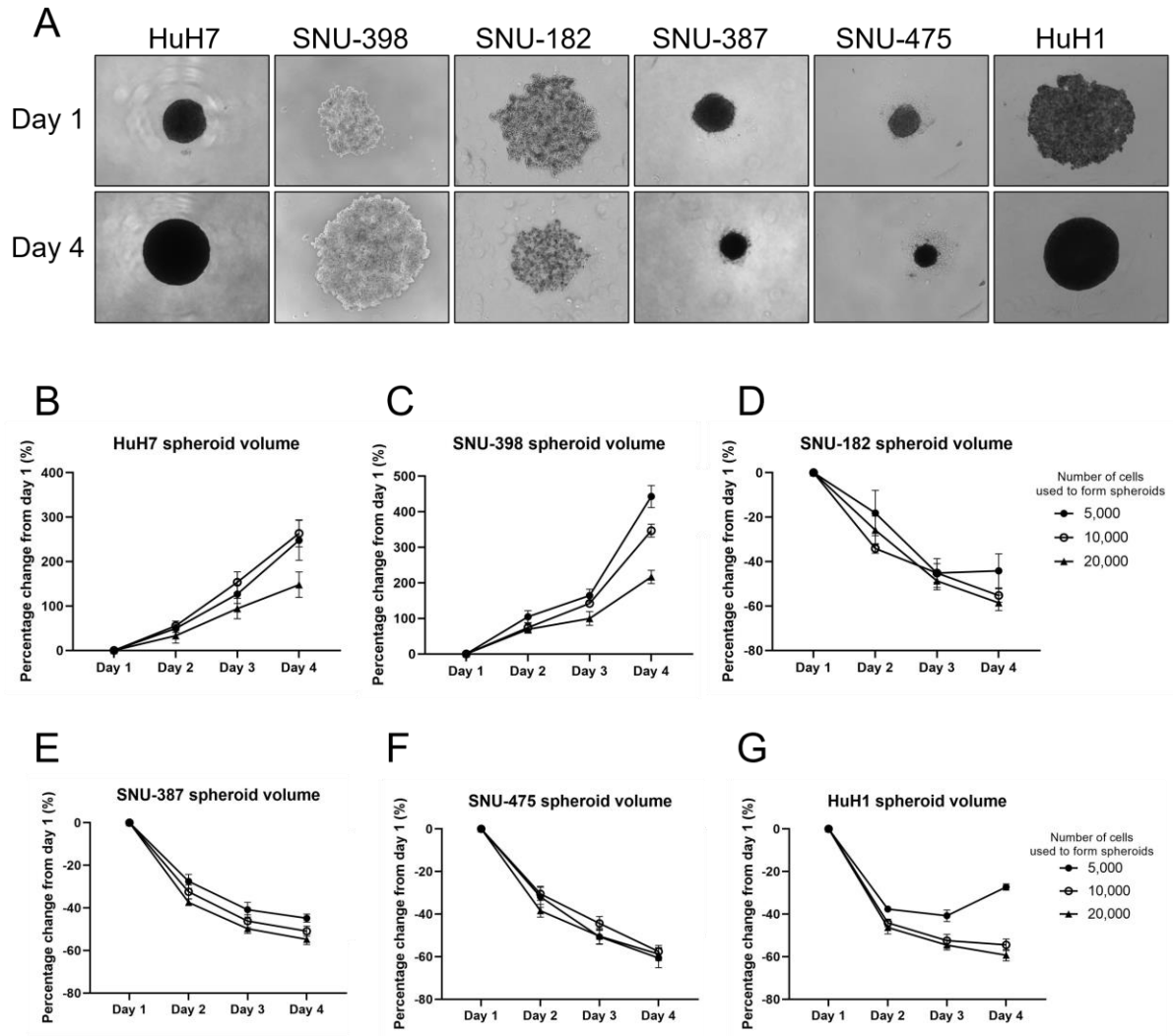

Figure 18. Spheroid generation from human HCC cell lines. (A) Representative brightfield images of spheroids generated from HuH7, SNU-398, SNU-182, SNU-387, SNU-475 and HuH1 cell lines at day 1 and day 4, at 4X magnification. (B-G) Graphs showing changes in spheroid volume presented as percentage change from day 1, for (B) HuH7, (C) SNU-398, (D) SNU-182, (E) SNU-387, (F) SNU-475 and (G) HuH1. Data are mean ± SEM for N = 6 spheroids.

8.2.6 HuH7 spheroids engraft on, invade and proliferate in human PCLS

For initial quantification and visualisation of HuH7 spheroids implanted onto human PCLS, HuH7 cells were stably transfected with the vector tdTomato-N1 to induce the expression of the RFP tdTomato. Human liver tissue was obtained for PCLS generation from HCC or CRC metastases resections. Spheroids were generated from 10,000 HuH7 tdTomato cells 1 day prior to human PCLS generation, at which point the spheroids were implanted onto the PCLS and subsequently cultured for 4 days (Figure 19A).

H&E staining of HuH7 spheroid-engrafted PCLS revealed the spheroids embedded within the liver tissue, displaying densely packed cancer cells in comparison to the surrounding non-tumour liver tissue (Figure 19B). Multiphoton imaging was performed with assistance from Dr Glyn Nelson in the Newcastle University Bioimaging Unit, and the resulting intensity plot ascertained that HuH7 cells (red, tdTomato) implanted onto human PCLS (blue, Hoechst) displayed complete invasion throughout the 250 µM thick PCLS 1 day after spheroid implantation (Figure 19C). Quantification of RFP levels in HuH7 spheroid-PCLS harvested at different timepoints demonstrated that there were significantly higher RFP levels in PCLS 4 days after spheroid implantation compared to day 1 ($P<0.0001$), indicating that HuH7 spheroid proliferate within human PCLS (Figure 19D).

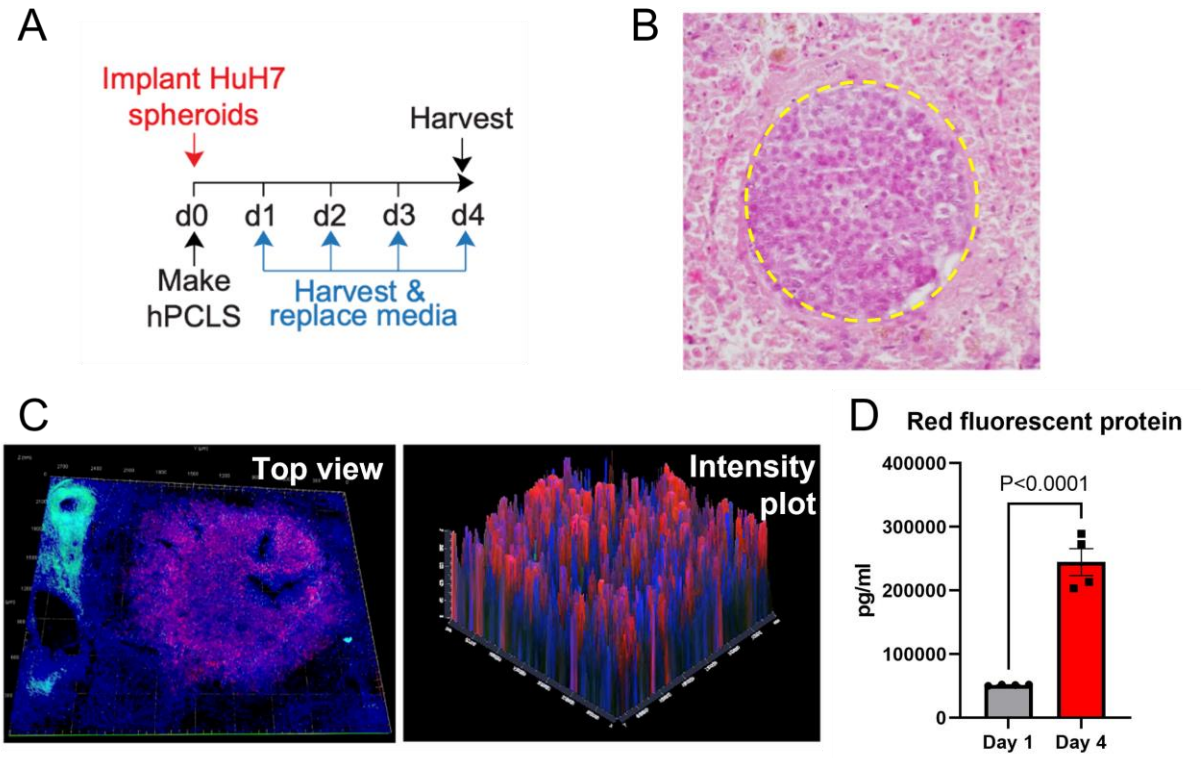

Figure 19. Development of the HuH7 spheroid-PCLS system. (A) Schematic detailing timeline of human PCLS generation and HuH7 spheroid implantation, and the subsequent culture period of 4 days. (B) Representative H&E image of a HuH7 spheroid embedded within a human PCLS 4 days after spheroid implantation. (C) Representative multiphoton images showing the top view and 2.5D intensity plot of HuH7 spheroids (red, tdTomato) embedded within human PCLS (blue, Hoechst) and second-generation harmonics (green) displaying a nearby vessel, confirming tissue invasion. Multiphoton images were taken with assistance from Dr Glyn Nelson. (D) Graph showing quantification of RFP in HuH7 spheroid-PCLS at day 1 and day 4 following spheroid implantation, demonstrating that HuH7 cells proliferate within PCLS ($P<0.0001$). Data are mean ± SEM for N = 4 PCLS.

8.2.7 Human HuH7 spheroid-PCLS respond to therapeutic intervention with TKIs

The NanoLuc secreted luciferase system provided a useful tool for the longitudinal tracking of HCC cell growth in the Hep-53.4 spheroid-PCLS model. The same system was therefore implemented in the human spheroid-PCLS model to accurately assess cancer growth throughout the culture period using paired media samples from the same spheroid-PCLS, avoiding the use of unpaired samples whereby PCLS must be homogenised to yield an RFP value. HuH7 cells were stably transfected with the vector pNL(sNLuc/CMV/NeoR) inducing the expression of a secreted NanoLuc luciferase, which could be measured in samples of culture media. To first determine the accuracy of the secreted luciferase system in HuH7 cells, spheroids generated from 10,000 HuH7 SecLuc cells were cultured for 4 days in a 96-well plate, with complete media changes and brightfield imaging conducted daily. In addition to a linear increase in volume, spheroids generated from 10,000 cells were selected due to their macroscopic size suitable for transfer with a 20 µl pipette tip. The luciferase levels were assessed in the harvested media samples and spheroid volumes were calculated from the diameter measurements taken on Zeiss Zen Blue software. There was a strong positive correlation between spheroid volume and the corresponding secreted luciferase levels (R^2=0.9223), indicating that exploiting the levels of secreted luciferase as a measure of cancer growth was comparable to spheroid volume in HuH7 cells, which notably form compact spheroids within 24 hours and henceforth increase in size (Figure 20A).

To investigate whether the anticancer effects of TKIs (employed to treat advanced HCC) on HuH7 cells could be detected via secreted luciferase, HuH7 SecLuc spheroids were generated from 10,000 cells 1 day prior to human PCLS generation and spheroid implantation, before treatment with a vehicle control, sorafenib (5 µM – 20 µM), lenvatinib (0.1 µM – 2.5 µM) or regorafenib (5 µM – 20 µM) between day 1 and day 4 (Figure 20B). In the context of HCC background liver tissue, there was a significant and dose-dependent reduction in secreted luciferase in response to sorafenib (20 µM; P<0.0001, 10 µM; P<0.0001 and 5 µM; P=0.0002) (Figure 20C) and lenvatinib (2.5 µM; P<0.0001, 0.63 µM; P=0.0001 and 0.1 µM; ns) (Figure 20D). Likewise, in the context of HCC background liver tissue the highest dose of 20 µM regorafenib resulted in significantly lower levels of secreted luciferase compared to the vehicle control (P=0.0174) (Figure 20E). In PCLS generated from CRC metastases resections HuH7 spheroids exhibited a very similar therapeutic response to TKIs: a significant and dose-

dependent decrease in secreted luciferase was observed in response to sorafenib (20 µM; P<0.0001, 10 µM; P<0.0001 and 5 µM; P=0.0005) (Figure 20F) and lenvatinib (2.5 µM; P<0.0001, 0.63 µM; P<0.0001 and 0.1 µM; P=0.0003) (Figure 20G). Reflective of the response observed in HCC background liver PCLS, the highest dose of 20 µM regorafenib resulted in a significant reduction in secreted luciferase compared to the vehicle control (P=0.0469) (Figure 20H).

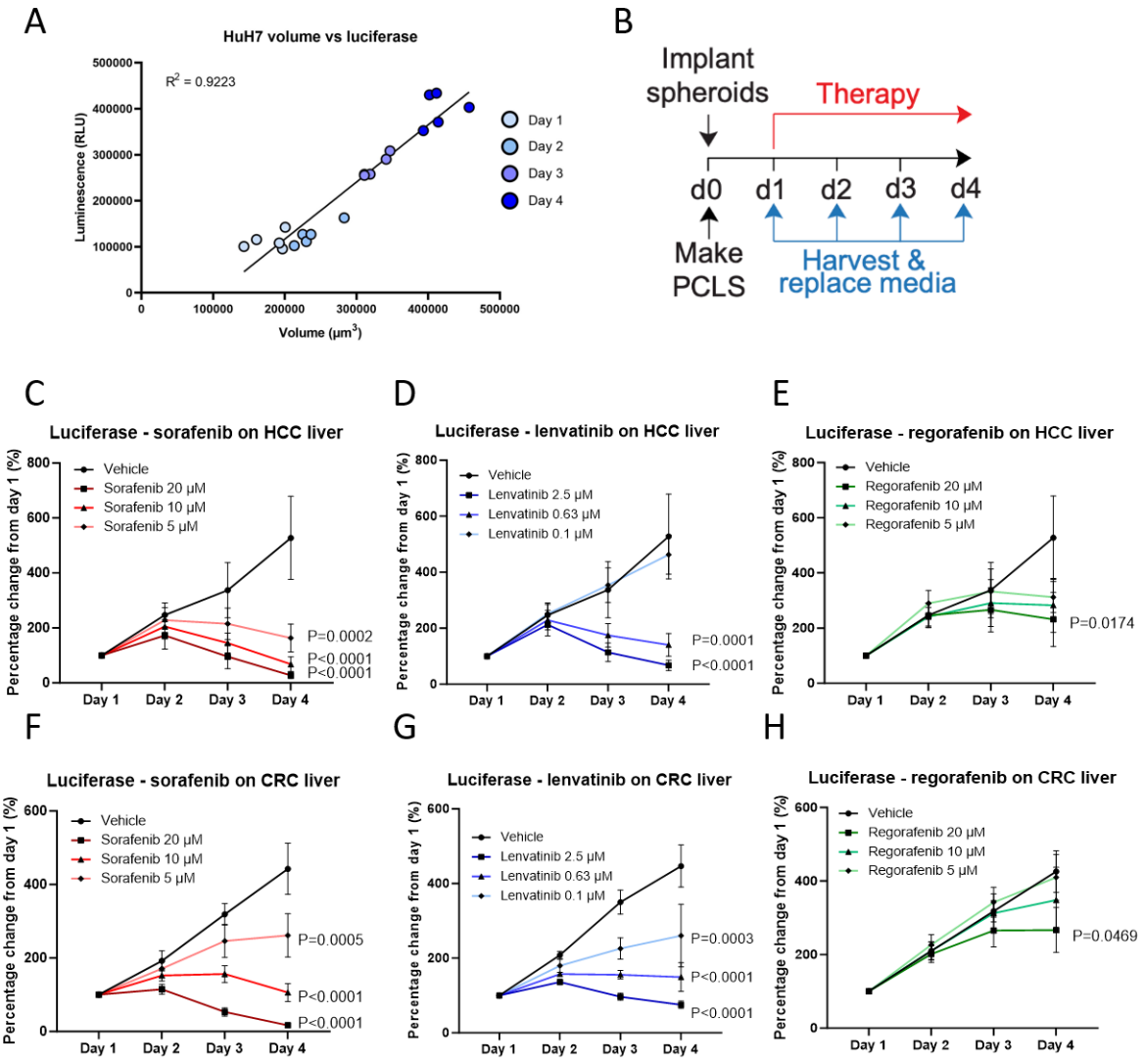

Figure 20. Secreted luciferase to measure therapeutic response in HuH7 spheroid-PCLS. (A) Graph showing correlation between spheroid volume and secreted luciferase levels (R^2=0.9223) of HuH7 SecLuc spheroids generated from 10,000 cells. N = 5 spheroids per timepoint. (B) Schematic detailing the timeline of human PCLS generation and HuH7 spheroid implantation, and the subsequent culture period of 4 days with and without TKIs. (C-E) Graphs showing secreted luciferase levels from HuH7 spheroid-PCLS (HCC background liver) treated with a vehicle control, (C) sorafenib (5 µM – 20 µM), (D) lenvatinib (0.1 µM – 2.5 µM) or (E) regorafenib (5 µM – 20 µM) between day 1 and day 4. Data are mean ± SEM for N = 3 HCC resection donor livers. (F-H) Graphs showing secreted luciferase levels from HuH7 spheroid-PCLS (CRC metastases background liver) treated with a vehicle control, (F) sorafenib (5 µM – 20 µM), (G) lenvatinib (0.1 µM – 2.5 µM) or (H) regorafenib (5 µM – 20 µM) between day 1 and day 4. Data are mean ± SEM for N = 5 CRC metastases resection donor livers.

8.2.8 Human PCLS viability is maintained following anticancer killing with TKIs

The spheroid-PCLS system provides a unique tool in that contributions from the surrounding TME in HCC can be accounted for, whilst the impact of various therapeutic agents on the surrounding non-tumour liver tissue can also be considered. In line with the viability assessments performed in the murine spheroid-PCLS model, soluble albumin and LDH levels secreted from human PCLS were quantified to measure hepatocyte viability and cytotoxicity respectively. The data obtained from all donor livers, regardless of whether the tissue was received from a HCC or CRC metastases resection, was combined to assess the overall impact of sorafenib, lenvatinib and regorafenib on PCLS viability. In response to sorafenib (5 µM – 20 µM) (Figure 21A), lenvatinib (0.1 µM – 2.5 µM) (Figure 21C) and regorafenib (5 µM – 20 µM) (Figure 21E) the levels of albumin in the daily media samples remained consistent; day 4 albumin levels were comparable to day 1 albumin levels indicating that PCLS remained viable throughout the culture period regardless of treatment dose. In terms of cellular cytotoxicity, elevated LDH levels were observed at day 1 due to the damage caused by the PCLS generation process. In response to sorafenib, the LDH followed the typical trend whereby the levels decreased from day 2 onwards. However, elevated but non-significant levels of LDH were detected in media samples at day 4 in response to the highest dose of 20 µM sorafenib, suggesting that this dose had a potentially toxic impact on the PCLS (Figure 21B). Following therapeutic intervention with lenvatinib and regorafenib, the levels of soluble LDH detected in the culture media decreased during the course of the culture period, with no differences in LDH concentration observed between different doses of each drug, indicating that these TKIs did not have cytotoxic effects on the PCLS (Figure 21D, F). Assessment of these factors could be usefully implemented in a scenario whereby a novel anticancer drug is incapable of exerting anticancer effects without also inducing cytotoxicity in the surrounding liver tissue.

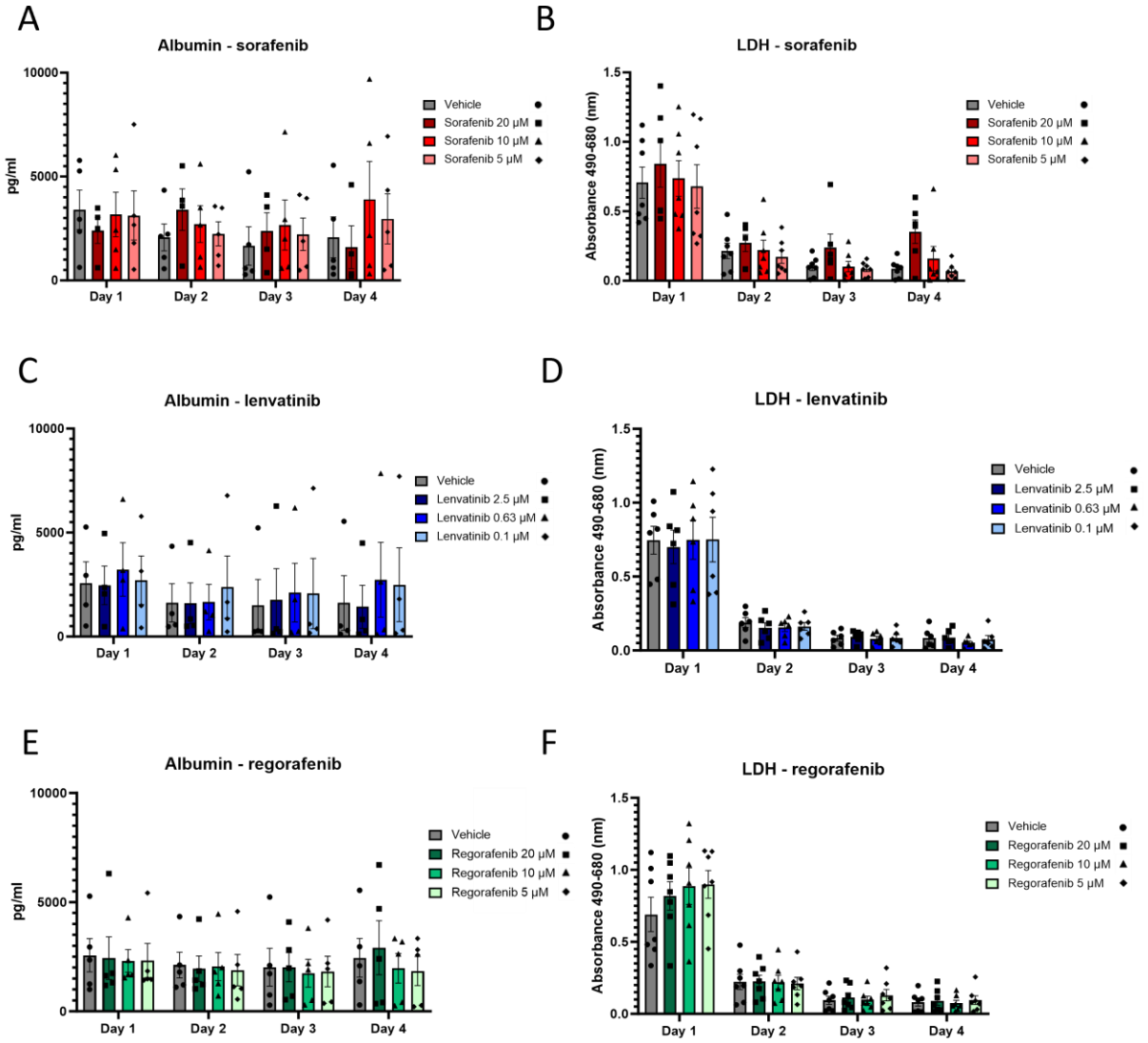

Figure 21. Human PCLS remain viable after therapeutic intervention with TKIs. (A-B) Graphs showing levels of soluble (A) albumin and (B) LDH secreted by HuH7-PCLS in response to a vehicle control or sorafenib (5 µM – 20 µM). (C-D) Graphs showing levels of soluble (C) albumin and (D) LDH secreted by HuH7-PCLS in response to a vehicle control or lenvatinib (0.1 µM – 2.5 µM). (E-F) Graphs showing levels of soluble (E) albumin and (F) LDH secreted by HuH7-PCLS in response to a vehicle control or regorafenib (5 µM – 20 µM). Data are mean ± SEM for N = 8 donor livers, with data from HCC and CRC metastases resections combined.

8.2.9 Characterisation of the HuH7 spheroid-PCLS model via immunohistochemistry

Initial characterisation was performed on the human HuH7 spheroid-PCLS model via immunohistochemistry to provide insight into the stromal and immune components of the model. Knowledge of these components offers the possibility to investigate varying therapeutic strategies that target numerous components in the TME, rather than targeting the HCC alone. Additionally, an understanding of how the components present in PCLS respond upon engraftment of a HCC spheroid may provide further insight into avenues of HCC development and progression.

Immunohistochemical staining on spheroid-PCLS samples harvested 4 days after spheroid engraftment determined that HuH7 spheroids engrafted on human PCLS remained highly proliferative; the implanted spheroids were positive for PCNA, and HuH7 cells interestingly appeared to migrate into the surrounding PCLS beyond the initial spheroid margin (Figure 22A). Regarding the stroma, positive αSMA staining was visible in the surrounding liver tissue and notably at the spheroid margin, surrounding the implanted HCC (Figure 22B). Pertaining to immune constituents, CD8+ T cells were visible within the spheroid in low numbers, indicating that cytotoxic T cells migrated from the PCLS in response to the engrafted HCC (Figure 22C). CD68+ macrophages (Figure 22D) and CD4+ T cells (Figure 22E) were visible in the PCLS surrounding the spheroid but were omitted from the spheroid itself. Interestingly, CD94+ NK cells were observed in abundance within the engrafted HuH7 spheroid, at a high density compared to the surrounding liver tissue (Figure 22F).

Immunohistochemical analysis of HuH7 spheroid-PCLS confirmed that the surrounding PCLS is reactive to the implanted HCC spheroid, as a bi-directional migration of cells was observed from the liver tissue into the spheroid and vice versa, alongside the presence of stromal components in response to the spheroid.

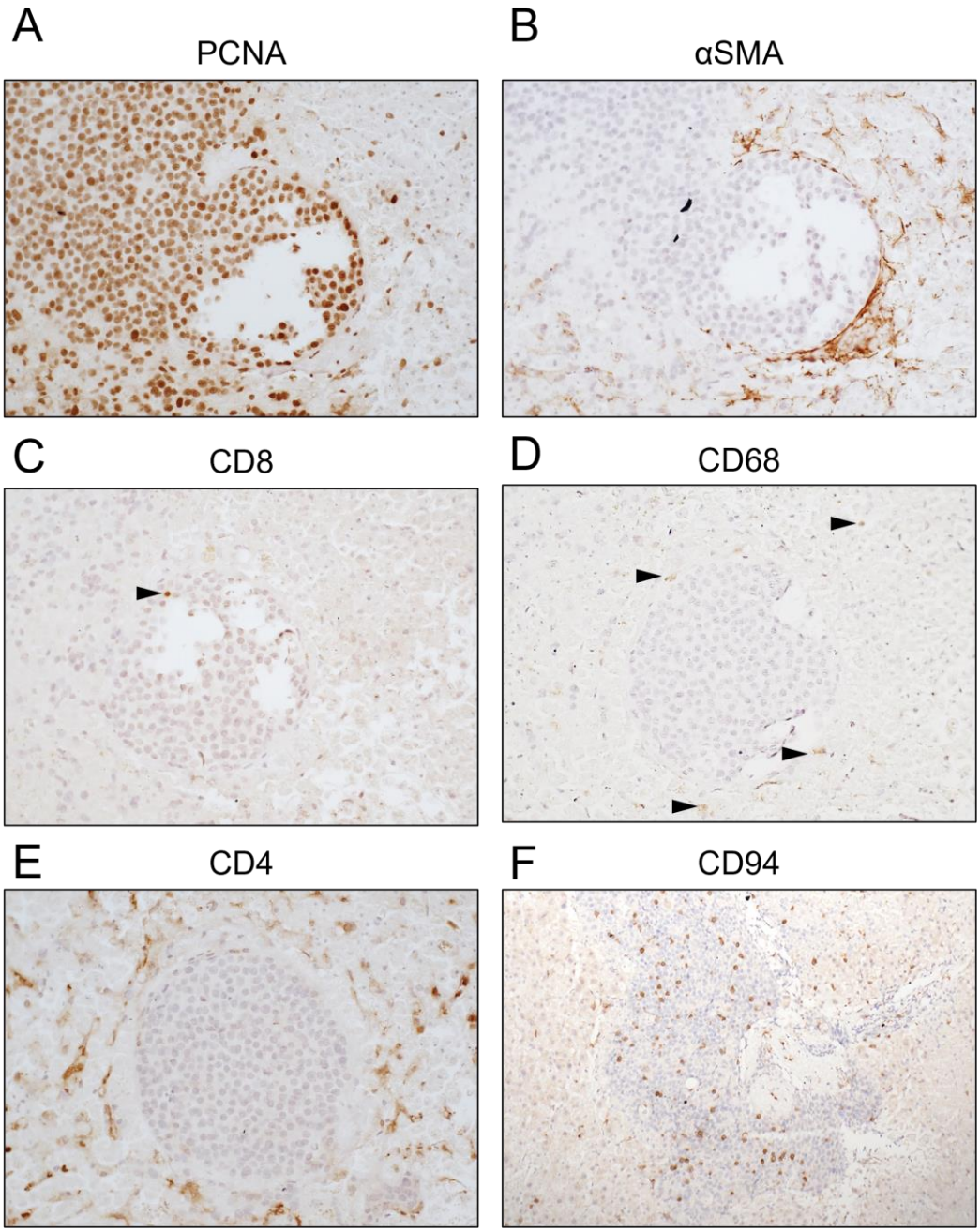

Figure 22. Immunohistochemical characterisation of HuH7 spheroid-PCLS. (A-F) Representative IHC images of HuH7 spheroids embedded within human PCLS: (A) PCNA, (B) αSMA, (C) CD8, (D) CD68 and (E) CD4 and (F) CD94. Black arrows denote positively stained cells. Images were taken at 20x magnification.

8.2.10 Characterisation of the HuH7 spheroid-PCLS model via Hyperion imaging mass cytometry

Immunohistochemical analysis of the human spheroid-PCLS model ascertained that immune components in human PCLS interacted with implanted HuH7 spheroids; invasion of proliferative HCC cells was observed into the surrounding liver tissue, while CD94+ and CD8+ cells were seen to migrate into the spheroid in different capacities. Despite providing preliminary knowledge of the interactions between human PCLS and an engrafted HCC spheroid, the methodology presented disadvantages. A formalin-fixed paraffin-embedded PCLS only has the capacity to provide a limited number of tissue sections for immunohistochemical staining due to the 250 µm thickness, and whilst dual IHC staining is possible, it does not enable multiple biomarkers from the same tissue section to be overlayed to indicate where certain markers are co-expressed. Moreover, microtomy often damaged the engrafted spheroid and dislodged sections of the implanted tissue (Figure 22). To provide a deeper insight into the multitude of cellular biomarkers and stromal components present in the samples, Hyperion imaging mass cytometry (IMC) was employed and performed by Erik Ramon-Gil from the Newcastle Fibrosis Research Group. Hyperion IMC allows the simultaneous imaging of more than 40 protein markers via IHC with metal-conjugated antibodies and time-of-flight mass spectrometry.

HuH7 spheroid-PCLS samples generated from both HCC and CRC metastases resections were harvested 4 days after spheroid implantation before being stained and ablated using the Hyperion Imaging System. The predominant observations were that engrafted HuH7 spheroids maintained a proliferative Ki67+ phenotype with vimentin present in the spheroid, while alpha-1 type I collagen and endothelial CD31 remained excluded from the spheroid in the surrounding PCLS; consistent with the findings from IHC, myeloid markers were largely excluded from the spheroid, with very few CD68+ or CD163+ cells observed within the spheroid (Figure 23). Marked differences between the three samples initially ablated appear in the lymphoid compartment: sample 1 on a HCC background liver exhibited a high influx of CD8+ and CD56+ cells with granzyme B present in the spheroid; co-expression of these markers was observed suggesting the presence of an NKT-like population of cells (Figure 23A). In contrast, there was no invasion of the lymphoid components into the HuH7 spheroid in a separate HCC background liver (Figure 23B) and very little in a HuH7 spheroid on a CRC

background liver, with low numbers of CD8+ and CD56+ cells observed inside the spheroid (Figure 23C). Hyperion IMC on an increased number of samples is vital to decipher whether immune responses to HuH7 spheroids can be stratified based on background liver disease or whether responses are simply patient-specific.

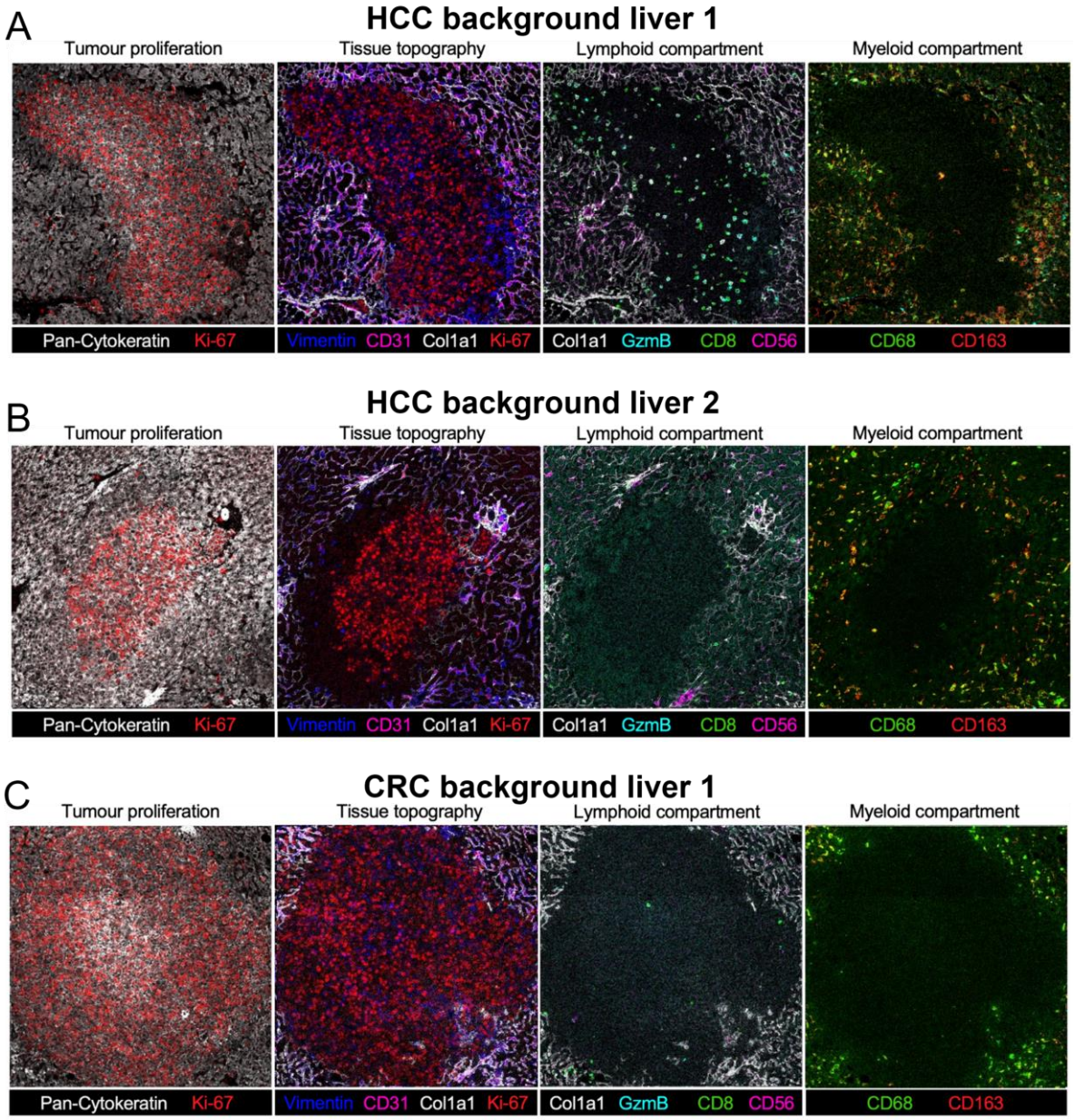

Figure 23. Hyperion imaging mass cytometry to characterise HuH7 spheroid-PCLS. (A-C) Images of HuH7 spheroid-PCLS generated via Hyperion imaging mass cytometry displaying tumour proliferation, tissue topography, lymphoid components and myeloid components in the contect of (A) HCC background liver 1, (B) HCC background liver 2 and (C) CRC background liver 1. The markers displayed are listed below the image in the colour that they appear in the image. Sample was stained and ablated by Erik Ramon-Gil.

8.2.11 Targeting HuH7 spheroid-PCLS with GPC3 CAR-T cells

CAR-T cell immunotherapy enables engineered T cells to target specific cancer antigens and encourages anticancer killing by T cells. The approach has demonstrated effectiveness in targeting B cell malignancies but thus far has shown limited efficacy in solid tumours. To investigate the impact of CAR-T cells introduced into the HuH7 spheroid-PCLS model, and potentially establish a method of modelling and improving CAR-T cell killing, engineered T cells were purchased from Amsbio. It was first necessary to determine which biomarkers relating to the liver and HCC that the HuH7 cell line expressed so CAR-T cells with the correct specificity could be employed. Fluorescent immunocytochemistry performed on 2D cells revealed that HuH7 cells expressed the HCC biomarkers GPC3, AFP and hepatocyte specific antigen/hepatocyte paraffin 1 (HepPar1), as well as the hepatocellular marker cytokeratin 18 (CK18) (Figure 24A). Following this discovery, CAR-T cells engineered to recognise GPC3 were selected and purchased.

HuH7 spheroids were generated from cells expressing either tdTomato or secreted NanoLuc luciferase and implanted onto human PCLS; GPC3 CAR-T cells were labelled with CellVue Jade Cell Labelling Kit and added to HuH7 spheroid-PCLS (approximately 85,000 per spheroid-PCLS) at day 4 and samples were harvested at day 5 and day 6 (Figure 24B). Utilising the levels of secreted luciferase as a measure of HuH7 growth, there was less luciferase in the day 5 media from HuH7 spheroid-PCLS cultured with added GPC3 CAR-T cells for 24 hours compared to those without the addition of CAR-T cells, while the luciferase levels at day 6 were comparable between the two conditions (Figure 24C). While GPC3 CAR-T cells potentially reduced HuH7 spheroid growth in the initial 24 hours after the addition of the cells, this effect was lost by day 6 suggesting that the CAR-T cells may have been unviable in the culture system by this timepoint. Prior to the addition of GPC3 CAR-T cells, the luciferase levels in the CAR-T treatment group were slightly lower than those in the control group. Therefore, to calculate the luciferase levels at day 6 relative to the initial levels observed prior to the addition of GPC3 CAR-T cells, the day 5 luminescence values were subtracted from the day 6 luminescence values. This demonstrated that within the initial 24 hours there were lower, albeit non-significant levels of luciferase secreted by HuH7 spheroid-PCLS cultured with GPC-3 CAR-T cells compared to the control ($P=0.0914$) (Figure 24D). There was a limited number of CAR-T cells

available for this experiment, but further work would involve replenishing the supply of CAR-T cells to the culture system rather than incorporating them at one day alone.

Multiphoton imaging was performed with assistance from the Newcastle University Bioimaging Unit to assess the invasive capacity of CAR-T cells added to the HuH7 spheroid-PCLS system. Z-stack images generated demonstrated that GPC3 CAR-T cells (green, CellVue Jade) invaded the HuH7 spheroid-PCLS (red, tdTomato), and were observed both inside the centre of the spheroid and at the spheroid margin, offering a platform with the potential to study improved CAR-T cell targeting of solid tumours (Figure 24E).

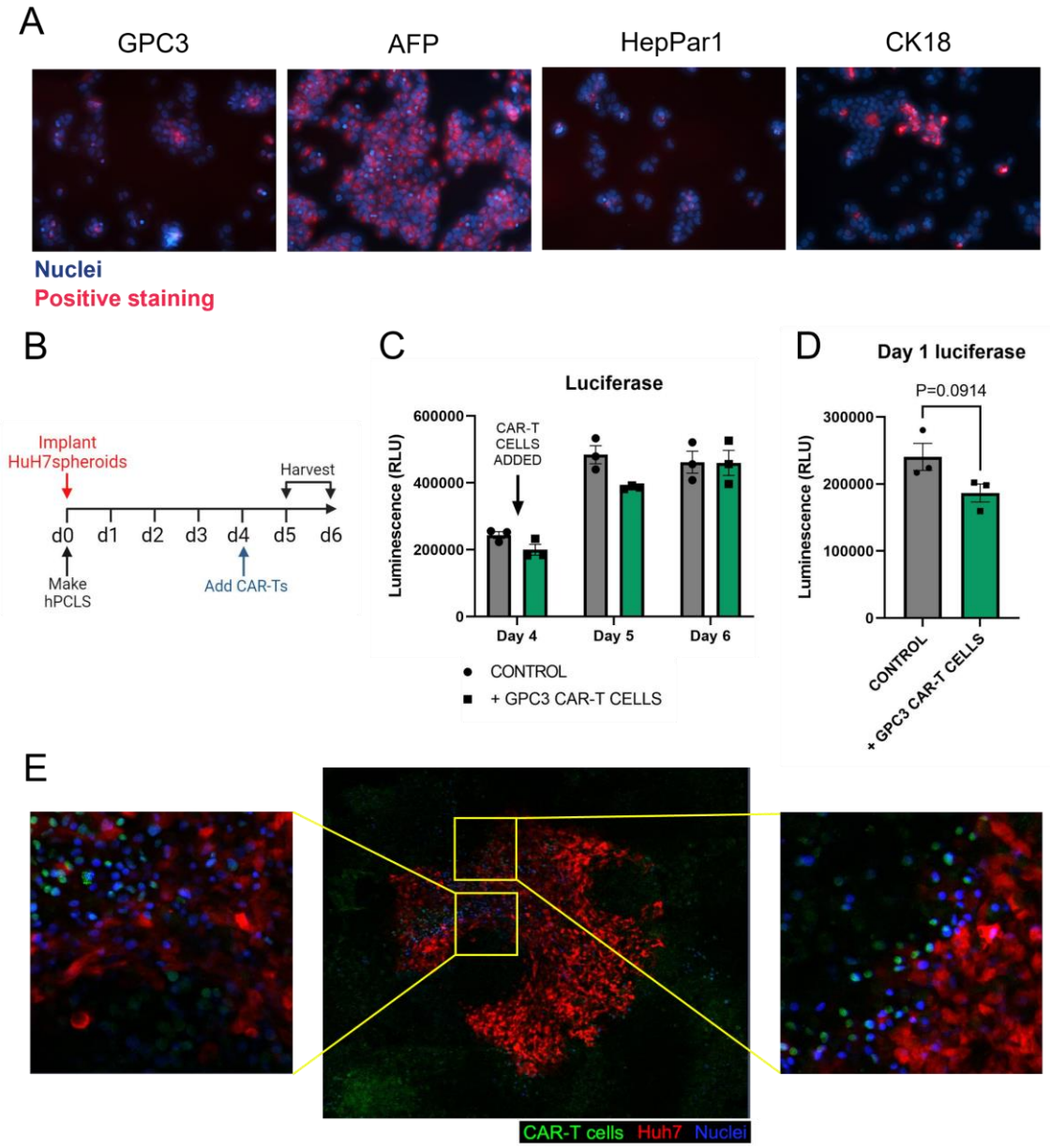

Figure 24. Targeting HuH7 spheroid-PCLS with GPC3 CAR-T cells. (A) Representative immunocytochemical images of HuH7 cells expressing GPC3, AFP, HepPar1 and CK18. (B) Schematic detailing timeline of implanting

HuH7 spheroids on human PCLS and subsequent culture period with the addition of GPC3 CAR-T cells. (C-D) Graphs showing luciferase assay data for (C) the final 3 days of the culture period where CAR-T cells were incorporated in the tissue culture and (D) the difference in luciferase secreted by HuH7 spheroid-PCLS cultured with and without CAR-T cells in the 24 hours after addition of CAR-T cells. (E) Multiphoton images of a HuH7 spheroid (red, tdTomato) engrafted in a human PCLS (blue, Hoechst) with invading GPC3 CAR-T cells (green, CellVue Jade) in the centre of the spheroid and at the spheroid margin.

8.3 Results summary

PCLS were engrafted with HCC spheroids with the intention of modelling HCC in the context of the surrounding TME and the manner in which TME factors may contribute to HCC growth and therapeutic responses. Initial optimisation of the model employed murine tissue and cells; following the successful use of Hep-53.4 cells in the orthotopic mouse model of HCC, the cell line was exploited to generate HCC spheroids which were subsequently implanted onto murine PCLS. Hep-53.4 cells expressing the RFP tdTomato were utilised to visualise the engraftment of HCC spheroids on PCLS, which progressed to confirmation of complete invasion into the 250 µm thick PCLS via z-stack images generated by multiphoton microscopy. Furthermore, quantifying the RFP present in PCLS harvested at 1 and 4 days after spheroid engraftment demonstrated that Hep-53.4 spheroids proliferated significantly within murine PCLS. These findings were mirrored in the development of a human spheroid-PCLS model; spheroids generated from the human HCC line HuH7 displayed complete invasion into human PCLS and proliferated within the tissue on which they were implanted.

These promising results prompted the development of a system which could provide a method of longitudinally tracking HCC growth within the same spheroid-PCLS sample, as the previous method of assessing RFP levels via ELISA required the sample to be homogenised. A custom-made vector supplied by Promega provided this opportunity; HCC cells were transfected to express a luciferase which was secreted and could therefore be measured in samples of daily culture media. Using this “SecLuc” system, HuH7 spheroid-PCLS cultured with the TKIs sorafenib, lenvatinib and regorafenib displayed significant and dose-dependent reductions in HCC growth, indicating that the platform developed offers a utility to assess anticancer therapeutic responses. Importantly, the presence of non-tumour PCLS surrounding the HCC spheroids enabled the viability and cellular cytotoxicity of surrounding liver tissue to be investigated. In response to the three TKIs employed here, albumin ELISAs demonstrated

that tissue viability was maintained, whilst LDH quantification provided a method of communicating whether specific interventions or doses were cytotoxic to the PCLS.

Initial characterisation via immunohistochemistry identified that the HuH7 spheroid-PCLS model exhibited bi-directional migration of various cell types, as implanted HCC cells invaded the surrounding PCLS and immune cells such as NK cells and T cells migrated into the spheroid. The model was further characterised through the employment of Hyperion imaging mass cytometry, which identified proliferative spheroids alongside ECM components and endothelial cells in the surrounding liver tissue. While myeloid components were largely excluded from the spheroids, a large influx of lymphoid cells was observed in a specific sample, with CD8+ and CD56+ cells observed in the spheroid. The co-expression of these markers suggests the presence of an NKT-like subtype of cells which possess the characteristics of both T cells and NK cells. This characterisation demonstrated that the surrounding TME is reactive to implanted HCC spheroids.

The effectiveness of CAR-T cell immunotherapy in the HuH7 spheroid-PCLS model was assessed by targeting the GPC3+ HuH7 spheroids with CGP3 CAR-T cells. Multiphoton imaging identified that CAR-T cells added to the culture media of HuH7 spheroid-PCLS could invade the tissue, with populations of CAR-T cells observed both in the centre and at the spheroid margin. Utilising the “SecLuc” system, slightly lower levels of luciferase were secreted by spheroid-PCLS cultured with GPC3 CAR-T cells for 24 hours, suggesting that they were potentially limiting HCC growth.

8.4 Discussion

The use of HCC spheroids bypasses some of the limitations presented by 2D cell culture. Interactions between different cell types are accounted for and the mechanical stress exerted on cells by plastic is avoided (366). Moreover, spheroids mirror the spatial conformation and heterogeneous access to nutrients of solid tumours (367). Precision cut liver slices are an alternative example of a 3D culture model whereby the original tissue architecture and function are retained whilst the tissue maintains viability in culture (339, 362). The combination of PCLS with HCC spheroids has culminated in an *ex vivo* 3D TME which accounts for both the HCC and the surrounding liver tissue containing various immune and stromal components. The resulting tool has potential utility as a tool for therapeutic screening and further understanding HCC tumorigenesis.

Spheroids were initially implanted on PCLS using murine cells and tissue as a proof of concept before developing a human model. Hep-53.4 cells had previously been utilised to generate rapidly-growing tumours in an orthotopic model of HCC, and were employed once again to generate Hep-53.4 spheroids. This demonstrated that HCC spheroids implanted on murine PCLS display tissue engraftment and invasion and proliferate within the surrounding liver tissue. Despite Hep-53.4 cells proliferating within PCLS, Hep-53.4 spheroids cultured alone typically decreased in volume unless generated with a very low number of cells. Two suggestions for this observation are that factors from the surrounding PCLS influenced HCC proliferation, or that Hep-53.4 spheroids cultured alone became more compact instead of increasing in volume, whilst still proliferating.

The HuH7 cell line was selected to further develop the model with human cells and PCLS due to the ability of the cell line to form compact spheroids that exhibited high growth rates. The compactness of the spheroid enabled spheroids to be transferred onto a PCLS without disaggregating, allowing reproducible spheroid implantation. PCLS were generated from HCC or CRC metastases resections. The same findings relating to engraftment, invasion and proliferation were observed with HuH7 spheroids and human PCLS. The supply of human liver tissue for PCLS generation was limited at the start of the project due to the COVID-19 pandemic. Given more time, HCC spheroids generated from numerous other cell lines would ideally be implanted onto human PCLS. Developing the spheroid-PCLS model with HCC cells displaying differing characteristics and mutations would allow differences in therapeutic

response and TME to be attributed to these factors. Spheroids were also generated with the immortalised human HCC cell lines SNU-182, SNU-387, SNU-398, SNU-475 and HuH1. Comparable to HuH7 spheroids, SNU-398 spheroids exhibited high growth rates in terms of volume when cultured alone, indicating that they may have displayed high proliferation rates within PCLS. SNU-387, SNU-475 and HuH1 spheroids were compact in appearance and would therefore be transferrable to PCLS without disaggregating. Similarly, the formation of multicellular tumour spheroids (MCTS) comprised of HCC cells alongside other cell types, such as fibroblasts, may further progress the model to reflect the TME in which a multitude of cell types interact to influence tumour progression, invasion and therapeutic response (370, 371).

Quantification of RFP provided an end-point measurement of HCC growth within PCLS. However, the method did not provide an insight into HCC growth or treatment response at earlier timepoints throughout the culture period. A custom-made expression vector was designed by Promega, inducing the expression of secreted NanoLuc® luciferase capable of being measured in the culture medium. NanoLuc® luciferase is approximately three times smaller than Firefly luciferase and 100 times brighter than both Firefly and Renilla luciferases (372, 373). This was an important feature of the system, considering that the relevant luciferase assay needed to have a high enough sensitivity to detect the luciferase secreted by approximately 10,000 cells in a total media volume of 3 ml in the bioreactor plates. Furthermore, secreted NanoLuc luciferase remains stable in culture media for more than 4 days at 37°C (372). PCLS undergo a complete media change once every 24 hours, therefore attributing the luciferase signal to the previous 24 hours as opposed to an accumulation throughout the culture period.

Following therapeutic intervention with the TKIs sorafenib, lenvatinib and regorafenib a dose-dependent reduction in the levels of secreted luciferase were observed, indicative of a reduction in HuH7 proliferation. Drug concentrations were selected according to previous studies whereby HCC cell lines were probed in 2D and 3D culture with various small molecule inhibitors (374, 375). Lenvatinib was initially applied at higher doses than stated in this report, however the therapeutic response to the higher concentrations was indistinguishable from the 2.5 µM dose. A therapeutic response was observed irrespective of whether HuH7 spheroids were engrafted with PCLS generated from a HCC resection or a CRC metastases resection, suggesting that there were not factors specific to each type of cancer that

influenced the anticancer effect of the TKIs. Compared to the first-line TKIs sorafenib and lenvatinib, the second-line therapy regorafenib exerted a lesser therapeutic effect on the HuH7-engrafted PCLS. The highest applied dose of 20 µM regorafenib resulted in decreases in secreted luciferase equivalent to 1-star significance (P = 0.0174 on HCC resection PCLS; P = 0.0469 on CRC metastases resection PCLS), whilst lower doses exerted non-significant effects. A potential explanation for this is that regorafenib predominantly targets VEGF receptors with limited functionality in PCLS which are isolated from the circulation, whilst sorafenib and lenvatinib possess potency for a wider range of targets that may be present in the PCLS (70, 249, 252, 256).

Over the past 6 years there have been advances in immunotherapy for the treatment of advanced HCC. The current "gold standard" treatment strategy is the combination of atezolizumab targeting PD-L1 alongside bevacizumab targeting VEGFA (261, 376). The potential use of the spheroid-PCLS platform as a screening tool for immunotherapies improves its utility in a field where immunotherapy is becoming a more prevalent option. The consideration that the implanted HCC spheroid and the PCLS are not derived from the same donor impedes the possibility of a therapeutic response with agents such as anti-PD1, as the liver-resident T cells will not recognise the MHC class I molecules presenting tumour-associated antigens. The incorporation of allogenic CAR-T cells into the spheroid-PCLS system enables an immunotherapeutic approach to be taken (377). The use of GPC3 CAR-T cells in the HuH7 spheroid-PCLS system demonstrated the capacity for employing the model to investigate and improve CAR-T cell immunotherapy. Although a non-significant decrease in secreted luciferase was observed in the 24 hours following addition of CAR-T cells to the culture system, the experiment was severely limited by the number of CAR-T cells available. The CAR-T cells purchased for the experiment lacked the ability to proliferate and were limited to approximately 1 million cells, which were divided between a total of 12 PCLS. Future collaborative work with experts in the field of CAR-T cells could further exploit the technology and provide a greater source of CAR-T cells for optimisation of the system, allowing greater numbers of CAR-T cells to be repeatedly added to the same PCLS. Multiphoton imaging of a HuH7 spheroid-PCLS sample with added GPC3 CAR-T cells demonstrated that CAR-T cells were capable of invading the tissue but were predominantly observed in clusters close to the spheroid margin. IHC analysis identified the formation of an αSMA-positive stroma

surrounding the implanted spheroid, indicating that there is a physical, and potentially chemical barrier which may impact the invasion of CAR-T cells. These findings are in line with the evidence demonstrating that CAR-T cell therapy has limited efficacy in solid tumours. An interesting intervention would involve modulating the matrix, for example via inhibition of TGF-β type I receptor kinase (ALK5), to investigate whether CAR-T cell invasion and anticancer effect is improved. The multiphoton image of the sample cultured with CAR-T cells displays areas on each side of the spheroid where the tdTomato-positive HuH7 cells are not visible. This is an observation that was not visible on samples untreated with CAR-T cells. Exploring whether these regions co-localise with caspases may reveal whether CAR-T cells have exerted a therapeutic effect.

Hyperion IMC provided insight into the spatial configuration of the HuH7 spheroid surrounded by a multitude of immune, stromal and matrix components in samples harvested 4 days post spheroid implantation. HuH7 spheroids embedded within PCLS from both HCC and CRC metastases resections were highly proliferative and infiltrating immune cells were observed, particularly in one spheroid-PCLS from a HCC resected liver. CD56 and CD8 positivity is visible in the HuH7 spheroid. Moreover, these cellular markers are co-expressed by a number of cells suggesting the presence of NKT-like cells – T lymphocytes which express NK-associated receptors and have previously been identified in diseased livers (378, 379). Stimulation with IL-15 may enhance the functional capacity of NK cells resulting in an increased IFN-γ response (380). Vimentin positivity was also visible in the HuH7 spheroid and surrounding liver tissue. Vimentin has been shown to promote angiogenesis and immune suppression, which can be overcome by blocking vimentin activity (381), leading to the hypothesis that targeting HuH7 spheroid-PCLS with an anti-vimentin antibody will stimulate a migration of immune cells into the spheroid and attenuate HCC growth. The majority of myeloid cells were excluded from the spheroid and could be visualised in the surrounding liver tissue; an observation that could potentially be overcome via vimentin inhibition. Performing Hyperion IMC on samples at timepoints earlier than 4 days could provide a visualisation of the TME responding and migrating into the implanted spheroid. Likewise, live imaging of PCLS beginning promptly after spheroid implantation would offer a real-time visualisation of the various interactions within the HuH7 spheroid-PCLS platform.

A difficulty encountered when harvesting the spheroid-PCLS was that microtomy performed on formalin-fixed paraffin-embedded samples occasionally disrupted the tissue and appeared to tear the spheroid from the remaining PCLS tissue. Consequently, numerous PCLS were engrafted with spheroids in order to obtain intact paraffinised spheroid-PCLS samples for IHC and Hyperion analysis. Current experiments within the laboratory involve miniaturising the model to create a 96-well system whereby PCLS 3 mm in diameter and engrafted with HuH7 spheroids. Optimisation will be required to accurately implant the spheroids onto a smaller tissue surface area. Nevertheless, the development of a higher throughput 96-well system will elevate the therapeutic screening abilities of the model. Standard 2D and 3D cell culture will not comprehensively reveal the effects of potential anticancer therapies that exert responses on TME components rather than specifically targeting HCC, and the spheroid-PCLS model described here has been utilised with an industrial collaborator to assess the potency of a novel therapeutic agent.

9 Generating a patient-derived HCC cell line library to engineer precision medicine platforms

9.1 Introduction

The merging of HCC spheroids with PCLS resulted in an exciting tool in which HCC growth and therapeutic response could be considered without omitting potential contributions from the surrounding liver tissue, more closely reflecting *in situ* HCC than 3D spheroid culture alone. Although development of the human HCC spheroid-PCLS model was performed using the HuH7 cell line, the model design allows the HCC cell line to be interchanged to recapitulate specific factors, such as the genetic profile of the cell line. HuH7 cells were isolated from a liver tumour in a 57-year-old Japanese male, representing a specific age, sex and ethnicity (382). Whilst the employment of HuH7 cells pertains to the initial patient from which the cells were isolated in 1982, the use of HuH7 and other immortalised cell lines does not capture the highly heterogeneous landscape present in most HCC tumours. As a consequence of repeated passages, cell lines are subject to genetic drift with stark differences in morphology, gene expression and drug responsiveness observed between the "same" cell line acquired from different sources, despite the previous assumption that cell lines are clonal (383, 384). This knowledge points to limitations presented by immortalised cell lines that do not accurately reflect diverse multicellular HCC tumours, although they do yield reproducible results at a low cost (385).

The isolation of primary cells directly from human tissue provides a supply of cells whereby the functional and morphological characteristics are more reflective of the *in vivo* human situation. Primary cells isolated from original tumour tissue have displayed a higher retention of tumour markers and microRNAs compared to immortalised cell lines, therefore more reliably mirroring the cancers from which they were derived (386). However, the lifespan of primary cells is typically limited as repeated passages often result in functional and morphological changes. Changes in gene expression, proliferation rate and drug responses have been observed in primary cells that have been subjected to a low number of passages (387). Despite the difficulties presented by primary cells due to potential scarcity of tissue and phenotype alteration, they offer a promising system to improve precision medicine regimens (388).

Here I describe the generation and characterisation of a patient-derived HCC cell line library from patient tissue biopsies, and the subsequent incorporation of these primary cell lines into the previously described spheroid-PCLS model of HCC to produce a platform capable of improving precision medicine strategies.

9.2 Results

9.2.1 A patient-derived primary HCC cell line library: 2D and 3D culture

A primary HCC cell line library was generated to provide a bank of cells with a higher resemblance to diverse *in vivo* tissue than previously employed immortalised cell lines, such as HuH7. HCC biopsies were obtained from patients with advanced stage HCC, and primary cells were isolated by digesting the sample using a cocktail of human tumour dissociation enzymes. The isolation and characterisation of the patient-derived HCC cell lines was performed by Maja Laszczewska. The resulting isolated cells were seeded and expanded on collagen-coated plates to reflect the *in vivo* situation and ECM more closely. Of the 35 patient biopsies obtained (ML016-ML051), 6 were dismissed following pathology reports that identified no HCC in the samples. Considering the remaining 29 biopsies, 8 biopsies yielded successful patient-derived lines capable of expansion and re-animation after cryopreservation: a success rate of 28%. The nomenclature assigned to these lines was ML018B, ML024, ML031, ML032, ML043, ML044, ML050 and ML051 (Figure 25). The remaining samples were discarded or dismissed due to a lack of cell proliferation or significant de-differentiation following the initial passages after digestion.

Patient-derived HCC spheroids were formed by seeding 20,000 primary cells per well in low-adhesion round-bottom 96-well plates. All primary lines formed compact spheroids with the exception of ML044 (Figure 25). ML032 formed a loose spheroid which could be transferred via pipette and formalin-fixed for histological staining, while ML044 cells did not form spheroids with the necessary integrity for transfer and fixation, and therefore could not be histologically assessed. H&E staining was performed on fixed spheroids, as well as immunohistochemical staining for CK18 to highlight that the cell lines are derived from hepatocytes, and αSMA to highlight the presence of fibroblasts (Figure 25). Information pertaining to the underlying liver aetiology and previous treatment strategies applied to the patients from which the HCC biopsies were obtained are detailed in Table 6.

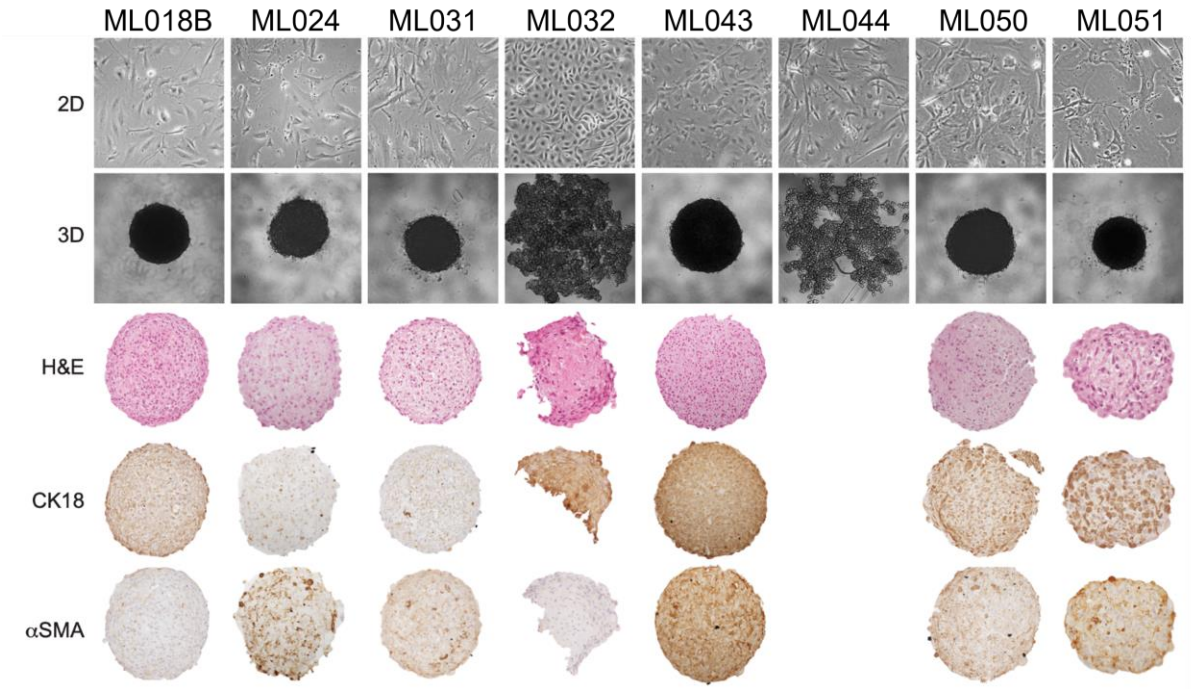

Figure 25. Generating a patient derived HCC cell line library. (A) Representative images of 8 HCC cell lines generated from patient biopsies, in 2D monolayer culture and 3D spheroid culture: ML018B, ML024, ML031, ML032, ML043, ML044, ML050 and ML051. Spheroids were H&E-stained and stained via immunocytochemistry for CK18 and αSMA. Cell populations displayed in this figure were isolated by Maja Laszczewska.

Table 6. Liver aetiology and therapeutic interventions received by HCC biopsy donors. The therapeutic interventions listed include those received by the donor both pre- and post-biopsy. BSC stands for best supportive care.

Primary cell line	Liver aetiology	Cirrhosis	Pre-biopsy therapy	Post-biopsy therapy
ML018B	No CLD	No	Resection	Ablation
ML024	MASLD/ALD	Yes	None	TACE, then sorafenib
ML031	MASLD/ALD	Yes	BSC	None
ML032	MASLD/ALD	Yes	None	Atezolizumab/bevacizumab
ML043	No CLD	No	None	Sorafenib
ML044	MASLD/ALD	Yes	None	Ablation
ML050	ALD	Yes	BSC	None
ML051	No CLD	No	None	Resection

9.2.2 Characterisation of patient-derived primary HCC cell lines

To develop the spheroid-PCLS model with patient-derived HCC cell lines, three of the eight primary lines were selected for further investigation due to the limited access to human liver,

since there would not be sufficient PCLS generation to implant all available cell lines. Compact spheroids were formed by ML018B, ML031 and ML043 (Figure 25), so these three cell lines were consequently selected since the spheroids would be easily transferrable. Immunofluorescence staining was performed to characterise the patient-derived HCC lines generated for the presence of classic HCC and hepatic biomarkers: AFP, GPC3, HepPar1 and CK18. As well as providing potential identifying markers for each of the cell lines, the staining provided potential therapeutic targets. Determining the expression of CK18 confirmed that the HCC cell lines originally derived from hepatocytes. Additionally, the cell lines were assessed for the expression of αSMA to evaluate the presence of stromal cells or cells undergoing EMT (Figure 26). The findings from this immunofluorescence staining are summarised in Table 7.

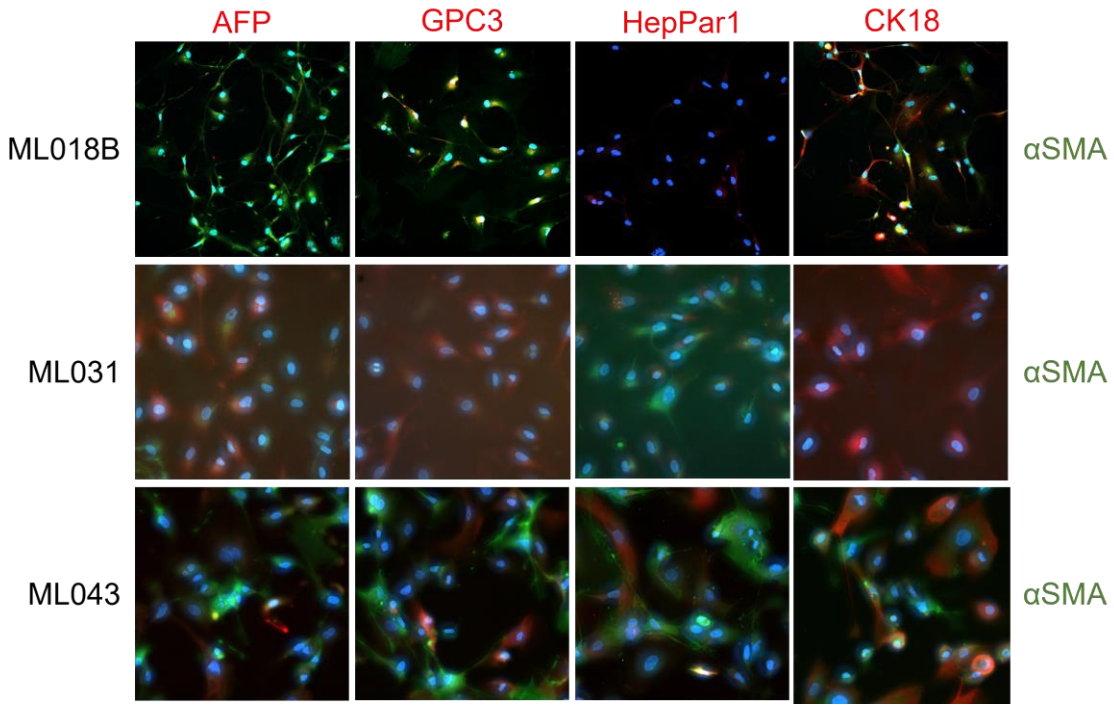

Figure 26. Characterisation of patient-derived primary HCC cell lines. Representative immunofluorescent images of the patient-derived HCC lines ML018B, ML031 and ML043 stained for the HCC and hepatic biomarkers AFP, GPC3, HepPar1 and CK18 (red). The cell lines were also stained for αSMA to assess the presence of stromal or mesenchymal cells (green).

Table 7. Characterisation of patient-derived primary HCC cell lines – expression of biomarkers. ML018B, ML031 and ML043 cells were assessed for their ability to express a number of biomarkers related to HCC (AFP, GPC3 and HepPar1) and hepatocytes (CK18). Expression of αSMA was also assessed to evaluate the presence of stromal or mesenchymal cells.

Primary cell line	AFP	GPC3	HepPar1	CK18	αSMA
ML018B	+ (weak)	+	+	+	+
ML031	+	+	+	+	+
ML043	+	+	+	+	+

9.2.3 Whole exome sequencing (WES) data for ML018B, ML031 and ML043

Whole exome sequencing (WES) was performed on the three cell lines selected for further model development – ML018B, ML031 and ML043. The 20 most commonly mutated genes in HCC were identified via the COSMIC database, and these genes were therefore interrogated to determine the number of single nucleotide variants (SNV) present in each cell line, alongside the type of mutation that had occurred (Figure 27A, D & G). Whilst similarities were observed in the mutated genes between ML018B, ML031 and ML043, each cell line possessed a unique mutational signature. The three cell lines displayed similar mutations in the commonly mutated genes TP53, ARID1A and AXIN1. However, the type of mutation responsible for the SNVs varied slightly, depending on whether the mutation was intronic, intergenic, upstream, downstream, UTR5, UTR3, a splice-site mutation, or another type of mutation. Of note, ML018B and ML031 displayed a number of SNVs in CTNNB1, whilst ML043 was completely absent for CTNNB1 mutations. The WES data was also interrogated to determine the percentage of mutations per chromosome (Figure 27B, E & H), and the base substitutions responsible for the SNVs (Figure 27C, F & I), whereby similar trends were observed for each cell line.

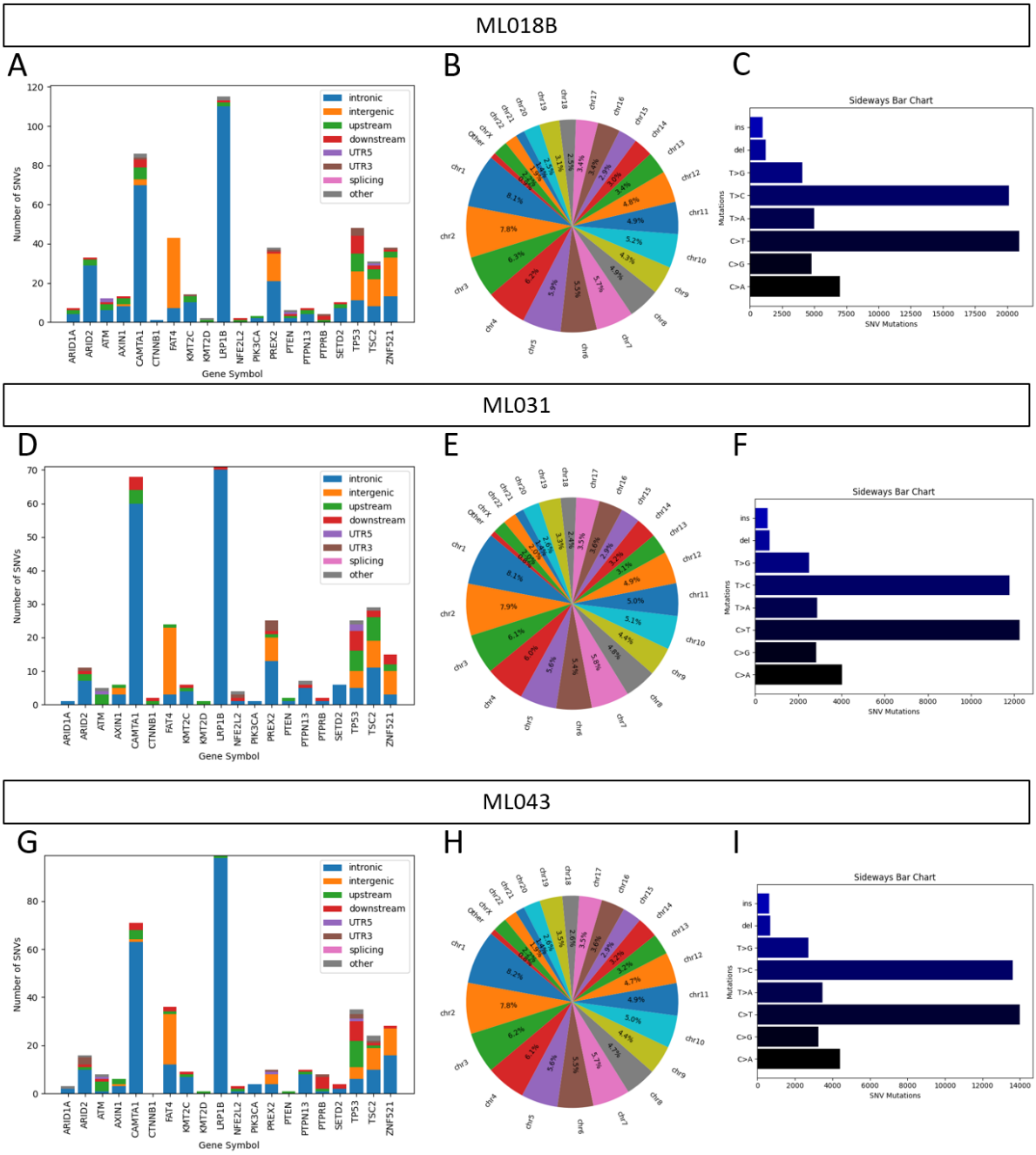

Figure 27. Whole exome sequencing (WES) data for ML018B, ML031 and ML043. WES data for (A-C) ML018B, (D-F) ML031 and (G-I) ML043 displaying type of mutation in the 20 most commonly mutated genes in HCC (D, E, F), percentage of mutations per chromosome (B, E, H) and base substitutions that occurred resulting in SNVs (C, F, I).

9.2.4 Responses of patient-derived primary HCC cell lines to first-line TKIs

Prior to implanting the patient-derived spheroids onto human PCLS, the response of ML018B, ML031 and ML043 to the first-line TKIs sorafenib and lenvatinib was assessed. The cells were seeded in 2D in a 96-well plate (10,000 cells per well) and cultured with a vehicle control, sorafenib (5 µM or 10 µM) or lenvatinib (0.1 µM or 0.63 µM) from day 1 to day 4, at which point a BrdU assay was performed to evaluate cellular proliferation levels (Figure 28A).

The level of BrdU incorporation in cells cultured with a vehicle control was measured to gauge the proliferative capacity of each cell line in comparison to each other. This determined that ML031 was the most proliferative of the three cell lines, while ML043 was the least proliferative (Figure 28B). In relation to sorafenib and lenvatinib, ML018B displayed reduced proliferation in response to 10 µM sorafenib (P<0.0001), 5 µM sorafenib (P<0.0001), 0.63 µM lenvatinib (P<0.0001) and 0.1 µM lenvatinib (P<0.0001) compared to the vehicle control treated group (Figure 28C). In contrast, ML031 did not exhibit a reduction in proliferation in response to the sorafenib or lenvatinib at any dose (Figure 28D). ML043 exhibited a reduction in proliferation in response to 10 µM sorafenib (P=0.0003), 5 µM sorafenib (P=0.0068), 0.63 µM lenvatinib (P=0.0005) and 0.1 µM lenvatinib (P=0.0005) compared to the vehicle control treated group (Figure 28E).

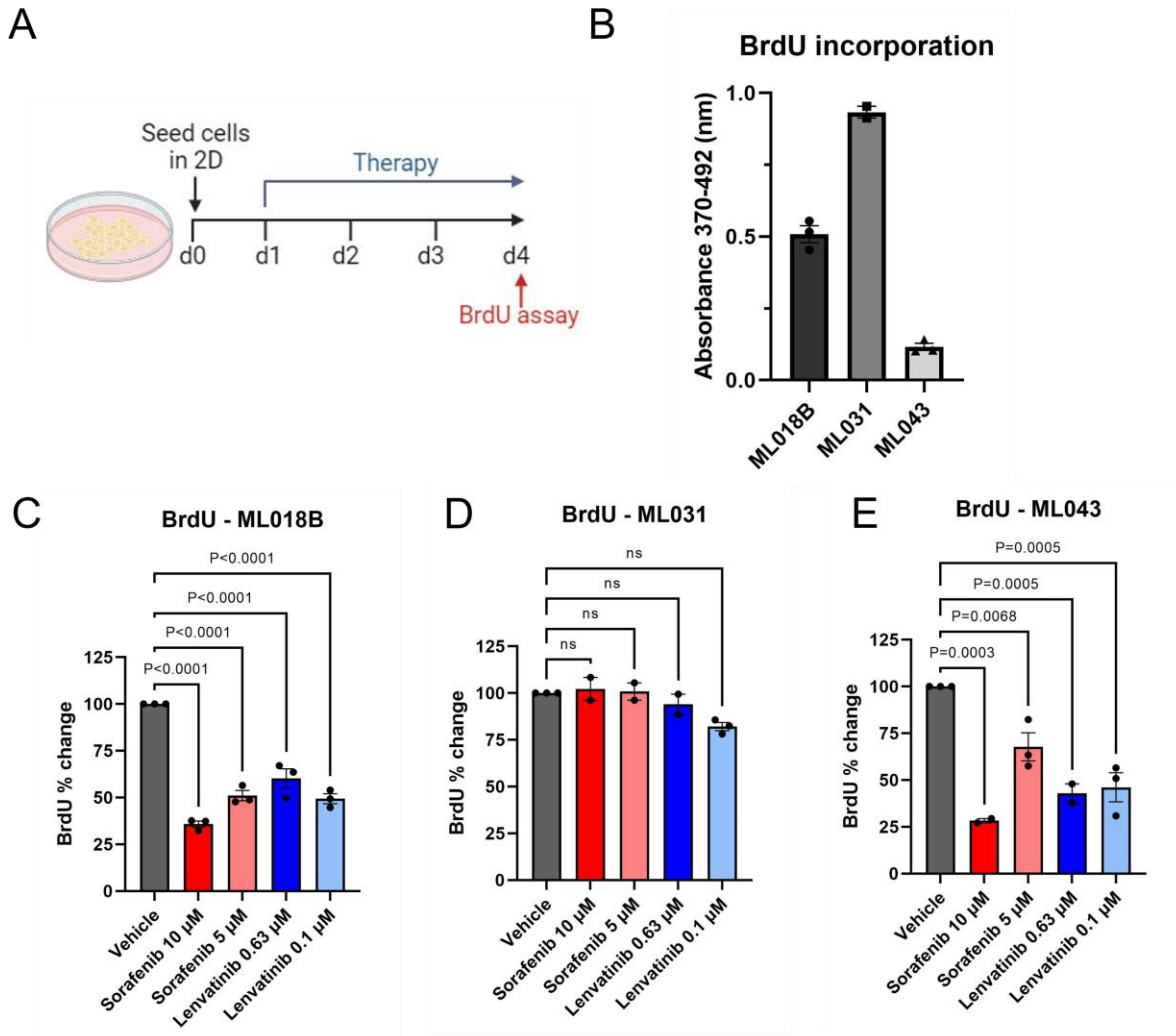

Figure 28. Response of patient-derived HCC cell lines to sorafenib and lenvatinib. (A) Schematic detailing the timeline of primary cell culture with a vehicle control, sorafenib (5 µM or 10 µM) or lenvatinib (0.1 µM or 0.63

μM), before a BrdU assay was performed to assess proliferation. (B) Graph showing BrdU incorporation in ML018B, ML031 and ML043. (C-E) Graphs showing percentage change in BrdU compared to the vehicle control in (C) ML018B, (D) ML031 and (E) ML043 cultured with sorafenib (5 μM or 10 μM) or lenvatinib (0.1 μM or 0.63 μM). Data are mean ± SEM for N = 3 wells.

9.2.5 Assessing the migratory potential of patient-derived HCC cell lines

An *in vitro* scratch assay was performed to analyse the migratory potential of the three patient-derived HCC cell lines selected for further model development: ML018B, ML031 and ML043. The cells were seeded into collagen-coated Incucyte Imagelock 96-well plates for 90% confluency the following day. To ensure that cell migration was the parameter assessed, the cells were treated with 4 μg/ml mitomycin c for 2 hours prior to scratch generation to prevent cellular proliferation. The mitomycin c was removed and a standardised scratch was generated in each well using the Sartorius wound generator. The cells were washed and cultured with their typical cell culture media, before being incubated in the Incucyte Live-Cell Analysis System with hourly imaging for 72 hours (Figure 29A).

The relative wound density was calculated using Incucyte 2022B Rev1 software for each of the 72 images generated per cell line, which refers to the ratio of the area occupied by cells in the scratch to the initial area of the scratch. This demonstrated that each of the cell lines exhibited a faster rate of wound healing and migration in the initial 20 hours, before wound healing slowed or plateaued. In the linear phase of “wound healing”, ML018B and ML043 behaved similarly and displayed faster rates of migration than ML031 cells. ML043 cells appeared to reach a maximum wound density of approximately 75% after 25 hours, while ML018B and ML031 cells reached a wound density of approximately 90% and 95% respectively after 72 hours, though these lines still appeared to exhibit migration at a slow rate at this timepoint (Figure 29B-C).

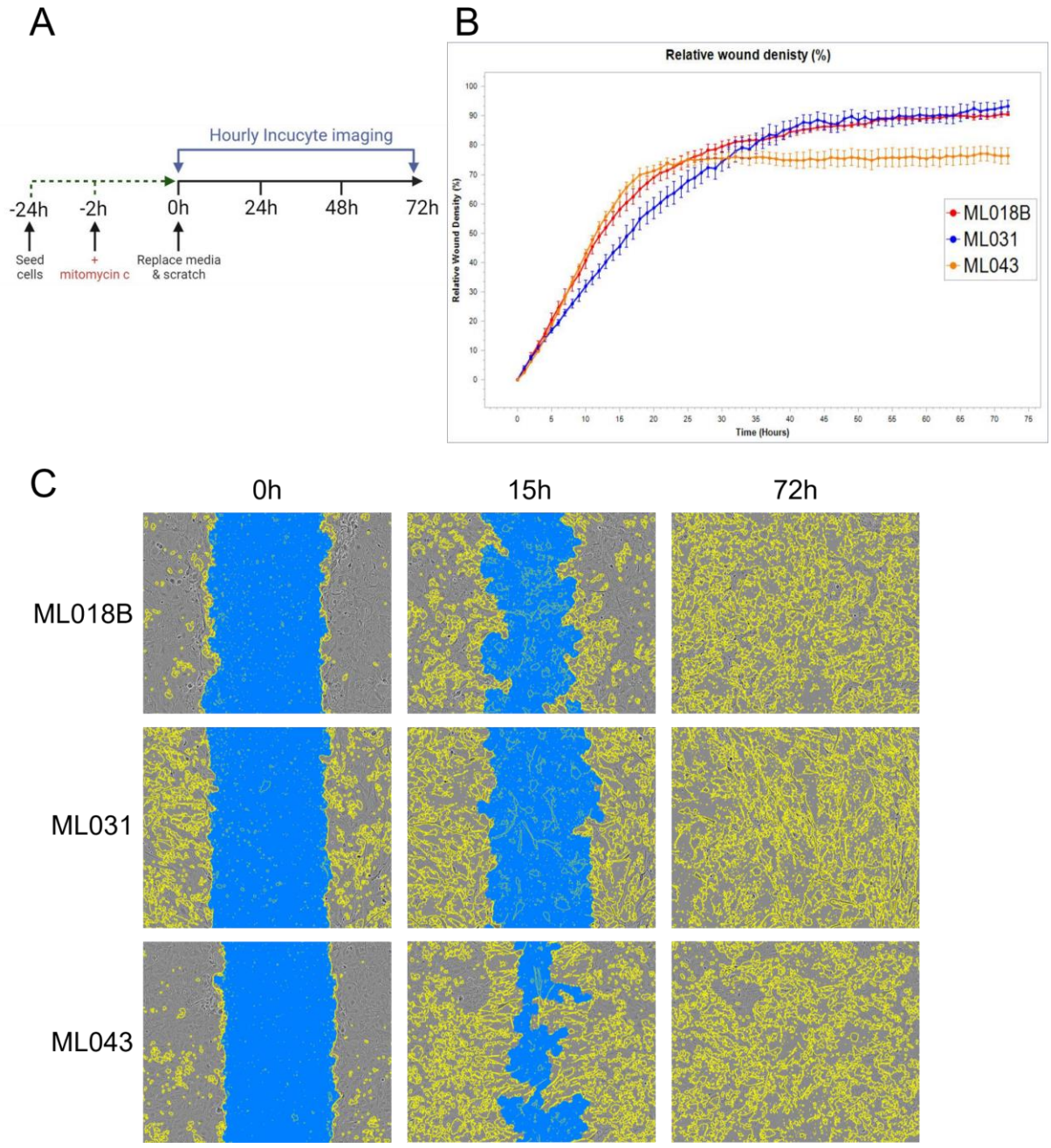

Figure 29. Assessing the migratory potential of patient-derived HCC cells. (A) Schematic detailing the timeline of a scratch assay on patient-derived HCC cell lines using Incucyte Live-Cell Analysis System. (B) Graph showing relative wound density from scratch assay performed on ML018B, ML031 and ML043 cells across 72 hours. Data are mean ± SEM for N = 6 repeats. (C) Representative images of ML018B, ML031 and ML043 cells from scratch assay taken by Incucyte Live-Cell Analysis System at 0, 15 and 72 hours, where blue repesents the generated scratch and yellow lines surround confluent areas.

9.2.6 Generating spheroids from patient-derived HCC cell lines

Prior to implanting the patient-derived spheroids onto human PCLS, the growth rate and metabolic activity of patient-derived spheroids alone in culture was assessed. Spheroids were

generated from 20,000 ML018B, ML031 or ML043 cells and cultured for 5 days; metabolic activity was assessed via resazurin assay at day 1 and day 5, and brightfield images of the spheroids were taken daily for volume measurements (Figure 30A). Spheroids generated from all three lines displayed a decrease in volume from day 1 to day 5; ML018B, ML031 and ML043 spheroids possessed volumes that were 53.7%, 49.0% and 27.5% of their original volume respectively at day 5 (Figure 30B). The spheroids created from all three lines appeared to be dense at day 1 and day 5, while the appearance of debris surrounding the spheroids suggests that there may have been cell death, particularly in relation to ML018B and ML043 (Figure 30C). Whilst it is difficult to determine whether the decrease in spheroid volume was due to the spheroids increasing in compactness or cell death, assessment of the metabolic activity of the spheroids via resazurin assay demonstrated that spheroids generated from all three cell lines displayed decreased metabolic function at day 5 compared to day 1 (Figure 30D).

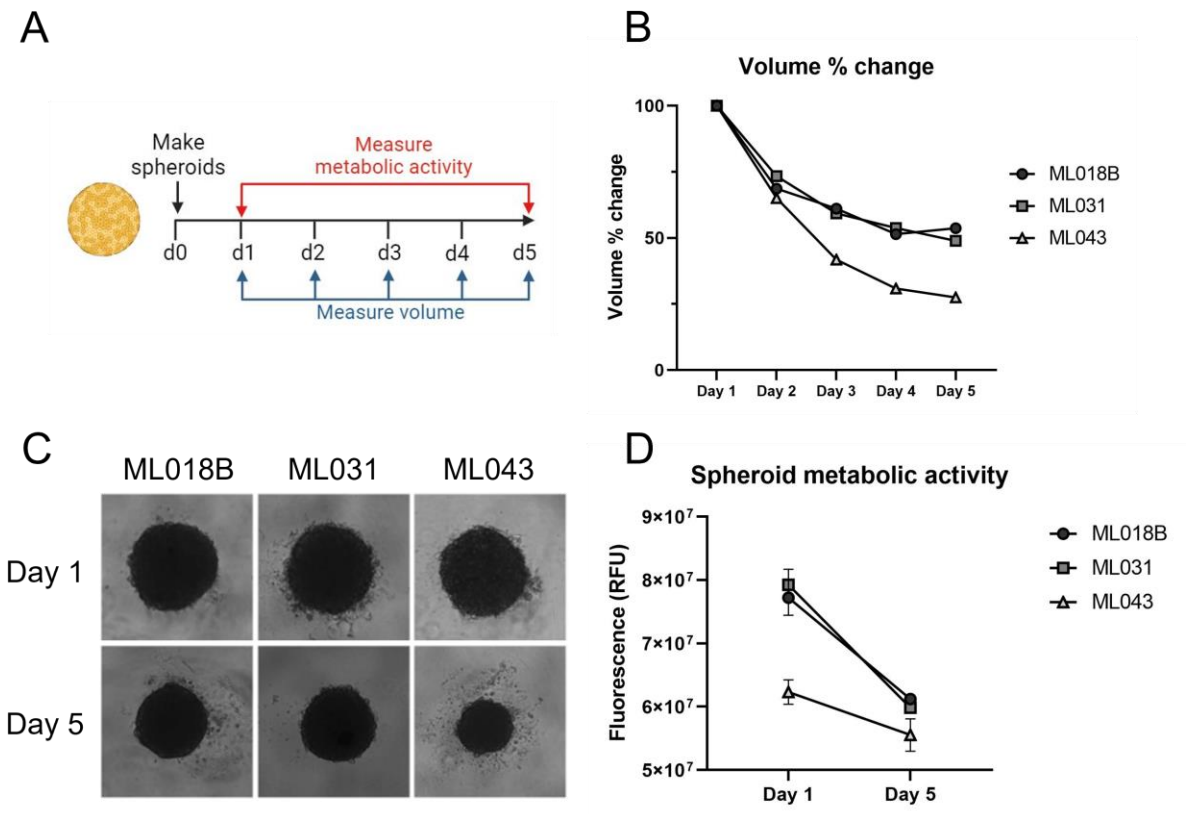

Figure 30. Generating spheroids from patient-derived HCC cells. (A) Schematic detailing the timeline of patient-derived spheroid generation and subsequent culture period of 5 days, with assessments of metabolic activity and spheroid volume. (B) Graph showing percentage change in volume of ML018B, ML031 and ML043 spheroids between day 1 and day 5. (C) Representative brightfield images of ML018B, ML031 and ML043 spheroids at day 1 and day 5. (D) Graph showing fluorescence values pertaining to metabolic activity from resazurin assay performed on ML018B, ML031 and ML043 spheroids at day 1 and day 5. Data are mean ± SEM for N = 4 spheroids.

9.2.7 Patient-derived HCC spheroids engraft on human PCLS

Spheroids generated from patient-derived HCC cells were implanted onto human PCLS to tailor to spheroid-PCLS model for utility in precision medicine. Initially, stable transfections were performed on the patient-derived HCC cell lines to induce the expression tdTomato or the NanoLuc secreted luciferase in the same manner as the immortalised cell lines HuH7 and Hep-53.4. However, this severely impacted the viability of the cells and the transfections were unsuccessful. Consequently, the patient-derived cells were transduced with a pLV[Exp]-mCherry:T2A:Puro-CMV>MetLuc lentivirus to induce the expression of the RFP mCherry and a secreted Metridia luciferase. Initial validation determined that once implanted onto PCLS, the relevant luciferase assay kit was not sensitive enough to detect the Metridia luciferase secreted from the patient-derived spheroids. The expressed mCherry was therefore used to both visualise the patient-derived cells and provide and end-point quantification of cell growth.

Spheroids were generated from 20,000 mCherry+ ML018B, ML031 and ML043 cells and PCLS were generated from human liver CRC metastases resections; the patient-derived spheroids were implanted onto PCLS at day 1 and cultured for a further 4 days with daily fluorescent imaging (Figure 31A). Human PCLS with implanted ML018B, ML031 or ML043 mCherry+ spheroids were imaged daily via brightfield and fluorescence microscopy, which demonstrated that spheroids generated from all three cell lines successfully engrafted on PCLS, remaining adhered to the same region of tissue throughout the culture period (Figure 31B). Spheroids from the three patient-derived HCC cell lines engrafted with a success rate of >90%.

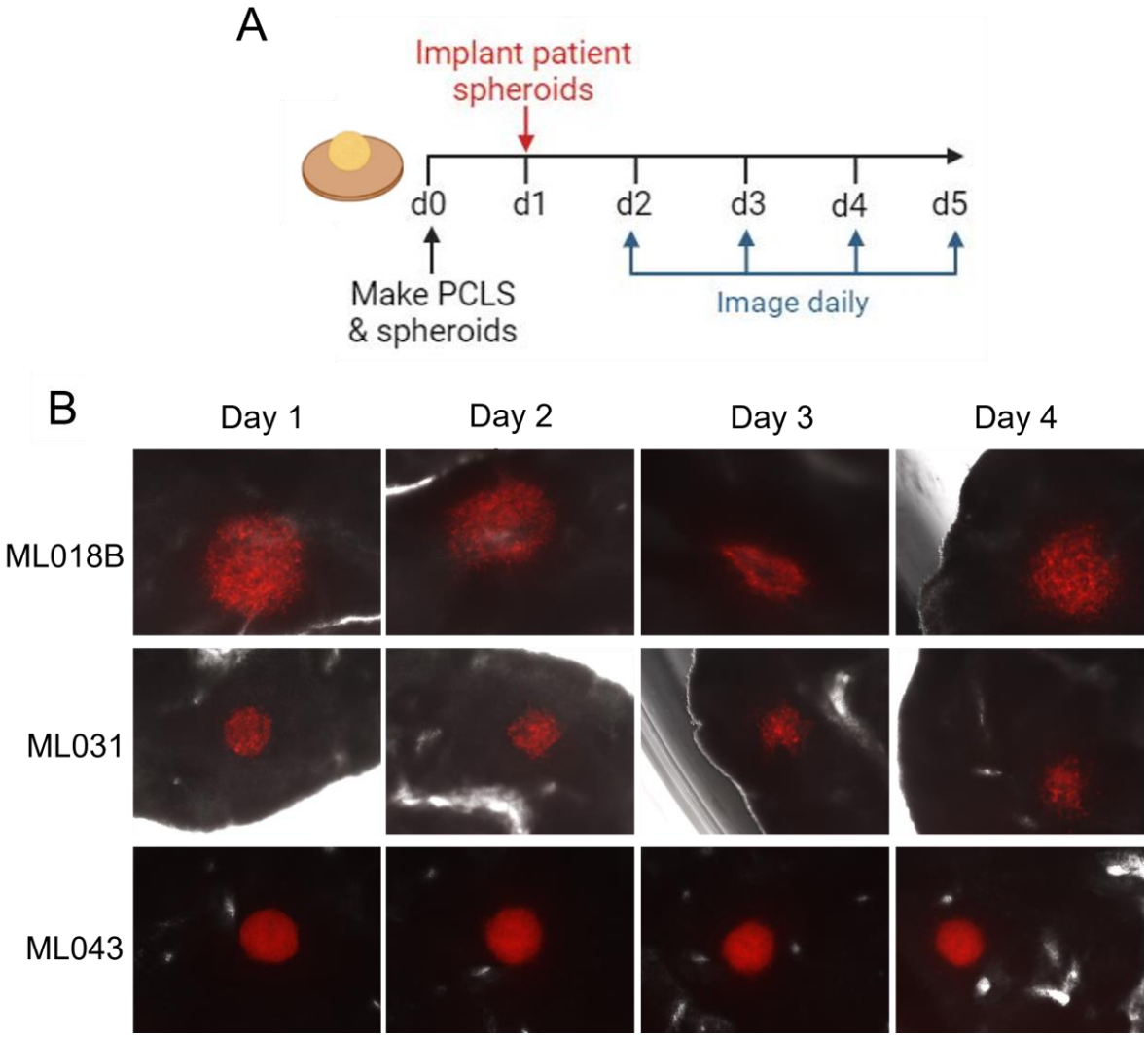

Figure 31. Patient-derived HCC spheroids engraft on human PCLS. (A) Schematic detailing the timeline of engrafting ML018B, ML031 and ML043 spheroids on human PCLS and subsequent culture period. (B) Representative brightfield and fluorescent images of ML018B, ML031 or ML043 spheroids (red, mCherry), engafted on human PCLS (black), across a 4 day period.

9.2.8 Patient-derived HCC spheroids invade human PCLS

With assistance from Dr Glyn Nelson in the Newcastle University Bioimaging Unit, multiphoton imaging was performed on PCLS engrafted with patient-derived spheroids to assess to level of HCC invasion in the liver tissue. PCLS were engrafted with mCherry+ spheroids generated from 20,000 ML018B, ML031 or ML043 cells at day 1 of the culture period, before z-stack images were generated from unpaired samples at day 2 and day 5 to investigate HCC invasion at 24- and 96-hours post spheroid implantation respectively (Figure 32).

In addition to tissue engraftment, all three patient-derived HCC cell lines displayed invasion into the PCLS at day 2, 24 hours after spheroid implantation. ML018B spheroids displayed a high level of invasion at day 2, with mCherry+ HCC cells visible throughout the z-plane of the PCLS. In contrast, ML031 and ML043 spheroids displayed a lower level of tissue invasion at day 2, with the implanted mCherry+ spheroid appearing to protrude from the top of the PCLS in the z-plane. However, a higher level of tissue invasion by ML031 and ML043 spheroids was observed at day 5, with the mCherry+ HCC cells more evenly dispersed throughout the z-plane of the PCLS. In addition to becoming embedded within the PCLS, HCC cells from all three patient-derived cell lines invaded the PCLS in the x- and y-planes, migrating past the spheroid margin into the surrounding liver tissue (Figure 32).

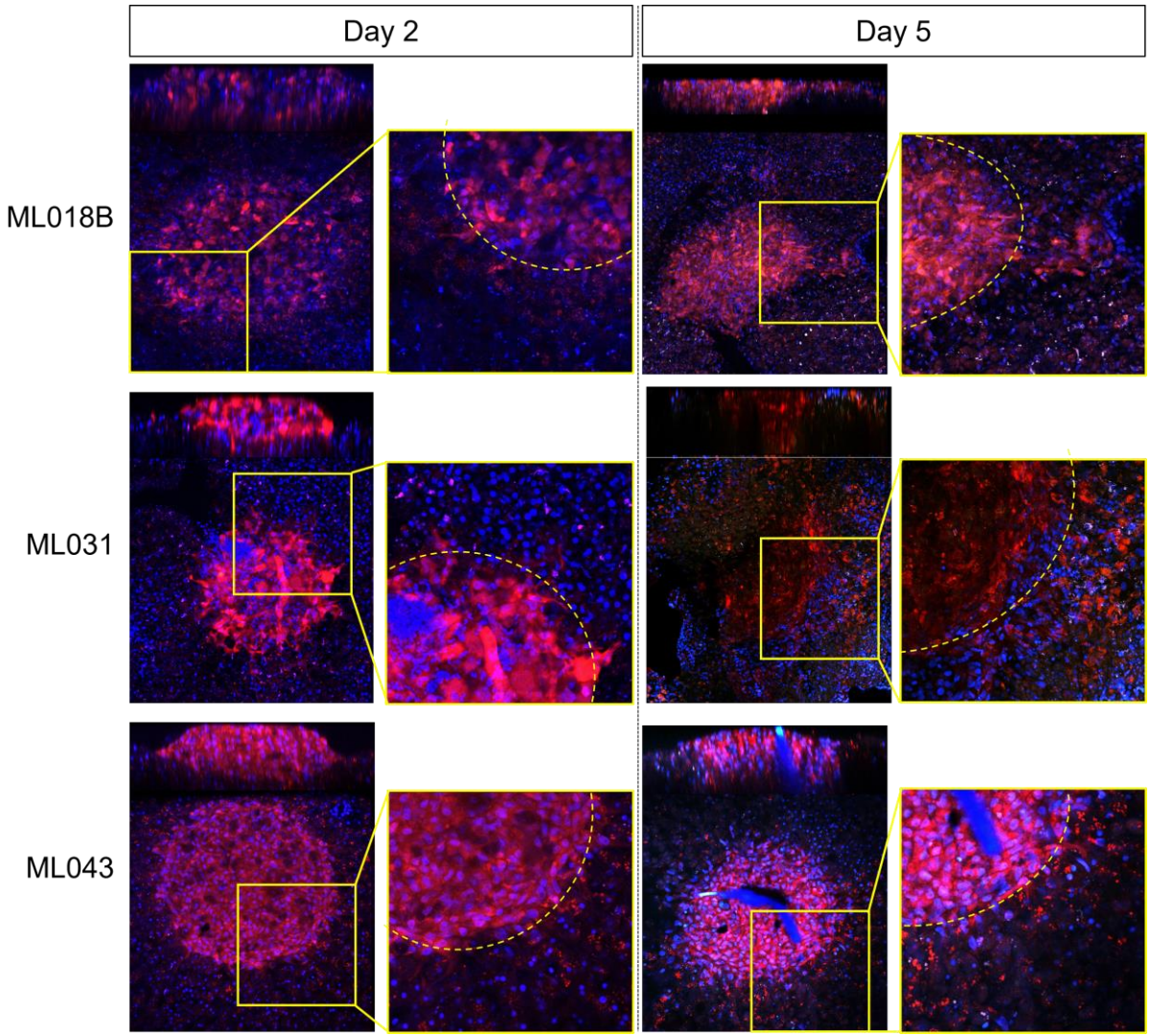

Figure 32. Patient-derived HCC spheroids invade human PCLS. Representative orthogonal view multiphoton images of mCherry+ ML018B, ML031 and ML043 spheroids (red, mCherry) invading human PCLS (blue, Hoechst) at day 2 (24 hours post spheroid implantation) and day 5 (96 hours post spheroid implantation). Yellow dotted line denotes spheroid margin.

9.2.9 Assessing the invasive potential of patient-derived HCC spheroids in human PCLS

The extent of HCC invasion into the surrounding PCLS was measured for ML018B, ML031 and ML043 spheroids. Not only could the invasive potential of the patient-derived HCC cell lines be assessed, but this data could be compared to the migration data obtained from the scratch assay to ascertain whether contributing factors from the PCLS affect the behaviour of HCC cells. The level of invasion was assessed in patient-derived spheroid-engrafted PCLS at day 2, or 24 hours after spheroid implantation. Fiji ImageJ image processing software was employed to generate compressed images of the patient-derived spheroid-PCLS from the z-stack images generated via multiphoton imaging. This enabled the visualisation of cells throughout the z-stack, as opposed to the top view alone. First, a circle was drawn at the spheroid margin, separating the implanted spheroid from the surrounding liver tissue. Straight lines were then drawn from the circle denoting the spheroid perimeter to the centre of any mCherry+ HCC cells visible in the surrounding liver tissue (Figure 33B). An important consideration was the separation of genuine HCC cells, which contained a nucleus, from the autofluorescence present in the liver which presented with a red speckled appearance.

The largest average invasion distance from the spheroid perimeter was observed by ML031 cells (195 µm), followed by ML018B cells (191 µm). ML043 cells displayed a smaller average invasion distance of 95 µm (Figure 33A). These findings contrasted with the migration data obtained from the scratch assay performed on the patient-derived HCC cell lines, which revealed ML031 to possess to lowest migratory potential. This suggests that factors present in the PCLS may communicate to influence the behaviour of the implanted HCC cells. Additionally, the drastic difference in stiffness between liver tissue (approximately 6-8 KPA) and plastic (in excess of 1000 Kpa) may contribute to the change in migration observed.

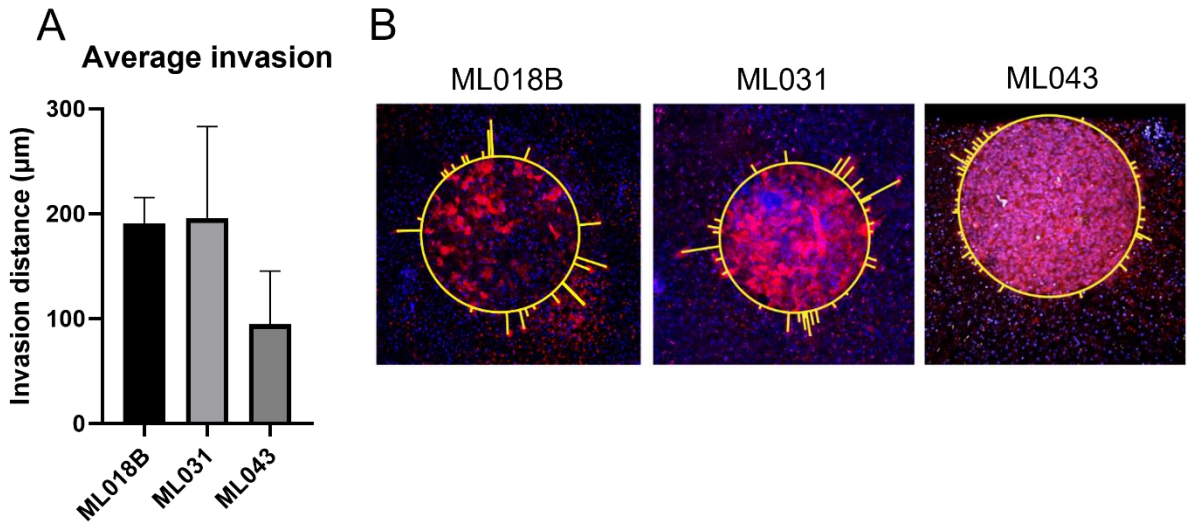

Figure 33. Assessing the invasive potential of patient-derived HCC spheroids. (A) Graph showing the average invasion distance of ML018B, ML031 and ML043 spheroids in PCLS. Data are mean ± SEM for up to N = 6 spheroid-PCLS. (B) Representative compressed multiphoton images of ML018B, ML031 or ML043 spheroids (red, mCherry) 24 hours after engraftment on human PCLS (blue, Hoechst), where yellow circles denote the spheroid margin and straight yellow lines denote distance from spheroid margin to invading HCC cells.

9.2.10 Assessing the growth of patient-derived HCC spheroids in human PCLS

Spheroids generated from ML018B, ML031 and ML043 cells did not display an increase in growth when cultured alone in a 96-well plate; all spheroids decreased in both volume and metabolic activity between day 1 and day 5. To investigate whether the same trend was observed in the patient-derived HCC spheroids engrafted on human PCLS, mCherry+ ML018B, ML031 or ML043 spheroids generated from 20,000 cells were implanted on human PCLS at day 1, before samples were harvested at day 2 and day 5 for mCherry quantification (Figure 34A).

ELISA quantification of mCherry in PCLS engrafted with patient-derived HCC spheroids determined that ML018B and ML043 spheroids displayed a 37% and 23% increase in mCherry respectively between day 2 and day 5, indicating that spheroids generated from these cell lines proliferated within the PCLS. In contrast, ML031 spheroids did not grow when engrafted on human PCLS, and displayed a 14% reduction in mCherry between day 2 and day 5 (Figure 34B). Focussing specifically on the mCherry concentration within spheroid-engrafted PCLS, an ML018B spheroid-PCLS contained an average of 67,797 pg/ml mCherry at day 2 and 92,939 pg/ml at day 5 (P=0.3448) (Figure 34C), ML031 spheroid-PCLS contained an average of 65,938

pg/ml mCherry at day 2 and 56,840 pg/ml at day 5 (Figure 34D), and ML043 spheroid-PCLS contained an average of 49,637 pg/ml mCherry at day 2 and 61,297 pg/ml at day 5 (P=0.2141) (Figure 34E).

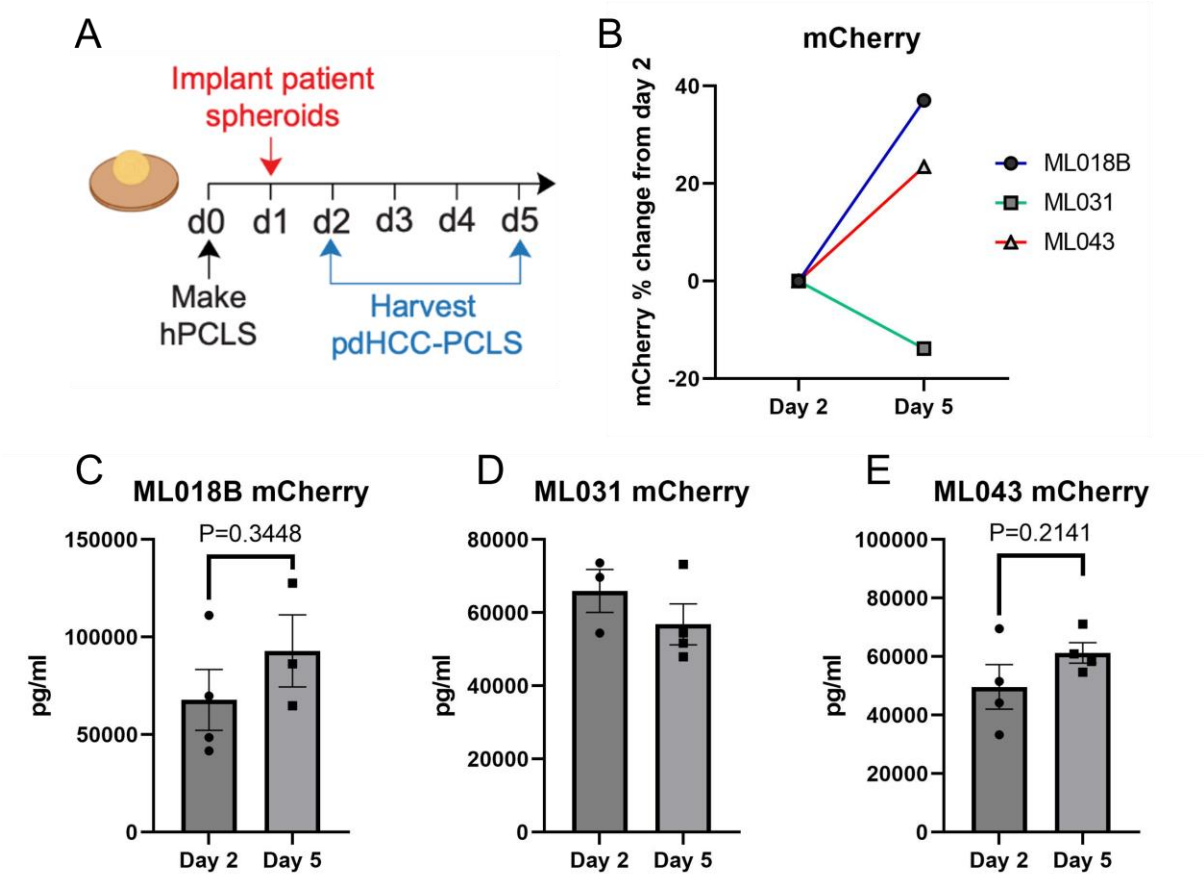

Figure 34. Assessing the growth of patient-derived HCC spheroids in human PCLS. (A) Schematic detailing the timeline of implanting patient-derived spheroids on human PCLS and subsequent harvest at day 2 and day 5 for mCherry quantification. (B) Graph showing percentage change in mCherry in PCLS engrafted with ML018B, ML031 or ML043 spheroids at day 2 and day 5. (C-E) Graphs showing mCherry concentration in PCLS engrafted with (C) ML018B, (D) ML031 or (E) ML043 spheroids at day 2 and day 5. Data are mean ± SEM for up to N = 4 spheroid-PCLS.

9.2.11 The therapeutic response of patient-derived HCC-PCLS to first-line TKIs

To determine whether patient-derived HCC spheroids engrafted on human PCLS responded to therapeutic intervention with the first-line TKIs sorafenib and lenvatinib, mCherry+ ML018B, ML031 or ML043 spheroids were generated from 20,000 cells and implanted on human PCLS at day 1; the spheroid-PCLS were cultured with a vehicle control, 10 µM sorafenib or 0.63 µM lenvatinib between day 2 and day 5, at which point the spheroid-PCLS were harvested for mCherry quantification (Figure 35A).

In relation to ML018B spheroid-PCLS, no reduction in mCherry concentration, and by extension HCC growth, was observed between the vehicle control and TKI-treated groups (Figure 35B). An unexpected increase in mCherry was observed in ML031 spheroid-PCLS treated with TKIs compared to the vehicle control samples, particularly in response to treatment with 0.63 µM lenvatinib (Figure 35C). Once implanted on human PCLS, ML031 spheroids appeared visibly smaller in size compared to ML018B and ML043 spheroids (Figure 31B), and it is therefore possible that the inconsistent mCherry values could be overcome by creating larger spheroids comprised of more than 20,000 cells. ML043 spheroid-PCLS displayed a trend towards a decrease in mCherry concentration following treatment with sorafenib and lenvatinib, though the data was not significant (Figure 35D). 2D culture of the patient-derived HCC cell lines with sorafenib and lenvatinib revealed that ML018B and ML043 cells displayed a significant reduction in proliferation in response to therapeutic intervention (Figure 28). The loss of this obvious therapeutic response in PCLS indicates that the surrounding liver tissue presents physical and chemical barriers which contribute to drug resistance, demonstrating that 2D drug responses do not necessarily translate in more physiologically accurate systems.

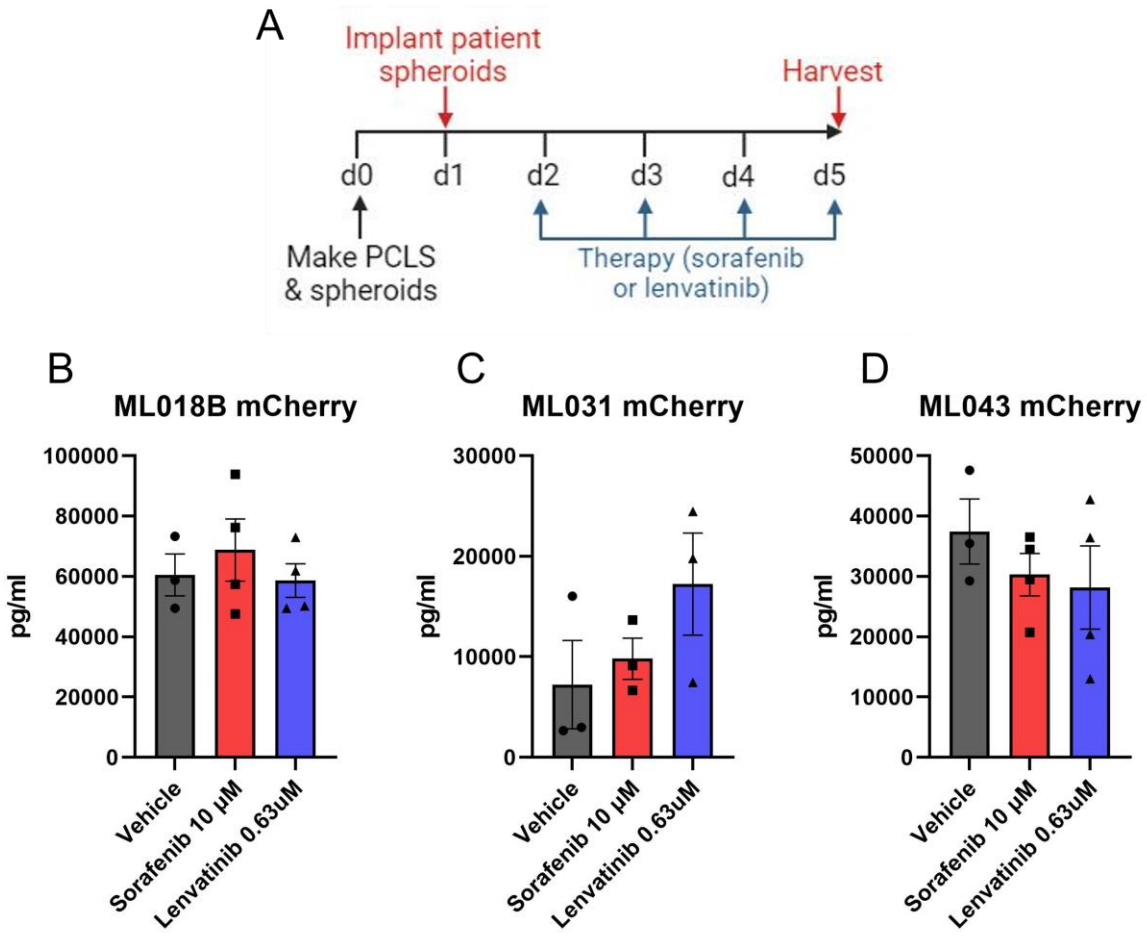

Figure 35. Therapeutic responses of patient-derived HCC spheroid-PCLS to first-line TKIs. (A) Schematic detailing the timeline of patient-derived spheroid implantation on human PCLS and subsequent culture period, including therapeutic intervention with a vehicle control, 10 µM sorafenib or 0.63 µM lenvatinib between day 2 and day 5. (B-D) Graphs showing mCherry concentration for (B) ML018B, (C) ML031 or (D) ML043 spheroid-PCLS harvested at day 5 following treatment with a vehicle control, 10 µM sorafenib or 0.63 µM lenvatinib. Data are mean ± SEM for up to N = 4 spheroid-PCLS.

9.2.12 Hyperion imaging mass cytometry characterisation of ML018B HCC-PCLS

Hyperion IMC characterisation of HuH7 spheroid-PCLS yielded a variety of information pertaining to the topography of the spheroid and surrounding liver tissue, as well as insight into the lymphoid and myeloid cellular components present in the tissue. The technique allowed a wide range of biomarkers to be probed for in just one 5 µm thick paraffinised tissue section, as opposed to classical IHC which would require multiple tissue sections. Limited tissue sections can be obtained via microtomy from a 250 µm thick PCLS, and this obstacle is overcome by employing Hyperion IMC. Additionally, information regarding the spatial configuration of multiple cell types and stromal components can be gained using this technology. Therefore, the patient-derived spheroid-PCLS samples were stained and ablated by Erik Ramon-Gil using the Hyperion Imaging System.

Investigation into a human PCLS from a CRC metastases resection engrafted with an ML018B spheroid determined that a low number of proliferative Ki67+ cells were present in the spheroid (Figure 36A). There was positivity for type I collagen and the type III intermediate filament protein vimentin in the spheroid, alongside CD31+ cells in both the spheroid and surrounding liver tissue, suggesting the potential occurrence of neoangiogenesis within the spheroid (Figure 36B). Regarding lymphocytes, CD8 and CD56 positivity was visible in both the spheroid and surrounding tissue and was accompanied by the presence of the serine protease granzyme B (Figure 36C). CD3 and CD4 T cells were present in low numbers: there was CD3 positivity inside the spheroid and in the surrounding tissue, while CD4+ cells appeared to be present in the surrounding tissue at the spheroid margin. The surrounding “peri-tumour” liver tissue expressed high levels of CD16 (Figure 36D). In relation to myeloid components, the spheroid expressed a high positivity for CD68 and the monocyte lineage marker CD163, indicating that there was a high influx of macrophages in response to the engrafted ML018B spheroid (Figure 36E). There was positivity for p21 in the spheroid indicating that the implanted HCC cells are in growth arrest and may have become senescent, a finding which is consistent with the lack of Ki67 positivity (Figure 36F), and PD-1 was expressed in low levels in and around the spheroid (Figure 36G). The expression of αSMA both within the spheroid and in the surround PCLS suggested that myofibroblasts were present throughout the sample (Figure 36H).

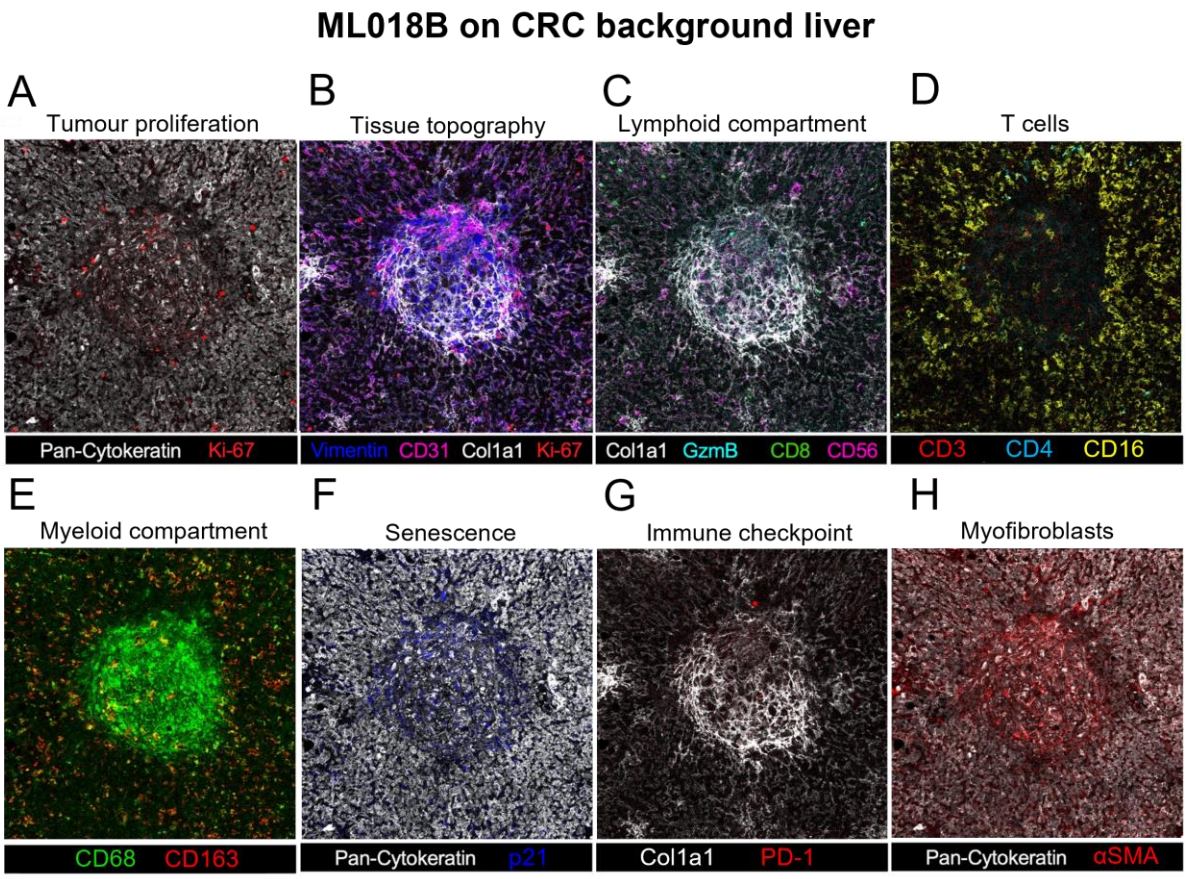

Figure 36. Hyperion IMC characterisation of ML018B spheroid-PCLS. Images obtained from Hyperion IMC performed on a human PCLS engrafted with a ML018B spheroid, showing (A) tumour proliferation, (B) tissue topography, (C) lymphoid components, (D) T cells, (E) myeloid components, (F) senescence, (G) the immune checkpoint PD-1, and (H) myofibroblasts. Sample was stained and ablated by Erik Ramon-Gil.

9.2.13 Hyperion imaging mass cytometry characterisation of ML043 HCC-PCLS

Hyperion IMC was employed once again to provide spatial characterisation of a human PCLS engrafted with a ML043 HCC spheroid. Half of the spheroid was ablated and is visible in the bottom half of the region of interest due to a large scratch present on the sample immediately below this area. The characteristics of the ML043 spheroid-PCLS were similar to the findings gained following ablation of a ML018B spheroid-PCLS. There were very few proliferative Ki-67+ cells in the ML043 spheroid and surrounding tissue (Figure 37A), while the spheroid displayed positivity for both vimentin and the endothelial marker CD31 (Figure 37B). CD56 and granzyme B was expressed in the tissue surrounding the ML043 spheroid, alongside positivity for CD8 both inside the spheroid and in the surrounding PCLS (Figure 37C). Further analysis of lymphoid cells determined that there was positivity for CD4 in the surrounding liver tissue, and a low number of CD3+ and CD16+ cells within the spheroid (Figure 37D). The spheroid displayed a high positivity for CD68, while CD163 was expressed both inside the spheroid and in the surrounding PCLS (Figure 37E). Expression of p21 in the spheroid suggested that the implanted ML043 spheroid contained senescent cells (Figure 37F), and there was no visible positivity for the immune checkpoint PD-1 (Figure 37G). αSMA expression was visible across the sample, both in the spheroid and in the surrounding tissue (Figure 37H).

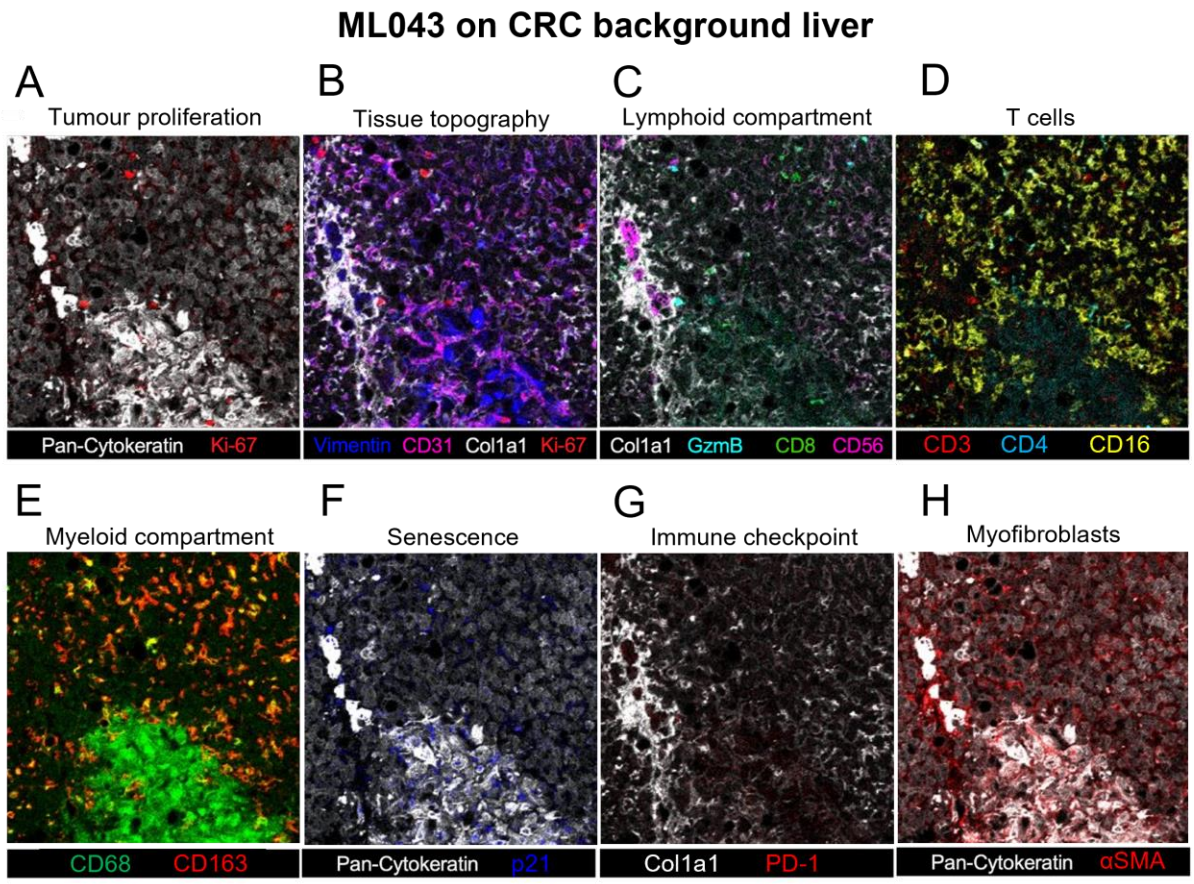

Figure 37. Hyperion IMC characterisation of ML043 spheroid-PCLS. Images obtained from Hyperion IMC performed on a human PCLS engrafted with a ML043 spheroid, showing (A) tumour proliferation, (B) tissue topography, (C) lymphoid components, (D) T cells, (E) myeloid components, (F) senescence, (G) the immune checkpoint PD-1, and (H) myofibroblasts. Sample was stained and ablated by Erik Ramon-Gil.

9.3 Results summary

Precision medicine enables specific treatment strategies to be tailored to individual patients according to the morphological, genetic, and cellular characteristics of their HCC. Through the generation of a patient-derived HCC cell line library there was potential to modify the spheroid-PCLS model previously developed with the immortalised cell line HuH7. The isolation and characterisation of cells derived from patient HCC biopsies yielded a total of 8 different patient-derived cell lines, possessing different expression profiles for typical HCC biomarkers and with differing spheroid-forming abilities.

Given the limited access to human liver tissue for PCLS generation, 3 of the patient-derived HCC cell lines were selected to further develop the spheroid-PCLS model. ML018B, ML031 and ML043 cells were selected due to their ability to form compact spheroids. Prior to combining the patient-derived HCC cell lines with PCLS to engineer the HCC tumour microenvironment, it was demonstrated that in 2D culture, ML018B and ML043 displayed significant reductions in proliferation in response to the TKIs sorafenib and lenvatinib, whilst ML031 did not respond to the therapies. A scratch assay performed on the three patient-derived HCC cell lines determined that ML031 cells possessed a higher migratory potential than ML018B and ML043. Spheroids generated from all three cell lines did not appear to grow in 96-well plates, exhibiting a decrease in volume and metabolic activity between day 1 and day 5.

To visualise the cells, ML018B, ML031 and ML043 cells were transduced with a lentivirus to express mCherry before they were implanted onto human PCLS. Multiphoton imaging confirmed that the implanted mCherry+ spheroids invaded the PCLS, both in terms of invading through the 250 µm thick PCLS and by migrating outwards into the tissue beyond the initial spheroid margin. The level of invasion into the PCLS contrasted with the migration data obtained from the scratch assay on 2D cells, implying that certain components in the PCLS may influence the behaviour of the implanted patient-derived spheroids. Unlike the 2D cultures of ML018B and ML043 cells, patient-derived spheroid-PCLS displayed no response to the TKIs sorafenib and lenvatinib, indicating that the spheroid-PCLS model exhibits an increased therapeutic resistance compared to 2D cells which do not reflect *in vivo* disease.

Hyperion IMC was employed to characterise PCLS engrafted with patient-derived HCC spheroids generated from ML018B or ML043 cells. This technique ascertained that the

implanted spheroids displayed little to no proliferation and had become senescent. Interestingly, there was a high positivity for the endothelial cell marker CD31 within the spheroids, suggesting that neoangiogenesis potentially occurred. Additionally, the implanted spheroids displayed positivity for CD68, as well as CD8 and CD3 in lower levels. Evidence that the spheroid-PCLS model contains an interactive system whereby the tumour microenvironment reacts to invading HCC cells demonstrates that it is a unique 3D tool for HCC modelling.

9.4 Discussion

An emerging approach in the treatment of cancer is precision medicine, which considers the specific genetic and cellular components of an individual patients' tumour, in addition to lifestyle factors and comorbidities which may contribute to tumorigenesis. Treatment approaches can be tailored to individuals according to the oncogenic drivers and immune landscape of the tumour (389). In HCC alterations in the CTNNB1 gene encoding β-catenin are typically associated with a suppressed immune landscape with limited numbers of infiltrating T cells, and typical immunotherapeutic approaches that target T cells in the TME are therefore ineffective (78, 84). HCC biopsies enable a patient's cells to be isolated and exploited in various models of HCC, providing an understanding of the tumour composition and most appropriate therapy for the specific patient. After generation of a spheroid-engrafted PCLS model using the HuH7 cell line, patient-derived HCC cell lines were isolated and subsequently implanted onto human PCLS in spheroid form. The isolated patient-derived lines were grown as mixed populations of cells to better reflect highly heterogeneous HCC tumours. Initially, transfections were performed on the isolated cell lines to induce expression of either tdTomato or the secreted NanoLuc luciferase, in line with the HuH7 cells used in the earlier development of the model. Three separate transfection kits, one specifically targeted at primary cells, resulted in complete cell death. Consequently, the cell lines were transduced with a lentivirus to induce the expression of the RFP mCherry.

Prior to the generation of a patient-derived HCC cell line library, the HCC biopsies obtained were digested and used to form HCC organoids. HCC organoids generated from primary liver cancer cells have been previously described, retaining the structure, genomic landscape and gene expression of the original tumours. This has enabled both the identification of biomarkers and therapeutic screening (390). Although the utility of HCC organoids has been proven in xenograft studies, indicating that organoids may be successfully implanted onto tissue such as a PCLS, cell line generation was ultimately selected as an alternative to organoid generation. This was due to the low success rate of organoid generation, whilst cell line generation maximised the use of the HCC biopsies acquired. Additionally, cell lines enabled high numbers of standardised spheroids to be generated for subsequent tissue implantation – an important consideration in the development of a reliable drug screening platform. Whilst a number of the isolated patient-derived cell lines appeared to rapidly undergo partial

epithelial to mesenchymal transition (EMT) and dedifferentiated, to express both epithelial and mesenchymal markers, others maintained the original epithelial phenotype throughout numerous passages. Three patient-derived HCC cell lines were selected for initial model development due to the limited access to human liver tissue for PCLS generation. The cell lines ML018B, ML031 and ML043 were selected after demonstrating that they form compact spheroids capable of maintaining their integrity when transferred and processed.

Spheroids generated from the three selected patient-derived cell lines displayed a decrease in volume when cultured in a 96-well plate for 5 days. Typically, these observations could potentially be attributed to an increase in compactness of the spheroids. However, the spheroids displayed a compact appearance at the beginning of the culture period, and the volume data was accompanied by resazurin data revealing that the metabolic activity of the spheroids also decreased over time, indicating that the patient-derived spheroids were displaying a decrease in proliferation and metabolic activity. In contrast, mCherry quantification demonstrated that once implanted onto human PCLS, the levels of patient-derived HCC cells present in the tissue remained stable or displayed a slight, albeit non-significant, increase in growth. Growth factors present in the PCLS, such as HGF and FGF, may act as mitogens encouraging growth of the patient-derived HCC lines (391). Moreover, the presence of cytokine-secreting immune cells in the surrounding liver tissue may promote proliferation and inhibit apoptosis of HCC cells (70, 392). Another consideration is that cells in the centre of a spheroid typically become necrotic as the access to oxygen and nutrients are limited (393), whereas cells within a HCC spheroid implanted onto a PCLS are able to invade and migrate into the tissue enabling them to better access nutrients.

The invasive potential of engrafted patient-derived HCC spheroids was assessed by measuring the distance of migrated HCC cells in PCLS from the spheroid margin. To distinguish invading mCherry HCC cells from the autofluorescence visible in the liver tissue, HCC cells were identified by their large nuclei which was in contrast to both the autofluorescence and surrounding hepatocytes. Spheroids generated from ML043 cells displayed a lower level of invasion into the PCLS compared to those generated from ML018B and ML031 cells. It was observed that ML043 spheroids were more compact in appearance, and therefore the low level of invasion could be due to the strong aggregation of the HCC cells prior to implantation on the PCLS. In accordance with this, z-stack images generated via multiphoton microscopy

demonstrated that 24 hours after spheroid implantation ML043 spheroids appeared to protrude from the top of the PCLS, whereas ML018B spheroids displayed complete invasion throughout the 250 μm PCLS at this timepoint. A scratch assay was performed on ML018B, ML031 and ML043 cells cultured in 2D to assess the migratory potential of the cells. This demonstrated that in the linear wound closing phase ML018B and ML043 cells displayed similar rates of migration, although ML043 cells did not achieve the same relative wound density as ML018B suggesting that in 2D, ML043 will not reach the same level of confluency. Interestingly, ML031 displayed the slowest migration, taking longer in time to plateau in relation to relative wound density compared to both ML018B and ML043 cells. This contrasts with the findings that ML031 HCC cells display the highest invasion in PCLS, indicating that factors present in the surrounding liver tissue may influence the behaviour of the implanted HCC cells. These findings reiterate that the behaviour of cells in 2D is not reflective of how 3D cells and tissues interact, further emphasising the requirement for improved HCC models.

The response of the patient-derived HCC cell lines to the TKIs sorafenib and lenvatinib differs between 2D cultured cells and 3D spheroid-engrafted PCLS. Whilst ML018B and ML043 cells demonstrated a significant reduction in proliferation in response to the therapies, this therapeutic response was lost when they were treated in the form of HCC spheroids implanted on PCLS. This is another example of how the behaviour and therapeutic response of 2D cells does not translate to 3D models and by extension human disease. Increased mCherry levels are observed in ML031 spheroid-PCLS in response to sorafenib and lenvatinib compared to the vehicle treated samples. An explanation for this unexpected finding is that the ML031 spheroids implanted in this experiment were much smaller in appearance compared to ML018B and ML043 spheroids, and spheroids generated from a greater number of cells may result in ML031 spheroids of a more reliable and consistent size. As described in Table 6, the three patients from which the ML018B, ML031 and ML043 biopsies were obtained received no treatment with TKIs or immunotherapy prior to the biopsy procedure. The cells obtained from these biopsies were therefore not subjected to targeting or manipulation by HCC therapies prior to their *in vitro* cell culture. Interestingly, the patient from which ML043 was obtained received treatment with sorafenib following the biopsy. It would be fascinating to determine how efficacious treatment with sorafenib was for this patient, given that ML043

cells responded significantly to sorafenib when in 2D culture, but not when incorporated into the 3D spheroid-PCLS model.

Whole exome sequencing (WES) was performed on ML018B, ML031 and ML043 to determine the mutational signatures of each of the cell lines, with a specific focus on the 20 most commonly mutated genes in HCC as identified by the COSMIC database. Although trends were observed in the chromosomal locations and types of mutations present, the mutational signature for each of the lines was unique, and it is this heterogeneity that may explain the difference in behaviour observed relating to proliferation, invasion and therapeutic response. The sequencing data may provide a method of selecting certain cell lines according to the desired characteristics of a study. For example, ML043 displayed no mutations in CTNNB1 and may therefore prove useful if modelling wild type β-catenin HCC. The knowledge that the patient-derived HCC cells are mixed populations rather than clonal, alongside the heterogeneity highlighted by the WES data suggests that “cell lines” may be an inaccurate term for their description, and “cell populations” may be more apt.

The treatment of advanced HCC with immunotherapies is an increasingly prevalent therapeutic approach. To enable the patient-derived spheroid-PCLS model to be utilised to test the efficacy of therapies such as anti-PD1 and anti-PDL1 on specific patient spheroids it would require T cells to be isolated from the same donor that the HCC biopsy was obtained from in order for self-recognition of MHC molecules to occur. This would be logistically difficult given that the appropriate ethical approval is currently not in place, in addition to the length of time it would take to isolate, expand and transduce the patient-derived HCC cell lines. Akin to the HuH7 spheroid-PCLS model, interrogating patient-derived spheroid-PCLS with CAR-T cells will provide an alternative route to test immunotherapies. The use of allogenic CAR-T cells circumvents the use of matched HCC and T cells, and would require the use of appropriate CAR-T cells with a specificity for a HCC biomarker expressed by the cell line in question (377).

Characterisation of two PCLS engrafted with either a ML018B or ML043 spheroid was performed via Hyperion IMC. Both of these samples were harvested 4 days after spheroid implantation so represent a late stage of the culture period. The ML043 spheroid-PCLS sample only displays half of the spheroid as the sample was scratched just below this ROI. Although Ki-67 positivity is visible in the samples and is largely confined to the spheroids, the level of

proliferative cells is low compared to the HuH7 spheroid-PCLS ablated previously that were also harvested at day 4. This coincides with the expression of p21 in the spheroids, suggesting that the HCC cells were in growth arrest or had become senescent at this time point and is an explanation for why they were no longer proliferative. Analysis of samples at earlier timepoints may provide insight into whether the implanted HCC cells were initially more proliferative and at which point the cells displayed a more senescent phenotype. The spheroids displayed expression of collagen type 1, alongside positivity for αSMA. Since the patient-derived HCC cell lines were mixed populations of cells, many of which expressed the mesenchymal markers αSMA or vimentin, the likelihood is this collagen was produced by mesenchymal cells in the original spheroid. A number of immune cell markers are visualised in the spheroids, including CD8, CD56, CD3 and CD163. Most notably, the spheroids appeared to be highly infiltrated by CD68+ macrophages. Macrophages have previously been identified to prevent T cell infiltration by inducing fibrosis and promote angiogenesis and cancer cell invasion (394, 395). Thus, inhibiting macrophage activity may exert a therapeutic effect in the spheroid-PCLS model. Moreover, the checkpoint molecule CD47 interacts with SIRPα on macrophages, and previous studies have shown its inhibition to result in macrophage-mediated destruction of cancer cells (396). The expression of CD31 was visible alongside vimentin in the spheroids, suggesting the possible occurrence of neoangiogenesis in the spheroids. Vimentin has previously been shown to be implicated in angiogenesis (381), leading to the hypothesis that blocking vimentin activity in this model will reduce the expression of the endothelial marker CD31 and potentially impact HCC growth. Analysis at earlier timepoints would again provide insight into the rate of migration of various immune populations into the spheroid, alongside the formation of endothelial markers. Live cell imaging may offer a superior method of visualising these changes.

Difficulties encountered when creating the patient-derived spheroid-PCLS HCC include complications in successfully generating HCC cell lines from all biopsies obtained. In the circumstance that this model was to be exploited for precision medicine, obtaining larger HCC biopsies from the patients may increase the chances of successful cell line generation for each individual patient. Similarly, a number of isolated cell lines did not successfully form spheroids which could be transferred and fixed for analysis. This difficulty should be overcome if the platform is to be offered as a precision medicine platform, whether different methods of

spheroid generation or different cell culture conditions are the answer. An alternative use of the isolated patient-derived cell lines would be to generate xenograft models in humanised mice, providing an insight into the behaviour and therapeutic response of patient-specific HCC cells in the context of a whole physiological system. Samples of the patient-derived HCC cell lines employed thus far have been sent for whole exome sequencing (WES), and this information will provide an awareness of how differing cell lines can be applied to study HCC in the context of various mutations. The use of a secreted luciferase provided a unique tool to monitor HCC growth in the HuH7 spheroid-PCLS model. The lentivirus employed here to transduce the patient-derived HCC cells induced the dual-expression of mCherry and a secreted Metridia luciferase. Although the secreted Metridia luciferase could be detected in smaller media volumes, the relevant luciferase assay kit was unfortunately unable to detect the levels of luciferase secreted by the HCC spheroids in the 3 ml volume of culture media in the bioreactor plates. A number of luciferase assay kits were employed in an attempt to overcome this. Moving forward, we could engraft more HCC cells onto tissue slices in a 12-well plate system (standard model) or scale the model to a 96 well format to increase the cell to media ratio. Further development may require the design of a custom-made lentivirus that incorporates a reporter for the brighter NanoLuc luciferase, which could subsequently be detected in the required larger media volume in the 12-well bioreactor plates.

10 General discussion

Liver cancer is the third most common cause of cancer-related mortality worldwide, and HCC accounts for the majority of primary liver cancer cases. HCC is typically diagnosed when the disease is at the advanced stages, at which point the treatment options are limited to systemic therapies that do not offer the hope of survival beyond a small number of months (397). There is therefore an urgent need for novel anticancer agents for the treatment of advanced HCC, which requires realistic HCC models to enable preclinical therapeutic responses to translate to human disease in a clinical setting. The development of multiple *ex vivo* HCC models using precision-cut tissue slices as the basis enables the HCC TME to be modelled and provides utility as a potential therapeutic screening platform. Additionally, the retention of many TME features present the models as tools to aid the understanding of HCC pathogenesis.

Table 8. Advantages and disadvantages of the HCC models developed.

Model	Advantages	Disadvantages
In vivo **orthotopic Hep-53.4 model**	▪ Enables whole physiological system and infiltrating immune cells to be represented ▪ Allows response to immunotherapeutic agents to be investigated ▪ Allows manipulation to recreate states of underlying liver disease ▪ Generates large, fast-growing tumours with infiltrating immune cells	▪ Does not represent human biology ▪ Involves surgical procedure to be performed by fully trained and competent persons ▪ Requires large numbers of mice undergoing moderate severity procedures ▪ High costs
Ex vivo **murine PCTS model**	▪ Accounts for the tumour and a variety of TME components ▪ Allows response to immunotherapeutic agents to be investigated ▪ Allows manipulation to recreate states of underlying liver disease ▪ Enables multiple treatment arms to be tested in tissue from one mouse – fewer mice utilised ▪ More cost efficient than *in vivo* experiments	▪ Does not represent human biology ▪ Limitation presented by viability of *ex vivo* tissue compared to life span of mouse ▪ Involves surgical procedure to be performed by fully trained and competent persons ▪ Does not consider whole physiological system and infiltrating immune cells
HuH7 spheroid-PCLS model	▪ Utilises human tissue and cells ▪ Accounts for HCC and surrounding TME ▪ Allows manipulation to recreate states of underlying liver disease ▪ Model can be modified to include different cell lines	▪ Relies on availability of viable human liver tissue ▪ Limitation presented by viability timeline of *ex vivo* tissue ▪ Cell lines represent homogenous population of cells not reflective of real tumours – will not provide utility for precision medicine

	▪ Allows therapeutic response to small molecule inhibitors and potentially CAR therapies to be investigated ▪ Simple method of spheroid engraftment ▪ Includes SecLuc output	▪ Inability to screen T cell immunotherapies due to unpaired HCC cell lines and liver tissue ▪ Does not represent whole physiological human system
Patient-derived spheroid-PCLS model	▪ Most physiologically relevant model ▪ Cell isolation from patient biopsies yields heterogeneous cell populations more reflective of HCC tumours ▪ Accounts for HCC and surrounding TME ▪ Allows manipulation to recreate states of underlying liver disease ▪ Identification of most suitable therapy for each patient-derived cell population (precision medicine) ▪ Simple method of spheroid engraftment	▪ Relies on availability of viable human liver tissue ▪ Limitation presented by viability timeline of *ex vivo* tissue ▪ Difficulty generating sufficient cells and spheroids from all HCC biopsies obtained ▪ Model does not include SecLuc output for longitudinal tracking ▪ Inability to screen T cell immunotherapies due to unpaired HCC cell lines and liver tissue ▪ Does not represent whole physiological human system

A limitation of the project was the access to resected human liver tissue for PCLS generation at the start of the project. The project began in September 2020 and although the access to the laboratory was only partially impacted by the COVID-19 pandemic at this point, the schedule of liver resections was limited due to the postponement of many surgeries. Future developments for the spheroid-PCLS model would be to develop a breadth of models using a range of cell lines to provide comparisons between different phenotypes and genetic alterations in HCC. Likewise, the formation of multicellular tumour spheroids (MCTS) containing a multitude of cell types, such as CAFs and immune cells, would provide a higher resemblance to heterogeneous tumours and implanting MCTS onto human PCLS may further improve the physiologic aspect of the model. Demonstrating that PCLS can be manipulated to display various phenotypes of liver disease and investigating whether this impacts HCC growth or therapeutic response was another experimental idea that given more time I would have been keen to pursue.

The primary limitation of both the PCTS and spheroid-PCLS models is that the *ex vivo* culture of tissue does not represent a whole physiological organism. Despite precision cut tissue slices retaining the structural architecture and function of *in situ* tissue (340, 362), they do not consider *in vivo* effects that would typically be exerted from outside of the liver. Although many important immune components are retained in PCTS and PCLS, the model does not account for the continual supply of lymphocytes and myeloid cells that infiltrate the liver and

progress through phases of maturation as they travel from the bone marrow and blood into the liver (398, 399). There is increasing evidence describing neutrophils as key mediators in the progression of HCC (165); unfortunately, due to the short lifespan of neutrophils the cell type is not retained in PCLS and PCTS beyond the initial 24 hours. It is possible to repeatedly supplement the tissue culture system with isolated human or murine neutrophils, though this is an artificial compromise whereby the number and the activity of the neutrophils that successfully infiltrate the tissue slices may not be typical of *in situ* liver tissue. PCLS viability can be maintained for approximately one week in the rocked bioreactor system, while investigations are ongoing to decipher how long PCTS remain viable in either rocked or static culture. Culture periods of approximately 4 to 5 days were utilised here to demonstrate therapeutic responses in PCTS and spheroid-PCLS after application of TKIs and immunotherapy to the culture system. However, if a longer period of time was required to induce a disease phenotype in the tissue before screening a novel therapy, the viability of the tissue would be a limiting factor. *Ex vivo* precision-cut tissue slice models may reduce the financial costs and ethical implications of animal use, either through the use of human tissue or by enabling multiple treatment strategies to be tested in the tissue from one animal. It may be the case that these *ex vivo* systems are utilised to initially prove hypotheses prior to confirming the findings in a whole physiological system, therefore reducing the number of animals used.

In a similar manner to spheroid implantation on PCLS, the implantation of HCC organoids onto liver tissue may provide an alternative technique to model HCC in the context of the TME. Organoid generation yielded a number of difficulties, and spheroid generation was therefore focussed on during this project. However, further development of the model could involve determining whether an organoid-engrafted PCLS model provides a more physiologically realistic system that the spheroid-PCLS model. Similarly, 3D bioprinting of HCC cells onto PCLS is an exciting prospect which considers the important ECM components in HCC. The design of disease-specific hydrogels reflects the mechanical and biochemical characteristics of the native ECM, whilst HCC cells can be bioprinted alongside relevant cell types and growth factors in bioinks to recreate the TME (400, 401). Although it has not been described here, ReJI bioprinting has been utilised to print Hep-53.4 cells and 3T3 fibroblasts onto murine PCLS. This has demonstrated that bioprinted Hep-53.4 cells are capable of invading PCLS – activity which

is further promoted by the presence of fibroblasts. A miniature version of the ReJI bioprinting system is currently under construction and will enable the bioprinting of human cells onto human PCLS inside a laminar flow hood. At present, this is not possible as the current ReJI bioprinter is an open system in a common user lab which isn't set up for the use of primary human tissue.

Live imaging would elevate both the PCTS and the spheroid-PCLS models by providing a real-time understanding of how the components in the tissue migrate and interact. Dr Leo Carlin at The Beatson Institute in Glasgow has applied live cell imaging to successfully visualise the migration of leukocytes through the lung vasculature, and further work involves collaborating to appreciate how the TME components behave in *ex vivo* precision-cut tissue slices.

Finally, the utility of the models developed here is not restricted solely to HCC. Both PCTS and spheroid-engrafted tissue slices have the potential to model various other solid tumours; for example, colorectal cancer, lung cancer, melanoma and pancreatic cancer. In addition to PCLS, the Newcastle Fibrosis Research Group regularly generates precision-cut slices from kidney and lung tissue, and has collaborated with other teams to produce tissue slices from brain, pancreatic and prostate tissue. The HCC models generated here may provide a transferrable basis to screen therapies and further understand the pathogenesis of alternative diseases.

11 References

1. Llovet JM, Zucman-Rossi J, Pikarsky E, Sangro B, Schwartz M, Sherman M, et al. Hepatocellular carcinoma. Nature Reviews Disease Primers. 2016;2(1):16018.
2. Sung H, Ferlay J, Siegel RL, Laversanne M, Soerjomataram I, Jemal A, et al. Global Cancer Statistics 2020: GLOBOCAN Estimates of Incidence and Mortality Worldwide for 36 Cancers in 185 Countries. CA: A Cancer Journal for Clinicians. 2021;71(3):209-49.
3. Vogel A, Meyer T, Sapisochin G, Salem R, Saborowski A. Hepatocellular carcinoma. The Lancet. 2022;400(10360):1345-62.
4. Akinyemiju T, Abera S, Ahmed M, Alam N, Alemayohu MA, Allen C, et al. The Burden of Primary Liver Cancer and Underlying Etiologies From 1990 to 2015 at the Global, Regional, and National Level: Results From the Global Burden of Disease Study 2015. JAMA Oncol. 2017;3(12):1683-91.
5. Siegel RL, Miller KD, Fuchs HE, Jemal A. Cancer statistics, 2022. CA: A Cancer Journal for Clinicians. 2022;72(1):7-33.
6. Villanueva A, Llovet JM. Targeted Therapies for Hepatocellular Carcinoma. Gastroenterology. 2011;140(5):1410-26.
7. Petrick JL, Florio AA, Znaor A, Ruggieri D, Laversanne M, Alvarez CS, et al. International trends in hepatocellular carcinoma incidence, 1978–2012. International Journal of Cancer. 2020;147(2):317-30.
8. Forner A, Llovet JM, Bruix J. Hepatocellular carcinoma. The Lancet. 2012;379(9822):1245-55.
9. Rinella ME, Lazarus JV, Ratziu V, Francque SM, Sanyal AJ, Kanwal F, et al. A multi-society Delphi consensus statement on new fatty liver disease nomenclature. Journal of Hepatology. 2023.
10. Tilg H, Effenberger M. From NAFLD to MAFLD: when pathophysiology succeeds. Nature Reviews Gastroenterology & Hepatology. 2020;17(7):387-8.
11. El-Serag HB. Epidemiology of Viral Hepatitis and Hepatocellular Carcinoma. Gastroenterology. 2012;142(6):1264-73.e1.
12. Chen CJ, Yang HI, Su J, Jen CL, You SL, Lu SN, et al. Risk of hepatocellular carcinoma across a biological gradient of serum hepatitis B virus DNA level. Jama. 2006;295(1):65-73.
13. Dave S, Park S, Murad MH, Barnard A, Prokop L, Adams LA, et al. Comparative Effectiveness of Entecavir Versus Tenofovir for Preventing Hepatocellular Carcinoma in Patients with Chronic Hepatitis B: A Systematic Review and Meta-Analysis. Hepatology. 2021;73(1):68-78.
14. Kanwal F, Kramer JR, Asch SM, Cao Y, Li L, El-Serag HB. Long-Term Risk of Hepatocellular Carcinoma in HCV Patients Treated With Direct Acting Antiviral Agents. Hepatology. 2020;71(1):44-55.
15. Chiang C-J, Yang Y-W, You S-L, Lai M-S, Chen C-J. Thirty-Year Outcomes of the National Hepatitis B Immunization Program in Taiwan. JAMA. 2013;310(9):974-6.
16. Younossi Z, Anstee QM, Marietti M, Hardy T, Henry L, Eslam M, et al. Global burden of NAFLD and NASH: trends, predictions, risk factors and prevention. Nature Reviews Gastroenterology & Hepatology. 2018;15(1):11-20.

17. Marquardt JU, Galle PR, Teufel A. Molecular diagnosis and therapy of hepatocellular carcinoma (HCC): An emerging field for advanced technologies. Journal of Hepatology. 2012;56(1):267-75.
18. Gellert-Kristensen H, Richardson TG, Davey Smith G, Nordestgaard BG, Tybjærg-Hansen A, Stender S. Combined Effect of PNPLA3, TM6SF2, and HSD17B13 Variants on Risk of Cirrhosis and Hepatocellular Carcinoma in the General Population. Hepatology. 2020;72(3).
19. Stickel F, Buch S, Nischalke HD, Weiss KH, Gotthardt D, Fischer J, et al. Genetic variants in PNPLA3 and TM6SF2 predispose to the development of hepatocellular carcinoma in individuals with alcohol-related cirrhosis. Am J Gastroenterol. 2018;113(10):1475-83.
20. Abul-Husn NS, Cheng X, Li AH, Xin Y, Schurmann C, Stevis P, et al. A Protein-Truncating HSD17B13 Variant and Protection from Chronic Liver Disease. New England Journal of Medicine. 2018;378(12):1096-106.
21. Shibata T. Genomic landscape of hepatocarcinogenesis. Journal of Human Genetics. 2021;66(9):845-51.
22. Yoo JJ, Park MY, Cho EJ, Yu SJ, Kim SG, Kim YJ, et al. Smoking Increases the Risk of Hepatocellular Carcinoma and Cardiovascular Disease in Patients with Metabolic-Associated Fatty Liver Disease. J Clin Med. 2023;12(9).
23. Huang DQ, Mathurin P, Cortez-Pinto H, Loomba R. Global epidemiology of alcohol-associated cirrhosis and HCC: trends, projections and risk factors. Nature Reviews Gastroenterology & Hepatology. 2023;20(1):37-49.
24. Ganne-Carrié N, Nahon P. Hepatocellular carcinoma in the setting of alcohol-related liver disease. J Hepatol. 2019;70(2):284-93.
25. Toh MR, Wong EYT, Wong SH, Ng AWT, Loo LH, Chow PK, et al. Global Epidemiology and Genetics of Hepatocellular Carcinoma. Gastroenterology. 2023;164(5):766-82.
26. Renehan AG, Tyson M, Egger M, Heller RF, Zwahlen M. Body-mass index and incidence of cancer: a systematic review and meta-analysis of prospective observational studies. Lancet. 2008;371(9612):569-78.
27. Estes C, Razavi H, Loomba R, Younossi Z, Sanyal AJ. Modeling the epidemic of nonalcoholic fatty liver disease demonstrates an exponential increase in burden of disease. Hepatology. 2018;67(1):123-33.
28. Yang JD, Hainaut P, Gores GJ, Amadou A, Plymoth A, Roberts LR. A global view of hepatocellular carcinoma: trends, risk, prevention and management. Nature Reviews Gastroenterology & Hepatology. 2019;16(10):589-604.
29. Liao S-H, Chen C-L, Hsu C-Y, Chien K-L, Kao J-H, Chen P-J, et al. Long-term effectiveness of population-wide multifaceted interventions for hepatocellular carcinoma in Taiwan. Journal of Hepatology. 2021;75(1):132-41.
30. van der Meer AJ, Veldt BJ, Feld JJ, Wedemeyer H, Dufour J-F, Lammert F, et al. Association Between Sustained Virological Response and All-Cause Mortality Among Patients With Chronic Hepatitis C and Advanced Hepatic Fibrosis. JAMA. 2012;308(24):2584-93.
31. Janjua NZ, Chong M, Kuo M, Woods R, Wong J, Yoshida EM, et al. Long-term effect of sustained virological response on hepatocellular carcinoma in patients with hepatitis C in Canada. J Hepatol. 2017;66(3):504-13.
32. Lazarus JV, Mark HE, Anstee QM, Arab JP, Batterham RL, Castera L, et al. Advancing the global public health agenda for NAFLD: a consensus statement. Nature Reviews Gastroenterology & Hepatology. 2022;19(1):60-78.

33. Simon TG, Duberg A-S, Aleman S, Chung RT, Chan AT, Ludvigsson JF. Association of Aspirin with Hepatocellular Carcinoma and Liver-Related Mortality. New England Journal of Medicine. 2020;382(11):1018-28.
34. Singh S, Singh PP, Singh AG, Murad MH, Sanchez W. Statins Are Associated With a Reduced Risk of Hepatocellular Cancer: A Systematic Review and Meta-analysis. Gastroenterology. 2013;144(2):323-32.
35. Hsiao-Ping C, Jeng-Jer S, Chia-Che C, Tzu-Ting C, Jaw-Town L, Ming-Shiang W, et al. Metformin decreases hepatocellular carcinoma risk in a dose-dependent manner: population-based and in vitro studies. Gut. 2013;62(4):606.
36. Zhang B, Yang B. Combined α fetoprotein testing and ultrasonography as a screening test for primary liver cancer. Journal of Medical Screening. 1999;6(2):108-10.
37. SINGAL A, VOLK ML, WALJEE A, SALGIA R, HIGGINS P, ROGERS MAM, et al. Meta-analysis: surveillance with ultrasound for early-stage hepatocellular carcinoma in patients with cirrhosis. Alimentary Pharmacology & Therapeutics. 2009;30(1):37-47.
38. EASL Clinical Practice Guidelines: Management of hepatocellular carcinoma. J Hepatol. 2018;69(1):182-236.
39. Vogel A, Cervantes A, Chau I, Daniele B, Llovet JM, Meyer T, et al. Hepatocellular carcinoma: ESMO Clinical Practice Guidelines for diagnosis, treatment and follow-up††FootnotesApproved by the ESMO Guidelines Committee: August 2018. Annals of Oncology. 2018;29:iv238-iv55.
40. Llovet JM, Montal R, Sia D, Finn RS. Molecular therapies and precision medicine for hepatocellular carcinoma. Nature Reviews Clinical Oncology. 2018;15(10):599-616.
41. Cabillic F, Corlu A. Regulation of Transdifferentiation and Retrodifferentiation by Inflammatory Cytokines in Hepatocellular Carcinoma. Gastroenterology. 2016;151(4):607-15.
42. Kim Y-Y, Kim M-J, Kim EH, Roh YH, An C. Hepatocellular Carcinoma versus Other Hepatic Malignancy in Cirrhosis: Performance of LI-RADS Version 2018. Radiology. 2019;291(1):72-80.
43. Schulze K, Nault JC, Villanueva A. Genetic profiling of hepatocellular carcinoma using next-generation sequencing. J Hepatol. 2016;65(5):1031-42.
44. Ogunwobi OO, Harricharran T, Huaman J, Galuza A, Odumuwagun O, Tan Y, et al. Mechanisms of hepatocellular carcinoma progression. World journal of gastroenterology. 2019;25(19):2279-93.
45. Villanueva A. Hepatocellular Carcinoma. New England Journal of Medicine. 2019;380(15):1450-62.
46. Torrecilla S, Sia D, Harrington AN, Zhang Z, Cabellos L, Cornella H, et al. Trunk mutational events present minimal intra- and inter-tumoral heterogeneity in hepatocellular carcinoma. Journal of Hepatology. 2017;67(6):1222-31.
47. Geh D, Anstee QM, Reeves HL. NAFLD-Associated HCC: Progress and Opportunities. J Hepatocell Carcinoma. 2021;8:223-39.
48. Lieber CS, Rubin E, DeCarli LM. Hepatic microsomal ethanol oxidizing system (MEOS): Differentiation from alcohol dehydrogenase and NADPH oxidase. Biochemical and Biophysical Research Communications. 1970;40(4):858-65.
49. Seitz HK, Stickel F. Molecular mechanisms of alcohol-mediated carcinogenesis. Nature Reviews Cancer. 2007;7(8):599-612.

50. Chiba T, Marusawa H, Ushijima T. Inflammation-Associated Cancer Development in Digestive Organs: Mechanisms and Roles for Genetic and Epigenetic Modulation. Gastroenterology. 2012;143(3):550-63.
51. Hernandez-Meza G, von Felden J, Gonzalez-Kozlova EE, Garcia-Lezana T, Peix J, Portela A, et al. DNA Methylation Profiling of Human Hepatocarcinogenesis. Hepatology. 2021;74(1):183-99.
52. Um TH, Kim H, Oh BK, Kim MS, Kim KS, Jung G, et al. Aberrant CpG island hypermethylation in dysplastic nodules and early HCC of hepatitis B virus-related human multistep hepatocarcinogenesis. J Hepatol. 2011;54(5):939-47.
53. Gazelakis K, Majeed A, Kemp W, Di Muzio B, Gerstenmaier J, Cheung W, et al. Liver disease severity predicts carcinogenesis of dysplastic liver nodules in cirrhosis. Scientific Reports. 2021;11(1):20954.
54. Zucman-Rossi J, Villanueva A, Nault J-C, Llovet JM. Genetic Landscape and Biomarkers of Hepatocellular Carcinoma. Gastroenterology. 2015;149(5):1226-39.e4.
55. Craig AJ, von Felden J, Garcia-Lezana T, Sarcognato S, Villanueva A. Tumour evolution in hepatocellular carcinoma. Nature Reviews Gastroenterology & Hepatology. 2020;17(3):139-52.
56. Nault JC, Bioulac–Sage P, Zucman–Rossi J. Hepatocellular Benign Tumors—From Molecular Classification to Personalized Clinical Care. Gastroenterology. 2013;144(5):888-902.
57. Micchelli STL, Vivekanandan P, Boitnott JK, Pawlik TM, Choti MA, Torbenson M. Malignant transformation of hepatic adenomas. Modern Pathology. 2008;21(4):491-7.
58. Margolskee E, Bao F, de Gonzalez AK, Moreira RK, Lagana S, Sireci AN, et al. Hepatocellular adenoma classification: a comparative evaluation of immunohistochemistry and targeted mutational analysis. Diagnostic Pathology. 2016;11(1):27.
59. Bluteau O, Jeannot E, Bioulac-Sage P, Marqués JM, Blanc J-F, Bui H, et al. Bi-allelic inactivation of TCF1 in hepatic adenomas. Nature Genetics. 2002;32(2):312-5.
60. Nahon P, Zucman-Rossi J. Single nucleotide polymorphisms and risk of hepatocellular carcinoma in cirrhosis. Journal of Hepatology. 2012;57(3):663-74.
61. Wang Y, Kato N, Hoshida Y, Yoshida H, Taniguchi H, Goto T, et al. Interleukin-1β gene polymorphisms associated with hepatocellular carcinoma in hepatitis C virus infection. Hepatology. 2003;37(1):65-71.
62. Nahon P, Sutton A, Rufat P, Ziol M, Akouche H, Laguillier C, et al. Myeloperoxidase and superoxide dismutase 2 polymorphisms comodulate the risk of hepatocellular carcinoma and death in alcoholic cirrhosis. Hepatology. 2009;50(5):1484-93.
63. Yuan J-M, Lu SC, Van Den Berg D, Govindarajan S, Zhang Z-Q, Mato JM, et al. Genetic polymorphisms in the methylenetetrahydrofolate reductase and thymidylate synthase genes and risk of hepatocellular carcinoma. Hepatology. 2007;46(3):749-58.
64. Yoon YJ, Chang HY, Ahn SH, Kim JK, Park YK, Kang DR, et al. MDM2 and p53 polymorphisms are associated with the development of hepatocellular carcinoma in patients with chronic hepatitis B virus infection. Carcinogenesis. 2008;29(6):1192-6.
65. Villanueva A, Hoshida Y, Battiston C, Tovar V, Sia D, Alsinet C, et al. Combining clinical, pathology, and gene expression data to predict recurrence of hepatocellular carcinoma. Gastroenterology. 2011;140(5):1501-12.e2.
66. Llovet JM, Pinyol R, Kelley RK, El-Khoueiry A, Reeves HL, Wang XW, et al. Molecular pathogenesis and systemic therapies for hepatocellular carcinoma. Nature Cancer. 2022;3(4):386-401.

67. Schulze K, Imbeaud S, Letouzé E, Alexandrov LB, Calderaro J, Rebouissou S, et al. Exome sequencing of hepatocellular carcinomas identifies new mutational signatures and potential therapeutic targets. Nature Genetics. 2015;47(5):505-11.
68. Nault JC, Mallet M, Pilati C, Calderaro J, Bioulac-Sage P, Laurent C, et al. High frequency of telomerase reverse-transcriptase promoter somatic mutations in hepatocellular carcinoma and preneoplastic lesions. Nature Communications. 2013;4(1):2218.
69. Cancer Genome Atlas Research Network. Electronic address wbe, Cancer Genome Atlas Research N. Comprehensive and Integrative Genomic Characterization of Hepatocellular Carcinoma. Cell. 2017;169(7):1327-41.e23.
70. Llovet JM, Kelley RK, Villanueva A, Singal AG, Pikarsky E, Roayaie S, et al. Hepatocellular carcinoma. Nature Reviews Disease Primers. 2021;7(1):6.
71. Gilson E, Géli V. How telomeres are replicated. Nature reviews Molecular cell biology. 2007;8(10):825-38.
72. Satyanarayana A, Manns MP, Rudolph KL. Telomeres and telomerase: A dual role in hepatocarcinogenesis. Hepatology. 2004;40(2):276-83.
73. Yuan X, Larsson C, Xu D. Mechanisms underlying the activation of TERT transcription and telomerase activity in human cancer: old actors and new players. Oncogene. 2019;38(34):6172-83.
74. Lee SE, Chang S-H, Kim WY, Lim SD, Kim WS, Hwang TS, et al. Frequent somatic TERT promoter mutations and CTNNB1 mutations in hepatocellular carcinoma. Oncotarget. 2016;7(43):69267-75.
75. Nault J-C, Ningarhari M, Rebouissou S, Zucman-Rossi J. The role of telomeres and telomerase in cirrhosis and liver cancer. Nature Reviews Gastroenterology & Hepatology. 2019;16(9):544-58.
76. Nault JC, Calderaro J, Di Tommaso L, Balabaud C, Zafrani ES, Bioulac-Sage P, et al. Telomerase reverse transcriptase promoter mutation is an early somatic genetic alteration in the transformation of premalignant nodules in hepatocellular carcinoma on cirrhosis. Hepatology. 2014;60(6):1983-92.
77. Pinyol R, Tovar V, Llovet JM. TERT promoter mutations: gatekeeper and driver of hepatocellular carcinoma. J Hepatol. 2014;61(3):685-7.
78. Liu J, Xiao Q, Xiao J, Niu C, Li Y, Zhang X, et al. Wnt/β-catenin signalling: function, biological mechanisms, and therapeutic opportunities. Signal Transduction and Targeted Therapy. 2022;7(1):3.
79. Gao C, Chen YG. Dishevelled: The hub of Wnt signaling. Cell Signal. 2010;22(5):717-27.
80. Perugorria MJ, Olaizola P, Labiano I, Esparza-Baquer A, Marzioni M, Marin JJG, et al. Wnt-β-catenin signalling in liver development, health and disease. Nat Rev Gastroenterol Hepatol. 2019;16(2):121-36.
81. Sun T, Annunziato S, Bergling S, Sheng C, Orsini V, Forcella P, et al. ZNRF3 and RNF43 cooperate to safeguard metabolic liver zonation and hepatocyte proliferation. Cell Stem Cell. 2021;28(10):1822-37.e10.
82. Rebouissou S, Franconi A, Calderaro J, Letouzé E, Imbeaud S, Pilati C, et al. Genotype-phenotype correlation of CTNNB1 mutations reveals different ß-catenin activity associated with liver tumor progression. Hepatology. 2016;64(6).
83. Nusse R, Clevers H. Wnt/β-Catenin Signaling, Disease, and Emerging Therapeutic Modalities. Cell. 2017;169(6):985-99.

84. Xiao X, Mo H, Tu K. CTNNB1 mutation suppresses infiltration of immune cells in hepatocellular carcinoma through miRNA-mediated regulation of chemokine expression. International Immunopharmacology. 2020;89:107043.
85. Li W, Wang H, Ma Z, Zhang J, Ou-Yang W, Qi Y, et al. Multi-omics Analysis of Microenvironment Characteristics and Immune Escape Mechanisms of Hepatocellular Carcinoma. Front Oncol. 2019;9:1019.
86. Tornillo L, Carafa V, Sauter G, Moch H, Minola E, Gambacorta M, et al. Chromosomal Alterations in Hepatocellular Nodules by Comparative Genomic Hybridization: High-Grade Dysplastic Nodules Represent Early Stages of Hepatocellular Carcinoma. Laboratory Investigation. 2002;82(5):547-54.
87. Falleti E, Cussigh A, Cmet S, Fabris C, Toniutto P. PNPLA3 rs738409 and TM6SF2 rs58542926 variants increase the risk of hepatocellular carcinoma in alcoholic cirrhosis. Dig Liver Dis. 2016;48(1):69-75.
88. Chen Y-L, Jeng Y-M, Chang C-N, Lee H-J, Hsu H-C, Lai P-L, et al. TERT promoter mutation in resectable hepatocellular carcinomas: A strong association with hepatitis C infection and absence of hepatitis B infection. International Journal of Surgery. 2014;12(7):659-65.
89. Hoshida Y, Villanueva A, Sangiovanni A, Sole M, Hur C, Andersson KL, et al. Prognostic Gene Expression Signature for Patients With Hepatitis C–Related Early-Stage Cirrhosis. Gastroenterology. 2013;144(5):1024-30.
90. Abu Dayyeh BK, Yang M, Fuchs BC, Karl DL, Yamada S, Sninsky JJ, et al. A Functional Polymorphism in the Epidermal Growth Factor Gene Is Associated With Risk for Hepatocellular Carcinoma. Gastroenterology. 2011;141(1):141-9.
91. Nault JC, Paradis V, Cherqui D, Vilgrain V, Zucman-Rossi J. Molecular classification of hepatocellular adenoma in clinical practice. J Hepatol. 2017;67(5):1074-83.
92. Rebouissou S, Franconi A, Calderaro J, Letouzé E, Imbeaud S, Pilati C, et al. Genotype-phenotype correlation of CTNNB1 mutations reveals different ß-catenin activity associated with liver tumor progression. Hepatology. 2016;64(6):2047-61.
93. Pilati C, Letouzé E, Nault J-C, Imbeaud S, Boulai A, Calderaro J, et al. Genomic Profiling of Hepatocellular Adenomas Reveals Recurrent FRK-Activating Mutations and the Mechanisms of Malignant Transformation. Cancer Cell. 2014;25(4):428-41.
94. Comprehensive and Integrative Genomic Characterization of Hepatocellular Carcinoma. Cell. 2017;169(7):1327-41.e23.
95. Llovet JM, Montal R, Villanueva A. Randomized trials and endpoints in advanced HCC: Role of PFS as a surrogate of survival. Journal of Hepatology. 2019;70(6):1262-77.
96. Zhu AX, Kang YK, Yen CJ, Finn RS, Galle PR, Llovet JM, et al. Ramucirumab after sorafenib in patients with advanced hepatocellular carcinoma and increased α-fetoprotein concentrations (REACH-2): a randomised, double-blind, placebo-controlled, phase 3 trial. Lancet Oncol. 2019;20(2):282-96.
97. Zehir A, Benayed R, Shah RH, Syed A, Middha S, Kim HR, et al. Mutational landscape of metastatic cancer revealed from prospective clinical sequencing of 10,000 patients. Nature Medicine. 2017;23(6):703-13.
98. Singal AG, Hoshida Y, Pinato DJ, Marrero J, Nault JC, Paradis V, et al. International Liver Cancer Association (ILCA) White Paper on Biomarker Development for Hepatocellular Carcinoma. Gastroenterology. 2021;160(7):2572-84.
99. Losic B, Craig AJ, Villacorta-Martin C, Martins-Filho SN, Akers N, Chen X, et al. Intratumoral heterogeneity and clonal evolution in liver cancer. Nature Communications. 2020;11(1):291.

100. Huang A, Zhao X, Yang X-R, Li F-Q, Zhou X-L, Wu K, et al. Circumventing intratumoral heterogeneity to identify potential therapeutic targets in hepatocellular carcinoma. Journal of Hepatology. 2017;67(2):293-301.
101. Petrizzo A, Buonaguro L. Application of the Immunoscore as prognostic tool for hepatocellular carcinoma. J Immunother Cancer. 2016;4:71-.
102. Vauthey J-N, Lauwers GY, Esnaola NF, Do K-A, Belghiti J, Mirza N, et al. Simplified Staging for Hepatocellular Carcinoma. Journal of Clinical Oncology. 2002;20(6):1527-36.
103. Okuda K, Ohtsuki T, Obata H, Tomimatsu M, Okazaki N, Hasegawa H, et al. Natural history of hepatocellular carcinoma and prognosis in relation to treatment study of 850 patients. Cancer. 1985;56(4):918-28.
104. Faria SC, Szklaruk J, Kaseb AO, Hassabo HM, Elsayes KM. TNM/Okuda/Barcelona/UNOS/CLIP International Multidisciplinary Classification of Hepatocellular Carcinoma: concepts, perspectives, and radiologic implications. Abdominal Imaging. 2014;39(5):1070-87.
105. Lu W, Dong J, Huang Z, Guo D, Liu Y, Shi S. Comparison of four current staging systems for Chinese patients with hepatocellular carcinoma undergoing curative resection: Okuda, CLIP, TNM and CUPI. Journal of Gastroenterology and Hepatology. 2008;23(12):1874-8.
106. Nanashima A, Sumida Y, Morino S, Yamaguchi H, Tanaka K, Shibasaki S, et al. The Japanese integrated staging score using liver damage grade for hepatocellular carcinoma in patients after hepatectomy. European Journal of Surgical Oncology (EJSO). 2004;30(7):765-70.
107. Chevret S, Trinchet J-C, Mathieu D, Rached AA, Beaugrand M, Chastang C. A new prognostic classification for predicting survival in patients with hepatocellular carcinoma. Journal of hepatology. 1999;31(1):133-41.
108. Llovet JM, Bruix J. Prospective validation of the Cancer of the Liver Italian Program (CLIP) score: a new prognostic system for patients with cirrhosis and hepatocellular carcinoma. Hepatology. 2000;32(3):679-80.
109. Chan SL, Mo FKF, Johnson PJ, Liem GS, Chan TC, Poon MC, et al. Prospective validation of the Chinese University Prognostic Index and comparison with other staging systems for hepatocellular carcinoma in an Asian population. Journal of Gastroenterology and Hepatology. 2011;26(2):340-7.
110. Llovet JM, Brú C, Bruix J. Prognosis of Hepatocellular Carcinoma: The BCLC Staging Classification. Semin Liver Dis. 1999;19(03):329-38.
111. Nanashima A, Sumida Y, Morino S, Yamaguchi H, Tanaka K, Shibasaki S, et al. The Japanese integrated staging score using liver damage grade for hepatocellular carcinoma in patients after hepatectomy. Eur J Surg Oncol. 2004;30(7):765-70.
112. Mesropyan N, Kupczyk PA, Dold L, Praktiknjo M, Chang J, Isaak A, et al. Assessment of liver cirrhosis severity with extracellular volume fraction MRI. Scientific Reports. 2022;12(1):9422.
113. Peng Y, Qi X, Guo X. Child-Pugh Versus MELD Score for the Assessment of Prognosis in Liver Cirrhosis: A Systematic Review and Meta-Analysis of Observational Studies. Medicine (Baltimore). 2016;95(8):e2877.
114. Kudo M, Chung H, Osaki Y. Prognostic staging system for hepatocellular carcinoma (CLIP score): its value and limitations, and a proposal for a new staging system, the Japan Integrated Staging Score (JIS score). Journal of Gastroenterology. 2003;38(3):207-15.

115. Kudo M, Chung H, Haji S, Osaki Y, Oka H, Seki T, et al. Validation of a new prognostic staging system for hepatocellular carcinoma: The JIS score compared with the CLIP score. Hepatology. 2004;40(6):1396-405.
116. Faria SC, Szklaruk J, Kaseb AO, Hassabo HM, Elsayes KM. TNM/Okuda/Barcelona/UNOS/CLIP International Multidisciplinary Classification of Hepatocellular Carcinoma: concepts, perspectives, and radiologic implications. Abdom Imaging. 2014;39(5):1070-87.
117. Kitai S, Kudo M, Minami Y, Ueshima K, Chung H, Hagiwara S, et al. A new prognostic staging system for hepatocellular carcinoma: value of the biomarker combined Japan integrated staging score. Intervirology. 2008;51 Suppl 1:86-94.
118. Farinati F, Rinaldi M, Gianni S, Naccarato R. How should patients with hepatocellular carcinoma be staged? Validation of a new prognostic system. Cancer. 2000;89(11):2266-73.
119. Pons F, Varela M, Llovet JM. Staging systems in hepatocellular carcinoma. HPB (Oxford). 2005;7(1):35-41.
120. Chevret S, Trinchet JC, Mathieu D, Rached AA, Beaugrand M, Chastang C. A new prognostic classification for predicting survival in patients with hepatocellular carcinoma. Groupe d'Etude et de Traitement du Carcinome Hépatocellulaire. J Hepatol. 1999;31(1):133-41.
121. Cillo U, Bassanello M, Vitale A, Grigoletto FA, Burra P, Fagiuoli S, et al. The critical issue of hepatocellular carcinoma prognostic classification: which is the best tool available? J Hepatol. 2004;40(1):124-31.
122. Leung TWT, Tang AMY, Zee B, Lau WY, Lai PBS, Leung KL, et al. Construction of the Chinese University Prognostic Index for hepatocellular carcinoma and comparison with the TNM staging system, the Okuda staging system, and the Cancer of the Liver Italian Program staging system. Cancer. 2002;94(6):1760-9.
123. Yang T, Zhang J, Lu JH, Yang LQ, Yang GS, Wu MC, et al. A new staging system for resectable hepatocellular carcinoma: comparison with six existing staging systems in a large Chinese cohort. J Cancer Res Clin Oncol. 2011;137(5):739-50.
124. Befeler AS, di Bisceglie AM. Hepatocellular carcinoma: Diagnosis and treatment. Gastroenterology. 2002;122(6):1609-19.
125. Duseja A. Staging of Hepatocellular Carcinoma. Journal of Clinical and Experimental Hepatology. 2014;4:S74-S9.
126. Llovet JM, Bustamante J, Castells A, Vilana R, Ayuso MDC, Sala M, et al. Natural history of untreated nonsurgical hepatocellular carcinoma: Rationale for the design and evaluation of therapeutic trials. Hepatology. 1999;29(1):62-7.
127. Makary MS, Khandpur U, Cloyd JM, Mumtaz K, Dowell JD. Locoregional Therapy Approaches for Hepatocellular Carcinoma: Recent Advances and Management Strategies. Cancers (Basel). 2020;12(7):1914.
128. Marrero JA, Kudo M, Bronowicki JP. The challenge of prognosis and staging for hepatocellular carcinoma. Oncologist. 2010;15 Suppl 4:23-33.
129. Kaseb AO, Abbruzzese JL, Vauthey JN, Aloia TA, Abdalla EK, Hassan MM, et al. I-CLIP: improved stratification of advanced hepatocellular carcinoma patients by integrating plasma IGF-1 into CLIP score. Oncology. 2011;80(5-6):373-81.
130. Calderaro J, Ziol M, Paradis V, Zucman-Rossi J. Molecular and histological correlations in liver cancer. Journal of hepatology. 2019;71(3):616-30.

131. Sia D, Jiao Y, Martinez-Quetglas I, Kuchuk O, Villacorta-Martin C, Castro de Moura M, et al. Identification of an Immune-specific Class of Hepatocellular Carcinoma, Based on Molecular Features. Gastroenterology. 2017;153(3):812-26.
132. Galon J, Bruni D. Approaches to treat immune hot, altered and cold tumours with combination immunotherapies. Nature Reviews Drug Discovery. 2019;18(3):197-218.
133. Llovet JM, Castet F, Heikenwalder M, Maini MK, Mazzaferro V, Pinato DJ, et al. Immunotherapies for hepatocellular carcinoma. Nat Rev Clin Oncol. 2022;19(3):151-72.
134. Carla M, Florian C, Philipp KH, Roser P, Miguel T-M, Laura T, et al. Inflamed and non-inflamed classes of HCC: a revised immunogenomic classification. Gut. 2023;72(1):129.
135. Galon J, Mlecnik B, Bindea G, Angell HK, Berger A, Lagorce C, et al. Towards the introduction of the 'Immunoscore' in the classification of malignant tumours. J Pathol. 2014;232(2):199-209.
136. Topalian SL, Hodi FS, Brahmer JR, Gettinger SN, Smith DC, McDermott DF, et al. Safety, Activity, and Immune Correlates of Anti–PD-1 Antibody in Cancer. New England Journal of Medicine. 2012;366(26):2443-54.
137. Hodi FS, O'Day SJ, McDermott DF, Weber RW, Sosman JA, Haanen JB, et al. Improved Survival with Ipilimumab in Patients with Metastatic Melanoma. New England Journal of Medicine. 2010;363(8):711-23.
138. Hanahan D, Coussens LM. Accessories to the crime: functions of cells recruited to the tumor microenvironment. Cancer Cell. 2012;21(3):309-22.
139. Maslak E, Gregorius A, Chlopicki S. Liver sinusoidal endothelial cells (LSECs) function and NAFLD; NO-based therapy targeted to the liver. Pharmacological Reports. 2015;67(4):689-94.
140. Sørensen KK, Simon-Santamaria J, McCuskey RS, Smedsrød B. Liver Sinusoidal Endothelial Cells. Comprehensive Physiology2015. p. 1751-74.
141. Mates JM, Yao Z, Cheplowitz AM, Suer O, Phillips GS, Kwiek JJ, et al. Mouse Liver Sinusoidal Endothelium Eliminates HIV-Like Particles from Blood at a Rate of 100 Million per Minute by a Second-Order Kinetic Process. Front Immunol. 2017;8:35.
142. Smedsrød B. Clearance function of scavenger endothelial cells. Comp Hepatol. 2004;3 Suppl 1(Suppl 1):S22.
143. Li R, Oteiza A, Sørensen KK, McCourt P, Olsen R, Smedsrød B, et al. Role of liver sinusoidal endothelial cells and stabilins in elimination of oxidized low-density lipoproteins. Am J Physiol Gastrointest Liver Physiol. 2011;300(1):G71-81.
144. Shetty S, Lalor PF, Adams DH. Liver sinusoidal endothelial cells — gatekeepers of hepatic immunity. Nature Reviews Gastroenterology & Hepatology. 2018;15(9):555-67.
145. Uhrig A, Banafsche R, Kremer M, Hegenbarth S, Hamann A, Neurath M, et al. Development and functional consequences of LPS tolerance in sinusoidal endothelial cells of the liver. J Leukoc Biol. 2005;77(5):626-33.
146. Pinato DJ, Guerra N, Fessas P, Murphy R, Mineo T, Mauri FA, et al. Immune-based therapies for hepatocellular carcinoma. Oncogene. 2020;39(18):3620-37.
147. Ihling C, Naughton B, Zhang Y, Rolfe PA, Frick-Krieger E, Terracciano LM, et al. Observational Study of PD-L1, TGF-β, and Immune Cell Infiltrates in Hepatocellular Carcinoma. Front Med (Lausanne). 2019;6:15.
148. Wu LQ, Zhang WJ, Niu JX, Ye LY, Yang ZH, Grau GE, et al. Phenotypic and Functional Differences between Human Liver Cancer Endothelial Cells and Liver Sinusoidal Endothelial Cells. Journal of Vascular Research. 2007;45(1):78-86.

149. Li H. Intercellular crosstalk of liver sinusoidal endothelial cells in liver fibrosis, cirrhosis and hepatocellular carcinoma. Digestive and Liver Disease. 2022;54(5):598-613.
150. Lu LC, Chang CJ, Hsu CH. Targeting myeloid-derived suppressor cells in the treatment of hepatocellular carcinoma: current state and future perspectives. J Hepatocell Carcinoma. 2019;6:71-84.
151. Connolly MK, Mallen-St Clair J, Bedrosian AS, Malhotra A, Vera V, Ibrahim J, et al. Distinct populations of metastases-enabling myeloid cells expand in the liver of mice harboring invasive and preinvasive intra-abdominal tumor. J Leukoc Biol. 2010;87(4):713-25.
152. Borregaard N. Neutrophils, from marrow to microbes. Immunity. 2010;33(5):657-70.
153. Kaplan MJ, Radic M. Neutrophil extracellular traps: double-edged swords of innate immunity. J Immunol. 2012;189(6):2689-95.
154. Robinson JM. Phagocytic leukocytes and reactive oxygen species. Histochemistry and Cell Biology. 2009;131(4):465-9.
155. Nguyen GT, Green ER, Mecsas J. Neutrophils to the ROScue: Mechanisms of NADPH Oxidase Activation and Bacterial Resistance. Front Cell Infect Microbiol. 2017;7:373-.
156. Kolaczkowska E, Kubes P. Neutrophil recruitment and function in health and inflammation. Nature Reviews Immunology. 2013;13(3):159-75.
157. Li Y, Wang W, Yang F, Xu Y, Feng C, Zhao Y. The regulatory roles of neutrophils in adaptive immunity. Cell Commun Signal. 2019;17(1):147.
158. Rosales C. Neutrophil: A Cell with Many Roles in Inflammation or Several Cell Types? Front Physiol. 2018;9:113.
159. Fridlender ZG, Sun J, Kim S, Kapoor V, Cheng G, Ling L, et al. Polarization of tumor-associated neutrophil phenotype by TGF-beta: "N1" versus "N2" TAN. Cancer Cell. 2009;16(3):183-94.
160. Masucci MT, Minopoli M, Carriero MV. Tumor Associated Neutrophils. Their Role in Tumorigenesis, Metastasis, Prognosis and Therapy. Frontiers in Oncology. 2019;9(1146).
161. Gregory AD, McGarry Houghton A. Tumor-Associated Neutrophils: New Targets for Cancer Therapy. Cancer Research. 2011;71(7):2411.
162. Sagiv JY, Michaeli J, Assi S, Mishalian I, Kisos H, Levy L, et al. Phenotypic diversity and plasticity in circulating neutrophil subpopulations in cancer. Cell Rep. 2015;10(4):562-73.
163. Takeshima T, Pop LM, Laine A, Iyengar P, Vitetta ES, Hannan R. Key role for neutrophils in radiation-induced antitumor immune responses: Potentiation with G-CSF. Proc Natl Acad Sci U S A. 2016;113(40):11300-5.
164. Rice CM, Davies LC, Subleski JJ, Maio N, Gonzalez-Cotto M, Andrews C, et al. Tumour-elicited neutrophils engage mitochondrial metabolism to circumvent nutrient limitations and maintain immune suppression. Nat Commun. 2018;9(1):5099.
165. Geh D, Leslie J, Rumney R, Reeves HL, Bird TG, Mann DA. Neutrophils as potential therapeutic targets in hepatocellular carcinoma. Nature Reviews Gastroenterology & Hepatology. 2022;19(4):257-73.
166. Liu K, Wang FS, Xu R. Neutrophils in liver diseases: pathogenesis and therapeutic targets. Cell Mol Immunol. 2021;18(1):38-44.
167. Brostjan C, Oehler R. The role of neutrophil death in chronic inflammation and cancer. Cell Death Discov. 2020;6:26.
168. Margetts J, Ogle LF, Chan SL, Chan AWH, Chan KCA, Jamieson D, et al. Neutrophils: driving progression and poor prognosis in hepatocellular carcinoma? Br J Cancer. 2018;118(2):248-57.

169. Wilson CL, Jurk D, Fullard N, Banks P, Page A, Luli S, et al. NFκB1 is a suppressor of neutrophil-driven hepatocellular carcinoma. Nature communications. 2015;6:6818-.
170. Lagnado A, Leslie J, Ruchaud-Sparagano M-H, Victorelli S, Hirsova P, Ogrodnik M, et al. Neutrophils induce paracrine telomere dysfunction and senescence in ROS-dependent manner. The EMBO Journal. 2021;40(9):e106048.
171. van der Windt DJ, Sud V, Zhang H, Varley PR, Goswami J, Yazdani HO, et al. Neutrophil extracellular traps promote inflammation and development of hepatocellular carcinoma in nonalcoholic steatohepatitis. Hepatology. 2018;68(4):1347-60.
172. Ding W, Xu X, Qian Y, Xue W, Wang Y, Du J, et al. Prognostic value of tumor-infiltrating lymphocytes in hepatocellular carcinoma: A meta-analysis. Medicine (Baltimore). 2018;97(50):e13301.
173. Farhood B, Najafi M, Mortezaee K. CD8+ cytotoxic T lymphocytes in cancer immunotherapy: A review. Journal of Cellular Physiology. 2019;234(6):8509-21.
174. Ma J, Zheng B, Goswami S, Meng L, Zhang D, Cao C, et al. PD1(Hi) CD8(+) T cells correlate with exhausted signature and poor clinical outcome in hepatocellular carcinoma. J Immunother Cancer. 2019;7(1):331.
175. Chocarro L, Blanco E, Zuazo M, Arasanz H, Bocanegra A, Fernández-Rubio L, et al. Understanding LAG-3 Signaling. Int J Mol Sci. 2021;22(10).
176. He Y, Cao J, Zhao C, Li X, Zhou C, Hirsch FR. TIM-3, a promising target for cancer immunotherapy. Onco Targets Ther. 2018;11:7005-9.
177. Leone P, Solimando AG, Fasano R, Argentiero A, Malerba E, Buonavoglia A, et al. The Evolving Role of Immune Checkpoint Inhibitors in Hepatocellular Carcinoma Treatment. Vaccines (Basel). 2021;9(5).
178. Parry RV, Chemnitz JM, Frauwirth KA, Lanfranco AR, Braunstein I, Kobayashi SV, et al. CTLA-4 and PD-1 receptors inhibit T-cell activation by distinct mechanisms. Mol Cell Biol. 2005;25(21):9543-53.
179. Patsoukis N, Brown J, Petkova V, Liu F, Li L, Boussiotis VA. Selective effects of PD-1 on Akt and Ras pathways regulate molecular components of the cell cycle and inhibit T cell proliferation. Sci Signal. 2012;5(230):ra46.
180. Chang H, Jung W, Kim A, Kim HK, Kim WB, Kim JH, et al. Expression and prognostic significance of programmed death protein 1 and programmed death ligand-1, and cytotoxic T lymphocyte-associated molecule-4 in hepatocellular carcinoma. Apmis. 2017;125(8):690-8.
181. Jung HI, Jeong D, Ji S, Ahn TS, Bae SH, Chin S, et al. Overexpression of PD-L1 and PD-L2 Is Associated with Poor Prognosis in Patients with Hepatocellular Carcinoma. Cancer Res Treat. 2017;49(1):246-54.
182. Zhou G, Sprengers D, Boor PPC, Doukas M, Schutz H, Mancham S, et al. Antibodies Against Immune Checkpoint Molecules Restore Functions of Tumor-Infiltrating T Cells in Hepatocellular Carcinomas. Gastroenterology. 2017;153(4):1107-19.e10.
183. Buchbinder EI, Desai A. CTLA-4 and PD-1 Pathways: Similarities, Differences, and Implications of Their Inhibition. Am J Clin Oncol. 2016;39(1):98-106.
184. Grosso JF, Kelleher CC, Harris TJ, Maris CH, Hipkiss EL, De Marzo A, et al. LAG-3 regulates CD8+ T cell accumulation and effector function in murine self- and tumor-tolerance systems. J Clin Invest. 2007;117(11):3383-92.
185. Tawbi HA, Schadendorf D, Lipson EJ, Ascierto PA, Matamala L, Castillo Gutiérrez E, et al. Relatlimab and Nivolumab versus Nivolumab in Untreated Advanced Melanoma. New England Journal of Medicine. 2022;386(1):24-34.

186. Amaria RN, Postow M, Burton EM, Tetzlaff MT, Ross MI, Torres-Cabala C, et al. Neoadjuvant relatlimab and nivolumab in resectable melanoma. Nature. 2022;611(7934):155-60.
187. Shi AP, Tang XY, Xiong YL, Zheng KF, Liu YJ, Shi XG, et al. Immune Checkpoint LAG3 and Its Ligand FGL1 in Cancer. Front Immunol. 2021;12:785091.
188. Li F, Li N, Sang J, Fan X, Deng H, Zhang X, et al. Highly elevated soluble Tim-3 levels correlate with increased hepatocellular carcinoma risk and poor survival of hepatocellular carcinoma patients in chronic hepatitis B virus infection. Cancer Manag Res. 2018;10:941-51.
189. Liu F, Liu Y, Chen Z. Tim-3 expression and its role in hepatocellular carcinoma. J Hematol Oncol. 2018;11(1):126.
190. Zheng X, Jin W, Wang S, Ding H. Progression on the Roles and Mechanisms of Tumor-Infiltrating T Lymphocytes in Patients With Hepatocellular Carcinoma. Front Immunol. 2021;12:729705.
191. Sas Z, Cendrowicz E, Weinhäuser I, Rygiel TP. Tumor Microenvironment of Hepatocellular Carcinoma: Challenges and Opportunities for New Treatment Options. Int J Mol Sci. 2022;23(7).
192. Alissafi T, Hatzioannou A, Legaki AI, Varveri A, Verginis P. Balancing cancer immunotherapy and immune-related adverse events: The emerging role of regulatory T cells. Journal of Autoimmunity. 2019;104:102310.
193. Ren L, Yu Y, Wang L, Zhu Z, Lu R, Yao Z. Hypoxia-induced CCL28 promotes recruitment of regulatory T cells and tumor growth in liver cancer. Oncotarget. 2016;7(46):75763-73.
194. Ringelhan M, Pfister D, O'Connor T, Pikarsky E, Heikenwalder M. The immunology of hepatocellular carcinoma. Nat Immunol. 2018;19(3):222-32.
195. Li X, Ramadori P, Pfister D, Seehawer M, Zender L, Heikenwalder M. The immunological and metabolic landscape in primary and metastatic liver cancer. Nature Reviews Cancer. 2021;21(9):541-57.
196. Larmonier N, Marron M, Zeng Y, Cantrell J, Romanoski A, Sepassi M, et al. Tumor-derived CD4+CD25+ regulatory T cell suppression of dendritic cell function involves TGF-β and IL-10. Cancer Immunology, Immunotherapy. 2007;56(1):48-59.
197. Langhans B, Nischalke HD, Krämer B, Dold L, Lutz P, Mohr R, et al. Role of regulatory T cells and checkpoint inhibition in hepatocellular carcinoma. Cancer Immunol Immunother. 2019;68(12):2055-66.
198. Kumar V, Patel S, Tcyganov E, Gabrilovich DI. The Nature of Myeloid-Derived Suppressor Cells in the Tumor Microenvironment. Trends Immunol. 2016;37(3):208-20.
199. Chen Y, Huang Y, Reiberger T, Duyverman AM, Huang P, Samuel R, et al. Differential effects of sorafenib on liver versus tumor fibrosis mediated by stromal-derived factor 1 alpha/C-X-C receptor type 4 axis and myeloid differentiation antigen-positive myeloid cell infiltration in mice. Hepatology. 2014;59(4):1435-47.
200. Hoechst B, Ormandy LA, Ballmaier M, Lehner F, Krüger C, Manns MP, et al. A New Population of Myeloid-Derived Suppressor Cells in Hepatocellular Carcinoma Patients Induces CD4+CD25+Foxp3+ T Cells. Gastroenterology. 2008;135(1):234-43.
201. Iwata T, Kondo Y, Kimura O, Morosawa T, Fujisaka Y, Umetsu T, et al. PD-L1+MDSCs are increased in HCC patients and induced by soluble factor in the tumor microenvironment. Scientific Reports. 2016;6(1):39296.
202. Liu H, Ling CC, Yeung WHO, Pang L, Liu J, Zhou J, et al. Monocytic MDSC mobilization promotes tumor recurrence after liver transplantation via CXCL10/TLR4/MMP14 signaling. Cell Death & Disease. 2021;12(5):489.

203. Zhang Y, Li JQ, Jiang ZZ, Li L, Wu Y, Zheng L. CD169 identifies an anti-tumour macrophage subpopulation in human hepatocellular carcinoma. J Pathol. 2016;239(2):231-41.
204. MacParland SA, Liu JC, Ma XZ, Innes BT, Bartczak AM, Gage BK, et al. Single cell RNA sequencing of human liver reveals distinct intrahepatic macrophage populations. Nat Commun. 2018;9(1):4383.
205. Ding T, Xu J, Wang F, Shi M, Zhang Y, Li SP, et al. High tumor-infiltrating macrophage density predicts poor prognosis in patients with primary hepatocellular carcinoma after resection. Hum Pathol. 2009;40(3):381-9.
206. Mantovani A, Sozzani S, Locati M, Allavena P, Sica A. Macrophage polarization: tumor-associated macrophages as a paradigm for polarized M2 mononuclear phagocytes. Trends in Immunology. 2002;23(11):549-55.
207. Ostrand-Rosenberg S, Sinha P, Beury DW, Clements VK. Cross-talk between myeloid-derived suppressor cells (MDSC), macrophages, and dendritic cells enhances tumor-induced immune suppression. Seminars in Cancer Biology. 2012;22(4):275-81.
208. Xiang X, Wang J, Lu D, Xu X. Targeting tumor-associated macrophages to synergize tumor immunotherapy. Signal Transduction and Targeted Therapy. 2021;6(1):75.
209. Xiao P, Long X, Zhang L, Ye Y, Guo J, Liu P, et al. Neurotensin/IL-8 pathway orchestrates local inflammatory response and tumor invasion by inducing M2 polarization of Tumor-Associated macrophages and epithelial-mesenchymal transition of hepatocellular carcinoma cells. Oncoimmunology. 2018;7(7):e1440166.
210. Yang J, Zhang JX, Wang H, Wang GL, Hu QG, Zheng QC. Hepatocellular carcinoma and macrophage interaction induced tumor immunosuppression via Treg requires TLR4 signaling. World J Gastroenterol. 2012;18(23):2938-47.
211. Sun Y, Wu L, Zhong Y, Zhou K, Hou Y, Wang Z, et al. Single-cell landscape of the ecosystem in early-relapse hepatocellular carcinoma. Cell. 2021;184(2):404-21.e16.
212. Zhang Q, He Y, Luo N, Patel SJ, Han Y, Gao R, et al. Landscape and Dynamics of Single Immune Cells in Hepatocellular Carcinoma. Cell. 2019;179(4):829-45.e20.
213. Bozward AG, Warricker F, Oo YH, Khakoo SI. Natural Killer Cells and Regulatory T Cells Cross Talk in Hepatocellular Carcinoma: Exploring Therapeutic Options for the Next Decade. Front Immunol. 2021;12:643310.
214. Juengpanich S, Shi L, Iranmanesh Y, Chen J, Cheng Z, Khoo AK, et al. The role of natural killer cells in hepatocellular carcinoma development and treatment: A narrative review. Transl Oncol. 2019;12(8):1092-107.
215. Shi F-D, Ljunggren H-G, La Cava A, Van Kaer L. Organ-specific features of natural killer cells. Nature Reviews Immunology. 2011;11(10):658-71.
216. Hudspeth K, Donadon M, Cimino M, Pontarini E, Tentorio P, Preti M, et al. Human liver-resident CD56(bright)/CD16(neg) NK cells are retained within hepatic sinusoids via the engagement of CCR5 and CXCR6 pathways. J Autoimmun. 2016;66:40-50.
217. Kelly AM, Golden-Mason L, Traynor O, Geoghegan J, McEntee G, Hegarty JE, et al. Changes in hepatic immunoregulatory cytokines in patients with metastatic colorectal carcinoma: implications for hepatic anti-tumour immunity. Cytokine. 2006;35(3-4):171-9.
218. Sun H, Huang Q, Huang M, Wen H, Lin R, Zheng M, et al. Human CD96 Correlates to Natural Killer Cell Exhaustion and Predicts the Prognosis of Human Hepatocellular Carcinoma. Hepatology. 2019;70(1):168-83.
219. Sun H, Liu L, Huang Q, Liu H, Huang M, Wang J, et al. Accumulation of Tumor-Infiltrating CD49a+ NK Cells Correlates with Poor Prognosis for Human Hepatocellular Carcinoma. Cancer Immunology Research. 2019;7(9):1535-46.

220. Sun C, Sun H-y, Xiao W-h, Zhang C, Tian Z-g. Natural killer cell dysfunction in hepatocellular carcinoma and NK cell-based immunotherapy. Acta Pharmacologica Sinica. 2015;36(10):1191-9.
221. Li T, Yang Y, Hua X, Wang G, Liu W, Jia C, et al. Hepatocellular carcinoma-associated fibroblasts trigger NK cell dysfunction via PGE2 and IDO. Cancer Lett. 2012;318(2):154-61.
222. Tumino N, Di Pace AL, Besi F, Quatrini L, Vacca P, Moretta L. Interaction Between MDSC and NK Cells in Solid and Hematological Malignancies: Impact on HSCT. Front Immunol. 2021;12:638841.
223. Wu Y, Kuang DM, Pan WD, Wan YL, Lao XM, Wang D, et al. Monocyte/macrophage-elicited natural killer cell dysfunction in hepatocellular carcinoma is mediated by CD48/2B4 interactions. Hepatology. 2013;57(3):1107-16.
224. Liu Y, Cheng Y, Xu Y, Wang Z, Du X, Li C, et al. Increased expression of programmed cell death protein 1 on NK cells inhibits NK-cell-mediated anti-tumor function and indicates poor prognosis in digestive cancers. Oncogene. 2017;36(44):6143-53.
225. Cariani E, Pilli M, Barili V, Porro E, Biasini E, Olivani A, et al. Natural killer cells phenotypic characterization as an outcome predictor of HCV-linked HCC after curative treatments. Oncoimmunology. 2016;5(8):e1154249.
226. Easom NJW, Marks M, Jobe D, Gillmore R, Meyer T, Maini MK, et al. ULBP1 Is Elevated in Human Hepatocellular Carcinoma and Predicts Outcome. Front Oncol. 2020;10:971.
227. Ghadially H, Brown L, Lloyd C, Lewis L, Lewis A, Dillon J, et al. MHC class I chain-related protein A and B (MICA and MICB) are predominantly expressed intracellularly in tumour and normal tissue. British Journal of Cancer. 2017;116(9):1208-17.
228. Kamimura H, Yamagiwa S, Tsuchiya A, Takamura M, Matsuda Y, Ohkoshi S, et al. Reduced NKG2D ligand expression in hepatocellular carcinoma correlates with early recurrence. J Hepatol. 2012;56(2):381-8.
229. Sheppard S, Guedes J, Mroz A, Zavitsanou AM, Kudo H, Rothery SM, et al. The immunoreceptor NKG2D promotes tumour growth in a model of hepatocellular carcinoma. Nat Commun. 2017;8:13930.
230. Zhang J, Gu C, Song Q, Zhu M, Xu Y, Xiao M, et al. Identifying cancer-associated fibroblasts as emerging targets for hepatocellular carcinoma. Cell Biosci. 2020;10(1):127.
231. Robert S, Gicquel T, Bodin A, Lagente V, Boichot E. Characterization of the MMP/TIMP Imbalance and Collagen Production Induced by IL-1β or TNF-α Release from Human Hepatic Stellate Cells. PLoS One. 2016;11(4):e0153118.
232. Neaud V, Faouzi S, Guirouilh J, Le Bail B, Balabaud C, Bioulac-Sage P, et al. Human hepatic myofibroblasts increase invasiveness of hepatocellular carcinoma cells: Evidence for a role of hepatocyte growth factor. Hepatology. 1997;26(6):1458-66.
233. Jiang G, Yang HR, Wang L, Wildey GM, Fung J, Qian S, et al. Hepatic stellate cells preferentially expand allogeneic CD4+ CD25+ FoxP3+ regulatory T cells in an IL-2-dependent manner. Transplantation. 2008;86(11):1492-502.
234. Filliol A, Saito Y, Nair A, Dapito DH, Yu L-X, Ravichandra A, et al. Opposing roles of hepatic stellate cell subpopulations in hepatocarcinogenesis. Nature. 2022;610(7931):356-65.
235. Khan GJ, Sun L, Khan S, Yuan S, Nongyue H. Versatility of Cancer Associated Fibroblasts: Commendable Targets for Anti-tumor Therapy. Curr Drug Targets. 2018;19(13):1573-88.
236. Zhang Y, Zhao W, Li S, Lv M, Yang X, Li M, et al. CXCL11 promotes self-renewal and tumorigenicity of α2δ1(+) liver tumor-initiating cells through CXCR3/ERK1/2 signaling. Cancer Lett. 2019;449:163-71.

237. Liu G, Sun J, Yang ZF, Zhou C, Zhou PY, Guan RY, et al. Cancer-associated fibroblast-derived CXCL11 modulates hepatocellular carcinoma cell migration and tumor metastasis through the circUBAP2/miR-4756/IFIT1/3 axis. Cell Death Dis. 2021;12(3):260.
238. Xu H, Zhao J, Li J, Zhu Z, Cui Z, Liu R, et al. Cancer associated fibroblast–derived CCL5 promotes hepatocellular carcinoma metastasis through activating HIF1α/ZEB1 axis. Cell Death & Disease. 2022;13(5):478.
239. Jafarnejad M, Sové RJ, Danilova L, Mirando AC, Zhang Y, Yarchoan M, et al. Mechanistically detailed systems biology modeling of the HGF/Met pathway in hepatocellular carcinoma. NPJ Syst Biol Appl. 2019;5:29.
240. Xiong S, Wang R, Chen Q, Luo J, Wang J, Zhao Z, et al. Cancer-associated fibroblasts promote stem cell-like properties of hepatocellular carcinoma cells through IL-6/STAT3/Notch signaling. Am J Cancer Res. 2018;8(2):302-16.
241. R. Seo H. Roles of Tumor Microenvironment in Hepatocelluar Carcinoma. Current Cancer Therapy Reviews. 2015;11(2):82-93.
242. Sahai E, Astsaturov I, Cukierman E, DeNardo DG, Egeblad M, Evans RM, et al. A framework for advancing our understanding of cancer-associated fibroblasts. Nature Reviews Cancer. 2020;20(3):174-86.
243. Wu F, Yang J, Liu J, Wang Y, Mu J, Zeng Q, et al. Signaling pathways in cancer-associated fibroblasts and targeted therapy for cancer. Signal Transduction and Targeted Therapy. 2021;6(1):218.
244. Reig M, Forner A, Rimola J, Ferrer-Fàbrega J, Burrel M, Garcia-Criado Á, et al. BCLC strategy for prognosis prediction and treatment recommendation: The 2022 update. J Hepatol. 2022;76(3):681-93.
245. Llovet JM, Real MI, Montaña X, Planas R, Coll S, Aponte J, et al. Arterial embolisation or chemoembolisation versus symptomatic treatment in patients with unresectable hepatocellular carcinoma: a randomised controlled trial. The Lancet. 2002;359(9319):1734-9.
246. Raoul JL, Forner A, Bolondi L, Cheung TT, Kloeckner R, de Baere T. Updated use of TACE for hepatocellular carcinoma treatment: How and when to use it based on clinical evidence. Cancer Treat Rev. 2019;72:28-36.
247. Llovet JM, Burroughs A, Bruix J. Hepatocellular carcinoma. The Lancet. 2003;362(9399):1907-17.
248. Bruix J, Cheng AL, Meinhardt G, Nakajima K, De Sanctis Y, Llovet J. Prognostic factors and predictors of sorafenib benefit in patients with hepatocellular carcinoma: Analysis of two phase III studies. J Hepatol. 2017;67(5):999-1008.
249. Llovet JM, Ricci S, Mazzaferro V, Hilgard P, Gane E, Blanc JF, et al. Sorafenib in advanced hepatocellular carcinoma. N Engl J Med. 2008;359(4):378-90.
250. Wilhelm SM, Adnane L, Newell P, Villanueva A, Llovet JM, Lynch M. Preclinical overview of sorafenib, a multikinase inhibitor that targets both Raf and VEGF and PDGF receptor tyrosine kinase signaling. Mol Cancer Ther. 2008;7(10):3129-40.
251. Llovet JM, Hernandez-Gea V. Hepatocellular Carcinoma: Reasons for Phase III Failure and Novel Perspectives on Trial Design. Clinical Cancer Research. 2014;20(8):2072.
252. Kudo M, Finn RS, Qin S, Han KH, Ikeda K, Piscaglia F, et al. Lenvatinib versus sorafenib in first-line treatment of patients with unresectable hepatocellular carcinoma: a randomised phase 3 non-inferiority trial. Lancet. 2018;391(10126):1163-73.
253. Yamashita T, Kudo M, Ikeda K, Izumi N, Tateishi R, Ikeda M, et al. REFLECT-a phase 3 trial comparing efficacy and safety of lenvatinib to sorafenib for the treatment of unresectable hepatocellular carcinoma: an analysis of Japanese subset. J Gastroenterol. 2020;55(1):113-22.

254. Bruix J, Qin S, Merle P, Granito A, Huang YH, Bodoky G, et al. Regorafenib for patients with hepatocellular carcinoma who progressed on sorafenib treatment (RESORCE): a randomised, double-blind, placebo-controlled, phase 3 trial. Lancet. 2017;389(10064):56-66.
255. Abou-Alfa GK, Meyer T, Cheng A-L, El-Khoueiry AB, Rimassa L, Ryoo B-Y, et al. Cabozantinib in Patients with Advanced and Progressing Hepatocellular Carcinoma. New England Journal of Medicine. 2018;379(1):54-63.
256. Wilhelm SM, Dumas J, Adnane L, Lynch M, Carter CA, Schütz G, et al. Regorafenib (BAY 73-4506): a new oral multikinase inhibitor of angiogenic, stromal and oncogenic receptor tyrosine kinases with potent preclinical antitumor activity. Int J Cancer. 2011;129(1):245-55.
257. Goyal L, Muzumdar MD, Zhu AX. Targeting the HGF/c-MET pathway in hepatocellular carcinoma. Clin Cancer Res. 2013;19(9):2310-8.
258. Zhu AX, Finn RS, Mulcahy M, Gurtler J, Sun W, Schwartz JD, et al. A phase II and biomarker study of ramucirumab, a human monoclonal antibody targeting the VEGF receptor-2, as first-line monotherapy in patients with advanced hepatocellular cancer. Clin Cancer Res. 2013;19(23):6614-23.
259. Brahmer JR, Tykodi SS, Chow LQ, Hwu WJ, Topalian SL, Hwu P, et al. Safety and activity of anti-PD-L1 antibody in patients with advanced cancer. N Engl J Med. 2012;366(26):2455-65.
260. Finn RS, Qin S, Ikeda M, Galle PR, Ducreux M, Kim TY, et al. Atezolizumab plus Bevacizumab in Unresectable Hepatocellular Carcinoma. N Engl J Med. 2020;382(20):1894-905.
261. Finn RS, Qin S, Ikeda M, Galle PR, Ducreux M, Kim T-Y, et al. IMbrave150: Updated overall survival (OS) data from a global, randomized, open-label phase III study of atezolizumab (atezo) + bevacizumab (bev) versus sorafenib (sor) in patients (pts) with unresectable hepatocellular carcinoma (HCC). Journal of Clinical Oncology. 2021;39(3_suppl):267-.
262. El-Khoueiry AB, Sangro B, Yau T, Crocenzi TS, Kudo M, Hsu C, et al. Nivolumab in patients with advanced hepatocellular carcinoma (CheckMate 040): an open-label, non-comparative, phase 1/2 dose escalation and expansion trial. Lancet. 2017;389(10088):2492-502.
263. Zhu AX, Finn RS, Edeline J, Cattan S, Ogasawara S, Palmer D, et al. Pembrolizumab in patients with advanced hepatocellular carcinoma previously treated with sorafenib (KEYNOTE-224): a non-randomised, open-label phase 2 trial. Lancet Oncol. 2018;19(7):940-52.
264. Yau T, Park JW, Finn RS, Cheng AL, Mathurin P, Edeline J, et al. LBA38_PR - CheckMate 459: A randomized, multi-center phase III study of nivolumab (NIVO) vs sorafenib (SOR) as first-line (1L) treatment in patients (pts) with advanced hepatocellular carcinoma (aHCC). Annals of Oncology. 2019;30:v874-v5.
265. Finn RS, Ryoo BY, Merle P, Kudo M, Bouattour M, Lim HY, et al. Pembrolizumab As Second-Line Therapy in Patients With Advanced Hepatocellular Carcinoma in KEYNOTE-240: A Randomized, Double-Blind, Phase III Trial. J Clin Oncol. 2020;38(3):193-202.
266. Yau T, Kang Y-K, Kim T-Y, El-Khoueiry AB, Santoro A, Sangro B, et al. Efficacy and Safety of Nivolumab Plus Ipilimumab in Patients With Advanced Hepatocellular Carcinoma Previously Treated With Sorafenib: The CheckMate 040 Randomized Clinical Trial. JAMA Oncology. 2020;6(11):e204564-e.
267. Medicine UNLo. A Study of Nivolumab in Combination With Ipilimumab in Participants With Advanced Hepatocellular Carcinoma (CheckMate 9DW) ClinicalTrials.gov2019 [Available from: https://clinicaltrials.gov/ct2/show/NCT04039607.

268. Pfister D, Núñez NG, Pinyol R, Govaere O, Pinter M, Szydlowska M, et al. NASH limits anti-tumour surveillance in immunotherapy-treated HCC. Nature. 2021;592(7854):450-6.
269. Leslie J, Mackey JBG, Jamieson T, Ramon-Gil E, Drake TM, Fercoq F, et al. CXCR2 inhibition enables NASH-HCC immunotherapy. Gut. 2022;71(10):2093-106.
270. Finn RS, Ikeda M, Zhu AX, Sung MW, Baron AD, Kudo M, et al. Phase Ib Study of Lenvatinib Plus Pembrolizumab in Patients With Unresectable Hepatocellular Carcinoma. J Clin Oncol. 2020;38(26):2960-70.
271. Torrens L, Montironi C, Puigvehí M, Mesropian A, Leslie J, Haber PK, et al. Immunomodulatory Effects of Lenvatinib Plus Anti–Programmed Cell Death Protein 1 in Mice and Rationale for Patient Enrichment in Hepatocellular Carcinoma. Hepatology. 2021;74(5).
272. Kelley RK, Rimassa L, Cheng AL, Kaseb A, Qin S, Zhu AX, et al. Cabozantinib plus atezolizumab versus sorafenib for advanced hepatocellular carcinoma (COSMIC-312): a multicentre, open-label, randomised, phase 3 trial. Lancet Oncol. 2022;23(8):995-1008.
273. Bonaventura P, Shekarian T, Alcazer V, Valladeau-Guilemond J, Valsesia-Wittmann S, Amigorena S, et al. Cold Tumors: A Therapeutic Challenge for Immunotherapy. Front Immunol. 2019;10:168-.
274. Hou AJ, Chen LC, Chen YY. Navigating CAR-T cells through the solid-tumour microenvironment. Nature Reviews Drug Discovery. 2021;20(7):531-50.
275. Sterner RC, Sterner RM. CAR-T cell therapy: current limitations and potential strategies. Blood Cancer Journal. 2021;11(4):69.
276. Yáñez L, Sánchez-Escamilla M, Perales MA. CAR T Cell Toxicity: Current Management and Future Directions. Hemasphere. 2019;3(2):e186.
277. Ikeda M, Okusaka T, Ohno I, Mitsunaga S, Kondo S, Ueno H, et al. Phase I studies of peptide vaccine cocktails derived from GPC3, WDRPUH and NEIL3 for advanced hepatocellular carcinoma. Immunotherapy. 2021;13(5):371-85.
278. Guo M, Zhang H, Zheng J, Liu Y. Glypican-3: A New Target for Diagnosis and Treatment of Hepatocellular Carcinoma. J Cancer. 2020;11(8):2008-21.
279. Docta RY, Ferronha T, Sanderson JP, Weissensteiner T, Pope GR, Bennett AD, et al. Tuning T-Cell Receptor Affinity to Optimize Clinical Risk-Benefit When Targeting Alpha-Fetoprotein-Positive Liver Cancer. Hepatology. 2019;69(5):2061-75.
280. Hay M, Thomas DW, Craighead JL, Economides C, Rosenthal J. Clinical development success rates for investigational drugs. Nature Biotechnology. 2014;32(1):40-51.
281. Oakley F, Gee LM, Sheerin NS, Borthwick LA. Implementation of pre-clinical methodologies to study fibrosis and test anti-fibrotic therapy. Current Opinion in Pharmacology. 2019;49:95-101.
282. Caruso S, Calatayud AL, Pilet J, La Bella T, Rekik S, Imbeaud S, et al. Analysis of Liver Cancer Cell Lines Identifies Agents With Likely Efficacy Against Hepatocellular Carcinoma and Markers of Response. Gastroenterology. 2019;157(3):760-76.
283. Blidisel A, Marcovici I, Coricovac D, Hut F, Dehelean CA, Cretu OM. Experimental Models of Hepatocellular Carcinoma-A Preclinical Perspective. Cancers (Basel). 2021;13(15).
284. López-Terrada D, Cheung SW, Finegold MJ, Knowles BB. Hep G2 is a hepatoblastoma-derived cell line. Hum Pathol. 2009;40(10):1512-5.
285. Godoy P, Hewitt NJ, Albrecht U, Andersen ME, Ansari N, Bhattacharya S, et al. Recent advances in 2D and 3D in vitro systems using primary hepatocytes, alternative hepatocyte sources and non-parenchymal liver cells and their use in investigating mechanisms of hepatotoxicity, cell signaling and ADME. Arch Toxicol. 2013;87(8):1315-530.

286. Jensen C, Teng Y. Is It Time to Start Transitioning From 2D to 3D Cell Culture? Frontiers in Molecular Biosciences. 2020;7(33).
287. Gómez-Lechón MJ, Donato MT, Castell JV, Jover R. Human hepatocytes as a tool for studying toxicity and drug metabolism. Curr Drug Metab. 2003;4(4):292-312.
288. Ponsoda X, Pareja E, Gómez-Lechón MJ, Fabra R, Carrasco E, Trullenque R, et al. Drug biotransformation by human hepatocytes. In vitro/in vivo metabolism by cells from the same donor. Journal of hepatology. 2001;34(1):19-25.
289. Quevedo R, Smirnov P, Tkachuk D, Ho C, El-Hachem N, Safikhani Z, et al. Assessment of Genetic Drift in Large Pharmacogenomic Studies. Cell Syst. 2020;11(4):393-401.e2.
290. Brown ZJ, Heinrich B, Greten TF. Mouse models of hepatocellular carcinoma: an overview and highlights for immunotherapy research. Nature Reviews Gastroenterology & Hepatology. 2018;15(9):536-54.
291. Heindryckx F, Colle I, Van Vlierberghe H. Experimental mouse models for hepatocellular carcinoma research. International journal of experimental pathology. 2009;90(4):367-86.
292. Newell P, Villanueva A, Friedman SL, Koike K, Llovet JM. Experimental models of hepatocellular carcinoma. Journal of hepatology. 2008;48(5):858-79.
293. Katz SF, Lechel A, Obenauf AC, Begus-Nahrmann Y, Kraus JM, Hoffmann EM, et al. Disruption of Trp53 in livers of mice induces formation of carcinomas with bilineal differentiation. Gastroenterology. 2012;142(5):1229-39.e3.
294. Liu Y, Qi X, Zeng Z, Wang L, Wang J, Zhang T, et al. CRISPR/Cas9-mediated p53 and Pten dual mutation accelerates hepatocarcinogenesis in adult hepatitis B virus transgenic mice. Scientific Reports. 2017;7(1):2796.
295. Conner EA, Lemmer ER, Omori M, Wirth PJ, Factor VM, Thorgeirsson SS. Dual functions of E2F-1 in a transgenic mouse model of liver carcinogenesis. Oncogene. 2000;19(44):5054-62.
296. Pitot HC, Dragan YP. Facts and theories concerning the mechanisms of carcinogenesis. Faseb j. 1991;5(9):2280-6.
297. Kawanishi S, Hiraku Y, Murata M, Oikawa S. The role of metals in site-specific DNA damage with reference to carcinogenesis. Free Radic Biol Med. 2002;32(9):822-32.
298. Verna L, Whysner J, Williams GM. N-nitrosodiethylamine mechanistic data and risk assessment: bioactivation, DNA-adduct formation, mutagenicity, and tumor initiation. Pharmacol Ther. 1996;71(1-2):57-81.
299. Uehara T, Pogribny IP, Rusyn I. The DEN and CCl4-Induced Mouse Model of Fibrosis and Inflammation-Associated Hepatocellular Carcinoma. Current Protocols in Pharmacology. 2014;66(1):14.30.1-14.30.10.
300. Hansen HH, Ægidius HM, Oró D, Evers SS, Heebøll S, Eriksen PL, et al. Human translatability of the GAN diet-induced obese mouse model of non-alcoholic steatohepatitis. BMC Gastroenterol. 2020;20(1):210.
301. Ikawa-Yoshida A, Matsuo S, Kato A, Ohmori Y, Higashida A, Kaneko E, et al. Hepatocellular carcinoma in a mouse model fed a choline-deficient, L-amino acid-defined, high-fat diet. Int J Exp Pathol. 2017;98(4):221-33.
302. He L, Tian DA, Li PY, He XX. Mouse models of liver cancer: Progress and recommendations. Oncotarget. 2015;6(27):23306-22.
303. Gu CY, Lee TKW. Preclinical mouse models of hepatocellular carcinoma: An overview and update. Experimental Cell Research. 2022;412(2):113042.

304. He JD, Wang Z, Li SP, Xu YJ, Yu Y, Ding YJ, et al. Vitexin suppresses autophagy to induce apoptosis in hepatocellular carcinoma via activation of the JNK signaling pathway. Oncotarget. 2016;7(51):84520-32.
305. Kim KJ, Kim JH, Lee SJ, Lee EJ, Shin EC, Seong J. Radiation improves antitumor effect of immune checkpoint inhibitor in murine hepatocellular carcinoma model. Oncotarget. 2017;8(25):41242-55.
306. Zhang SS, Ni YH, Zhao CR, Qiao Z, Yu HX, Wang LY, et al. Capsaicin enhances the antitumor activity of sorafenib in hepatocellular carcinoma cells and mouse xenograft tumors through increased ERK signaling. Acta Pharmacol Sin. 2018;39(3):438-48.
307. Lee DH, Nam JY, Chang Y, Cho H, Kang SH, Cho YY, et al. Synergistic effect of cytokine-induced killer cell with valproate inhibits growth of hepatocellular carcinoma cell in a mouse model. Cancer Biol Ther. 2017;18(1):67-75.
308. Morton JJ, Bird G, Refaeli Y, Jimeno A. Humanized Mouse Xenograft Models: Narrowing the Tumor-Microenvironment Gap. Cancer Res. 2016;76(21):6153-8.
309. Day CP, Merlino G, Van Dyke T. Preclinical mouse cancer models: a maze of opportunities and challenges. Cell. 2015;163(1):39-53.
310. Allen TM, Brehm MA, Bridges S, Ferguson S, Kumar P, Mirochnitchenko O, et al. Humanized immune system mouse models: progress, challenges and opportunities. Nat Immunol. 2019;20(7):770-4.
311. Collins SD, Yuen G, Tu T, Budzinska MA, Spring K, Bryant K, et al. In Vitro Models of the Liver: Disease Modeling, Drug Discovery and Clinical Applications. In: Tirnitz-Parker JEE, editor. Hepatocellular Carcinoma. Brisbane (AU): Codon Publications

312. Nuciforo S, Fofana I, Matter MS, Blumer T, Calabrese D, Boldanova T, et al. Organoid Models of Human Liver Cancers Derived from Tumor Needle Biopsies. Cell Reports. 2018;24(5):1363-76.
313. Broutier L, Mastrogiovanni G, Verstegen MMA, Francies HE, Gavarró LM, Bradshaw CR, et al. Human primary liver cancer–derived organoid cultures for disease modeling and drug screening. Nature Medicine. 2017;23(12):1424-35.
314. Weiswald L-B, Bellet D, Dangles-Marie V. Spherical Cancer Models in Tumor Biology. Neoplasia. 2015;17(1):1-15.
315. Friedrich J, Seidel C, Ebner R, Kunz-Schughart LA. Spheroid-based drug screen: considerations and practical approach. Nature Protocols. 2009;4(3):309-24.
316. Nath S, Devi GR. Three-dimensional culture systems in cancer research: Focus on tumor spheroid model. Pharmacology & therapeutics. 2016;163:94-108.
317. Song Y, Kim S-h, Kim KM, Choi EK, Kim J, Seo HR. Activated hepatic stellate cells play pivotal roles in hepatocellular carcinoma cell chemoresistance and migration in multicellular tumor spheroids. Scientific Reports. 2016;6(1):36750.
318. Jung H-R, Kang HM, Ryu J-W, Kim D-S, Noh KH, Kim E-S, et al. Cell Spheroids with Enhanced Aggressiveness to Mimic Human Liver Cancer In Vitro and In Vivo. Scientific Reports. 2017;7(1):10499.
319. Lee S-Y, Hwang HJ, Lee DW. Optimization of 3D-aggregated spheroid model (3D-ASM) for selecting high efficacy drugs. Scientific Reports. 2022;12(1):18937.
320. Lee SY, Teng Y, Son M, Ku B, Hwang HJ, Tergaonkar V, et al. Three-Dimensional Aggregated Spheroid Model of Hepatocellular Carcinoma Using a 96-Pillar/Well Plate. Molecules. 2021;26(16).

321. Leung CM, de Haan P, Ronaldson-Bouchard K, Kim G-A, Ko J, Rho HS, et al. A guide to the organ-on-a-chip. Nature Reviews Methods Primers. 2022;2(1):33.
322. Low LA, Mummery C, Berridge BR, Austin CP, Tagle DA. Organs-on-chips: into the next decade. Nature Reviews Drug Discovery. 2021;20(5):345-61.
323. Zhu J, Ji L, Chen Y, Li H, Huang M, Dai Z, et al. Organoids and organs-on-chips: insights into predicting the efficacy of systemic treatment in colorectal cancer. Cell Death Discovery. 2023;9(1):72.
324. Zhang X, Wang T, Wang P, Hu N. High-Throughput Assessment of Drug Cardiac Safety Using a High-Speed Impedance Detection Technology-Based Heart-on-a-Chip. Micromachines (Basel). 2016;7(7).
325. Shik Mun K, Arora K, Huang Y, Yang F, Yarlagadda S, Ramananda Y, et al. Patient-derived pancreas-on-a-chip to model cystic fibrosis-related disorders. Nat Commun. 2019;10(1):3124.
326. Musah S, Dimitrakakis N, Camacho DM, Church GM, Ingber DE. Directed differentiation of human induced pluripotent stem cells into mature kidney podocytes and establishment of a Glomerulus Chip. Nat Protoc. 2018;13(7):1662-85.
327. Esch MB, Mahler GJ, Stokol T, Shuler ML. Body-on-a-chip simulation with gastrointestinal tract and liver tissues suggests that ingested nanoparticles have the potential to cause liver injury. Lab Chip. 2014;14(16):3081-92.
328. Vunjak-Novakovic G, Ronaldson-Bouchard K, Radisic M. Organs-on-a-chip models for biological research. Cell. 2021;184(18):4597-611.
329. Ashammakhi N, Ahadian S, Xu C, Montazerian H, Ko H, Nasiri R, et al. Bioinks and bioprinting technologies to make heterogeneous and biomimetic tissue constructs. Materials Today Bio. 2019;1:100008.
330. Rosales AM, Anseth KS. The design of reversible hydrogels to capture extracellular matrix dynamics. Nature Reviews Materials. 2016;1(2):15012.
331. Montalbano G, Toumpaniari S, Popov A, Duan P, Chen J, Dalgarno K, et al. Synthesis of bioinspired collagen/alginate/fibrin based hydrogels for soft tissue engineering. Materials Science and Engineering: C. 2018;91:236-46.
332. da Conceicao Ribeiro R, Pal D, Ferreira AM, Gentile P, Benning M, Dalgarno K. Reactive jet impingement bioprinting of high cell density gels for bone microtissue fabrication. Biofabrication. 2018;11(1):015014.
333. Skardal A, Devarasetty M, Kang H-W, Mead I, Bishop C, Shupe T, et al. A hydrogel bioink toolkit for mimicking native tissue biochemical and mechanical properties in bioprinted tissue constructs. Acta Biomaterialia. 2015;25:24-34.
334. Sun L, Yang H, Wang Y, Zhang X, Jin B, Xie F, et al. Application of a 3D Bioprinted Hepatocellular Carcinoma Cell Model in Antitumor Drug Research. Frontiers in Oncology. 2020;10(878).
335. Xie F, Sun L, Pang Y, Xu G, Jin B, Xu H, et al. Three-dimensional bio-printing of primary human hepatocellular carcinoma for personalized medicine. Biomaterials. 2021;265:120416.
336. Kolesky DB, Truby RL, Gladman AS, Busbee TA, Homan KA, Lewis JA. 3D bioprinting of vascularized, heterogeneous cell-laden tissue constructs. Adv Mater. 2014;26(19):3124-30.
337. Kolesky DB, Homan KA, Skylar-Scott MA, Lewis JA. Three-dimensional bioprinting of thick vascularized tissues. Proc Natl Acad Sci U S A. 2016;113(12):3179-84.
338. Nguyen DG, Funk J, Robbins JB, Crogan-Grundy C, Presnell SC, Singer T, et al. Bioprinted 3D Primary Liver Tissues Allow Assessment of Organ-Level Response to Clinical Drug Induced Toxicity In Vitro. PLOS ONE. 2016;11(7):e0158674.

339. Palma E, Doornebal EJ, Chokshi S. Precision-cut liver slices: a versatile tool to advance liver research. Hepatol Int. 2019;13(1):51-7.
340. Paish HL, Reed LH, Brown H, Bryan MC, Govaere O, Leslie J, et al. A Bioreactor Technology for Modeling Fibrosis in Human and Rodent Precision-Cut Liver Slices. Hepatology. 2019;70(4):1377-91.
341. Westra IM, Mutsaers HAM, Luangmonkong T, Hadi M, Oosterhuis D, de Jong KP, et al. Human precision-cut liver slices as a model to test antifibrotic drugs in the early onset of liver fibrosis. Toxicology in Vitro. 2016;35:77-85.
342. Koch A, Saran S, Tran DDH, Klebba-Färber S, Thiesler H, Sewald K, et al. Murine precision-cut liver slices (PCLS): a new tool for studying tumor microenvironments and cell signaling ex vivo. Cell Commun Signal. 2014;12:73-.
343. Unger F, Bentz S, Kruger J, Rosenbrock C, Schaller J, Pursche K, et al. Precision Cut Cancer Tissue Slices in Anti-Cancer Drug Testing. Journal of Molecular Pathophysiology. 2015;4:108.
344. Roelants C, Pillet C, Franquet Q, Sarrazin C, Peilleron N, Giacosa S, et al. Ex-Vivo Treatment of Tumor Tissue Slices as a Predictive Preclinical Method to Evaluate Targeted Therapies for Patients with Renal Carcinoma. Cancers (Basel). 2020;12(1).
345. Parajuli N, Doppler W. Precision-cut slice cultures of tumors from MMTV-neu mice for the study of the ex vivo response to cytokines and cytotoxic drugs. In Vitro Cell Dev Biol Anim. 2009;45(8):442-50.
346. Brown ZJ, Heinrich B, Greten TF. Mouse models of hepatocellular carcinoma: an overview and highlights for immunotherapy research. Nat Rev Gastroenterol Hepatol. 2018;15(9):536-54.
347. Wu T, Heuillard E, Lindner V, Bou About G, Ignat M, Dillenseger JP, et al. Multimodal imaging of a humanized orthotopic model of hepatocellular carcinoma in immunodeficient mice. Sci Rep. 2016;6:35230.
348. Hollands C. The Animals (scientific procedures) Act 1986. Lancet. 1986;2(8497):32-3.
349. Hubrecht RC, Carter E. The 3Rs and Humane Experimental Technique: Implementing Change. Animals (Basel). 2019;9(10).
350. Davies EJ, Dong M, Gutekunst M, Närhi K, van Zoggel HJAA, Blom S, et al. Capturing complex tumour biology in vitro: histological and molecular characterisation of precision cut slices. Scientific Reports. 2015;5(1):17187.
351. Kern MA, Haugg AM, Eiteneuer E, Konze E, Drebber U, Dienes HP, et al. Ex vivo analysis of antineoplastic agents in precision-cut tissue slices of human origin: effects of cyclooxygenase-2 inhibition in hepatocellular carcinoma. Liver Int. 2006;26(5):604-12.
352. Dimou P, Trivedi S, Liousia M, D'Souza RR, Klampatsa A. Precision-Cut Tumor Slices (PCTS) as an Ex Vivo Model in Immunotherapy Research. Antibodies (Basel). 2022;11(2).
353. Koch A, Saran S, Tran DD, Klebba-Färber S, Thiesler H, Sewald K, et al. Murine precision-cut liver slices (PCLS): a new tool for studying tumor microenvironments and cell signaling ex vivo. Cell Commun Signal. 2014;12:73.
354. Sivakumar R, Chan M, Shin JS, Nishida-Aoki N, Kenerson HL, Elemento O, et al. Organotypic tumor slice cultures provide a versatile platform for immuno-oncology and drug discovery. Oncoimmunology. 2019;8(12):e1670019.
355. Yan M, Li H, Zhao F, Zhang L, Ge C, Yao M, et al. Establishment of NOD/SCID mouse models of human hepatocellular carcinoma via subcutaneous transplantation of histologically intact tumor tissue. Chin J Cancer Res. 2013;25(3):289-98.

356. Xin H, Wang K, Hu G, Xie F, Ouyang K, Tang X, et al. Establishment and characterization of 7 novel hepatocellular carcinoma cell lines from patient-derived tumor xenografts. PLoS One. 2014;9(1):e85308.
357. Ma X, Shen D, Li H, Zhang Y, Lv X, Huang Q, et al. MicroRNA-185 inhibits cell proliferation and induces cell apoptosis by targeting VEGFA directly in von Hippel-Lindau-inactivated clear cell renal cell carcinoma. Urol Oncol. 2015;33(4):169.e1-11.
358. Zeng FC, Zeng MQ, Huang L, Li YL, Gao BM, Chen JJ, et al. Downregulation of VEGFA inhibits proliferation, promotes apoptosis, and suppresses migration and invasion of renal clear cell carcinoma. Onco Targets Ther. 2016;9:2131-41.
359. Guo C, Sharp A, Gurel B, Crespo M, Figueiredo I, Jain S, et al. Targeting myeloid chemotaxis to reverse prostate cancer therapy resistance. Nature. 2023.
360. Wang GG, Calvo KR, Pasillas MP, Sykes DB, Häcker H, Kamps MP. Quantitative production of macrophages or neutrophils ex vivo using conditional Hoxb8. Nat Methods. 2006;3(4):287-93.
361. Khoyratty TE, Ai Z, Ballesteros I, Eames HL, Mathie S, Martín-Salamanca S, et al. Distinct transcription factor networks control neutrophil-driven inflammation. Nat Immunol. 2021;22(9):1093-106.
362. Jagatia R, Doornebal EJ, Rastovic U, Harris N, Feyide M, Lyons AM, et al. Patient-derived precision cut tissue slices from primary liver cancer as a potential platform for preclinical drug testing. EBioMedicine. 2023;97:104826.
363. Zheng H, Peng X, Yang S, Li X, Huang M, Wei S, et al. Targeting tumor-associated macrophages in hepatocellular carcinoma: biology, strategy, and immunotherapy. Cell Death Discovery. 2023;9(1):65.
364. Tian Z, Hou X, Liu W, Han Z, Wei L. Macrophages and hepatocellular carcinoma. Cell & Bioscience. 2019;9(1):79.
365. Winkler J, Abisoye-Ogunniyan A, Metcalf KJ, Werb Z. Concepts of extracellular matrix remodelling in tumour progression and metastasis. Nature Communications. 2020;11(1):5120.
366. Weiswald LB, Bellet D, Dangles-Marie V. Spherical cancer models in tumor biology. Neoplasia. 2015;17(1):1-15.
367. Friedrich J, Seidel C, Ebner R, Kunz-Schughart LA. Spheroid-based drug screen: considerations and practical approach. Nat Protoc. 2009;4(3):309-24.
368. Jung HR, Kang HM, Ryu JW, Kim DS, Noh KH, Kim ES, et al. Cell Spheroids with Enhanced Aggressiveness to Mimic Human Liver Cancer In Vitro and In Vivo. Sci Rep. 2017;7(1):10499.
369. van Os EA, Cools L, Eysackers N, Szafranska K, Smout A, Verhulst S, et al. Modelling fatty liver disease with mouse liver-derived multicellular spheroids. Biomaterials. 2022;290:121817.
370. Kubo N, Araki K, Kuwano H, Shirabe K. Cancer-associated fibroblasts in hepatocellular carcinoma. World J Gastroenterol. 2016;22(30):6841-50.
371. Au - Zaki MYW, Au - Shetty S, Au - Wilkinson AL, Au - Patten DA, Au - Oakley F, Au - Reeves H. A Three-Dimensional Spheroid Model to Investigate the Tumor-Stromal Interaction in Hepatocellular Carcinoma. JoVE. 2021(175):e62868.
372. England CG, Ehlerding EB, Cai W. NanoLuc: A Small Luciferase Is Brightening Up the Field of Bioluminescence. Bioconjug Chem. 2016;27(5):1175-87.
373. Walker JR, Hall MP, Zimprich CA, Robers MB, Duellman SJ, Machleidt T, et al. Highly Potent Cell-Permeable and Impermeable NanoLuc Luciferase Inhibitors. ACS Chem Biol. 2017;12(4):1028-37.

374. Lee S-Y, Teng Y, Son M, Ku B, Hwang HJ, Tergaonkar V, et al. Three-Dimensional Aggregated Spheroid Model of Hepatocellular Carcinoma Using a 96-Pillar/Well Plate. Molecules [Internet]. 2021; 26(16).
375. Rodríguez-Hernández MA, Chapresto-Garzón R, Cadenas M, Navarro-Villarán E, Negrete M, Gómez-Bravo MA, et al. Differential effectiveness of tyrosine kinase inhibitors in 2D/3D culture according to cell differentiation, p53 status and mitochondrial respiration in liver cancer cells. Cell Death & Disease. 2020;11(5):339.
376. Sangro B, Sarobe P, Hervás-Stubbs S, Melero I. Advances in immunotherapy for hepatocellular carcinoma. Nature Reviews Gastroenterology & Hepatology. 2021;18(8):525-43.
377. Depil S, Duchateau P, Grupp SA, Mufti G, Poirot L. 'Off-the-shelf' allogeneic CAR T cells: development and challenges. Nature Reviews Drug Discovery. 2020;19(3):185-99.
378. Kaszubowska L, Foerster J, Kmieć Z. NKT-like (CD3 + CD56+) cells differ from T cells in expression level of cellular protective proteins and sensitivity to stimulation in the process of ageing. Immunity & Ageing. 2022;19(1):18.
379. Huang WC, Easom NJ, Tang XZ, Gill US, Singh H, Robertson F, et al. T Cells Infiltrating Diseased Liver Express Ligands for the NKG2D Stress Surveillance System. J Immunol. 2017;198(3):1172-82.
380. Jayaraman A, Jackson DJ, Message SD, Pearson RM, Aniscenko J, Caramori G, et al. IL-15 complexes induce NK- and T-cell responses independent of type I IFN signaling during rhinovirus infection. Mucosal Immunology. 2014;7(5):1151-64.
381. van Beijnum JR, Huijbers EJM, van Loon K, Blanas A, Akbari P, Roos A, et al. Extracellular vimentin mimics VEGF and is a target for anti-angiogenic immunotherapy. Nature Communications. 2022;13(1):2842.
382. Nakabayashi H, Taketa K, Miyano K, Yamane T, Sato J. Growth of human hepatoma cells lines with differentiated functions in chemically defined medium. Cancer Res. 1982;42(9):3858-63.
383. Ben-David U, Siranosian B, Ha G, Tang H, Oren Y, Hinohara K, et al. Genetic and transcriptional evolution alters cancer cell line drug response. Nature. 2018;560(7718):325-30.
384. Hughes P, Marshall D, Reid Y, Parkes H, Gelber C. The costs of using unauthenticated, over-passaged cell lines: how much more data do we need? Biotechniques. 2007;43(5):575, 7-8, 81-2 passim.
385. Centenera MM, Raj GV, Knudsen KE, Tilley WD, Butler LM. Ex vivo culture of human prostate tissue and drug development. Nat Rev Urol. 2013;10(8):483-7.
386. Pastor DM, Poritz LS, Olson TL, Kline CL, Harris LR, Koltun WA, et al. Primary cell lines: false representation or model system? a comparison of four human colorectal tumors and their coordinately established cell lines. Int J Clin Exp Med. 2010;3(1):69-83.
387. Mouriaux F, Zaniolo K, Bergeron M-A, Weidmann C, De La Fouchardière A, Fournier F, et al. Effects of Long-term Serial Passaging on the Characteristics and Properties of Cell Lines Derived From Uveal Melanoma Primary Tumors. Investigative Ophthalmology & Visual Science. 2016;57(13):5288-301.
388. Kar R, Sharma C, Sen S, Jain SK, Gupta SD, Singh N. Response of primary culture of human ovarian cancer cells to chemotherapy: In vitro individualized therapy. J Cancer Res Ther. 2016;12(2):1050-5.
389. Gambardella V, Tarazona N, Cejalvo JM, Lombardi P, Huerta M, Roselló S, et al. Personalized Medicine: Recent Progress in Cancer Therapy. Cancers (Basel). 2020;12(4).

390. Broutier L, Mastrogiovanni G, Verstegen MM, Francies HE, Gavarró LM, Bradshaw CR, et al. Human primary liver cancer-derived organoid cultures for disease modeling and drug screening. Nat Med. 2017;23(12):1424-35.
391. Wang X, Ding J, Feng Y, Weng L, Zhao G, Xiang J, et al. Targeting of growth factors in the treatment of hepatocellular carcinoma: The potentials of polysaccharides. Oncol Lett. 2017;13(3):1509-17.
392. Hou J, Zhang H, Sun B, Karin M. The immunobiology of hepatocellular carcinoma in humans and mice: Basic concepts and therapeutic implications. J Hepatol. 2020;72(1):167-82.
393. Nath S, Devi GR. Three-dimensional culture systems in cancer research: Focus on tumor spheroid model. Pharmacol Ther. 2016;163:94-108.
394. Nielsen SR, Quaranta V, Linford A, Emeagi P, Rainer C, Santos A, et al. Macrophage-secreted granulin supports pancreatic cancer metastasis by inducing liver fibrosis. Nat Cell Biol. 2016;18(5):549-60.
395. Quaranta V, Rainer C, Nielsen SR, Raymant ML, Ahmed MS, Engle DD, et al. Macrophage-Derived Granulin Drives Resistance to Immune Checkpoint Inhibition in Metastatic Pancreatic Cancer. Cancer Res. 2018;78(15):4253-69.
396. Weiskopf K, Jahchan NS, Schnorr PJ, Cristea S, Ring AM, Maute RL, et al. CD47-blocking immunotherapies stimulate macrophage-mediated destruction of small-cell lung cancer. J Clin Invest. 2016;126(7):2610-20.
397. Llovet JM, Zucman-Rossi J, Pikarsky E, Sangro B, Schwartz M, Sherman M, et al. Hepatocellular carcinoma. Nat Rev Dis Primers. 2016;2:16018.
398. Kumar BV, Connors TJ, Farber DL. Human T Cell Development, Localization, and Function throughout Life. Immunity. 2018;48(2):202-13.
399. Weiskopf K, Schnorr PJ, Pang WW, Chao MP, Chhabra A, Seita J, et al. Myeloid Cell Origins, Differentiation, and Clinical Implications. Microbiol Spectr. 2016;4(5).
400. Montalbano G, Toumpaniari S, Popov A, Duan P, Chen J, Dalgarno K, et al. Synthesis of bioinspired collagen/alginate/fibrin based hydrogels for soft tissue engineering. Mater Sci Eng C Mater Biol Appl. 2018;91:236-46.
401. Mancha Sánchez E, Gómez-Blanco JC, López Nieto E, Casado JG, Macías-García A, Díaz Díez MA, et al. Hydrogels for Bioprinting: A Systematic Review of Hydrogels Synthesis, Bioprinting Parameters, and Bioprinted Structures Behavior. Front Bioeng Biotechnol. 2020;8:776.